Reflectivity Ferromagnetic Resonance For Layer-Resolved Dynamic Study of Multi-Layered Systems



Jack Bollard

Lady Margaret Hall

Department of Physics

University of Oxford

A thesis submitted for the degree of

Doctor of Philosophy

October 2025

Abstract

This thesis develops and applies *Reflectivity Ferromagnetic Resonance* (RFMR) as a novel technique for probing depth-resolved magnetisation dynamics in magnetic thin films and multilayers. By combining the depth resolution of X-ray Resonant Magnetic Reflectivity (XRMR) with the temporal control of X-ray detected Ferromagnetic Resonance (XFMR), RFMR enables the reconstruction of layer-specific precessional motion on the nanometre scale with picosecond resolution.

After establishing the necessary understanding of optical properties in RFMR and the advanced modelling required to interpret the data, we demonstrate the capabilities of RFMR through three progressive case studies. First, we examine a NiFe single-layer magnetic film, which exhibits a uniform mode alongside indications of damped precession at the interfaces. Here, we show that the RFMR signal is sensitive to the waveform of the RF driving field. This sensitivity is leveraged to distinguish the FMR modal structure under different waveform excitations (sinusoidal versus distorted).

In the second case, we investigate magnetic trilayers with different ferromagnetic layers separated by a Chromium spacer. Vibrating Sample Magnetometry (VSM) and Vector Network Analyzer Ferromagnetic Resonance (VNA-FMR) reveals distinct, interlayer-coupled modes (acoustic and optical). RFMR measurements reveal this allows for the engineering of the trilayer's depth-profile by tuning the applied static field across the resonance conditions.

Finally, we explore a complex $[\mathrm{Ta/CoFeB/MgO}]_4$ heterostructure stack, where the FMR modes exhibit depth-dependent profiles that can be uniquely identified only in RFMR. Using VSM, VNA-FMR, Magnetic Force Microscopy and micromagnetic simulations, we identify a Spin-Reorientation Transition (SRT) as t_{CoFeB} is varied across 1.50 nm. XRMR and RFMR measurements reveal that the depth profile of the magnetisation undergoes significant changes across the SRT, with the dynamics becoming increasingly complex in thinner layers. Through RFMR measurements at multiple polarisations, we reconstruct the full three-dimensional magnetisation trajectories, uncovering signatures of nonlinearity critical for future spintronic computing architectures.

Acknowledgements

As I reach the end of this thesis, I am struck by the fact that very little of the last four years was ever truly done alone. If this project has taught me anything, it is that science is not an individual pursuit but a collective adventure, one held together by the expertise, patience, and good humour of those around me. To everyone who carried me through this journey: I am deeply grateful.

It has been a true honour to be part of the ambitious and exciting RFMR project. For guiding me through it, I thank my supervisors, Professor Gerrit van der Laan and Professor Thorsten Hesjedal. To Gerrit: despite being one of the most influential figures in our field, you always found time for my beamline work. Your daily presence during beamtime, whether driven by academic curiosity or hunting for tinned heron, was a source of immense support. To Thorsten: your technical guidance in Oxford, inquisitive ideas at Diamond, and your questionable yet unfailingly memorable YOUTUBE recommendations were all equally essential. It was a true honour to work with and learn from you both.

At the Clarendon Laboratory, I was surrounded by people whose knowledge and friendship defined my time there. Dr. Barat Achinuq and Dr. Angad Singh gave me both a grounding in the craft and the means to survive my earliest beamtimes. Dr. Safeer Chenattukuzhiyil, Dr. Ryuji Fujita, and Dr. JC Lin contributed immeasurable wisdom and guidance. And to Joshua Bibby, Emily Heppell, Ethan Arnold, Jacob Zohar, our collective crew of master's students, and the guys at LMH, thank you for the sanity, the cricket, and the constant reminder that research should still be fun.

I owe a great deal to the team at I10, who made Diamond feel like a second home. Dr. Raymond Fan and Dr. David Burn were the bedrock of this work, their meticulous expertise in X-ray reflectivity, RASOR, and magneto-optics made everything possible. To Mr. Mark Sussmuth, whose encyclopedic technical knowledge and uncanny ability to be in two places at once made the impossible look routine. Beyond them, my sincere thanks go to the entire I10 team for their constant support on both beamline branches, their contagious passion for the project, and for motivating me to join the RAL Rec Soc gym. On the topic of Diamond-based gratitude a shout-out to my Fatima House flatmates is also in

order, for the late-night chats that revealed the shared commonality of life on any beamline.

This project has a bright future, thanks in large part to our international collaborators, the 'Shang-gang'. The generosity of Professor Shilei Zhang's team in Shanghai has shaped this project in profound ways, from sample preparation and experimental design to remote night shifts conducted across the globe. For this I especially thank Dr. Kejing Ran, Dr. Haonan Jin, and Dr. Jinghui Wang, whose jet-lag endurance remains unparalleled, as well as Mr. Wang Yu, Ms. Jingyi Chen, and Mr. Chenhao Zhang, for the wonderful tours of SSRF and for being such gracious hosts at ShanghaiTech.

In truth, I am nothing but a mosaic of the people who have entered my life. This becomes clearest when I think of family and friends. To my parents, Maeve and Donal: thank you for your love, your enthusiasm, and for never letting me doubt that I could finish this. Thank you also for politely nodding along while I fumbled over scattering theory and neuromorphic computing to you at the dinner table. To my siblings, Louis, Eva, and Nessa: I simply do not thank, this was to spite you (though I suspect you know how grateful I really am). To my undergrad friends, who pushed me to pursue physics (and maybe try biology), and to my school friends, who knew exactly when to send holiday photos (at 2am during beamtimes): your timing was impeccable.

Finally, to Jen: your continuous support, motivation, and patience made this whole process not only bearable, but overwhelmingly joyful. I look forward to returning the favour.

And for the upcoming students joining the lab, my unsolicited advice: 1. Say yes to more opportunities, little in our work is imperative, but also less is impossible. 2. Learn to play chess, I've never met a member of OxMBE who couldn't. 3. Write your 3 am beamtime scripts at 3 pm.

"Jaja"

– Unknown, 2025

Contents

List of Abbreviations **8**

1 Motivations **10**

1.1 Innovation Within the Field of Magnetism 10

1.2 Why Do We Need Depth-Dependent FMR Techniques? 12

1.3 Thesis Outline 12

2 Introduction & Theoretical Background **15**

2.1 Magnetic Heterostructures & Their Interactions 15

2.2 Interlayer Coupling 18

2.3 Landau-Lifshitz-Gilbert Dynamics 19

2.4 Magneto-Optical Interactions 21

3 Experimental Techniques **27**

3.1 DC Magnetron Sputtering 28

3.2 Vector Network Analyzer Ferromagnetic Resonance 30

3.3 X-ray Resonant Magnetic Reflectivity 32

3.4 X-ray Detected Ferromagnetic Resonance 33

3.5 Reflectivity Ferromagnetic Resonance 34

4 Optical Properties of FMR modes **39**

4.1 Reflected Intensity from Phase-Modulated Magnetic Scattering 39

4.2 Calculation of the Optical Constants & Detection Techniques 40

4.3 Energy-Resolved RFMR & the Role of Charge Scattering 43

4.4 Moment Alignment Dependence 48

4.5 Energy & Polarisation Dependence 50

5 Building an RFMR model **52**

5.1 Mathematical Formalism Behind Reflectivity Calculations 52

5.2 Scattering Factor Considerations in RFMR 54

5.3 Macrospin Models, Magnetisation Precession & Susceptibility Tensor Formalism . . 56

5.4 Global Optimisation Based on Co-Fitting 58

5.5 Penalising Unphysical Results in the Optimiser 59

5.6 High-Dimensional Problems 61

5.7 Validating Best-Fit Models 62

6 Depth Profile of Magnetic Single Layers **64**

6.1 Micromagnetic Results 66

6.2 Sample Details 67

6.3 Experimental Details 68

6.4 Extracting Amplitude & Phase of the Dynamic Signal 71

6.5 Model Testing 73

6.5.1 Sensitivity Analysis 75

6.5.2 Model Limitations & Complexity via Sobol Indexing 76

6.6 Waveform Effects 78

7 Depth Profile of Magnetic Trilayers **84**

7.1 Motivations 85

7.2 Sample Growth & Characterisation 86

7.2.1 Interlayer Exchange Coupling 87

7.2.2 Dynamic Coupling 89

7.3 Sample Selection & Characterisation 92

7.4 Acoustic & Optical Mode Detection Using RFMR 94

7.5 Element & Mode-Specific Scattering Factors 99

7.6 Mapping Depth-dependent Dynamical Structure in RFMR 102

7.7 Increasing Cr Thickness 106

7.8 Depth-Profile Induced by Dynamic Coupling 107

7.9 Sensitivity Analysis 110

8 Depth Profile of Complex Heterostructures **111**

8.1 Motivations 113

8.2 Susceptibility in Complex Heterostructures 114
8.3 Modal Structure in Complex Heterostructures 118
8.4 Preliminary Characterisation 121
8.4.1 Vibrating Sample Magnetometry 122
8.4.2 Ferromagnetic Resonance 124
8.5 XMCD & XRMR 126
8.5.1 Depth Profile via XRMR 127
8.6 Characterising Unique FMR Modes 130
8.6.1 Field Scan Results 130
8.6.2 Reflectivity Results 132
8.6.3 Sensitivity Analysis 136
8.7 Exploiting Spin-Reorientation to Generate Depth-Dependent Dynamics 137
8.7.1 Temperature Dependence 139
8.8 Beyond the Macrospin Model: Ultra-Dense Non-Linear Magnetisation Dynamics . . 140
8.8.1 Experimental Measurement of Complex Dynamics 142
8.8.2 Three-Dimensional Vectorial Precession of Complex Dynamics in Heterostructures 143
8.8.3 Device Implications 146

9 Conclusions & Outlook **148**

9.1 List of Contributions 150

List of Abbreviations

AFM Antiferromagnetic

AM Acoustic Mode

BLADE BeamLine for Advanced Dichroism Experiments

CPW Coplanar Waveguide

DE Differential Evolution

DFMR Diffractive Ferromagnetic Resonance

DMI Dzyaloshinskii-Moriya Interaction

FFT Fast Fourier Transform

FM Ferromagnetic

FMR Ferromagnetic Resonance

FY Fluorescence Yield

GLAD Glancing Angle Deposition

GMR Giant Magnetoresistance

IEC Interlayer Exchange Coupling

IP In-Plane

LAA Linear Arbitrary Angle

LIA Lock-In Amplifier

LLG Landau-Lifshitz-Gilbert

LL Load-Lock

MFM Magnetic Force Microscopy

MC Main Chamber

MTJ Magnetic Tunnel Junction

OM Optical Mode

OOMMF Object Oriented Micromagnetic Framework

OOP Out-of-Plane

PMA Perpendicular Magnetic Anisotropy

PNR Polarised Neutron Reflectometry

POMS Portable Octopole Magnetic System

PSD Power Spectral Density

PSSW Perpendicular Standing Spin Wave

PVD Physical Vapor Deposition

RASOR Reflectivity and Advanced Scattering of Ordered Regimes

REXS Resonant Elastic X-ray Scattering

RFMR Reflectivity Ferromagnetic Resonance

RKKY Ruderman-Kittel-Kasuya-Yosida

SAF Synthetic Antiferromagnet

SC Storage Chamber

SLD Scattering Length Density

SRS Synchrotron Radiation Source

SRT Spin-Reorientation Transition

STT Spin-Transfer Torque

TEY Total Electron Yield

TMR Tunneling Magnetoresistance

UHV Ultra-High Vacuum

VNA-FMR Vector Network Analyzer Ferromagnetic Resonance

VSM Vibrating Sample Magnetometry

X-FEL X-ray Free-Electron Laser

XEOL X-ray Excited Optical Luminescence

XFMR X-ray detected Ferromagnetic Resonance

XMCD X-ray Magnetic Circular Dichroism

XRMR X-ray Resonant Magnetic Reflectivity

XRR X-ray Reflectivity

Chapter 1

Motivations

1.1 Innovation Within the Field of Magnetism

The development of synchrotron radiation facilities has profoundly advanced the study of materials, enabling researchers to explore their structure and dynamics through the use of brilliant X-ray beams. The Synchrotron Radiation Source (SRS) at Daresbury Laboratory in the UK was a milestone in this evolution, becoming the first dedicated synchrotron light source when it began operations in 1980. Unlike earlier facilities, which primarily served high-energy physics, the SRS was specifically designed to exploit the unique properties of synchrotron radiation for a wide array of scientific disciplines [1]. Its versatility and intensity revolutionized experimental techniques, allowing researchers to probe the atomic-scale structure and electronic properties of materials. Since it's first paper [2], this pioneering facility set the stage for the rapid advancement of synchrotron-based methods, laying the groundwork for increasingly sophisticated tools tailored to specific scientific inquiries [3].

Among the most impactful innovations in synchrotron science was X-ray Magnetic Circular Dichroism (XMCD) [4], first theoretically predicted to arise from the differential absorption of circularly polarised X-rays by magnetized materials [5]. This prediction suggested the technique could isolate spin and orbital magnetic contributions with element specificity by targeting resonant absorption edges. XMCD was quickly verified experimentally [6], which demonstrated its practical application and established it as a transformative tool for probing the magnetic properties of individual elements in complex systems.

While originally done in absorption, XMCD was found to work in all X-ray techniques, including scattering, diffraction, photoemission, imaging, and reflection [7]. By analysing the angular dependence of reflected X-rays at resonance conditions, X-ray Resonant Magnetic Reflectivity (XRMR)

enables the reconstruction of magnetic depth profiles within thin films and multilayer structures [8]. This depth sensitivity arises because reflectivity measurements probe the interference of X-rays reflected from different interfaces within a sample, analogous to polarised Neutron Reflectometry (PNR) [9]. XRMR has proven invaluable for investigating phenomena such as exchange coupling [10] and proximity effects at interfaces [11], advancing the understanding of magnetic heterostructures and spintronic devices.

Concurrently, X-ray detected Ferromagnetic Resonance (XFMR) emerged as a groundbreaking synchrotron-based technique for studying magnetisation dynamics [12], leveraging the pulsed structure of synchrotron radiation to enable time-resolved, element-specific measurements. Diamond Light Source, operating at 499.65 MHz, produces periodic X-ray pulses with a spacing of approximately 2 ns and a width of 35 ps, which are synchronized with an externally applied radio-frequency (RF) field. This synchronization, achieved using harmonics of the synchrotron master clock, allows stroboscopic probing of magnetic precession at GHz frequencies, offering picosecond temporal resolution.

XRMR and transverse geometry XFMR require advanced beamlines with precise X-ray pulses and dichroic capabilities. An example beamline for this is the aptly named *BeamLine for Advanced Dichroism Experiments* (BLADE), I10 at Diamond Light Source. XFMR here has traditionally been done in Luminescence, in the *Portable Octopole Magnetic System* (POMS) Endstation [12, 13]. Recent developments at BLADE have allowed for XFMR measurements to be conducted in a separate endstation, *Reflectivity and Advanced Scattering of Ordered Regimes* (RASOR) [14, 15]. This development has produced Reflectivity Ferromagnetic Resonance [16, 17], along with it's counterpart Diffractive Ferromagnetic Resonance (DFMR) [18, 19] to this lineage of techniques. By analysing the amplitude and phase of the reflected signal as a function of incident x-ray angle, RFMR provides detailed depth-dependent information on dynamics in magnetic thin films.

Looking forward to the emergence of X-ray Free Electron Lasers (X-FELs) [20, 21], with their femtosecond-scale time resolution, X-FELs could enable the investigation of ultrafast processes, such as demagnetisation and coherent spin waves, which are beyond the temporal reach of current synchrotron techniques. These capabilities have the potential to complement existing approaches, providing a more comprehensive view of magnetic dynamics across different timescales. As experimental methods evolve, the integration of X-FEL-based techniques with established synchrotron methods may lead to new discoveries, deepening our understanding of magnetic systems and informing the design of next-generation spintronic devices.

1.2 Why Do We Need Depth-Dependent FMR Techniques?

To probe and optimise magnetic heterostructures, a suite of complementary techniques is typically employed. XMCD provides element-specific sensitivity to spin and orbital magnetic moments [12], while ferromagnetic resonance (FMR) reveals magnetisation dynamics in the frequency domain [22, 23, 24]. Their combination gives XFMR, which enables time-resolved, element-specific probing of spin dynamics. The first demonstration of XFMR was by Bailey *et al.* [25] on a Permalloy (Py = $Ni_{80}Fe_{20}$) thin film, where Ni and Fe moments were shown to precess coherently across all frequencies. Since then, XFMR has been widely applied across various systems. Marcham *et al.* [26] used XFMR to identify spin-transfer torque (STT) in a CoFe/Cu/Py spin-valve, where the field dependence of the fixed layer phase provided a clear signature of STT via spin pumping. In exchange-coupled systems such as NiFe/CoFe, XFMR revealed that the phase relationship between layers could be tuned by selecting which layer is driven, causing the non-driven layer to precess either in phase or in anti-phase [27]. XFMR has also been pivotal in further spin pumping studies. In NiFe/NiO/CoFe trilayers, evanescent spin waves were found to traverse the antiferromagnetic NiO and drive precession in the otherwise non-resonant CoFe layer [28]. Moreover, tuning the NiO thickness revealed that a 2 nm spacer could enhance spin pumping even beyond that of a direct contact [29].

These effects extend to topological systems: in NiFe/Bi_2Se_3/CoFe heterostructures, a spin-polarised current was shown to transmit spin angular momentum across the interface, with potential for further enhancement using 2D nanocrystalline topological insulators [30]. Similarly, in magnetic tunnel junctions, XFMR measurements have revealed that pure spin currents can mediate exchange coupling, resulting in anisotropic absorption with respect to the applied field direction [31].

Qualitative depth information has also been achieved in time-resolved magneto-optical Kerr effect (TR-MOKE) studies. By exploiting the distinct probing depths of Kerr rotation and ellipticity, Wieczorek *et al.* [32] were able to disentangle the timescales associated with non-local spin transport and local spin-flip scattering in Co/Cu(001). More recently, this concept was extended to reflectivity-based XMCD to resolve spin dynamics in buried layers of MBE-grown Cu/Co(15 ML)/$Ni_{31}Mn_{69}$(20 ML)/Cu(001) structures [33].

1.3 Thesis Outline

Chapter 2 introduces the theoretical background necessary to understand magnetisation dynamics in magnetic heterostructures. It begins with fundamental magnetic interactions and builds toward

the Landau–Lifshitz–Gilbert (LLG) equation and its linearised solution. The chapter also outlines the magneto-optical principles that underpin reflectivity-based techniques, establishing the basis for understanding RFMR.

Chapter 3 introduces the experimental techniques used throughout the project. This includes fabrication of magnetic multilayers via DC magnetron sputtering, and magnetic characterisation using VNA-FMR. It also details the synchrotron-based experiments inside the RASOR endstation, and the specific set-up for RFMR when conducted at the Diamond Light Source.

Chapter 4 introduces how the optical properties manifest in RFMR signals. It provides treatment of the charge and magnetic scattering factors, their dependence on energy, angle, and polarisation, and explains how these differ from standard XRMR or XFMR formulations. Experimental observations of RFMR signals are discussed, along with methods for extracting the angular and time dependence of scattering coefficients.

These principles are then translated into a working analysis framework in Chapter 5, where a Python-based implementation of the Fresnel reflectivity formalism is used to model RFMR data. This macrospin model incorporates depth-dependent dynamic parameters, enabling fits to amplitude and phase profiles of precession across multilayer stacks. The structure of the fitting procedure is explained in detail, including global optimisation strategies, penalisation of unphysical solutions, sensitivity analysis, and validation of models.

Moving to the case studies; Chapter 6 focuses on single magnetic layers. A detailed study of a NiFe(25 nm)/Pt(3 nm) film demonstrates the difficulty in asserting the presence of depth-dependent mode profiles, without strict priors on experimental RFMR data. The chapter discusses how to describe the reflectivity data and shows how subdividing the magnetic layer into discrete sublayers aids fitting. Sensitivity and Sobol analyses are used to assess model uniqueness and test the spatial resolution of RFMR. The depth-profile of the FMR mode was constructed via co-fitting with different driving RF waveforms, where significant differences were required between the models to accurately fit the data, and hence demonstrating the capacity of the FMR modes depth profile to compute a simple binary classification task.

Building on this, Chapter 7 examines coupled trilayer structures, specifically CoFeB/Cr/NiFe spin-valves, where both optical and acoustic FMR modes are resolved using RFMR. By combining XRMR and RFMR data, the dynamic structure of each mode is reconstructed. A particular focus is given to the interfacial CoFeB sublayer, which shows distinct phase and amplitude behaviour compared to the bulk. Micromagnetic simulations are used to verify the reconstructed profiles. By sweeping the static field across the optical mode, significant changes are observed within the depth-profile, which

can be described by a model which only varies the phase between three active layers NiFe, interfacial CoFeB, and bulk CoFeB.

Finally, Chapter 8 explores a complex $[Ta/CoFeB/MgO]_4$ heterostructure, where each chemically identical layer exhibits distinct depth-dependent dynamics due to interlayer coupling, varying local environments, and interfacial effects. RFMR is used to uniquely identify two distinct modes in this heterostructure that are invisible to volume integrating techniques like VNA-FMR. From there a Spin-Reorientation Transition (SRT) is observed as the CoFeB thickness is tuned through 1.50 nm, characterised using VSM, VNA-FMR, MFM, and micromagnetic simulations. XRMR and RFMR measurements reveal that the static and dynamic magnetisation profiles evolve significantly across the SRT, with thinner films exhibiting increasingly complex modal structure. By performing RFMR at multiple polarisations, the full three-dimensional magnetisation trajectories are reconstructed, exposing complex precession patterns and signatures of nonlinearity, features of great interest for future spintronic computing architecture.

Chapter 2

Introduction & Theoretical Background

2.1 Magnetic Heterostructures & Their Interactions

Magnetic heterostructures, composed of alternating layers of magnetic and non-magnetic materials, are fundamental to advancing our understanding of magnetism at the nanoscale [34]. These structures have become a critical focus in materials science and condensed matter physics due to their ability to host and modulate complex magnetic phenomena [35]. Their study provides valuable insights into how magnetism emerges, evolves, and interacts within layered systems, particularly at interfaces where these effects are most pronounced.

Magnetic heterostructures also serve as the basis for many spintronic devices [36], which exploit the intrinsic spin of electrons alongside their charge. Spin-valves and magnetic tunnel junctions (MTJs) are prominent examples, leveraging phenomena such as giant magnetoresistance (GMR) and tunneling magnetoresistance (TMR) for applications in data storage and magnetic sensing. Studying the fundamental mechanisms behind these effects, including interlayer coupling, and magnetisation dynamics, allows for refinement of device performance and the development of new functionalities.

At the heart of ferromagnetic resonance (FMR) lies a simple idea: magnetic moments precess under torque. This precession, driven by an effective magnetic field and damped by internal dissipation, is rich with information, especially when observed with depth sensitivity, as in RFMR. To understand what RFMR reveals, we begin with a streamlined tour of the key interactions shaping magnetisation dynamics in thin films.

Magnetisation and Energy Terms. Each electron contributes a magnetic moment from its spin and orbital motion; however, in bulk solids, the macrospin model for **M** is often applied, where it is the

sum of many moments per unit volume. Its behaviour is governed by an effective Hamiltonian :

$$\begin{aligned}
\mathcal{H} = &- \mu_0 \int_V \mathbf{M} \cdot \mathbf{H}\, dV && \text{(Zeeman)} \\
&= \frac{A}{M_s} \int_V (\nabla \mathbf{M})^2 \, \mathrm{d}V && \text{(Exchange)} \\
&- \frac{\mu_0}{2} \int_V \mathbf{M} \cdot \mathbf{H}_{\text{demag}}\, dV && \text{(Demagnetisation)} \\
&- K_u \sin^2 \theta, && \text{(Anisotropy)} \\
&- \sum_{\langle i,j \rangle} \mathbf{d}_{ij} \cdot (\mathbf{S}_i \times \mathbf{S}_j) && \text{(DMI)} \\
&+ \ldots && (2.1)
\end{aligned}$$

Each term captures a familiar force: The **Zeeman energy** is the simplest term, describing the tendency of magnetic moments to align with an external magnetic field. Here, μ_0 is the vacuum permeability, and the integral is over the volume of the magnetisation $\mathbf{M}$ with the field $\mathbf{H}$. This term energetically favours alignment of $\mathbf{M}$ with the external field $\mathbf{H}_{\text{ext}}$, producing a torque $\mathbf{N} = \mathbf{M} \times \mathbf{H}_{\text{ext}}$ that drives precession. The Zeeman effect was originally studied in atomic spectra by Pieter Zeeman in 1896 (splitting of spectral lines in a magnetic field), and in magnetism, it provides the primary handle for resonantly exciting spins, by adjusting the applied field, one tunes the precession frequency into resonance. In FMR experiments, a static field $\mathbf{H}$ defines the magnetisation's equilibrium direction, and the resonance condition occurs when the microwave frequency equals the Larmor precession frequency $\omega_0 = \gamma \mu_0 H$ (for a free moment, with γ the gyromagnetic ratio). All other magnetic interactions act as modifications to this basic precession.

Next, the **Exchange interaction** is the quantum-mechanical force responsible for aligning adjacent spins in a ferromagnet. It arises from the combination of Coulomb repulsion and the Pauli exclusion principle for electrons. Werner Heisenberg first explained in 1928 that ferromagnetic order stems from an exchange energy that is minimised when neighbouring electron spins are parallel. The exchange constant is given by $A = nJS^2/a$, where a is the lattice constant, S is the magnitude of the spin, and n is a factor arising from the crystal structure. where J_{ij} is the exchange constant between spins $\mathbf{S}_i$ and $\mathbf{S}_j$. A positive $J_{ij} > 0$ favours parallel alignment (ferromagnetism). The exchange interaction is incredibly strong at the atomic scale, resulting in internal fields of order tens of Tesla that keep spins locked together. Historically, after Heisenberg's introduction, exchange theory was developed throughout the 1930s and is now a cornerstone of magnetism theory.

A ferromagnet generates its own internal magnetic field due to the magnetisation. This **demag-**

netizing field (or stray field) arises from magnetic pole charges at surfaces and domain walls. The demagnetizing (demag) field $\mathbf{H}_{\text{demag}}$ points opposite to $\mathbf{M}$ (trying to demagnetize the sample) and gives rise to shape anisotropy. The 1/2 factor avoids double-counting the magnetostatic self-energy. Physically, this term favours orientations of $\mathbf{M}$ that minimise free magnetic charges on the sample surface. The demag field can be treated as $\mathbf{H}_{\text{demag}} = -\hat{N}\mathbf{M}$, where $\hat{N}$ is the demagnetizing factor (a tensor) dependent on sample geometry.

In addition to shape anisotropy from magnetostatics, ferromagnets often exhibit **magnetocrystalline anisotropy**, an energy preference for magnetisation to align along certain crystallographic directions, called the easy axes. This arises from spin–orbit coupling of the electron spins with the lattice. The atomic lattice symmetry makes some directions magnetically "harder" or "easier" to magnetize. For example, in hexagonal cobalt, the c-axis is an easy axis due to how orbitals overlap; in cubic iron, the $\langle 100 \rangle$ axes are easy [37]. The anisotropy energy can be expressed by an expansion in direction cosines of $\mathbf{M}$. Shown above is the simple form for uniaxial anisotropy (one easy axis), where θ is the angle between $\mathbf{M}$ and the easy axis. In thin films, interfacial anisotropy is of interest, at a film interface, broken symmetry and orbital bonding differences can induce a perpendicular anisotropy (favouring $\mathbf{M}$ along the film normal). This interface anisotropy, combined with the demag shape effect, determines whether a film's net easy axis is in-plane or out-of-plane. A strong perpendicular interface anisotropy can overcome the demag field and produce perpendicular magnetic anisotropy (PMA) [38, 39, 40]. For instance, CoFeB on MgO or Ta exhibits such interface-driven PMA [41, 42, 43], which is exploited in spin-torque MRAM devices.

The **Dzyaloshinskii–Moriya interaction** (DMI) is an antisymmetric exchange interaction between neighbouring spins, arising from relativistic spin–orbit coupling in systems with broken inversion symmetry. Unlike the conventional symmetric exchange (Heisenberg exchange) that favours parallel or antiparallel spin alignment, DMI energetically favours a canted or perpendicular alignment of spins with a fixed handedness (chirality). This interaction was originally introduced by Igor Dzyaloshinskii and refined by Toru Moriya to explain weak ferromagnetism in certain antiferromagnets [44, 45], a phenomenon where a small net magnetisation arises from canted spin configurations. In essence, DMI adds a term to the magnetic Hamiltonian of the form $\mathbf{D} \cdot (\mathbf{S}_i \times \mathbf{S}_j)$, where $\mathbf{D}$ is a vector (the Dzyaloshinskii–Moriya vector) set by the local crystal or interface symmetry. This term favours a twisting of the spins $\mathbf{S}_i$ and $\mathbf{S}_j$ in a particular rotational sense, imparting a chiral bias to the spin structure. The strength and sign of $\mathbf{D}$ depend on the material's atomic composition and symmetry, with the sign determining whether a clockwise or counterclockwise spin rotation is preferred.

In the micromagnetic continuum, DMI energy is expressed as:

$$E_{\mathrm{DMI}} = D \int \left(m_x \frac{\partial m_z}{\partial x} - m_z \frac{\partial m_x}{\partial x} + m_y \frac{\partial m_z}{\partial y} - m_z \frac{\partial m_y}{\partial y} \right) dx\, dy. \tag{2.2}$$

In magnetic thin films, DMI commonly emerges at interfaces and in multilayers due to structural inversion asymmetry. A typical scenario involves a ferromagnetic thin layer in contact with a heavy metal layer (such as Pt, Ir, or W) or an oxide layer, which provides the strong spin–orbit coupling needed for DMI. Because the top and bottom environments of the ferromagnet differ (e.g., vacuum or oxide on one side, heavy metal on the other), inversion symmetry is broken through the thickness of the film [46, 47]. DMI is only considered relevant in Chapter 8 of this thesis, but its presence can subtly modify mode profiles in RFMR, especially in asymmetric stacks.

2.2 Interlayer Coupling

When ferromagnetic films are separated by a non-magnetic spacer, a long-range interaction emerges that couples their magnetisations across the interlayer. First characterised in Fe/Cr systems around 1986 [48, 49], this Interlayer Exchange Coupling (IEC) is fundamental to the behaviour of magnetic multilayers.

Phenomenologically, the coupling energy per unit area, E_{IEC}, is described by bilinear and biquadratic terms that depend on the relative orientation of the two magnetisations, $\mathbf{M_1}$ and $\mathbf{M_2}$: [50]

$$E_{\mathrm{IEC}} \;=\; -J_1 \frac{\mathbf{M}_1 \cdot \mathbf{M}_2}{|\mathbf{M}_1||\mathbf{M}_2|} \;-\; J_2 \left(\frac{\mathbf{M}_1 \cdot \mathbf{M}_2}{|\mathbf{M}_1||\mathbf{M}_2|} \right)^2 \;=\; -J_1 \cos(\Delta\phi) \;-\; J_2 \big[\cos(\Delta\phi)\big]^2 \tag{2.3}$$

Here, E_{IEC} is the interlayer coupling energy density per unit area, and $\Delta\phi$ is the angle between the magnetisations of the films on either side of the interlayer. The coupling constants, J_1 and J_2, dictate the preferred alignment. The bilinear term J_1 typically dominates: a positive J_1 favours parallel, or ferromagnetic, alignment, while a negative J_1 favours antiparallel, or antiferromagnetic, alignment. A negative biquadratic term, J_2, promotes a perpendicular (90°) configuration [51, 52, 53, 54].

For thick non-magnetic spacers, the interlayer coupling is controlled by the magnetostatic or dipolar coupling. While a long-range oscillatory indirect magnetic exchange coupling has been reported for thin nonmagnetic spacers [55, 56]. The physical origin of this coupling is an indirect exchange mediated by the conduction electrons of the spacer layer, analogous to the Ruderman-Kittel-Kasuya-Yosida (RKKY) interaction [57]. The mechanism involves spin-dependent scattering of spacer electrons at the first interface, which creates an oscillating spin polarisation within the spacer. This

polarisation, in turn, interacts with the second magnetic layer. A key consequence of this mechanism is that the sign and magnitude of the coupling oscillate as a function of the spacer thickness. While the RKKY-type interaction is often dominant at ultrathin spacer thickness, other mechanisms such as magnetostatic "orange-peel" coupling or pin holes [58] can also contribute.

Beyond establishing a static magnetic configuration, the IEC profoundly influences magnetisation dynamics. It couples the precession of $\mathbf{M_1}$ and $\mathbf{M_2}$, leading to the formation of distinct collective excitations. While each layer has their own uniform mode [59], in the case of a magnetic trilayer IEC results in a low-frequency, in-phase *acoustic mode* and a high-frequency, out-of-phase *optic mode* [60]. The frequency of the out-of-phase mode is particularly sensitive to the coupling strength [38, 61, 62]. In this thesis, RFMR is used to capture both the static and dynamic signatures of these interactions in a layer-specific fashion, making it uniquely suited to investigating interlayer magnetic phenomena.

2.3 Landau-Lifshitz-Gilbert Dynamics

The evolution of $\mathbf{M}$ follows the LLG equation [63, 64]:

$$\frac{\partial \mathbf{M}}{\partial t} = -\gamma \mathbf{M} \times \mathbf{H}_{\text{eff}} + \frac{\alpha}{M_s} \mathbf{M} \times \frac{\partial \mathbf{M}}{\partial t}, \tag{2.4}$$

where γ is the gyromagnetic ratio and α is the Gilbert damping constant. The first term describes precession, and the second is a phenomenological damping term [65]. While the LLG can be solved numerically in micromagnetics software [66], it is useful to derive an analytical solution. To do this, we linearise the macrospin solution by considering small deviations from equilibrium. In this approach, the magnetisation vector can be written as:

$$\mathbf{M}(t) = M_s \hat{\mathbf{z}} + \mathbf{m}(t), \tag{2.5}$$

where $\mathbf{m}(t)$ represents small oscillations ($|\mathbf{m}| \ll M_s$) around the equilibrium direction $\hat{\mathbf{z}}$. Assuming a harmonic driving field $\mathbf{h}(t) = \mathbf{h}_0 e^{i\omega t}$, the LLG equation becomes:

$$\frac{\partial \mathbf{m}}{\partial t} = -\gamma (\mathbf{m} \times \mathbf{H}_{\text{eff}}) + \alpha \mathbf{m} \times \frac{\partial \mathbf{m}}{\partial t}. \tag{2.6}$$

Neglecting higher-order terms, the linearised equation yields [63]:

$$(\omega_0 - \omega - i\alpha\omega)\, m_x + i\gamma h_x = 0, \tag{2.7}$$

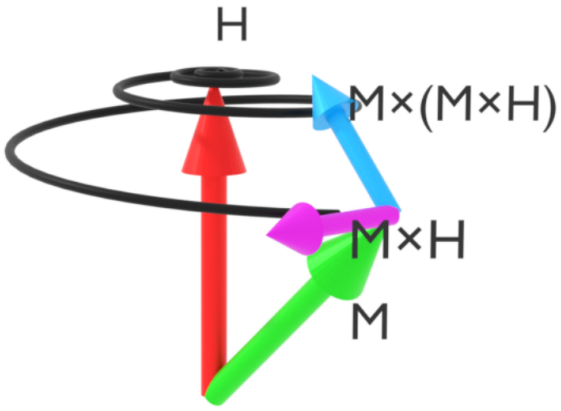


Figure 2.1: Schematic representation of precession of a single magnetic moment $\vec{M}$ in the external magnetic field around the z-axis, under phenomenological first-order damping.

$$(\omega_0 - \omega - i\alpha\omega)\, m_y - \gamma h_y = 0, \tag{2.8}$$

where $\omega_0 = \gamma H_{\text{eff}}$ is the resonance frequency. The dynamic response is characterised by the AC susceptibility $\chi(\omega)$, relating the magnetisation to the driving field:

$$\mathbf{m}(\omega) = \chi(\omega)\mathbf{h}(\omega). \tag{2.9}$$

Solving for $\chi(\omega)$ in our linearised macrospin model, we find:

$$\chi(\omega) = \frac{\chi'(\omega) + i\chi''(\omega)}{1 + i\alpha}, \tag{2.10}$$

$\chi'(\omega)$ (real part) represents the in-phase component, linked to energy storage, $\chi''(\omega)$ (imaginary part), linked to energy dissipation. The susceptibility peaks at resonance $\omega = \omega_0$, with the imaginary component quantifying damping. The resonance condition is described by the Kittel equation:

$$\omega_0 = \frac{\gamma}{2\pi}\sqrt{H_{\text{ext}}(H_{\text{ext}} + H_{\text{eff}})}, \tag{2.11}$$

where ω is the RF frequency, H_{ext} is the external magnetic field, H_{eff} is the effective anisotropy field, and γ is the gyromagnetic ratio. Further damping can be quantified by:

$$\Delta H = \Delta H_0 + \frac{2\alpha\omega_0}{\gamma} \tag{2.12}$$

where ΔH is the total linewidth, ΔH_0 is the intrinsic linewidth, α is the phenomenological Gilbert damping, with spin pumping contribution isolated by $\alpha = \alpha_0 + \alpha_{sp}$.

2.4 Magneto-Optical Interactions

The interaction between circularly polarised X-rays and magnetized matter underpins several powerful techniques for probing spin and orbital magnetism with elemental and depth specificity. The nature of this interaction depends on whether or not the incident photon energy $\hbar\omega$ is resonant with an electronic transition energy ΔE in the material. While non-resonant magnetic scattering exists, it is typically orders of magnitude weaker than its charge counterpart and is not the focus here [67], but is well covered in [10]. In this work, we focus on the resonant regime ($\hbar\omega \approx \Delta E$), where the magnetic interaction is dramatically enhanced, allowing for detailed investigation of magnetic properties. This is described by scattering cross section (σ), that governs all the scattering processes. From experiment, the scattered intensity I in the solid angle $d\Omega$ is obtained. In this very general approach, a proportion of the incident light I_0 is scattered into the angle segment $[\Omega, \Omega + d\Omega]$, defined by the proportionality factor, i.e., the differential scattering cross-section, is given by

$$\left(\frac{d\sigma}{d\Omega}\right)_{\text{scat}} = |f(\mathbf{Q}, E)|^2 = \frac{1}{I_0} P_{i\to f} \cdot \rho(E_f). \tag{2.13}$$

The intensity scattered into the solid angle $d\Omega$ is given by the square of the scattering amplitude $f(\mathbf{Q}, E)$, which is also known as the scattering length or scattering factor. This scattering amplitude is usually dependent on the direction of the incident light $\mathbf{k}$ or the momentum transfer $\mathbf{Q} = \mathbf{k} - \mathbf{k}'$ of the process, and on the energy of the incident X-ray photon. This also follows the approach by M. Blume [67] to describe charge and magnetic dipole scattering without anomalous dispersion, relating the scattered intensity to the transition probability $P_{i\to f}$ multiplied by the density of the intermediate states $\rho(E_f)$, and normalised to the intensity of the incident light I_0. To obtain the scattering amplitude of an atom, time-dependent perturbation theory has to be used. While the processes shown in Figure 2.2(a) and (c) can be described by a semi-classical treatment involving the respective dipole moments, the resonant effects in Figure 2.2(b) and (d) require a full quantum mechanical treatment.

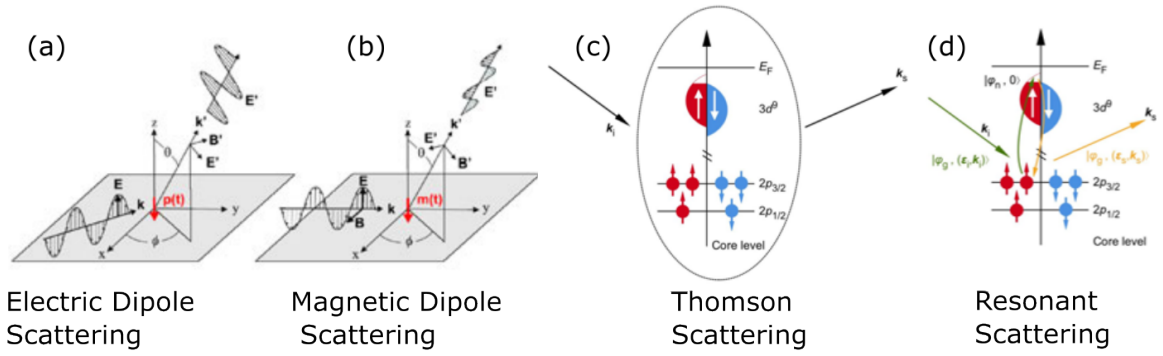


Figure 2.2: Different mechanisms for scattering of a polarised X-ray photon on an atom with (a, b) reproduced from reference [68], and (c, d) illustrating Thomson and resonant scattering processes shown in the single photon case. Scattering diagram is for Cu^{2+} ion ($2p \rightarrow 3d$). (c, d) Illustration credit; T. Hesjedal.

The transition probability $P_{i\rightarrow f}$ per unit time for second-order perturbation theory is given by:

$$P_{i\rightarrow f} = \frac{2\pi}{\hbar}\left|\langle f|H|i\rangle + \sum_n \frac{\langle f|H|n\rangle\langle n|H|i\rangle}{E_i - E_n}\right|^2 \delta(E_i - E_f). \tag{2.14}$$

The eigenstates $|i\rangle$ and $|f\rangle$ describe the initial and final states of the overall system, while $|n\rangle$ is the intermediate state of the excitation as defined in Figure 2.2(c). In the initial state $|i\rangle$, the material is characterised by an electronic ground state $|a\rangle$ and the incident photon with wavevector $\mathbf{k}$ and polarisation vector ε, thus $|i\rangle = |a;\mathbf{k},\varepsilon\rangle$. The Hamiltonian H, for example, might induce a transition of the system to a new eigenstate $|f\rangle = |b;\mathbf{k}',\varepsilon'\rangle$, where the photon now has the new wavevector $\mathbf{k}'$ and polarisation vector ε'.

The full quantum treatment is shown brilliantly in [10]. For simplicity in this derivation we ignore non-resonant effects, hence the interaction Hamiltonian in equation (2.14) can represent the interaction of the electromagnetic wave with the spin through:

$$H \propto \frac{e\hbar}{mc}\sum_n \mathbf{s}_j \cdot \left[\nabla \times \mathbf{A}(\mathbf{r}_j)\right] \tag{2.15}$$

Here, $\mathbf{A}(\mathbf{r}_j)$ is the vector potential of the electromagnetic wave, related to the electric field $\mathbf{E}(\mathbf{r})$ and magnetic field $\mathbf{B}(\mathbf{r})$ via Maxwell's equations. The electron states are described by position $\mathbf{r}_j$, and spin $\mathbf{s}_j$. Solving this leads allows us to express our scattering factor by the transition matrix element $M_i(\mathbf{k},\varepsilon)$.

$$f_{\text{res}} = \left[\frac{\hbar^2}{m} \sum_c \frac{\langle b|M_i(\mathbf{k}', \varepsilon')|c\rangle\langle c|M_j(\mathbf{k}, \varepsilon)|a\rangle}{E_a - E_c + \hbar\omega - i\Gamma_c/2} + \frac{\hbar^2}{m} \sum_c \frac{\langle b|M_j(\mathbf{k}, \varepsilon)|c\rangle\langle c|M_i(\mathbf{k}', \varepsilon')|a\rangle}{E_a - E_c - \hbar\omega} \right] (E_a - E_b + \hbar\omega - \hbar\omega') \tag{2.16}$$

Where the transition matrices $M_{i,j}(\mathbf{k}, \varepsilon)$ are given by

$$M_{i,j}(\mathbf{k}, \varepsilon) = \sum_h \left[\frac{\varepsilon \cdot \mathbf{P}^h_{i,j}}{\hbar} + i\,(\mathbf{k} \times \varepsilon) \cdot \mathbf{s}^h_{i,j} \right] e^{-i\mathbf{k}\cdot\mathbf{r}^h_{i,j}}. \tag{2.17}$$

These matrices contain a real part due to the interaction of the polarisation vector ε with the orbital momentum $\mathbf{P}_i$, and an imaginary part arising from the interaction of the spin moment $\mathbf{s}_i$ with the vector product $\mathbf{k} \times \varepsilon$. In the dipole approximation, the solution to the electric dipole transition (E1, ℓ=1) is presented by Hill [69]. Further the atomic scattering factor of a resonant magnetic atom is given by the formalism of Hannon *et al.* [70]:

$$f(q, \omega, \vec{e}_f, \vec{e}_i) = -(\vec{e}^*_f \cdot \vec{e}_i) \cdot [f_0(q) + f'(\omega) + if''(\omega)] + i(\vec{e}^*_f \times \vec{e}_i) \cdot \vec{b} \cdot [m'(\omega) + im''(\omega)]\,, \tag{2.18}$$

where $f_c = f_0 + f' + if''$ represents the isotropic charge scattering, and $f_m = m' + im''$ encodes the magnetic response, modulated by both the local magnetisation $\vec{b}$ and the photon polarisation.

The polarisation dependence can describe several distinct phenomena; birefringence: when two distinct indices of refraction exist for horizontally and vertically polarised light, or rotation of the direction of linear polarised light (e.g. Kerr, Faraday), and finally, dichroism, which describes polarisation dependent absorption in a material. The XMCD technique [4] measures the difference in X-ray absorption of a magnetic ion between parallel and antiparallel alignment of the samples magnetisation and the photon polarisation vector. The XMCD effect is directly proportional to the atomic magnetic moment or the net magnetisation $\mathbf{M}$ and given by:

$$\text{XMCD} = \mu^+ - \mu^- \propto \vec{k} \cdot \mathbf{M} \tag{2.19}$$

where $\mu^\pm$ are the absorption coefficients for each polarisation and $\vec{k}$ is for the photon polarisation vector. This notation here follows the general convention that the XMCD is calculated in a way that the L_3 XMCD is negative for positive circular X-rays. This thesis focuses on *3d* transition metals, where XMCD is typically measured at the $L_{2,3}$ absorption edges. These correspond to electric dipole

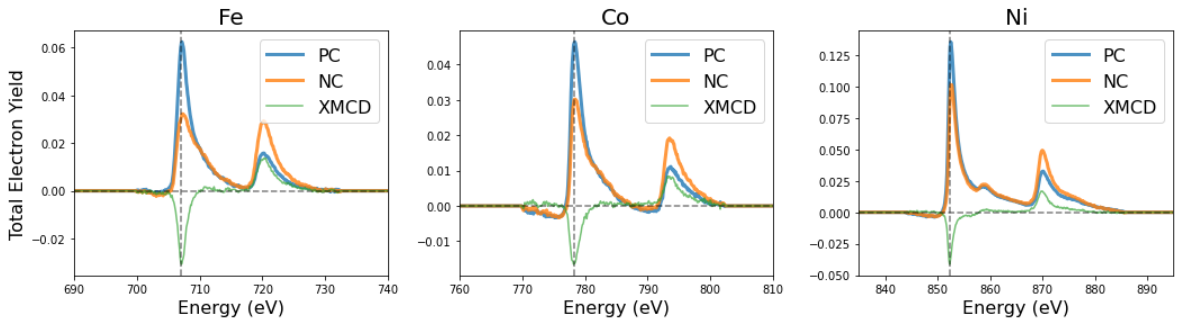


Figure 2.3: An example XMCD spectrum measured in Total Electron Yield (TEY) mode for a pseudo-spin-valve (CoFeB/Cr/NiFe) structure. The dichroic difference highlights the magnetisation contrast at the resonant edges. XAS signals are background subtracted here.

transitions from $2p \rightarrow 3d$, split by strong spin-orbit coupling in the core level:

- The L_3 edge ($2p_{3/2} \rightarrow 3d$) lies at lower energy and corresponds to parallel spin-orbit coupling.
- The L_2 edge ($2p_{1/2} \rightarrow 3d$) lies at higher energy with antiparallel coupling.

The net magnetisation in the material results in spin-polarised unoccupied states in the *3d* band. Due to the helicity dependence of dipole selection rules, left- and right-circularly polarised X-rays preferentially excite electrons of opposite spin, leading to a measurable dichroic signal. The strength of XMCD in *3d* metals is significantly larger than in the visible regime due to the strong localization of the *3d* orbitals and the large spin-orbit splitting in the core levels [4]. In the case of *3d* transition metals, the electric dipolar transition E1 is dominant, here ℓ=1 and m=0,±1 and the scattering amplitude takes the form

$$f_{\text{res}}^{\text{E1}} = \frac{3}{4k}(F_{11}+F_{1-1})\,(\varepsilon_0\cdot\varepsilon) - i\,\frac{3}{4k}(F_{11}-F_{1-1})\,(\varepsilon_0\times\varepsilon)\cdot\mathbf{M} + \frac{3}{4k}(2F_{10}-F_{11}-F_{1-1})\,(\varepsilon_0\cdot\mathbf{M})(\varepsilon\cdot\mathbf{M}). \tag{2.20}$$

This equation fully describes anomalous (resonant) scattering from both charge and magnetic contributions within the electric dipole (E1) approximation. It is fundamentally the same form as Eq. (2.18), however now in terms of F_{10},F_{11},$F_{1-1} \in \mathbb{C}$.

These principles extend naturally to the coherent scattering regime in XRMR, where resonant scattering is modulated by interference from multiple interfaces. The refractive index for X-rays is expressed as [8]

$$n = 1 - \delta(E) - i\beta(E), \tag{2.21}$$

with $\delta(E)$ and $\beta(E)$ representing the dispersion and absorption terms. Near resonance, both terms acquire a strong energy dependence through the complex scattering factor

$$f = f_0 + f_{\text{mag}}^{\text{non-res}} + f_0^{\text{charge}} + i f_0^{\prime\prime,\text{charge}} + f_0^{\text{mag}} + i f_0^{\prime\prime,\text{mag}}, \tag{2.22}$$

where f_0 is the normal Thomson (non-resonant) charge scattering amplitude, and $f_{\text{mag}}^{\text{non-res}}$ accounts for non-resonant magnetic contributions, which are far from any electronic resonances. .

The terms f_0^{charge} and $f_0^{\prime\prime,\text{charge}}$ represent the real and imaginary parts, respectively, of the anomalous charge scattering near a resonance. These are given by the first term in equation (2.20), and are proportional to $F_{11} + F_{1-1}$. They describe the resonant enhancement, commonly observed as "white lines" at the absorption edges of an atom.

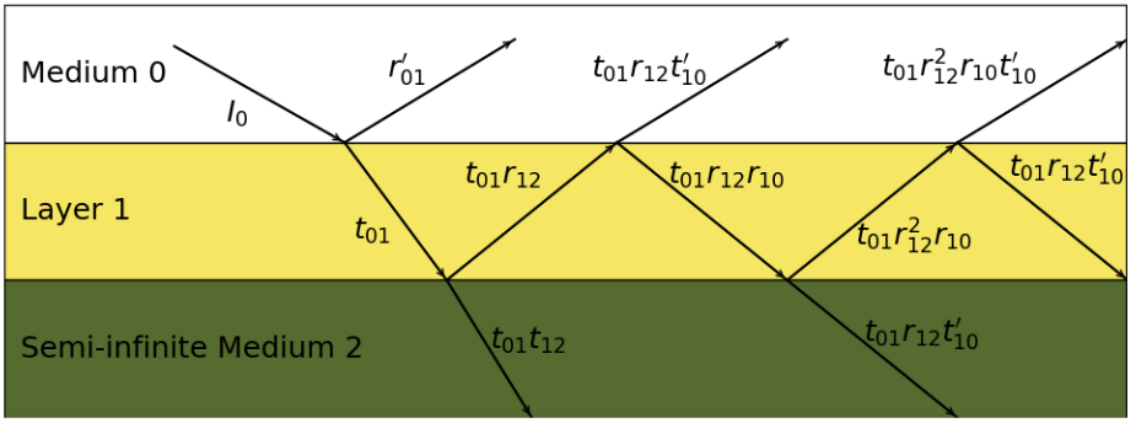


Figure 2.4: Reflection and transmission from a semi-infinite slab demonstrate the recursive process of the Parratt formalism in eq. (2.24)

Finally, f_0^{mag} and $f_0^{\prime\prime,\text{mag}}$ describe the real and imaginary parts of the magnetic resonant contribution, which arise from $F_{11} - F_{1-1}$. These terms explain the magnetic circular dichroism and are sensitive to the local magnetisation direction and strength. The reflectivity profile becomes polarisation-dependent, and the interference between charge and magnetic scattering leads to an asymmetry in the reflected intensity:

$$\text{Asymmetry} = \frac{I^+ - I^-}{I^+ + I^-}, \tag{2.23}$$

where $I^\pm$ are the reflected intensities for opposite helicities or field orientations. Reflectivity is computed using recursion methods, such as the Parratt formalism or matrix-based approaches, which account for the multilayer structure, interface roughness [71], and complex refractive index [72, 73]. This allows for the propagation of the wave through each layer in the heterostructure. In the case of two layers it takes the form:

$$r_{\text{slab}} = r_{01} + t_{01}t'_{10}r_{12}P^2 + t_{01}t'_{10}r^2_{12}r'_{10}P^4 + \dots \tag{2.24}$$

P^2 is a phase factor which changes the phase of waves travelling in opposite directions and is generalised as

$$P^2 = \exp(id_nQ_{zn}),$$

with d being the thickness of the n-th layer. Now that we have established the necessary understanding of the theoretical background, we are prepared to understand the relevant developments required to interpret RFMR data. In Chapter 4 we detail the prevalence of the scattering factors in RFMR, and emphasize their proper treatment. In Chapter 5 we demonstrate the explicit fitting procedure of the experimental data using the above principles.

Chapter 3

Experimental Techniques

This Chapter serves to detail the experimental methods developed and employed to fabricate, characterise, and measure sputtered thin films with tailored depth-dependent magnetic dynamics using RFMR. A central goal of this work was to engineer depth-dependent magnetisation dynamics, justifying their study using RFMR.

While even a single-layer ferromagnet (e.g., a 25 nm thick NiFe film) can exhibit intrinsic depth-dependent behaviour due to interfacial demagnetisation, standing spin wave modes, or magnon scattering, these effects are often subtle and difficult to isolate. Instead, this work pursued deliberate structural strategies to amplify and control depth dependence. One such strategy, explored in Chapter 7, involves introducing non-magnetic spacer layers to mediate interlayer coupling between magnetic layers. This principle is extended in Chapter 8, which investigates more complex heterostructures with multiple coupled layers.

Other approaches to achieving depth-dependent contrast were also explored during the course of this project. These included the use of compensated ferrimagnets (e.g., Co_xTb_{1-x}) to induce near-zero net moment with spatially varying sublattice dynamics, off-axis sputtering to promote columnar growth and static anisotropy gradients [74], and sputtered synthetic antiferromagnets (SAFs) to impose alternating magnetic configurations. While each of these methods holds promise for future RFMR studies, technical limitations during beamtimes constrained the quality of the data obtained from these systems. As such, they are not presented in this thesis, not as a judgment on their viability, but as a reflection of experimental feasibility under the constraints of available resources.

3.1 DC Magnetron Sputtering

Most samples used in this work were grown using a home-built, DC magnetron sputtering deposition system [75]. This system (termed *M*7) is specifically designed for precise magnetic heterostructures, enabling the growth of complex multilayered structures with controlled thickness, roughness, and composition.

Principle of Magnetron Sputtering

Magnetron sputtering is a physical vapor deposition (PVD) technique in which material from a solid target is ejected by the impact of energetic ions and deposited onto a substrate. The process involves the following steps:

1. A plasma is generated in the sputtering chamber by applying a high voltage to the target material. This plasma typically consists of inert gas ions (e.g., Ar^+) generated by collisions with electrons.

2. The positively charged ions are accelerated toward the negatively biased target (cathode), causing atoms to be ejected from the target surface via momentum transfer. This process is known as sputtering.

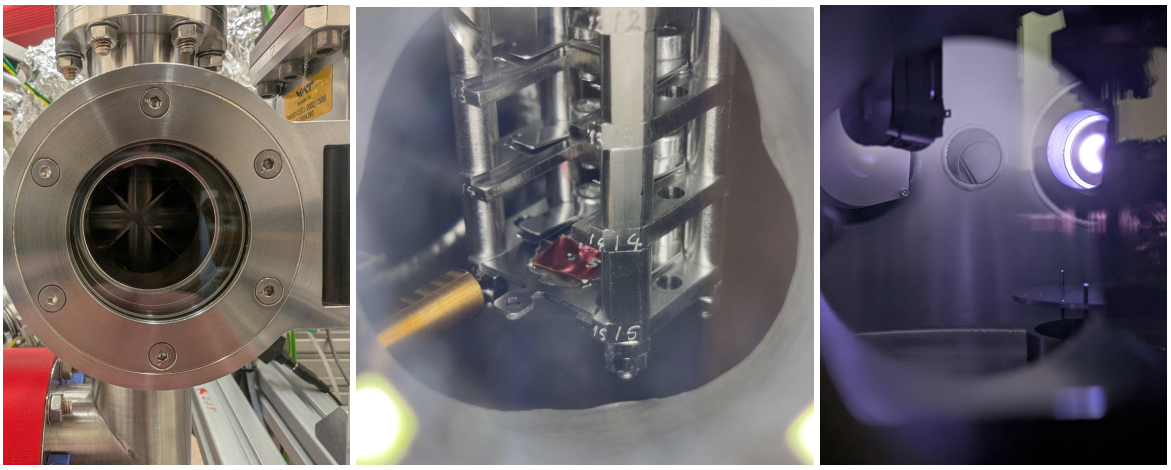
3. The sputtered atoms travel through the low-pressure chamber and condense on the substrate, forming a thin film. The deposition rate and film morphology depend on several factors, including target power, gas pressure, and substrate temperature.



Figure 3.1: Sputtering chamber used in this thesis.

The sputtering chamber used in this PhD is equipped with eight independent magnetron sources. A photo of the chamber is shown in Figure 3.1. Five sources are mounted in the horizontal plane, while two sources (e.g., Pt and Co) are positioned at a 17° angle below the horizontal plane, with their focal point at the centre of the chamber. This unique geometry ensures uniform deposition across the substrate and enables precise control over deposition angles.

Smooth interfaces are critical for reliable RFMR measurements, as structural roughness can induce magnetic roughness [76] and negatively impact dynamic coupling through mechanisms such as direct



(a) Load Lock (b) Storage Chamber (c) Main Chamber

Figure 3.2: Chambers within in sputtering system.

exchange coupling via pin holes [58], increased spin scattering, and the formation of additional interfaces caused by alloying [77]. Hence ultra-high vacuum (UHV) conditions were required. These were implemented via the following chambers and components:

- **Load Lock (LL) Figure 3.2(a)**: A small chamber equipped with a transfer arm, N_2 supply, scroll pump, mini turbopump, combination vacuum gauge, and a bake-out lamp. By applying a N_2 overpressure during sample transfers, the LL could quickly reach pressures on the order of 10^{-8} mbar.

- **Storage Chamber (SC) Figure 3.2(b)**: Situated between the LL and the main chamber, this intermediate chamber includes an elevator capable of holding up to 14 samples. It is equipped with its own transfer arm and an ion pump, enabling base pressures down to 10^{-10} mbar, and hence separating containment's from the LL entering the growth chamber,

- **Main Chamber (MC) Figure 3.2(c)**: The growth chamber is outfitted with a 5-axis manipulator (x, y, z, ϕ_S, and θ_S), including substrate heating capability. It is surrounded 360° by six operational sputter guns: three uniformly spaced at approximately 90° intervals and a co-sputter cluster, in which three additional targets share a common ϕ_S. The system is supplied with Ar regulated by a master flow controller, with independent Ar lines and water cooling for each gun. Pumping is achieved using a scroll pump and turbopump, isolated by a butterfly valve. All motor stages, power supplies, and shutters can be controlled via Python scripting, allowing for reproducible and programmable growth conditions.

The substrate is mounted at the centre of the chamber and is rotatable about two axes:

- ϕ_S: Rotation about the vertical z-axis.
- θ_S: Tilt around the surface normal $\mathbf{N}_S$ of the substrate.

The M7 growth chamber features a unique capability for glancing angle deposition (GLAD) [74]. The dual-axis substrate rotation (ϕ_S, θ_S) enables precise tuning of:

- α: The angle between the substrate normal and the deposition direction.
- β: The in-plane azimuthal angle between the coordinate system of the substrate and the projection of the deposition flux **M** onto the substrate plane.

Although the GLAD and co-sputtering capabilities were routinely used during experimental work, these are not further discussed in this thesis, as they not relevant to the RFMR studies presented.

3.2 Vector Network Analyzer Ferromagnetic Resonance

VNA-FMR is a versatile technique for investigating the dynamic response of magnetisation in ferromagnetic materials. This section details the experimental setups developed and utilized during this thesis, the physical mechanism underlying VNA-FMR, and the origin and analysis of the S_{21} and S_{11} scattering parameters.

VNA-FMR Setups

During this project, multiple VNA-FMR setups were developed and employed to accommodate different experimental constraints. Two custom-built setups were constructed in the Clarendon Laboratory: one for communal use across the research group, featuring an electromagnet capable of fields up to $\sim 0.5\,\mathrm{T}$; and a second, optimised for rapid measurements on M7-grown samples, with a reduced field capacity of $\sim 0.1\,\mathrm{T}$, and tailored for RFMR-related beamline work. Additional VNA-FMR measurements were performed at Diamond Light Source using (POMS) [13] and the (RASOR) [15] endstations. All setups shared several core components:

- **Vector Network Analyzers**: A range of VNAs was used, from compact devices such as the LibreVNA and NanoVNA, to high-performance instruments including the Anritsu VNA and Rohde&Schwarz ZNL and ZVB20. These were used to apply a broadband RF signal (H_{RF}) to the sample via the CoPlanar Waveguide (CPW). Scattering parameters S_{21} (transmission) and S_{11} (reflection) were recorded to determine resonance characteristics. All VNAs were Python-integrated for automated frequency sweeps and synchronization with the applied field.

- **Coplanar Waveguides (CPWs)**: Each system featured a unique CPW design. Samples were mounted either face up directly onto the CPW, or face-down and insulated via teflon tape, allowing the RF power (in dBm) delivered by the VNA to excite FMR.

- **Field Control**: Both Clarendon setups included unipolar, Python-controlled electromagnets. Fields were calibrated using a Hall probe and found to scale linearly with applied current, consistent with Ampère's law. Corrections were made for Joule heating by allowing thermal equilibrium prior to each scan. RASOR featured permanent magnets on a motorized rotation stage for varying the field angle θ_H from IP to OOP up to 180 mT. POMS, with its octopole magnet geometry, allowed for three-dimensional magnetic field control, enabling full angular mapping of resonance conditions up to 0.6 T.

- **In-Situ Control and Geometry**: As POMS and RASOR at Diamond were endstations designed for complex beamline experiments, they provided advanced in-situ capabilities. POMS featured two turbomolecular pumps backed by a scroll pump allowing it to reach 1×10^{-6} Torr in approximately one hour. The CPW and associated RF cabling are mounted on a Janis cryostat, which incorporates an oxygen-free high purity copper sample stage, heater and a thermocouple mounted close to the sample. The insert can be cooled by liquid nitrogen or liquid helium, with a base temperature of approximately 7 K, and good thermal stability in the range 10 K to 300 K.

VNA-FMR operates by coupling a microwave frequency RF field to a ferromagnetic sample placed on a coplanar waveguide (CPW). Under an applied static magnetic field, the magnetisation vector **M** precesses, absorbing energy from the RF field at resonance. Measurements were typically performed by fixing the external field and sweeping the RF stimulus applied from 0.5 GHz to 20 GHz, recording S_{21} adnd S_{11}. In this way the resonance frequency at a given field can be determined. However, due to losses in the cabling, the actual signal from the sample is not visible in such a measurement, and is instead obtained by subtracting this data from high field reference data, where the resonance of the sample is above 20 GHz. As the losses in the cabling are practically field-independent, this approach allows the resonance to be identified.

The S_{21} parameter represents the transmission of the RF signal through the waveguide. At resonance, energy is absorbed by the precessing magnetisation, resulting in a characteristic dip in imaginary component. The S_{11} parameter corresponds to the reflection of the RF signal at the input port. At resonance, energy is dissipated into the sample, reducing the reflected power. The VNA-FMR spectra are analysed by fitting the S_{21} or S_{11} response to a Lorentzian or derivative Lorentzian line shape. These fits provide critical parameters [78]:

- **Resonance Field ($H_{\mathbf{res}}$)**: The magnetic field at which resonance occurs, indicating the effective anisotropy.

- **Linewidth (ΔH)**: The full width at half maximum (FWHM) of the resonance peak, related to the Gilbert damping constant α.

3.3 X-ray Resonant Magnetic Reflectivity

XRMR is a synchrotron-based technique used to probe depth-resolved magnetisation in thin films and multilayers. By measuring the interference of soft X-rays reflected at different interfaces, XRMR is sensitive to variations in both structural and magnetic scattering length densities. Magnetic contrast arises when the X-ray energy is tuned near an absorption edge and the sample is illuminated with a well-defined polarisation, exploiting the X-ray magnetic circular (or linear) dichroism. Asymmetries in reflectivity measured under different magnetisation or polarisation states reveal the magnetic depth profile.

In this work, XRMR measurements were carried out at the Reflectivity and Advanced Scattering from Ordered Regimes endstation [15]. This is a high-precision soft X-ray diffractometer developed at Diamond Light Source for the study of magnetic and structural properties in thin films and single crystals. It is designed for both Resonant Elastic X-ray Scattering (REXS) and XRMR offering full polarisation analysis and low-temperature sample environments.

RASOR operates in a vertical scattering geometry optimised for the low vertical divergence of the synchrotron beam, which is critical for high-resolution reflectivity measurements. The diffractometer features motorized θ, 2θ, and χ rotations. Samples are mounted onto a liquid helium flow cryostat allowing temperature-dependent studies down to 12 K. x,y, and z motors could translate the sample into the centre of rotation, by encapsulating the cryostat in a larger bellow. The detection system includes high dynamic range photodiodes and channeltron electron multipliers, enabling both strong reflectivity and weak magnetic scattering measurements.

The APPLE-II undulators on the I10 beamline provide variable linear and circular polarisation. The system is controlled via EPICS and GDA, offering flexible and precise data acquisition for a wide range of scattering geometries. For XRMR/ RFMR experiments, either eggcup or pillar magnets would be installed alongside a Coplanar Waveguide.

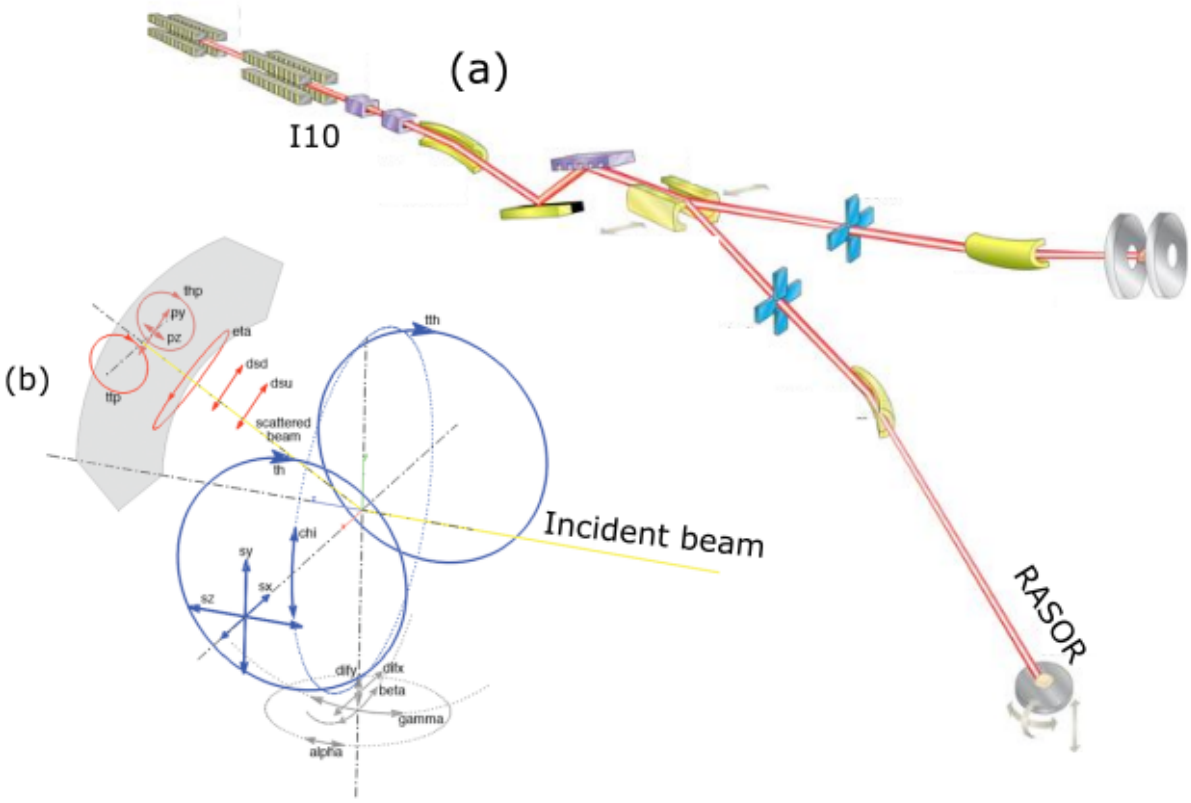


Figure 3.3: (a) A schematic of the I10 beamline layout, and (b) a schematic of the RASOR endstation scattering configuration, both images are taken from the DLS website.

3.4 X-ray Detected Ferromagnetic Resonance

XFMR is a cornerstone technique at Beamline I10 of Diamond Light Source [12, 28, 31], enabling time-resolved, element-specific measurements of spin precession in magnetic thin films. In transverse geometry XFMR, a polarised, periodically pulsed X-ray beam is incident through a CPW onto a ferromagnetic sample placed face-down.

The same RF signal used to generate the pulsed X-ray beam is routed through an electronic control system, granting users independent control over the phase delay between the RF excitation and X-ray pulse. This delayed signal is then passed through a harmonics generator to produce GHz-range frequencies corresponding to the ferromagnetic resonance condition of the sample, typically determined in advance using VNA-FMR.

To enable X-ray transmission through the sample, a small aperture is bored into the CPW. The X-ray beam passes through this hole and interacts with the magnetic thin film, inducing X-ray Excited Optical Luminescence (XEOL) within a luminescent substrate placed beneath. This emitted light is detected by a photodiode mounted behind the substrate.

Due to the typically small precessional cone angle ($\approx 1°$), the dynamic XMCD signal is weak,

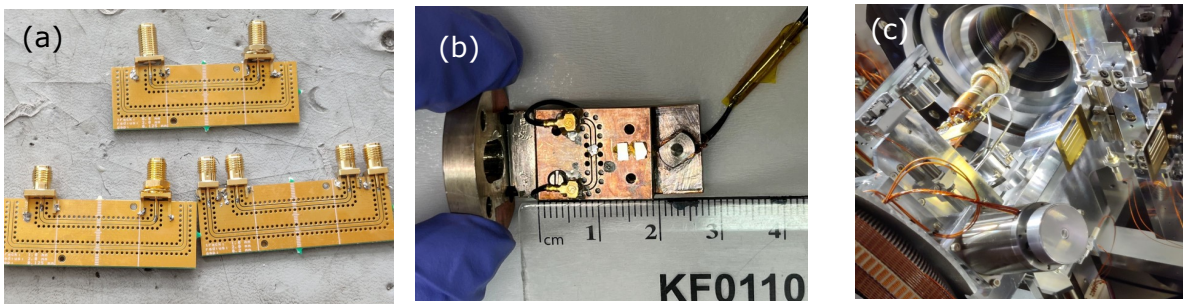


Figure 3.4: Custom CPW designs developed for RFMR experiments. (a) A wide signal-line CPW with standard SMA connectors soldered directly onto the board, enabling high-power transmission exceeding 20 dBm. However, the associated cabling also conducts significant thermal energy from the chamber walls, limiting suitability for cryogenic operation. (b) A micro-SMA compatible CPW variant, designed for lower thermal load, where miniature detachable connectors reduce heat conduction, rendering it more appropriate for low-temperature experiments. (c) Example of the a CPW mounted within the RASOR endstation, demonstrating integration with the experimental geometry.

with a typical dynamic-to-static XMCD ratio on the order of 10^{-3}. To enhance sensitivity, lock-in detection techniques are employed. Specifically, a π-phase modulation is applied to the RF signal at a modulation frequency of 3 kHz, maximising the contrast of the dynamic component. The modulated signal is then applied to the CPW, exciting ferromagnetic resonance in the sample with a well-defined phase delay relative to the X-ray pulses.

The dynamic magnetisation is probed by measuring the rotating component of the magnetic moment that is normal to the static magnetic field. By varying the phase delay between the RF signal and the X-ray pulse, the full precessional trajectory of the magnetic moment can be reconstructed, allowing for detailed mapping of the spin dynamics.

3.5 Reflectivity Ferromagnetic Resonance

Our soft X-ray RFMR experiments were performed on the RASOR diffractometer endstation on beamline I10 at the Diamond Light Source, UK. A schematic of the RFMR experiment, as conducted in the RASOR diffractometer, is shown in Figure 3.5.

The RF synchronization uses the same set-up for XFMR and RFMR, however now the sample must be placed face up, towards the beam, and the CPW is designed for a reflectivity experiment, and the lock-in amplifier (LIA) now requires an automated gain control, to handle the variations in reflected intensity with angle.

Incident X-rays impinge only on the central part of the CPW signal line, therefore avoiding non-uniform RF excitation [79]. At low angles the beam projection can grow exceedingly large, hence the signal line must lie along the scattering plane, this limitation removes RFMR's ability to apply the

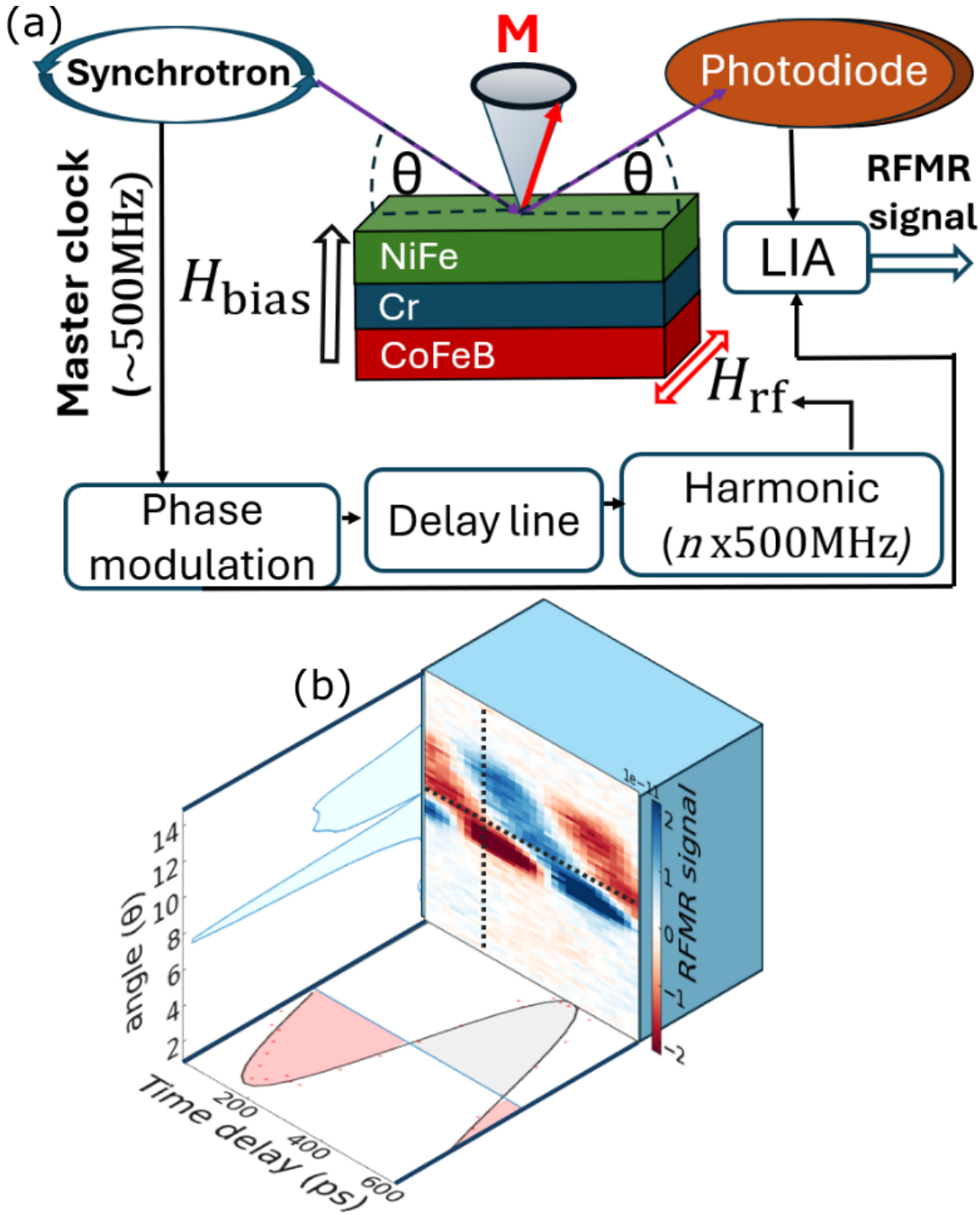


Figure 3.5: (a) Experimental RFMR setup. The ~500 MHz RF signal from the master clock oscillator, which is synchronous with the incident polarised X-ray beam, is routed through a ps-scale delay line and a harmonic generator to achieve resonance at the CPW with a controlled delay relative to the X-ray pulses. The system stroboscopically probes the sample in a θ-2θ geometry, where the photodiode output is passed into an LIA along with a modulating RF signal to extract the dynamic contribution superimposed on the static XMCD signal. (b) Schematic explanation of RFMR data acquisition and plotting. For a given incident X-ray angle, varying the delay between the RF signal (pump) and the X-ray pulse (probe) enables mapping of the precessional cone at a specified Q_z. The resulting data forms a sinusoidal curve corresponding to the RF excitation frequency (horizontal cross-section). Repeating this process across all incident X-ray angles in a θ-2θ geometry produces an XRMR curve of the dynamic contribution (vertical cross-section).

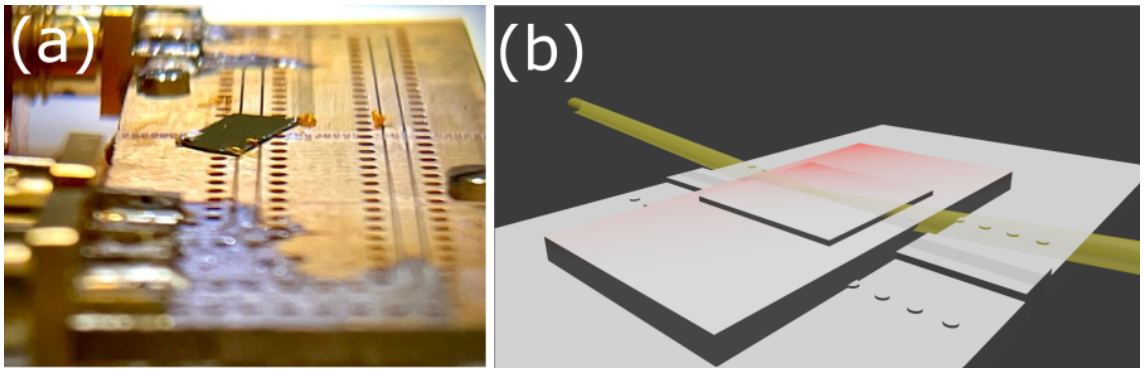


Figure 3.6: Illustration of beam projection geometry in RFMR. (a) In RFMR, the sample and the signal line lie flat within the scattering plane. (b) A schematic depiction of the incident X-ray beam intersecting multilayer structure during RFMR. At low incidence angles, the beam footprint becomes increasingly elliptical, elongating along the projection axis. This has important implications for experiment design: in particular, it necessitates careful alignment of the RF field and sufficient lateral sample dimensions to ensure uniform excitation and minimise angle-dependent variations in the detected magnetisation dynamics.

field in-plane, as is typically done in XFMR.

The reflected X-ray beam from the sample was collected in θ–2θ geometry using a photodiode and fed into an LIA. The LIA isolated the precessing magnetic component of the reflected beam at the kHz modulation frequency. The precessing magnetic signal was measured as a function of pump–probe delay time, for various values of the magnetic field and incident X-ray angle (determining Q_z). By sweeping the pump–probe delay time while keeping other parameters fixed, we obtained a sinusoidal signal whose period matches that of the RF driving frequency. The RFMR amplitude and phase were extracted from this data by fitting sinusoids to the RFMR signal as a function of delay time.

Phase-Modulating the Reflectivity Signal

In earlier implementations of XFMR, the time-resolved dynamic signal was obtained from a photodiode measuring the XEOL transmitted through the sample. This approach required the X-ray beam to pass through a pinhole in the CPW and reach the sample, which introduced experimental complexity, particularly in aligning and rotating the sample. However, once the beam was correctly aligned, the resulting XEOL signal was either independent of, or approximately linear with, the incident X-ray angle. Importantly, there was no experimental parameter in XEOL-based XFMR that caused an exponential drop-off in signal. As a result, the LIA settings could be optimised once and reused across the entire experiment, simplifying the setup significantly.

By contrast, RFMR measures the intensity of the reflected X-rays, which exhibits a steep decrease with increasing incidence angle due to reflectivity effects. This requires the LIA sensitivity settings to be continuously adjusted throughout a measurement, especially when performing angular scans.

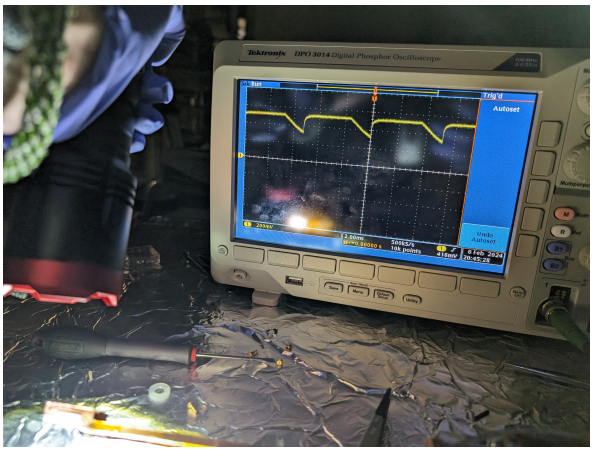


Figure 3.7: RFMR Photodiode response to a handheld torch observed on an oscilloscope. Here the 50 Hz flicker of the AC-powered torch is clearly resolved. In RFMR, the signal arises from phase modulation at the lock-in reference frequency (e.g. 3 kHz), not the X-ray repetition rate (e.g. 500 MHz), thereby relaxing requirements on detector and amplifier bandwidth.

Several strategies were developed during this PhD to address this challenge.

The simplest approach involved feeding the raw photodiode output (ranging from 10^{-6} to 10^{-9} A) directly into the current input of an analogue LIA (Stanford Research SR830). This setup worked well across regions with approximately linear reflectivity response, such as around the critical angle. However, the narrow current range accepted by the analogue LIA limited its applicability to wide-angle scans.

To allow broader control over the dynamic range, two strategies were implemented. In the first, the photodiode current was passed through a pre-current amplifier with internal controls for adjustable gain, and the amplified signal was then fed into the voltage input (0–5 V input range) of a digital LIA (Zurich MFLI) . This had the advantage of enabling flexible gain control and allowed demodulated signals to be recorded through external counting electronics, such as a V2F converter (which accepts only positive signals and offers high resolution) or an ADC module (which allows bipolar signals but with lower resolution). The drawback of this method is that uniform gain amplification can also increase the noise floor, potentially obscuring the small dynamic signal of interest.

The alternative approach was to connect the photodiode directly to the current input of a digital LIA and adjust the gain internally using a socket server connection. This allowed software-level control of the sensitivity in real time, making it suitable for dynamic experiments across a wide range of reflectivity values. However a limitation here arose from over-relying on the LIA's own gain control, which is not optimised for reflectivity experiments, such as the preamplifier used on RASOR.

A common misconception in work of this kind is that the pre-current amplifier, or the LIA need to have a temporal resolution above the X-ray pulse frequency (500 MHz), while this can be achieved

with instruments such as the Femto pre-current amplifier, and new Zurich LIA's, this is not necessary, the dynamic signal arises from the phase modulation ($\approx 3\,\mathrm{kHz}$) as opposed to the individual X-ray pulses. In-fact even the photodiode itself does not need total resolution of the X-ray pulses, as is demonstrated in Figure 3.7, where the 50 Hz oscillation of the torch is detected by the photodiode.

In Chapter 6, the signal was measured through the voltage input of the LIA, with the demodulated R output read via V2F and the X, Y, and phase (θ) components read via ADC. In Chapter 7, the Cr = 24 nm sample was measured using the voltage input, while the Cr = 2 nm sample employed the current input with socket server-based gain control. These two methods yielded noticeably different results: the current input configuration provided smoother data when the signal was strong, while the voltage input setup (with preamplification) offered improved resolution for weak signals, despite amplifying noise uniformly.

For the results presented in Chapter 8, a hybrid approach combining both readout strategies is used to balance sensitivity and signal fidelity.

Chapter 4

Optical Properties of FMR modes

This Chapter serves to demonstrate the process of calculating the scattering factors used in RFMR models, and why they are unique with respect to the scattering factors taken in XRMR measurements.

4.1 Reflected Intensity from Phase-Modulated Magnetic Scattering

To model RFMR accurately, it is essential to ground the dynamic signal in the formalism of X-ray reflectivity. Unlike XFMR, where the signal is simply directly proportional to the XMCD cross-section ($I_{\mathrm{XMCD}} \propto \vec{k} \cdot \mathbf{M}$), RFMR is governed by the full reflectivity response of a multilayer structure, where magnetic and charge scattering contributions interfere coherently. The assumption that all charge scattering cancels out in RFMR is therefore an oversimplification. In this work, the dynamic signal is considered to be governed by the Fresnel equations and the Hannon scattering formalism [70].

We begin with the Fresnel reflectivity equation for s-polarised light at a single flat interface:

$$R = \left| \frac{\cos\theta - \sqrt{n^2 - \sin^2\theta}}{\cos\theta + \sqrt{n^2 - \sin^2\theta}} \right|^2 , \tag{4.1}$$

where n is the complex refractive index and θ the grazing incidence angle.

In RFMR, the precessing magnetisation causes a time-dependent modulation of f_m, which alters the reflectivity amplitudes. For two magnetisation states related by a phase-modulated π-phase shift in precession, the corresponding complex reflectivity amplitudes are:

$$r_{\pm}(E) = \frac{\cos\theta - \sqrt{n_{\pm}^2 - \sin^2\theta}}{\cos\theta + \sqrt{n_{\pm}^2 - \sin^2\theta}}, \tag{4.2}$$

where $n_{\pm}$ is the complex refractive index associated with each magnetisation orientation.

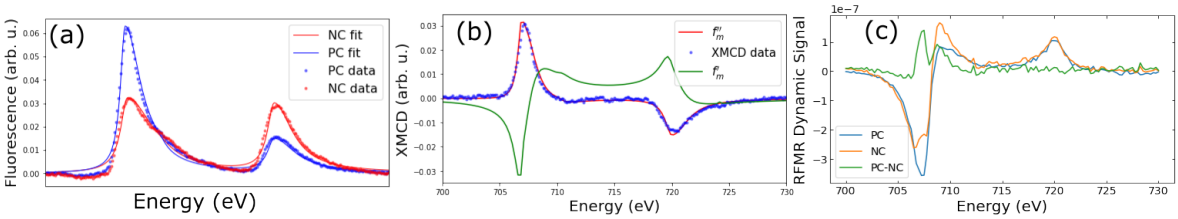


Figure 4.1: *Structure factor of dynamic reflectivity measurements:* Alongside the photodiode placed in θ-2θ geometry, we measured the absorption (XAS) by Fluorescence Yield (FY) using another photodiode placed 70° from the reflectivity peak. (a) By fitting the FY data with asymmetric Lorentzians on the $L_{3,2}$ peaks, we could take the Kramers-Kronig transformation of the fit to extract the real and imaginary component of the charge scattering (f_c' and f_c"). Plotted we see charge scattering at the Fe $L_{2/3}$ edges in positive/negative circular polarisation (PC/NC). (b) Subtracting the polarisations we obtained the real and imaginary component of the magnetic scattering (f_m' and f_m"), which could be fitted to the RFMR dynamic signal. In (c) we demonstrate a RFMR energy spectra. Here we are probing the oscillating component of the Fe moment during NiFe OOP resonance. This data is taken at 2 GHz, phase modulated RF, with the Fe moments canted towards the beam (400 ps), i.e. the peak in dynamic signal in PC measurements. PC and -NC RFMR measurements are shown, with a notable discrepancy between them after the L_3 edge.

The experimentally measured dynamic RFMR signal arises from modulating the RF field between these two magnetisation states at kHz frequencies and using a LIA to demodulate the difference in reflectivity. In the stroboscopic probing method, time dependence can be simplified by considering the intensity as a snapshot of the precessional state, this yields

$$\Delta R(E, \phi) = \mathrm{Re}\left[(r_+(E) - r_-(E))\right], \tag{4.3}$$

This expression naturally captures the angular and spectral dependence of the dynamic signal, including both real and imaginary contributions from the magnetic scattering term.

Importantly, this formalism reveals that the RFMR signal depends explicitly on the energy-dependent optical constants and their interplay with the X-ray polarisation and sample geometry. In the next section, we outline how these optical constants, δ, β, and the corresponding magnetic scattering components, are calculated from experimental absorption data and used to parameterize the full multilayer reflectivity response.

4.2 Calculation of the Optical Constants & Detection Techniques

Understanding the resonant magnetic scattering signal in RFMR requires detailed knowledge of the sample's energy-dependent optical constants. These constants govern how X-rays interact with the material near absorption edges and are encoded in the complex refractive index, $n(\omega, z) =$

$1 - \delta(\omega, z) + i\beta(\omega, z)$. Both δ and β are linked directly to the real and imaginary parts of the atomic scattering factor via [10]

$$\delta(\omega) = \frac{N_A \rho}{A} \frac{r_0 \lambda^2}{2\pi} f_1(\omega), \qquad \beta(\omega) = \frac{N_A \rho}{A} \frac{r_0 \lambda^2}{2\pi} f_2(\omega), \tag{4.4}$$

where N_A is Avogadro's number, r_0 the classical electron radius, ρ the mass density, A the atomic mass number, and λ the X-ray wavelength.

We can acquire X-ray absorption spectra using FY, detected via a photodiode mounted at 70° from the scattering plane. The attenuation of X-rays travelling through a material of thickness d is described by the Lambert-Beer law, which states that the intensity decreases exponentially with thickness according to

$$I(d, \lambda) = I_0 e^{-\mu(\lambda) d}. \tag{4.5}$$

Here, $\mu(\lambda)$ is the attenuation coefficient, which is directly related to the absorption properties of the material at the wavelength λ. The absorption coefficient $\mu(\omega)$ is extracted from FY and connects to the imaginary part of the atomic scattering factor through the optical theorem [80, 10]:

$$\mu = \frac{2\omega}{c} f_2, \tag{4.6}$$

$$f_2(\omega) = \frac{1}{2 r_0 \lambda(\omega)} \sigma_{\text{abs}}(\omega) = \frac{1}{2 r_0 \lambda(\omega) \rho_a} \mu(\omega), \tag{4.7}$$

where ρ_a is the atomic number density.

We collected XMCD spectra in "on-the-fly" mode, with the undulator in continuous motion. As a result, energy scans sampled slightly different energy points, so both were interpolated onto a shared energy grid, anchored by matching start and end energies. This was repeated for positive circular (PC, hereafter but equally considered circular right (CR)), and negative circular (NC, or equally CL), to measure dichroism.

The raw FY spectra were corrected for baseline offset and slope, normalised to the post-edge jump, and then scaled to match far-from-edge tabulated values using the Henke and Chantler reference datasets [81, 82]. These tables provide energy-dependent values for the atomic scattering factors f_1 and f_2, derived either from first-principles calculations or experimental data in the non-resonant regime (typically $> 100\,\text{eV}$ above edge). The Henke-Gullikson table [81] is based on early optical constant compilations, while the Chantler datasets [83, 84] extends this by incorporating relativistic effects, such as spin-orbit coupling in the $2p$ initial states. Although these databases do not directly provide

the full complex scattering amplitude f, they yield f_1 and f_2 in the small-angle (low $|Q|$) limit, which is appropriate for soft X-ray and grazing incidence applications. This scaling procedure, following the methodology outlined in [10], ensures a smooth transition between the measured near-edge structure and the tabulated high-energy asymptotics.

To describe the near-edge fine structure in $f_2(\omega)$, we adopted a physically motivated oscillator model [80]. Transitions between core levels and continuum final states in $3d$ metals give rise to characteristic line shapes that can be modelled by damped harmonic oscillators. The imaginary part of the scattering factor $f_2(\omega)$ was modelled as a sum over damped oscillators with an empirical asymmetry parameter α_{ij}.

$$f_2(\omega) \propto \sum_j \frac{f_{ij}\left[1 + \alpha_{ij}(\omega - \omega_{ij})\right]}{(\omega - \omega_{ij})^2 + \Gamma_{ij}^2}, \tag{4.8}$$

where f_{ij} is the oscillator strength, ω_{ij} the resonance energy, Γ_{ij} the half-width at half-maximum (HWHM).

Having obtained $f_2(\omega)$, we then calculated the corresponding real part $f_1(\omega)$ using the Kramers–Kronig relation:

$$f_1(\omega) = Z - \frac{2}{\pi}\mathcal{P}\int_0^\infty \frac{\epsilon^2 f_2(\epsilon)}{\epsilon^2 - \omega^2} d\epsilon, \tag{4.9}$$

with Z the atomic number. We implemented this integral numerically using a discrete Hilbert transform algorithm with trapezoidal integration. To ensure convergence, the fitted FY spectrum was smoothly merged into the Henke-Chantler tables beyond the measured range, extending the domain up to 400,000 eV as in [10].

From these two polarisation-resolved spectra, we defined the charge and magnetic scattering components as

$$f_c = \frac{f_+ + f_-}{2}, \qquad f_m = \frac{f_+ - f_-}{2}, \tag{4.10}$$

yielding both the real and imaginary parts of each. These derived scattering amplitudes were fed directly into the reflectivity simulation pipeline, enabling the modelling of RFMR signal contrast under different polarisations and RF phase delays, as seen in the final panel of Figure 4.1.

Detection Techniques

X-ray absorption spectra can be measured using either Fluorescence Yield or Total Electron Yield, each offering complementary advantages and limitations. FY detects the intensity of X-ray-induced secondary photon emission, while TEY measures the net current resulting from electron emission

caused by the photoelectric effect. The choice of technique impacts the effective probing depth and the fidelity of the resulting spectra.

FY is generally considered more bulk-sensitive, with an effective probing depth of 100 nm or more, as the escape depth of fluorescence photons is relatively long. However, FY is susceptible to self-absorption effects, particularly in strongly absorbing samples, which can distort the spectral line shape and reduce quantitative accuracy. This distortion limits the use of FY for sum rules analysis, where linearity of absorption with concentration is essential [85].

In contrast, TEY provides a more surface-sensitive probe, with an effective escape depth of photoelectrons typically around 2–5 nm in soft X-ray regimes. The absorption process in TEY is governed by the photoelectric effect: incident photons eject core-level electrons, and the resulting current, measured by grounding the sample through an ammeter, provides a direct measure of the absorption cross-section. TEY is less prone to saturation and non-linearities, making it highly reliable for normalised absorption analysis. However, it is also more sensitive to surface contamination and to changes in sample charging, especially in insulating or poorly grounded specimens [86].

In our work, many samples exceeded the electron escape depth, and the inclusion of RF circuitry on the sample holder introduced significant noise in the TEY signal, making FY the only practical in situ detection method. Consequently, TEY measurements had to be performed separately, often during a different beamtime. Despite these practical constraints, we carried out a comparative study of both methods at the Fe L_3 edge in pseudo-spin-valve samples from Chapter 7. We found that the imaginary part of the refractive index, $\mathbf{n}''$, derived from XMCD spectra measured via FY and TEY, yielded consistent results. This confirms the robustness of the approach for determining optical constants and magnetic scattering amplitudes in the upcoming chapters.

4.3 Energy-Resolved RFMR & the Role of Charge Scattering

To illustrate the role of photon energy in RFMR we show the spectral structure in RFMR measurements on CoFeB(20 nm)/Cr(24 nm)/NiFe(20 nm) pseudo-spin-valve in-phase precession, across the L_3 and L_2 absorption edges of Fe. A series of energy-dependent scans was performed at various pump-probe delay values and incidence angles (see Figure 4.2), revealing a pronounced variation in signal shape and amplitude between energies and angular configurations.

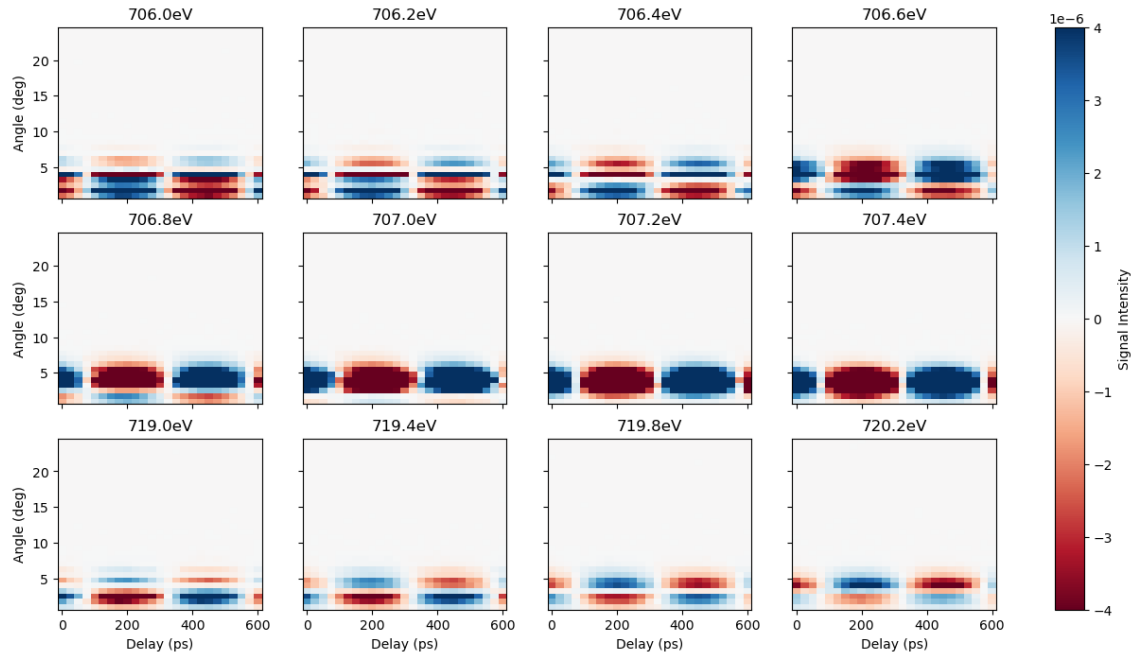


Figure 4.2: Raw RFMR Q_z scans were taken at different X-ray energies across the Fe $L_{3,2}$ edges in a CoFeB(20 nm)/Cr(24 nm)/NiFe(20 nm) trilayer. The measurements were performed under acoustic mode precession, driven by a 2 GHz RF field at a static applied field of 90 mT ($\theta_H = 0°$). The resulting delay-dependent signal evolves significantly between energies, demonstrating the importance of calculating the optical constants.

Initial Model Using Magnetic Scattering Alone

We began modelling the RFMR signal by assuming that the dynamic changes in reflectivity arise solely from magnetic scattering contributions. The refractive index was expressed as:

$$n(\omega) = 1 + a \cdot f'_m(\omega) + ib \cdot f''_m(\omega), \tag{4.11}$$

where f'_m and f''_m denote the real and imaginary parts of the magnetic scattering factor, respectively, derived from experimental XMCD and Kramers-Kronig transformation. The prefactors a and b are energy independent scaling coefficients extracted from fitting.

f'_m and f''_m were calculated in Figure 4.1(b), and the model was created using equations (4.1) with n from eq. (4.11) and fits were done by scaling f'_m and f''_m and following gradient descent based on appropriate initial guesses. However, this model proved inadequate. As shown in Figure 4.3, the energy dependence of the RFMR signal could not be reproduced across all incidence angles and delay conditions. Notably, the model was unable to account for sign reversals between the L_3 and L_2 edges and produced non-physical lineshapes at higher angles.

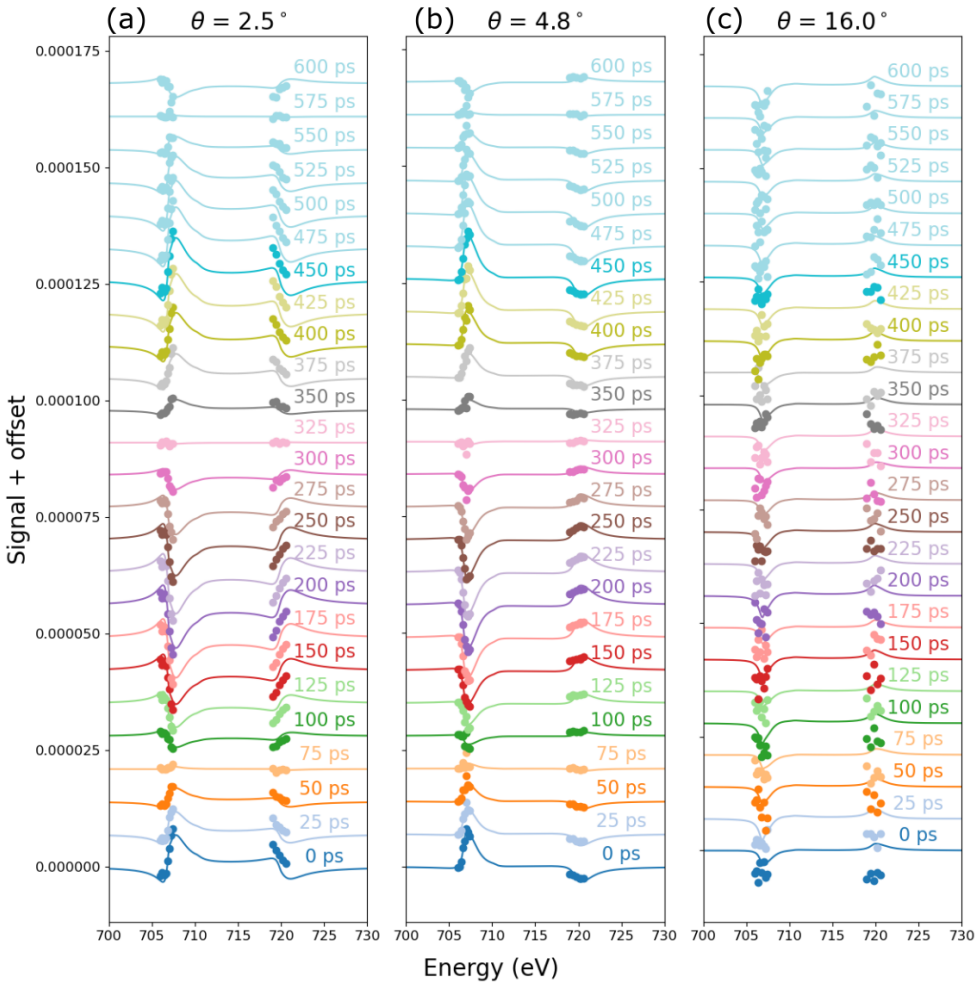


Figure 4.3: Comparison of measured RFMR spectra (points) and corresponding fits from the magnetic-only model (lines) from Figure 4.2, at incidence angles $\theta = 2.5°$, 4.8°, and 16.0° in panels (a), (b), and (c), respectively. The colour scale represents the pump-probe delay line from 0 to 600 ps, with 0 ps and 600 ps shown as blue due to periodicity. While the magnetic-only model captures some spectral features, it consistently fails to reproduce the full angular dependence and does not account for the observed sign reversal between the L_3 and L_2 edges.

Incorporating Charge Scattering Terms

To address these shortcomings, we extended our model to include charge scattering contributions:

$$n(\omega) = 1 + c \cdot f_c'(\omega) + id \cdot f_c''(\omega) + a \cdot f_m'(\omega) + ib \cdot f_m''(\omega), \tag{4.12}$$

where f_c', f_c'' are the real and imaginary parts of the charge scattering factor, obtained from PC/NC (CR/CL) XAS measurements and their Kramers-Kronig transform in Figure 4.1. The prefactors c, and d are now introduced into the model.

This generalized model provided a significantly improved fit, capturing both the amplitude modulation and sign changes across the Fe L_3 and L_2 edges (Figure 4.4). Including f_c allowed us to

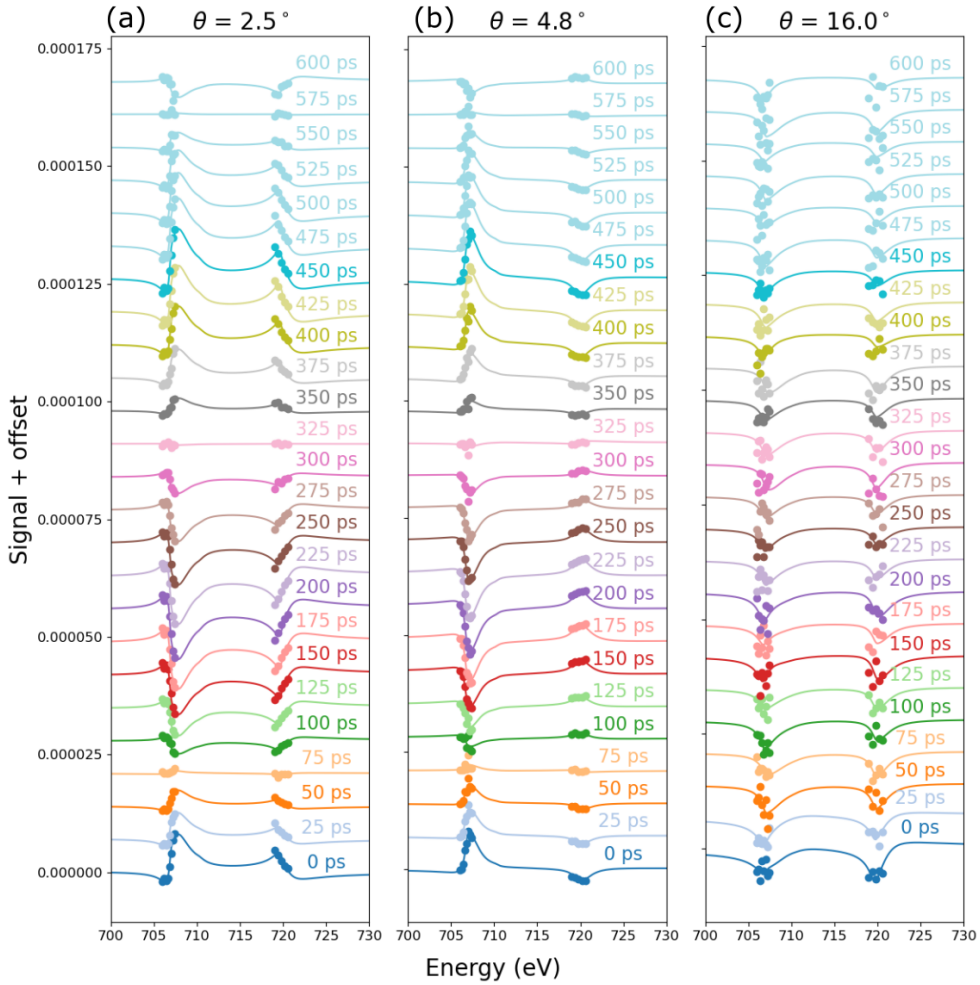


Figure 4.4: Improved fits arising from the comparison of measured RFMR spectra (points) and corresponding fits from the full refractive index model (lines), incorporating both magnetic and charge scattering contributions, at incidence angles $\theta = 2.5°$, $4.8°$, and $16.0°$ in panels (a), (b), and (c), respectively. In contrast to the magnetic-only model, this approach successfully reproduces both the angular dependence and the sign reversal between the L_3 and L_2 edges, yielding a more accurate description of the RFMR signal lineshape.

correctly reproduce the observed switch from opposite to same sign between L_3 and L_2 at high angle.

Extracting Angular Dependence of Scattering Coefficients

Using this expanded model, we fit energy-resolved delay scans at multiple incidence angles to extract the scaling coefficients a, b, c, and d. These coefficients reflect the relative sensitivity of the RFMR signal to each scattering component as a function of angle. Figure 4.5 presents the colormesh visualisation of these parameters and their delay-dependent phase behaviour. These results confirm the necessity of including charge contributions to fully capture the reflectivity-modulated FMR dynamics in metallic multilayers.

Model Limitations

Despite the success of our extended model incorporating both magnetic and charge scattering terms (f'_m, f''_m, f'_c, f''_c), we observe notable limitations at higher incidence angles. In particular, the extracted dispersive magnetic (f'_m) and charge (f'_c) scaling coefficients exhibit a rapid suppression above approximately $\theta = 8°$, appearing to vanish entirely. We outline several hypotheses that may explain this phenomenon.

Firstly, the magnetic scattering factors used in the model were derived from XMCD and XAS measurements performed in TEY mode, which probes only the top ~ 5 nm of the sample. One might suspect that at higher angles the X-ray penetration depth increases sufficiently to probe deeper into the heterostructure, potentially invalidating the use of TEY-derived quantities. However, we find this explanation unlikely, as FY measurements, known to be sensitive to a much larger depth, reproduce the same XMCD lineshape, suggesting the TEY/ FY spectra reliably represent the bulk magneto-optical response.

Second, a more subtle and likely explanation lies in the difference in magnetisation geometry between our static XMCD measurements and our RFMR experiments. The XMCD-derived f'_m and f''_m reflect the response of an OOP static magnetisation at that static field. In contrast, RFMR probes the time-dependent, IP precessional components of the magnetisation vector. Since magnetic scattering is inherently vectorial and anisotropic, this geometrical mismatch may lead to an incorrect scaling of the scattering amplitudes, particularly for the dispersive response, which is sensitive to phase lag and angular projection [70]. In this light, the suppression of f'_m above 8 degrees may reflect a failure to project the OOP-derived magnetic scattering tensor onto the IP dynamic precession axis relevant for RFMR.

Third, a more technical possibility arises from the interpretation of the reflectivity signal. The dispersive components of the scattering factors are associated with phase-sensitive (out-of-phase) responses and become purely imaginary at resonance. Since our signal extraction relies on the real part of the reflected amplitude (e.g., $\mathrm{Re}[r]$), the effective contribution from f'' terms may diminish or become masked at and above the absorption peak, especially if they are no longer projected onto the observable axis. This is a well known phenomena and termed the *optical phase problem*. This also motivated a sensitivity analysis to clarify whether the model is inherently insensitive to dispersive contributions in this regime. Here it was obvious that when the real components of the refractive index were set to 0, the results of the Fresnel equation are entirely imaginary, rendering the specific values for a and c obsolete.

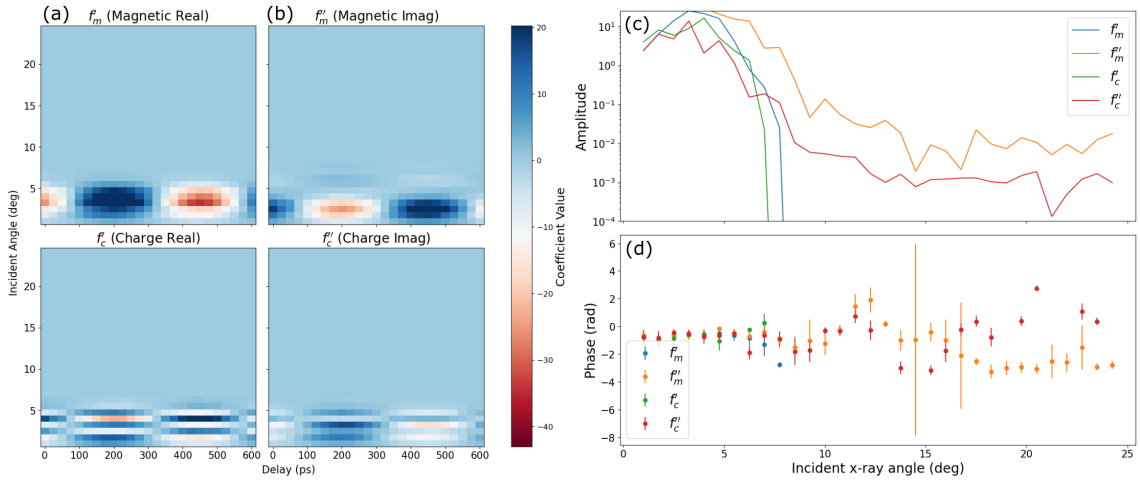


Figure 4.5: Summary of extracted refractive index contributions from RFMR fits using magnetic and charge scattering terms. (a) Angular and delay dependence of the fitted scaling coefficients for the real magnetic (f'_m) and real charge (f'_c) components. (b) Corresponding dependence for the imaginary magnetic (f''_m) and imaginary charge (f''_c) components. (c) The extracted amplitude and (d) phase of each of the four coefficients as a function of the incident X-ray angle. Phase is only shown when the corresponding amplitude is greater than 10^{-3}.

Lastly, our reflectivity model assumes a single interface and uniform magneto-optical parameters with depth. However, since the refractive index was constructed from experimentally measured quantities (rather than tabulated or theoretical values), we had assumed that it implicitly accounted for a more thorough response. The observed discrepancies suggest that this assumption breaks down at higher angles, where the phase accumulation and field distribution become increasingly sensitive to depth-dependent structure [73].

We stress that these limitations are not unique to our approach, but are broadly relevant in RFMR, XRMR, and other time-resolved magneto-optical reflectivity studies. Further work in this thesis will avoid the ambiguities of scattering factor nuance in order to discuss the depth-dependent nature of the magnetisation dynamics. The solution requires tensorial scattering models and simulations with explicit interface structure [87]. This lays the motivation for the necessity to use the complex, recursive modelling pipeline demonstrated in Chapter 5 and used exclusively throughout the rest of the Thesis.

4.4 Moment Alignment Dependence

In a typical XRMR project, you would not be surprised to find that the conclusion quantifies the variations in refractive index with depth, rather than the variations in moment. This is due to the intrinsic complexity of quantifying moment alignment, where models based on macrospin cease to succeed due to effects such as structural and magnetic roughness, diffusion demagnetism, SOT and DMI.

Further it is understood that the fundamental moment of each atom is unchanging, but rather its effective environment is the interesting change with depth. Hence you can usually discuss refractive index in static XRMR situations. In RFMR this is not as trivial due to the necessity to compute the actual moment rotation. In XFMR moment rotation is accounted for by applying a sinusoidal variation to the XMCD induced absorption $I_{XFMR} = \beta_M sin(\omega t)$. While in RFMR your intensity comes from Eq. (4.1), this reveals that I_{RFMR} is no longer explicitly sinusoidal.

Figure 4.6 describes the field dependence on dynamic signal spectra. In a trilayer sample with thick Cr spacing (CoFeB(20 nm/Cr(24 nm)/NiFe(20 nm)). Here, a photodiode is positioned in reflectivity geometry, and an RF signal, synchronized with the incoming X-ray and phase-modulated for dynamic measurements, is applied to the sample. By sweeping the energy across the $L_{3,2}$ edges of Fe, the FMR precession of the Fe moments can be measured. Additionally, by adjusting the field, the pseudo-spin-valve FMR mode can be switched from acoustic (in-phase oscillation of Fe moments) to optical (anti-phase oscillation). The Figure displays calculated $\mathbf{f'_m}$ from FY XAS analysis in orange at the top, and the complimentary calculated $\mathbf{f''_m}$ (KK transformed) at the bottom. Between this, we observe energy spectra taken across static field values transitioning from the optical mode to the acoustic mode. It is observed that in the optical mode, the dynamic signal resembles $\mathbf{f'_m}$, and in the acoustic mode it resembles $\mathbf{f''_m}$. In between the FMR modes a convolution of both components is required to fit the data. This shift from $\mathbf{f'_m}$ to $\mathbf{f''_m}$ is due to Fe moment alignment within the multilayer, with the acoustic mode having increased absorption due to more moments alignment with the incoming beam, and the optical mode providing a 90° moment rotation for f''_m to interact with. It is worth noting that when this experiment was repeated on negative circular polarisation, due to the reduced absorption, we have an increased penetration depth and slightly different results for the $\mathbf{f'_m}$ but consistent results on $\mathbf{f''_m}$. The fits for $\mathbf{f'_m}$ and $\mathbf{f''_m}$ were done on background-subtracted

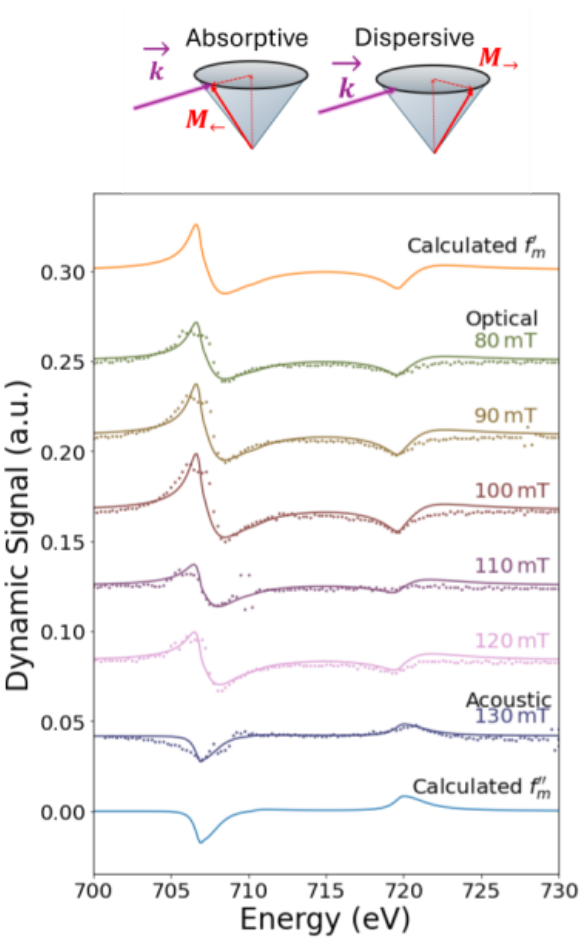


Figure 4.6: RFMR signal, while governed by the Fresnel equation, is proportional to $k \cdot M$, creating variations in the scattering factors when switching modes. Shown are the variations in dynamic spectra taken when switching the fields to induce a 90° rotation in the Fe moments throughout a spin-valve.

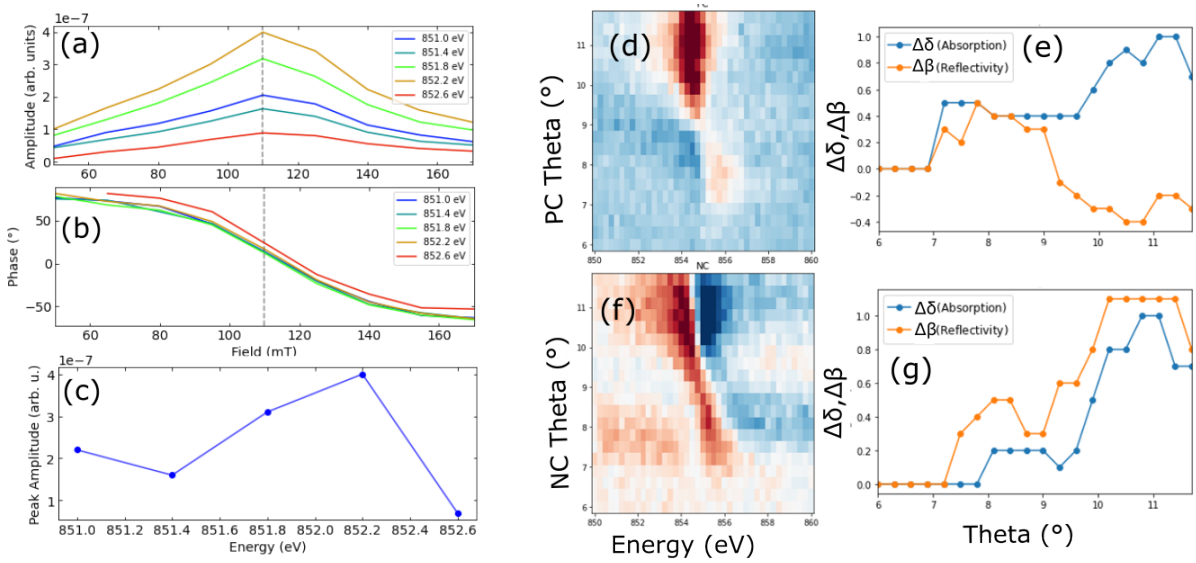


Figure 4.7: Energy and polarisation dependence of Ni RFMR response in CoFeB/Cr/NiFe. (a–b) Resonance conditions are identified from delay-scan (a) amplitude and (b) phase shift. (c) Dynamic signal amplitude across the Ni L_3 edge. (d–g) RFMR response as a function of angle and energy for (d) PC and (f) NC polarisation, with fitted dispersive and absorptive magnetic scattering contributions ($\Delta\delta$, $\Delta\beta$). A sign inversion in f'_m appears at the second fringe in PC only.

FY XAS spectra for Fe, with asymmetric Lorentzians corresponding to L_3 and L_2 edges (at 707.1 eV and 720.0 eV respectively), and a strong asymmetry to the L_3 edge, with a FWHM below the edge of 0.5 eV, and above the edge of 1.5 eV in PC measurements and 2.5 eV in NC. On the L_2 edge see a FWHM below the edge of 0.7 eV, and above the edge of 2.0 eV.

4.5 Energy & Polarisation Dependence

Figure 4.7 presents an analysis of both the energy and polarisation dependence of the Ni RFMR signal in the spin-valve trilayer. Under 2 GHz RF excitation, delay scans are well described by a 2 GHz sine curve, allowing extraction of the amplitude and phase of the dynamic signal. By sweeping the static magnetic field, resonance can be identified by a peak in the amplitude (a) and a corresponding 90° phase shift (b). The energy dependence of this dynamic signal, shown in (c), reveals a clear peak at 852.2 eV, coincident with the XMCD maximum observed in FY and reflectivity measurements. Notably, a detectable pre-edge signal is also present, whereas the post-edge region shows no such dynamic response.

The polarisation dependence of RFMR adds further complexity due to its directional sensitivity and the fact that inverting the RF phase is only equivalent to inverting the photon helicity at normal incidence. While in XMCD the dichroic signal obeys $I_{\mathrm{XMCD}} \propto \mathbf{k} \cdot \mathbf{M}$, this symmetry is broken in XRMR and RFMR due to variations in incident angle. As shown in panels (d-g), RFMR measurements

across a range of X-ray incidence angles in both PC and NC configurations exhibit distinct behaviours. At 400 ps delay in the optical mode (where the Ni moments are canted toward the beam), RFMR intensity is plotted against angle and energy for PC (d) and NC (f). Fits to the dispersive ($\Delta\delta$) and absorptive ($\Delta\beta$) parts of the magnetic scattering factor are shown in (e) and (g) for PC and NC, respectively.

Two distinct amplitude peaks are observed across the angular scan. In the first fringe, both PC and NC display similar behaviour, namely positive values for both $\Delta\delta$, $\Delta\beta$. In contrast, in the second fringe, an inversion occurs only in the dispersive component $\Delta\beta$ for the PC configuration, while NC remains unchanged. This indicates that the dispersive and absorptive parts of the magnetic scattering factor can decouple and vary independently with polarisation and angle. These findings extend the field-dependent phase inversion shown in Figure 4.6 by demonstrating that this behaviour also depends on the X-ray polarisation and energy.

Chapter 5

Building an RFMR model

This Chapter serves to demonstrate the modelling process developed over the course of this PhD. The magnetic modelling framework employed in this study is based on the Fresnel reflectivity formalism [72], incorporating depth-dependent variations in magnetic moments. This approach uses the experimentally derived optical properties to account for both resonant and non-resonant scattering contributions to simulate the reflectivity profile as a function of the incident X-ray angle and the depth-profile, enabling precise characterisation of the magnetisation dynamics within the multilayer structures.

The specific modelling used is an adaption to GenX's open source XRMR models, constructed in Python. It has been made open-source on the Author's GitHub.

5.1 Mathematical Formalism Behind Reflectivity Calculations

The RFMR modelling approach used in this thesis relies on the well-established formalism for specular reflectivity developed by Stepanov and Sinha [72], which generalizes the recursive optical matrix method to handle arbitrary complex scattering potentials. This formalism allows us to compute the reflectivity from stratified media, such as magnetic multilayers, incorporating both structural and magnetic contributions to the scattering length density.

The reflectivity problem is governed by the Helmholtz equation for the electric field $E(z)$ in the z-direction perpendicular to the film surface

$$\left[\frac{d^2}{dz^2} + k^2 n^2(z)\right] E(z) = 0, \tag{5.1}$$

where $k = 2\pi/\lambda$ is the vacuum wavevector, and $n(z)$ is the complex refractive index profile of the

film. For X-rays, the refractive index is typically written as:

$$n(z) = 1 - \delta(z) + i\beta(z), \tag{5.2}$$

where δ and β are related to the real and imaginary parts of the scattering length density, and can include magnetisation-dependent terms in the magnetic case. The total reflectivity $R(Q_z)$ as a function of momentum transfer Q_z is obtained by recursively computing reflection and transmission coefficients at each interface in a multilayer stack. Starting from the deepest (substrate) layer, we compute the wave amplitudes upwards using transfer matrices. For a stack of N layers, each with complex refractive index n_j and thickness d_j, the 2×2 matrix formalism gives the total reflection coefficient r

$$\begin{pmatrix} E_0^+ \\ E_0^- \end{pmatrix} = M \begin{pmatrix} E_N^+ \\ E_N^- \end{pmatrix}, \qquad M = \prod_{j=1}^{N} M_j, \tag{5.3}$$

where $E_j^{\pm}$ are the forward/backward propagating waves in layer j, and M_j are the characteristic transfer matrices describing wave propagation and interface reflections. Each layer matrix M_j incorporates both the phase accumulation over the layer thickness and Fresnel reflection at the boundaries

$$M_j = \begin{pmatrix} \cos(k_{z,j} d_j) & \frac{i}{k_{z,j}} \sin(k_{z,j} d_j) \\ i k_{z,j} \sin(k_{z,j} d_j) & \cos(k_{z,j} d_j) \end{pmatrix}, \tag{5.4}$$

where $k_{z,j}$ is the z-component of the wavevector in layer j

$$k_{z,j} = \sqrt{k^2 n_j^2 - Q_z^2}. \tag{5.5}$$

The reflectivity is finally computed from the amplitude reflection coefficient r as

$$R(Q_z) = |r(Q_z)|^2. \tag{5.6}$$

To compute the final signal $W(Q_z)$ corresponding to the RFMR observable, the model integrates reflectivity over the beam divergence and resolution

$$W(Q_z) = \int R(Q_z') \cdot \text{Resolution}(Q_z' - Q_z)\, dQ_z', \tag{5.7}$$

typically implemented via convolution with a Gaussian resolution function. The above formalism is implemented in the simulation backend using a recursive algorithm optimised for speed and numerical

stability. magnetisation dynamics (precession cone angle, tilt, and phase) are encoded into the complex magnetic scattering amplitudes in each layer, enabling simulation of RFMR contrast under arbitrary polarisation conditions.

5.2 Scattering Factor Considerations in RFMR

Scattering-based RFMR is conceptually based on XFMR, i.e., the element-selective detection of the dynamic FMR signal using synchrotron-based XMCD [12]. In transmission based XFMR, the amplitude of the dynamic signal directly corresponds to the amplitude of the precessing magnetic moment (i.e., the precessional opening angle), while the phase of the dynamic signal independently reflects the precession phase.

In contrast, in RFMR, the total reflected intensity is governed by the Fresnel reflectivity equation [80], which depends on complex magnetic scattering factors [88]. As a result, the amplitude and phase of the RFMR signal do not directly represent the precessing moments but must instead be matched to XRMR models to accurately extract the underlying dynamic parameters.

The process of the magnetic reflectivity model [89] is presented here. Here we simulate the X-ray as incident onto the sample in the y-z plane, with $\theta = 0$ corresponding to a beam path directly along the y-plane and half cutting the sample. The macrospin moments are saturated along the z-axis and hence oscillate in the x-y plane. By varying the moment phase a different reflectivity intensity is obtained. When all the moments throughout the film are in-phase there is a clear sinusoidal dependence on the dynamic signal, and this reflective asymmetry peaks when all the moments align with the beam, providing the largest XMCD contrast. This effect is independent of the incident angle, but by varying the incident angle a magnetic profiling of the sample can be extracted, with a behaviour in the amplitude of the dynamic signal that can be considered analogous to the asymmetry from a circular dichroism reflectivity measurement.

The situation becomes more complicated when the phase of the moments becomes a function of depth, such as in an optical mode of a spin-valve. Here, by varying the incident angle the penetration depth of the X-ray changes. This results in a significantly stronger dependence on moment rotation angle (delay line variable in RFMR experiments) as each layer will align with the beam at different times. As the reflected intensity from each layer changes with varying incident angle, there is a continuous variation in optimum moment rotation angle across different incident X-ray angles. In an ideal optic mode there are two layers oscillating out-of-phase, hence the delay time which maximises the dynamic signal undergoes a 180° phase shift across their respective interference conditions.

This results in a shearing style reflectivity profile as the most probed layer in the film changes with changing angle. The XRMR model used is described in [72], Incorporating recursion equations for 2×2 scattering matrices to calculate resonant X-ray reflection, alongside formalism for the polarisation dependent scattering character [73, 90]

$$A = l^2 \cdot \frac{r_e}{\pi} \cdot n_{FM} \cdot (F_{11} + F_{1\bar{1}}) \tag{5.8}$$

$$B = l^2 \cdot \frac{r_e}{\pi} \cdot n_{FM} \cdot (F_{11} - F_{1\bar{1}}) \tag{5.9}$$

$$C = l^2 \cdot \frac{r_e}{\pi} \cdot n_{FM} \cdot (2F_{10} - F_{11} - F_{1\bar{1}}) \tag{5.10}$$

Here, A corresponds to the resonant non-magnetic term of the susceptibility; B represents the resonant magnetic term that is linear in the magnetisation (i.e., the circular dichroism component); and C denotes the term that is quadratic in the magnetisation, responsible for magnetic linear dichroism effects. The variable l is the X-ray wavelength (typically tuned to the L_3 absorption edge of the ferromagnetic element), r_e is the classical electron radius, and n_{FM} is the number density of resonant magnetic atoms.

Using this formalism, one can calculate the intensity in reflectivity for any incidence angle θ, given theoretical values of F_{11}, $F_{1\bar{1}}$, and F_{10} for the resonant element, along with the structural and magnetic properties of the multilayer. By varying the magnetic moment as a function of depth, the full vector profile of each FMR mode can be reconstructed.

The recursive matrix method provides a particularly powerful approach to solving the reflectivity problem in these systems. Rather than relying on brute-force numerical integration, which can be computationally prohibitive for complex multilayers, this approach systematically propagates wave amplitudes through successive layers, enforcing continuity conditions at each interface. This makes it possible to efficiently calculate reflectivity profiles while maintaining high numerical stability. The algorithm naturally incorporates interfacial roughness via the formalism proposed by L. Nevot and P. Croce [71], which modifies the transfer matrix to account for a Gaussian distribution of interface heights. This approach describes the variation of optical constants using an error-function-like profile, enabling the modelling of graded transitions between layers, a feature often essential for accurately describing films grown by sputtering or molecular beam epitaxy.

5.3 Macrospin Models, Magnetisation Precession & Susceptibility Tensor Formalism

The ability of RFMR to measure magnetisation dynamics is governed by the magnetic susceptibility tensor $\boldsymbol{\chi}(\omega)$, which characterises the linear response of the magnetisation $\mathbf{M}$ to an applied oscillating field at frequency ω. The dynamic susceptibility determines the reflective intensity, providing insight into depth-dependent precession profiles.

Dynamic Susceptibility Tensor

The susceptibility tensor $\boldsymbol{\chi}(\omega)$ is defined in the form:

$$M_i(\omega) = \sum_j \chi_{ij}(\omega) H_j(\omega), \tag{5.11}$$

where $M_i(\omega)$ is the dynamic magnetisation component, and $H_j(\omega)$ is the applied oscillating field. For a ferromagnetic medium, assuming small-angle precession about an equilibrium magnetisation direction $\mathbf{M}_0$, the susceptibility takes the form:

$$\boldsymbol{\chi}(\omega) = \begin{bmatrix} \chi_{xx} & \chi_{xy} & \chi_{xz} \\ \chi_{yx} & \chi_{yy} & \chi_{yz} \\ \chi_{zx} & \chi_{zy} & \chi_{zz} \end{bmatrix}, \quad \chi_{xy}(\omega) = \chi'_{xy} + i\chi''_{xy}. \tag{5.12}$$

The on-diagonals refer to the eigenvalues of the tensor, and describe anisotropic effects. The off-diagonal components, e.g. χ_{xy} and χ_{yx} encode precessional motion and contain both real and imaginary parts. The real part χ'_{xy} describes in-phase response, whereas the imaginary part χ''_{xy} quantifies dissipative effects. The spectral weight distribution of these components governs the dynamic behaviour of magnetisation and can be experimentally inferred from RFMR.

Phase Lag of magnetisation Precession

The phase lag $\phi(z)$ of the precessing magnetisation at a depth z in the multilayer system is derived from the off-diagonal elements of the susceptibility tensor:

$$\phi(z) = \tan^{-1}\left(\frac{\mathrm{Im}(\chi_{xy}(z))}{\mathrm{Re}(\chi_{xy}(z))}\right). \tag{5.13}$$

Often phase lag arises within eigenmodes (e.g. optical and acoustic modes in trilayers, or the more complex FMR modes in Chapter 8), where the difference between precessing layers has a symmetrical value (180° in the optical mode), however in the presence of DMI, demagnetism, inhomogeneous dipolar fields, or spin pumping, phase lags can manifest in any manner.

Opening Angle of the magnetisation Precession

The opening angle ξ describes the amplitude of the magnetisation precession and is derived from the eigenvalues of the susceptibility tensor:

$$\xi = \tan^{-1}\left(\frac{\sqrt{\chi_{xx}^2 + \chi_{yy}^2}}{\chi_{zz}}\right). \tag{5.14}$$

This angle represents the deviation of the magnetisation vector from the static equilibrium direction and is influenced by the driving RF field amplitude, the damping coefficient α, and the strength of the external bias field.

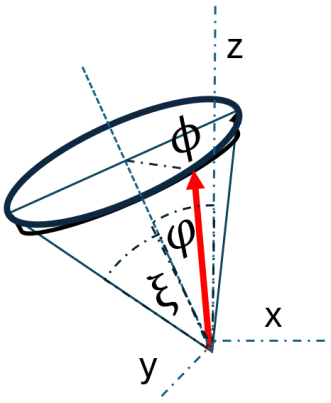
Tilt of the Precession Cone

The cone tilt ψ defines the equilibrium offset of the precessional trajectory from the film normal and is given by:

$$\psi = \tan^{-1}\left(\frac{\chi_{xz}}{\chi_{zz}}\right). \tag{5.15}$$

This parameter reflects the competition between PMA and external in-plane field contributions. In systems with strong DMI, ψ can exhibit a systematic dependence on interfacial spin-orbit effects.

The specific modelling used in this study begins defining the moment rotation throughout the depth of the thin film by the form shown below. For a given ξ (precessional opening angle), ϕ (precessional phase relative to pumping RF), and ψ (tilt from surface normal) this equation describes a precessional cone parametrized by time (t), with an angular frequency (ω). The nπ term here arises from the phase modulation applied by the LIA, where the dynamic signal (RFMR signal) is defined as the difference in reflected intensity for n=0 and n=1. The reflectivity model is generated by considering ξ, ϕ, and ψ as a function of depth, where ξ incorporates an interfacial layer for the magnetism of thickness (dd_l and dd_u), and the interfaces has roughnesses (σ_l, σ_u, σ). Then simulating repeated stroboscopic RFMR profiles for this film for each t across an entire precessional period of $t = 0 \rightarrow \frac{2\pi}{\omega}$. This results in a 2D reflectivity profile, with one axis corresponding to $\mathbf{Q_z}$, and the other to t. This resulting 2D



$$M = [M_x, M_y, M_z] =$$
$$[M_0 \sin(\xi)\cos(\omega t + \phi + n\pi),$$
$$M_0 \sin(\xi)(\sin(\omega t + \phi + n\pi)\cos(\psi) - \sin(\psi)),$$
$$M_0 \cos(\xi)(\cos(\omega t + \phi + n\pi)\sin(\psi) + \cos(\psi))]$$

Figure 5.1: The linearised solution to the LLG can be modelled with spherical coordinates: phase of precession $\phi(z)$, cone tilt from surface normal $\psi(z)$, and relative opening angle $\xi(z)$. Phase modulation is accounted for by $n\pi$.

profile can be fitted to real RFMR $\mathbf{Q_z}$ vs delay maps to determine the depth-dependent structure.

Optical constants δ and β were calculated according to Chapter 4 and [8]. β is directly measured XMCD absorption using a Fluorescence Yield detector placed 70° from the specular, then taking the Kramers-Kronig transformation to obtain δ. Form Factors are taken from the Henke tables [81].

5.4 Global Optimisation Based on Co-Fitting

The next step is to fit the generated RFMR simulation to RFMR data. Fitting reflectivity curves is already a well understood and developed process [91, 92]. The specific nuance in our work is adapting these protocols to account for dynamic scattering factors, phase modulation, and to apply them to fit the 2D resulting profile (Intensity vs $\mathbf{Q_z}$ vs time). This is done by following the global optimisation akin to the GenX software, which uses a Differential Evolution (DE) algorithm [93]. DE takes it's name from evolution in the animal kingdom, where populations will undergo random mutations, and crossovers, in order to maximise survival rate [94]. In our algorithm the goal is to trial multiple, initially random, parameter solutions, and to weight them inside a function termed an optimiser. The best-fit solutions are saved, where they then undergo small random changes (mutations), swap certain parameters with other solutions (crossovers), and then repeat the optimiser process over multiple generations until convergence is achieved across the populations. This is demonstrated in Figure 5.2, using the function $f(x, y) = (x - 0.5)^2 + (y - 0.5)^2 + 0.5\sin(20x) + \sin(20y)$, with the global minima highlighted as a red star, and arrows denoting the movement of candidates to the solution.

In order to probe the depth-dependence of the FMR modes, a novel XRMR-style code was developed to interpret the phase modulated experimental results. First the structural parameters are found using a lab-based Cu Kα XRR (8.048 keV), and fit using the GenX software. Next element

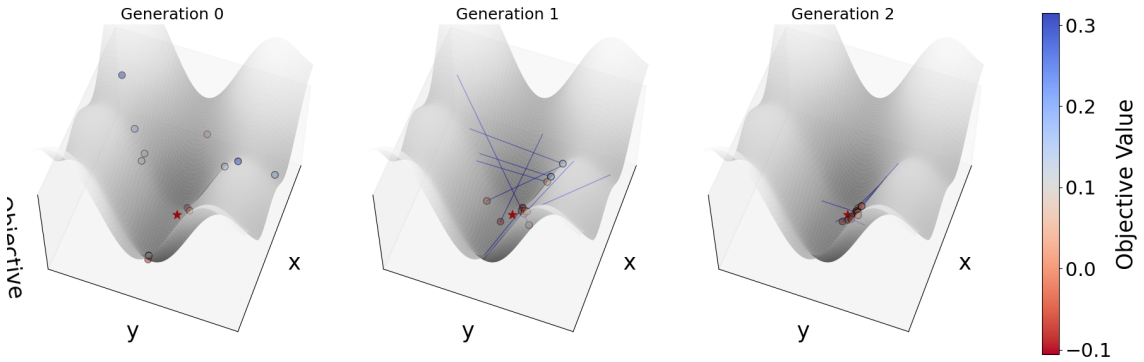


Figure 5.2: A visualisation of differential evolution in Python, minimising a predefined function containing both local and global minima. Over three generations, the initially random population undergoes crossover, mutation, and recombination (shown as arrows in generations 1 and 2), gradually converging toward the global minimum.

specific measurements were used to determine the static magnetic properties of the ferromagnetic materials. By tuning the photon energy to the L_3 edges, the magnetic component of each element can be revealed. This was further fit using GenX (Chapters 6, 7) or a python pipeline to co-fit multiple datasets (Chapter 8). The script includes parameter initialization, numerical simulation, optimisation via differential evolution or gradient descent, visualisation, SLD calculation, Sensitivity Analysis, and can import magnetisation data from micromagnetic results to return their reflectivity profile.

Next, a similar process can be used to interpret the RFMR, In all Chapters, this is Python-based and the code uses the `scipy.optimise.differential_evolution` algorithm to find global-optimum parameters. Degeneracy between parameters associated with the dynamic depth profile ($\xi(z)$, $\phi(z)$, $\psi(z)$) needed to be resolved. Typically this was done in this PhD by co-fitting two resonance modes in the one sample, such as the sine vs distorted data in the magnetic single film, the acoustic and optical modes in the Magnetic trilayers, or the more complex, unique FMR modes in the complex heterostructures.

5.5 Penalising Unphysical Results in the Optimiser

Throughout this project, the interpretation of best-fit parameter series has been guided by comparison with micromagnetic simulations. However, a purely numerical optimisation process, such as DE, is often prone to returning solutions that are mathematically valid but physically implausible [95]. This challenge becomes especially pronounced in RFMR, where the fitting procedure may produce noisy or erratic parameter profiles with little physical meaning unless constraints or regularization are applied.

A sensitivity analysis of the DE algorithm frequently reveals such pathologies. For example, consider a model where a ferromagnetic macrospin layer is divided into ten sublayers, each allowed

to precess independently with a unique phase, and a corkscrew-like correct result. The optimiser may return a best-fit phase profile such as:

$$[0, -100^\circ, 80^\circ, 20^\circ, -60^\circ, -40^\circ, 100^\circ, -20^\circ, 40^\circ, 60^\circ, -80^\circ],$$

which achieves a global minimum in the cost function but exhibits wild, discontinuous variations with depth. A slight perturbation, say, rearranging the phase series into a monotonically increasing trend:

$$[-100^\circ, -80^\circ, -60^\circ, \ldots, 100^\circ]$$

may result in a fit only marginally worse in terms of the objective function, yet is far simpler and more physically intuitive.

This reflects a broader principle: optimisation in the absence of physical priors or regularization can easily overfit noise in the data. Here, Occam's Razor (the preference for the simplest sufficient explanation) and principles from Bayesian analysis become relevant. One should not interpret the numerically optimal solution as definitive without incorporating physical plausibility into the fitting process.

To mitigate this, we incorporated qualitative physical priors directly into the cost function of the DE optimiser. In addition to minimising the squared residuals between experimental and simulated data, the cost function included a penalty term that discouraged sharp discontinuities in dynamic variables (such as the precession phase or opening angle) across depth. This was implemented by summing the finite differences of the fitted parameters and applying smoothing or regularization weights and shown in Figure 5.3.

An alternative approach would be to explore a set of physically motivated models with varying complexity to fit the RFMR data. For example, the 10 sub-layers could be assumed to exhibit uniform behaviour (i.e., $\frac{d\phi(z)}{dz} = 0$), or a linear variation with depth parametrized by just two variables, $\phi(z = 0)$ and the gradient $\frac{d\phi(z)}{dz}$. More complex profiles, such as a parabolic dependence or higher-order forms, could also be considered to capture potential curvature in the depth-dependent dynamics.

Furthermore, windowing functions were introduced to softly constrain the fitted parameters based on prior knowledge from complementary characterisation techniques. For example, structural layer thicknesses extracted from hard XRR, or bounds on magnetic scattering factors derived from XMCD, were used to guide the fit without imposing them as hard constraints. These external measurements are themselves subject to uncertainty, and so their influence was tuned via adjustable weights rather

$$
\begin{aligned}
&\textbf{FMR Mode 1} \qquad\qquad\qquad\qquad \textbf{FMR Mode 2} \\
\chi^2_{\text{total}} = &\underbrace{\sum_i \left(\frac{\log A^{(1)}_{\text{sim},i} - \log A^{(1)}_{\text{exp},i}}{\sigma^{(1)}_A} \right)^2 + \sum_i \left(\frac{\log A^{(2)}_{\text{sim},i} - \log A^{(2)}_{\text{exp},i}}{\sigma^{(2)}_A} \right)^2}_{\text{Amplitude error across modes}} \\
&+ \underbrace{\sum_i w^{(1)}_{\phi,i} \left(\frac{\phi^{(1)}_{\text{sim},i} - \phi^{(1)}_{\text{exp},i}}{\pi} \right)^2 + \sum_i w^{(2)}_{\phi,i} \left(\frac{\phi^{(2)}_{\text{sim},i} - \phi^{(2)}_{\text{exp},i}}{\pi} \right)^2}_{\text{Amplitude-weighted phase error across modes}} \\
&+ \lambda_1 \underbrace{\sum_j \left(\phi_{j+1} - \phi_j\right)^2 + \sum_j \left(\xi_{j+1} - \xi_j\right)^2}_{\text{Smoothness penalty on phase and cone angle depth profiles}} \\
&+ \lambda_2 \underbrace{\sum_k \left(\frac{t_k - t^{(0)}_k}{\sigma_{t_k}} \right)^2 + \sum_k \left(\frac{f_{m,k} - f^{(0)}_{m,k}}{\sigma_{f_k}} \right)^2}_{\text{Windowing penalty on structural and scattering parameters}}
\end{aligned}
$$

Figure 5.3: Total error function χ^2_{total} used in differential evolution optimisation to fit RFMR amplitude and phase profiles for two FMR modes. The cost function comprises four additive components: (1) normalised squared residuals between experimental and simulated amplitudes for both modes ($A^{(1)}_{exp}, A^{(1)}_{sim}, A^{(2)}_{exp}, A^{(2)}_{sim}$). (2) Amplitude-weighted squared residuals in the precession phase ($\phi^{(1)}_{exp}, \phi^{(1)}_{sim}, \phi^{(2)}_{exp}, \phi^{(2)}_{sim}$). (3) Smoothness regularization applied to the depth profiles of phase and cone angle, penalising discontinuities and unphysical sharp gradients. Finally, (4) soft windowing constraints on structural parameters (e.g., layer thicknesses) and magnetic scattering factors, centred around prior estimates from independent characterisations such as XRR or static XRMR. Regularization terms are weighted by tunable parameters λ_1 and λ_2.

than fixed boundaries.

5.6 High-Dimensional Problems

Recent advances in high-dimensional combinatorial optimisation, particularly driven by the demands of training deep neural networks [96], have catalysed a shift in algorithmic strategies [97]. While Differential Evolution remains a powerful global optimiser, especially in rugged or jagged landscapes typical of many real-world scenarios [98], its scalability beyond ∼100 parameters is known to suffer due to the curse of dimensionality and slow convergence in non-separable spaces. Traditional XRMR models typically involve 20–50 fitting parameters, where DE performs adequately. However, in our RFMR model shown in Chapter 8, the parameter space exceeds 100 dimensions, rendering classical DE variants inefficient without extensive tuning or decomposition.

Recent literature suggests a contrasting view in extremely high-dimensional optimisation: that gradient-based methods can in fact outperform genetic algorithms, particularly when the objective function exhibits local one-point convexity under convolutional smoothing [99]. In such scenarios, gradient descent or its stochastic variants (e.g., Adam, Adagrad) are less likely to be trapped by sharp local minima, as the probability of all parameters being simultaneously stuck in a poor basin is exponentially small with increasing dimensionality. Indeed, gradient noise can help escape saddle points and converge to flatter, more generalizable minima [100].

This insight is especially relevant for our RFMR fitting problem on the N=4 structure, where the large parameter count (complex structural fits, non-linear magnetisation terms and scattering factors across multiple layers) breaks the assumptions underpinning classical XRMR fitting routines. Our experiments show that while DE provides a reasonable global estimate, the local refinement needed for physical realism is better served by hybrid approaches. Motivated by techniques from deep learning optimisation [99, 100], we implement a three-stage fitting pipeline [101]: an intense fit-by-eye initialization, typically spanning at least a day per dataset, which accounts for setting parameter bounds, and learning obvious correlations and degeneracies. A coarse DE-based global search spanning millions of iterations, followed by a local gradient descent refinement using smoothed amplitude-phase loss landscapes [102]. This reflects a growing consensus in the literature that hybrid and gradient-based methods are more suited to navigating ultra-high-dimensional, mildly non-convex spaces [98].

5.7 Validating Best-Fit Models

Understanding the origins of depth-dependent magnetic dynamics in engineered heterostructures requires not only experimental sensitivity to the vertical structure, but also a theoretical framework capable of resolving dynamics across nanometre-scale layers [103]. To this end, micromagnetic simulations played a vital interpretive role throughout this work. Using the Object Oriented Micromagnetic Framework (OOMMF), interfaced through the high-level Python package UBERMAG, we were able to simulate the time-resolved, depth-resolved dynamics of layered ferromagnetic systems under experimental conditions similar to VNA-FMR, RFMR, XFMR, and VSM.

While RFMR provides a unique probe of element- and depth-resolved dynamics, interpretation of such data is often non-trivial due to modal hybridization, phase decoherence across interfaces, and competing interfacial effects. Micromagnetic simulations enabled us to test specific hypotheses, isolate the role of individual magnetic parameters, and reproduce trends observed in both lab- and

synchrotron-based measurements.

A typical simulation workflow begins by defining a thin-film multilayer geometry, discretised into cuboidal cells along the film normal (z-axis), where each layer is parametrized by its experimentally measured values of saturation magnetisation, exchange stiffness, damping, and anisotropy. These simulations adopt the thin-film approximation, i.e. assuming uniformity in the in-plane directions (x, y) and allowing magnetisation to vary only with depth. This reduces computational complexity while preserving the essential physics governing the depth profile of resonance modes.

The system is first relaxed in a bias field, typically along the OOP axis, followed by an IP sinc excitation pulse to simulate a broadband perturbation analogous to that used in VNA-FMR. By recording the time evolution of the magnetisation, particularly the transverse components, and applying a Fast Fourier Transform (FFT), we extract frequency-resolved spectra for each magnetic voxel. This approach not only reveals the resonance frequencies, but crucially the relative amplitude and phase of precession across the stack.

Simulations were repeated across a sweep of static fields to generate theoretical Kittel curves, which were used to assign modes observed experimentally. In coupled structures, particularly those with weak interlayer exchange or proximity-induced effects, the simulations revealed mode hybridization and amplitude asymmetries that matched those seen in RFMR profiles. The spatial resolution of OOMMF (down to 0.1 nm in depth) also allowed us to visualise precession nodes, phase reversals, and amplitude gradients indicative of dynamic coupling, which would otherwise be obscured in integral measurements.

Chapter 6

Depth Profile of Magnetic Single Layers

This Chapter serves to illustrate the principle of resolving the depth profile of a standard FMR mode in a single magnetic film structure, Si/NiFe(25 nm)/Pt(3 nm). Initially the origin of depth-dependence in out-of-plane Ferromagnetic Resonance modes, whether intrinsic modal structures or interfacial demagnetisation effects, was investigated using micromagnetic simulations. Here the inherent modal structure is observed throughout the depth of the film under continuous RF excitation. The macrospin model breaks down in the presence of interfacial magnetism, where an amplitude modulation envelopes the precession, resulting in a partial pinning at the interfaces, with a freely precessing bulk, normally with phase coherence throughout the entire layer. It is further observed that in the presence of a distorted RF, the precession can become highly non-linear, and chaotic in nature.

VSM, VNA-FMR, XMCD, XRMR, and RFMR was conducted on Si/NiFe(25 nm)/Pt(3 nm). While the XRMR data could be fit with a homogeneous magnetic profile (with considerations for magnetic roughness), in fitting simulations to the experimentally measured RFMR profiles, it was concluded that the macrospin model is insufficient to adequately describe the observed structure. However, convergence of the model was achieved by subdividing the NiFe layer into multiple smaller sublayers and treating the dynamic properties uniquely within each sublayer. It was found that a mode containing amplitude modulation with depth, analogous to the micromagnetic results was necessary to accurately fit the data [104], characterised by a reduced opening angle at the interfaces of the NiFe layer and an in-phase response across all sublayers [66].

A sensitivity analysis was done on the depth-varying dynamic parameters ($\xi(z)$, $\psi(z)$, $\phi(z)$) confirming that they are not degenerate when divided into 3 sub-layers, justifying the decision to model the stack as so.

Next, the Sobol index was calculated on $\xi(z)$ for a structure with 10 sub-layers, where the sensitivity of the model to each sublayer is quantified, and their correlations calculated. Here it was confirmed

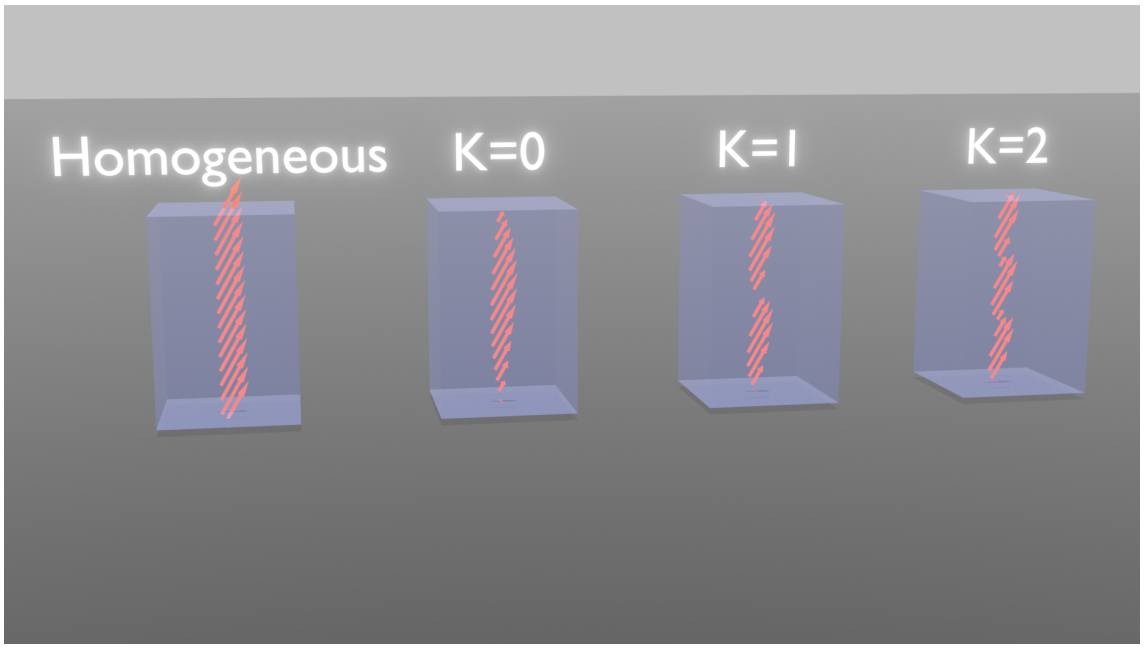


Figure 6.1: visualisation of OOP FMR modes in a magnetic thin film. Four transparent cubes represent different spin wave configurations: From left to right: Homogeneous precession with uniform amplitude and phase throughout the film; K=0 mode with a single antinode at the centre and nodes at the surfaces; K=1 mode exhibiting two full oscillation periods along the film thickness; and K=2 mode showing three full periods. The red arrows represent local magnetisation vectors, whose length and tilt correspond to the precession amplitude and direction, respectively. Illustration was created using Blender.

that the model was mostly sensitive to the top sub-layers in the structure, with the layers in the bulk showing degeneracy.

This degeneracy was due to the relatively subtle effect the dynamic parameters had on the overall reflectivity profile, as compared to other parameters in the model, namely the tightly constrained structural, static magnetic, and scattering factors. These could be further pinned down by including a co-fitted dataset, which shared all the same other parameters, and only varied the dynamics, hence lifting the degeneracy in $\xi(z)$. This is difficult to achieve as only the Kittel FMR mode was accessible in our 2-8 GHz 35 mT-180 mT RFMR set-up. Hence a solution was found by distorting the RF input using a defective amplifier, which produced significant changes to the RFMR results, and opened up the possibility of co-fitting to extract the dynamic parameters.

This brings us to the context of linear classification. The depth-profile of the NiFe was constructed via co-fitting the different driving RF resulting signals. Fitting the RFMR profiles revealed an even more pronounced reduction in the opening angle of precession at the NiFe interfaces in the distorted case.

This was further extended upon by analysing the other frequency contributions on our dynamic signals, where it was observed that the distorted RF experimental data showed significant contributions

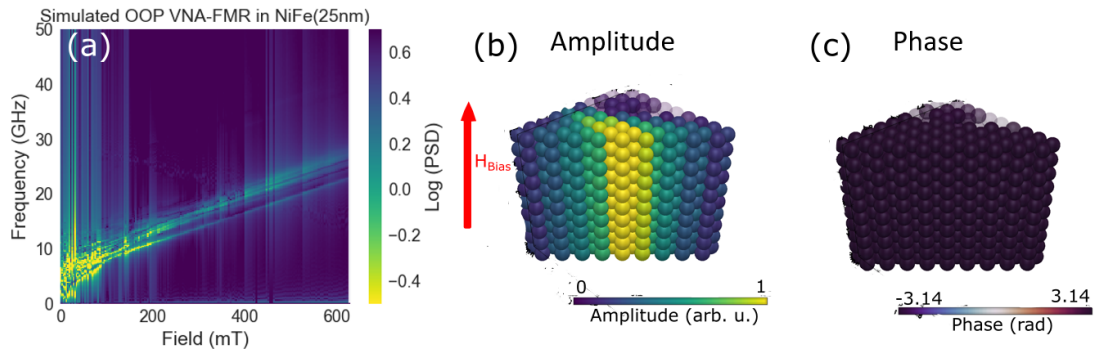


Figure 6.2: (a) UBERMAG simulations of OOP (OOP) VNA-FMR in NiFe (25 nm), revealing a resonant frequency consistent with experimental trends. (b) Simulated amplitude of magnetisation precession as a function of depth within the NiFe layer. Incorporating demagnetizing effects and interfacial anisotropy, the amplitude is found to diminish near the interfaces. (c) Simulated phase of precession, showing uniformity across the film thickness, indicative of a coherent mode.

from different frequencies. This effect could not be reproduced in a reflectivity model which assumes sinusoidal precession in the structure. Instead we imported the time-series 3D magnetisation data from micromagnetic results, motivated by the method detailed in the supplementary information of [105], which allowed the model to replicate nondriven frequency contributions. This confirms that through analysing the depth-profile of even simple FMR modes, linear classification can be achieved through recognition of unique RF inputs (pure sine or distorted).

6.1 Micromagnetic Results

Using *Ubermag*, we simulated the field-dependent magnetisation dynamics in a 3D NiFe film with dimensions 500×500×25 nm^3. The mesh consisted of $10 \times 10 \times 10$ cells, each of size 50×50×2.5 nm^3, with demagnetism applied.

The material parameters were chosen to reflect those extracted from VSM and VNA-FMR experiments: a saturation magnetisation of $M_s = 8 \times 10^5$ A/m, an exchange stiffness of $A = 1.3 \times 10^{-11}$ J/m, a damping constant $\alpha = 0.008$, and a gyromagnetic ratio $\gamma = 2.211 \times 10^5$ m/(A s). The system was initially relaxed along a nearly OOP magnetisation direction defined by the unit vector [0.020, 0.020, 0.999] (corresponding to an approximately 1.65° opening angle).

After relaxation, a field sweep was performed from 0 to 600 mT across 200 discrete steps. At each field step, the Zeeman field was applied OOP and the system was evolved dynamically for 5 ns with 1500 time steps. The magnetisation response was recorded via the spatial average of the m_y component. An FFT was applied to the resulting time trace to extract the power spectral density (PSD), revealing the frequency-dependent resonant response of the system.

The resulting field-frequency map is shown in Figure 6.2(a). Each row in the map corresponds to

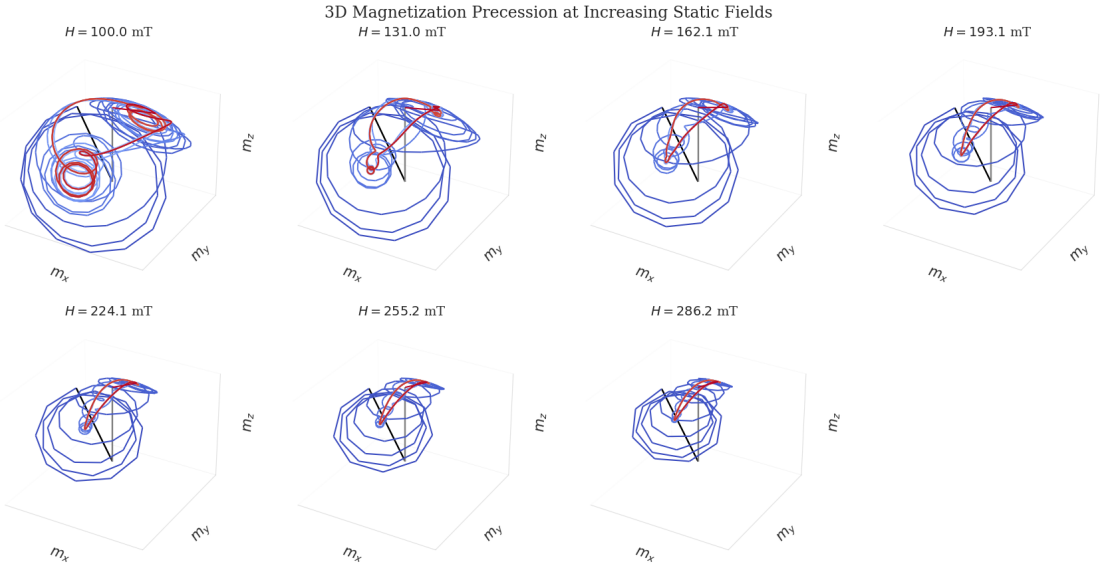


Figure 6.3: Magnetisation precession across a series of increasing static magnetic fields, simulated using a macrospin model driven by a continuous sine RF pulse (2 GHz). Each subplot corresponds to a different applied field, beginning with 100 mT and increasing in equal steps up to 286 mT. The precession trajectories exhibit a transition from large-angle, non-harmonic motion to more circular and uniform dynamics as the field increases, indicating progressive alignment with the external bias. coloured paths represent the tip of the magnetisation vector over time, with black and grey arrows denoting the initial and final states, respectively. Simulation Parameters used literature values for NiFe, and simulated a 500x500x25 nm^3 film.

the FFT of $m_y(t)$ at a specific field value, thus generating a simulated broadband VNA-FMR spectrum. Multiple modes are visible due to edge effects, and the sample is visualised in (b) by taking a cross section along the x=y plane where an FMR mode is visible along the centre voxels along the z-axis at 12.66 GHz 24 mT. There is no variation in (c) phase detected in this mode. This was further observed in Figure 6.3 by exciting the sample under continuous sinusoidal RF excitation at 2 GHz and tracing the 3D precessional path traced by the average magnetisation vector against time. For increasing static field the precession is found to pass through resonance, with variations in opening angle. A bimodal character is observed here, potentially due to the large H_{RF} amplitude, or the averaging across all voxels in our macrospin assumption.

6.2 Sample Details

A subtle yet significant challenge in RFMR lies in managing reflectivity across multiple interfaces. This issue becomes especially pronounced when a heavy metal cap is introduced. While materials such as Platinum (Pt) provide excellent protection for air-sensitive ferromagnets, they also introduce dominant reflection features due to their large scattering contrast and sharp interface with the underlying magnetic layer. In the context of RFMR, this strong reflectivity, despite originating from a layer of

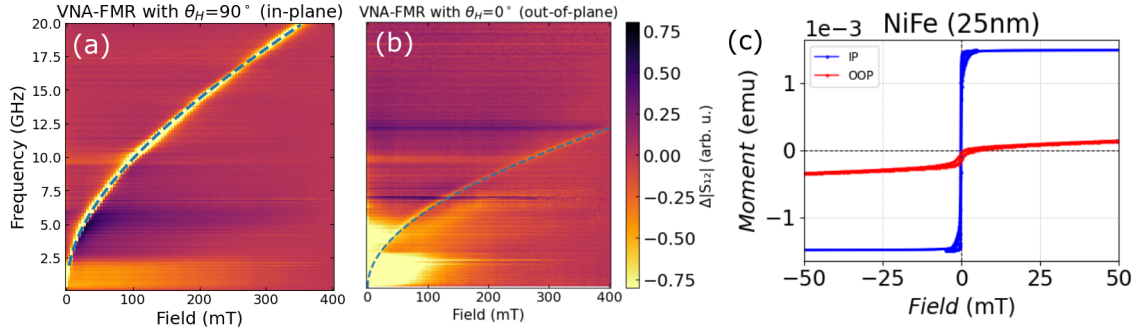


Figure 6.4: Experimental VNA-FMR measurements on Si/NiFe (25 nm)/Pt (3 nm) in the (a) IP and (b) OOP geometries. Fits to the dominant Kittel mode yield $\gamma = 0.15$ GHz/kOe, $4\pi M_s = 125$ Oe, and a Gilbert damping parameter $\alpha = 1.365 \times 10^{-3}$. (c) Complementary VSM measurements corroborate the extracted magnetic parameters.

limited magnetic relevance, can obscure the precessional signal of interest. A solution is to leave the sample uncapped, allowing a naturally formed oxidation layer to act as the termination. This oxidized boundary, while diffuse, tends to have a density much closer to that of the ferromagnetic layer itself, thus reducing reflectivity mismatches and enabling clearer access to the magnetic depth profile.

The project of focus in this chapter arise from two samples: `Si/NiFe(25 nm)/Pt(3 nm)` and `Si/NiFe(25 nm)`. These samples were also studied in an XRMR-based collaboration, though RFMR measurements were focused on the capped structure, and are the only results presented here.

The samples were prepared using DC magnetron sputtering in a home-built chamber with a base pressure of $\sim 5 \cdot 10^{-10}$ mbar [75], (Chapter 3). During deposition, Ar was employed as the sputtering gas, maintaining a working pressure of approximately $\sim 4 \cdot 10^{-3}$ mbar. The sputtering power was set at 30 W for the NiFe and Pt capping layer. The samples were deposited at room temperature with continuous azimuthal rotation to ensure uniform film growth. Following thin film growth, the samples were characterised using VSM, XRR, and VNA-FMR [106]. Unlike transmission-based XFMR, where the sample is mounted in a flip-chip configuration on a CPW, RFMR requires the film surface to be directly exposed to the X-ray beam while remaining close enough to the RF signal line to enable FMR excitation. To meet this requirement, the substrate thickness was reduced from 500 to 100 μm through hand polishing, optimizing the sample for RFMR measurements.

6.3 Experimental Details

Preliminary characterisation was performed on the Si/NiFe(25 nm)/Pt(3 nm) sample shown in Figure 6.4. VNA-FMR was conducted in (a) IP ($\theta_H = 90°$) and (b) OOP ($\theta_H = 0°$) geometries. Resonance fields were fitted using the Kittel equation (2.11), based on the peak position of the S_{21}

trace at each field value, and the Gilbert damping parameter was extracted via equation (2.12) from the FWHM of the same trace. VSM measurements were carried out in (c) IP (red) and OOP (blue), where the hysteresis data was fitted using a sum of two arctangent functions per branch, each with a distinct slope and amplitude. The fitted curves (shown as solid lines) were used to extract coercivity and remanence values. The difference in M_s between IP and OOP measurements is due to how saturation was not achieved in OOP. All results are summarized in Figure 6.4, with the extracted fit values listed below.

Table 6.1: Comparison of remanence and coercivity for IP ($\theta_H = 90°$) and OOP ($\theta_H = 0°$) VSM measurements on NiFe (10 mm × 10 mm × 25 nm).

Geometry	M_r **(**μ**emu)**	H_c **(mT)**
$\theta_H = 90°$ (IP)	864.77	0.15
$\theta_H = 0°$ (OOP)	103.49	3.08

A schematic of the XRMR experiment, as conducted on the RASOR diffractometer, is shown in Figure 3.5. The sample was mounted onto a CPW, as illustrated in Figure 3.4, and inserted into the RASOR chamber for measurement.

Initial characterisation was performed using XMCD, both in FY and reflectivity modes, as presented in Figure 6.5. The energy-dependent scattering factors were extracted using the FY data, employing the Kramers-Kronig relation (Eqns. 4.6 and 4.9). These complex scattering factors were then used in the modelling of XRMR data.

XRMR measurements were conducted in the saturated OOP geometry at 100 mT. The magnetic asymmetry was calculated as

$$\text{Asymmetry} = \frac{I_{\text{PC}} - I_{\text{NC}}}{I_{\text{PC}} + I_{\text{NC}}}, \tag{6.1}$$

where I_{PC} and I_{NC} represent the reflectivity intensities with positive and negative incident circular polarisation. The Asymmetry profiles were fitted using a DE algorithm implemented in GenX. Structural parameters were tightly constrained based on prior hard XRR fits (Measured by Kiranjot (DLS) with results of Pt (2.2±0.39 nm), Py (25.1±0.64 nm), Interface layer (1.5±0.35 nm)). The magnetic scattering from the NiFe layer was modelled using a homogeneous magnetisation profile. The model accounts for the overall magnetic moment, its spatial orientation (both IP and OOP components), and the degree of interfacial magnetic roughness. To allow for subtle interface-related effects, the magnetisation strength was permitted to vary slightly near the top and bottom surfaces of the film.

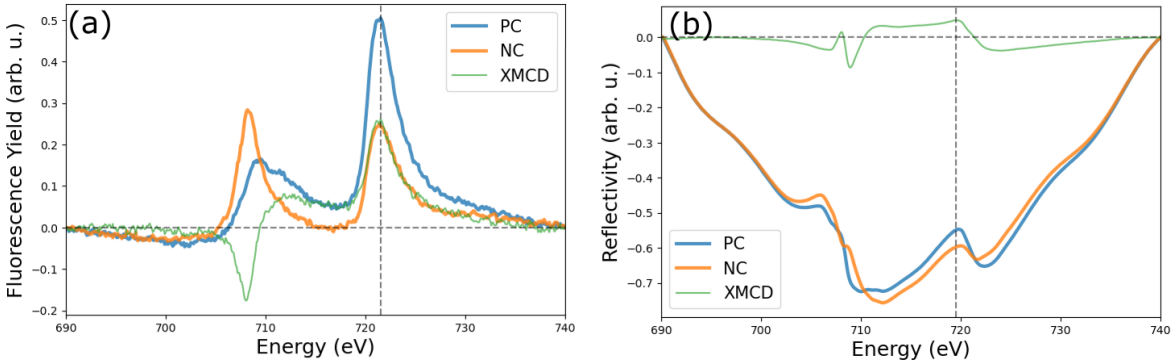


Figure 6.5: Simultaneous XMCD measurements at the Fe $L_{3,2}$ edges, acquired using both FY (a) and specular XRR (b). Positive (PC) and negative (NC) circular polarisations are shown in blue and orange, respectively, while the XMCD signal ($I_{\mathrm{PC}} - I_{\mathrm{NC}}$) is shown in green. All measurements were performed simultaneously at an incidence angle $\theta = 15°$, under a static field of 37 mT applied along $\theta_H = 0°$. The fluorescence yield detector was positioned at 70° from the specular direction. Data were normalised by subtracting a linear fit connecting the average signal outside the absorption edges (pre-edge < 695 eV and post-edge > 735 eV).

The resonant magnetic scattering was described using energy-dependent optical constants. This was accounted for by including both circular and linear dichroic contributions, which are sensitive to the direction and magnitude of the magnetisation relative to the X-ray polarisation and scattering geometry.

The results shown in Figure 6.6 show the Asymmetry data (black) alongside its GenX fit (red), we demonstrate that the homogeneous model is sufficient to describe the structure. In (b) the magnetic SLD for the resulting profile is shown with the best-fit parameters alongside.

Moving to dynamic measurements, the RF radiation was delivered to the NiFe sample through the CPW at the fourth harmonic (2 GHz) of the synchrotron master oscillator clock (500 MHz). The RF harmonic was produced directly from the master clock signal, ensuring a known phase relationship between the X-ray bunches and the applied RF. The phase relationship between the RF excitation (i.e., the pump) and the X-ray bunches (i.e., the probe) was controlled using a picosecond-resolution delay line. Throughout the experiment, NC polarisation was used.

The reflected X-ray beam from the sample was collected in θ–2θ geometry using a photodiode and fed into an LIA. The LIA isolated the dynamic component of the reflected beam at the kHz modulation frequency. Lock-in techniques were applied to increase the signal. In particular, a π phase modulation is applied to the RF field at a modulating frequency of ≈ 3 kHz, in order to maximise the contrast. Incident X-rays impinge only on the central part of the CPW signal line avoiding non-uniform RF excitation [79]. In this study we experimentally observed that both Amplitude modulation (RF field oscillates from on and off) and Phase modulation (RF field oscillates through π phase inversions) both produce stable magnetic precessions when modulating in the kHz regime. However, each modulation

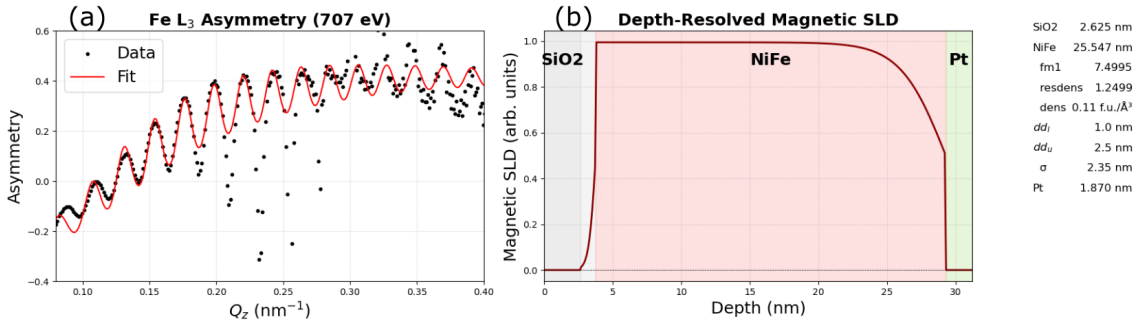


Figure 6.6: XRMR analysis of a SiO_2/NiFe/Pt at the Fe L_3 edge (707 eV). (a) Measured and fitted asymmetry as a function of OOP momentum transfer Q_z, highlighting resonant magnetic scattering from the NiFe layer. (b) Reconstructed depth-dependent magnetic scattering length density (SLD), showing a sharp onset and interfacial decay due to finite magnetic roughness. (Right) Summary of structural and magnetic parameters extracted from the fit, including magnetic contrast (f_{m1}), resonant fraction (ρ_{res}), density, and interfacial widths. Structural parameters were constrained based from hard XRR measurements.

type would produce a different LIA signal's Amplitude and Phase. The precessing magnetic signal was measured as a function of pump–probe delay time, for various values of the magnetic field and incident X-ray angle (determining Q_z). By sweeping the pump–probe delay time while keeping other parameters fixed, we obtained a sinusoidal signal whose period matches that of the driving. The RFMR amplitude and phase were extracted from this data by fitting sinusoids to the RFMR signal as a function of delay time.

6.4 Extracting Amplitude & Phase of the Dynamic Signal

While the experimental RFMR dataset consists of a 2D signal as a function of time delay and scattering vector $\mathbf{Q_z}$, extracting a meaningful depth profile directly from this high-dimensional space is non-trivial. The central assumption in this work is that the observed dynamics at each $\mathbf{Q_z}$ arise from harmonic precession at the driving frequency ω_{RF} (here, 2 GHz). Therefore, the signal can be effectively reduced to its amplitude and phase components at ω_{RF} as a function of $\mathbf{Q_z}$.

To extract these quantities, the RFMR intensity at each $\mathbf{Q_z}$ is fit to a sinusoidal function of the form:

$$I_{\text{RFMR}}(t) = A(\mathbf{Q_z}) \sin(\omega_{RF} t + P(\mathbf{Q_z})), \tag{6.2}$$

where A represents the amplitude of the oscillation and P the phase offset, both dependent on $\mathbf{Q_z}$. This fitting procedure is applied identically to both experimental and simulated time-domain data.

To ensure computational efficiency, the extraction is performed using the `scipy.optimise.curve_fit` routine in Python, which minimises residual error via gradient descent, starting from initial guesses

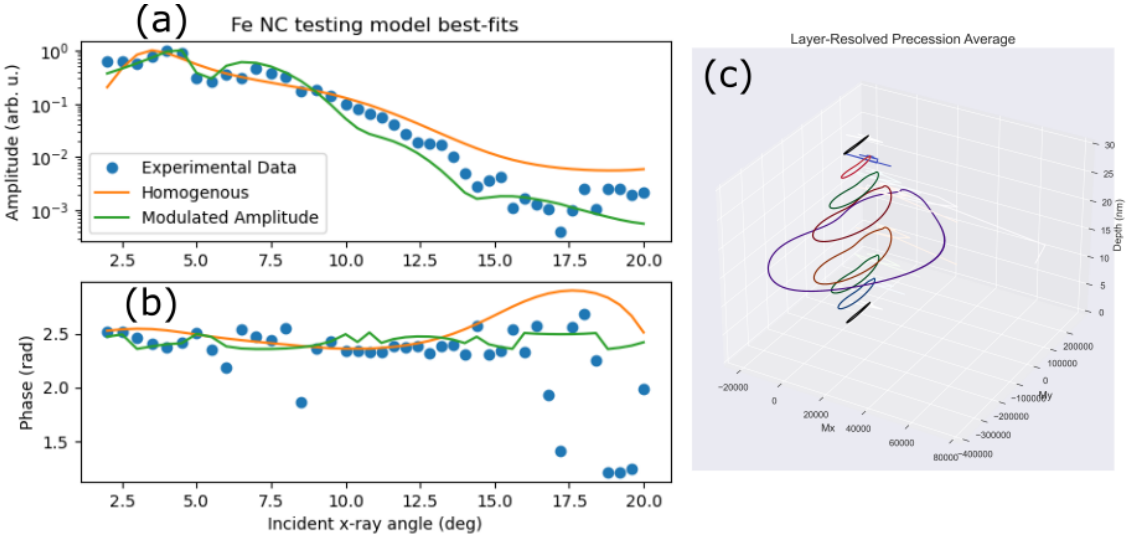


Figure 6.7: RFMR measurements performed on the OOP Kittel mode of Si/NiFe (30 nm)/Pt (3 nm) at 37 mT and 300 K, probing the Fe L_3 edge (707 eV) using negative circular polarisation in phase modulation. Data points (blue) are fitted using two models: a homogeneous precession model (orange) and a depth-modulated amplitude model (green). Both models were optimised using DE to obtain best-fit parameters. (a) Amplitude and (b) phase of the RFMR signal extracted from sinusoidal fits across delay for experimental or simulated data. (c) UBERMAG simulations illustrating possible damped precession profiles in NiFe (25 nm), consistent with interfacial pinning of the resonance mode at the film boundaries.

(A_0, P_0). Crucially, a key assumption made throughout this work is that $A(\mathbf{Q_z})$ and $P(\mathbf{Q_z})$ evolve smoothly with $\mathbf{Q_z}$. This continuity is enforced by propagating the best-fit values from one $\mathbf{Q_z}$ point to the next, using the fitted parameters at $\mathbf{Q_z}$ as the starting guess for $\mathbf{Q_z} + \delta\mathbf{Q_z}$.

To avoid ambiguity, amplitudes are constrained to be positive, while phase values are permitted to vary continuously over the real line. Phase wrapping is performed after fitting to maintain a physically meaningful evolution across $\mathbf{Q_z}$. This approach is necessary because later the DE optimiser must make local decisions at each point before a global best-fit model is known. Maintaining continuity in A and P ensures that the algorithm converges smoothly in the correct direction across $\mathbf{Q_z}$.

This decomposition into amplitude and phase is essential for the fitting framework used in the subsequent DE optimisation. Attempting to fit the entire 2D time-domain map directly would conflate independent contributions of amplitude and phase. For instance, even a small uniform error in $P(\mathbf{Q_z})$ could result in a large total residual, despite an otherwise accurate model for $A(\mathbf{Q_z})$. By treating A and P as independent observables, which are co-fitted with different weightings, the DE algorithm is able to evaluate candidate models based on their ability to reproduce the depth-dependent dynamic signal with greater fidelity.

This separation enables the optimiser to assign a meaningful and balanced fitness to each member of the parameter population, allowing amplitude and phase constraints to be evaluated on equal footing

and guiding the algorithm toward physically consistent solutions.

6.5 Model Testing

Due to the driving RF of 2 GHz, the magnetisation in our reflectivity models is assumed to take the form

$$\begin{aligned} M = [M_x, M_y, M_z] = \\ [M_0 sin(\xi)\cos(\omega t + \phi + n\pi), \\ M_0 sin(\xi)(\sin(\omega t + \phi + n\pi)\cos(\psi) - \sin(\psi)), \\ M_0 cos(\xi)(\cos(\omega t + \phi + n\pi)\sin(\psi) + \cos(\psi))] \end{aligned} \tag{6.3}$$

For a given ξ (precessional opening angle), ϕ (precessional phase relative to pumping RF), and ψ (tilt from surface normal) this equation describes a precessional cone parametrized by time (t), with an angular frequency (ω, 2 GHz). The reflectivity model is generated by considering ξ, ϕ, and ψ as a function of depth. This results in a 2D reflectivity profile, with one axis corresponding to $\mathbf{Q_z}$, and the other to t. This resulting 2D profile can be fitted to real RFMR $\mathbf{Q_z}$ vs delay maps to determine the depth-dependent structure.

Optical constants δ and β were calculated according to Chapter 4 and [8]. β is directly measured XMCD absorption using a Fluorescence Yield detector placed 70° from the specular, then taking the Kramers-Kronig transformation to obtain δ. Form Factors are taken from the Henke tables [81]. As discussed in Chapter 4, the optical constants are not inherently the same for XRMR and RFMR, and proper treatment of δ and β would include measuring the time resolved component, hence computing them via XFMR, as opposed to XMCD, which this work does not cover. Although this can be done by measuring the LIA signal from the FY diode instead of the reflectivity, the signal was too small in this experiment to be resolved.

The next step is to fit the generated RFMR simulation to RFMR data. This was done following the DE algorithm outlined in Chapter 5. Despite the success of the homogeneous model in fitting the static XRMR data, it proved insufficient to describe the RFMR response of the Si/NiFe(25 nm)/Pt(3 nm) sample. Specifically, the homogeneous precession model failed to reproduce the experimentally observed amplitude fringes and phase variations. Moreover, best-fit parameters from this model deviated significantly from those obtained from independent structural XRR measurements.

To better capture the depth-dependent magnetisation dynamics, a model incorporating amplitude modulation across the film thickness was required, to emulate a precessional damping at the interfaces,

this is reminiscent of either the micromagnetic results or a sort of Perpendicular Standing Spin Wave (PSSW). In this approach, the NiFe layer was divided into ten 3 nm magnetic sublayers, each with identical structural properties but independent dynamic parameters. Interlayer roughness and intermixing between adjacent sublayers were set to zero. The dynamic magnetisation amplitude (i.e., the precessional cone opening angle ξ) was parametrized using a sinusoidal function of depth:

$$\xi_i = A \cdot \sin\left(\frac{n\pi(i+0.5)}{N}\right) + B \tag{6.4}$$

Here, A is the amplitude of modulation, B is an offset representing partial surface pinning, n is the standing spin wave mode number (typically $n = 1$), N is the number of sublayers, and i indexes each sublayer from 0 to $N - 1$. This profile naturally produces a precession amplitude that is suppressed at the interfaces and peaked near the centre of the film, consistent with the boundary conditions expected under interfacial pinning.

The adoption of this sinusoidal depth profile was guided by micromagnetic simulations, which revealed that in sufficiently thin films (e.g., 25 nm), for an OOP FMR mode, depth variations in amplitude can arise under continuous-wave sinusoidal excitation when interfacial magnetizing effects are included. This behaviour is illustrated in Figs. 6.2 and 6.7. While further simulations indicated that depth-dependent cone tilt could also be induced by interfacial anisotropy, this effect is not strongly supported by experimental data and was therefore excluded from the final model. However the cone tilt of the total macrospin moment was allowed to vary out-of the scattering plane within the reflectivity model within sensitivity analysis.

Finally, the micromagnetic simulations showed that in strongly exchange-coupled materials such as NiFe, it is challenging to produce significant depth-dependent phase lags without also introducing substantial amplitude modulation. This underscores the physical plausibility of the fitted ξ-damped mode and justifies its use in describing the experimental RFMR data.

Results between the models are shown in Figure 6.7. Here the homogeneous model struggles to replicate the fringe pattern in the experimental data without deviating too far from the structural XRR, and magnetic XRMR fits. The additional freedom in the model provided by eq. (6.4) allowed for a better fit that more closely replicated the data.

6.5.1 Sensitivity Analysis

To assess the relative importance of dynamic parameters at different depths within the NiFe layer, a series of 3D sensitivity analyses were performed. Differential Evolution was used to explore the effect of varying three representative sublayer regions: top (sublayers 0–2), bulk (sublayers 3–6), and bottom (sublayers 7–9), for each dynamic parameter: opening angle ξ_i, azimuthal tilt φ_i, and precession phase ϕ_i. All other parameters were held fixed at their best-fit values.

For each DE generation, the population size was increased to 100 with Sobol-sequence initialization to ensure broad coverage. The optimiser was run for 10 generations to enhance the density of solutions near the minima. A non-standard mutation strategy ('rand2bin') was employed to promote greater exploration of the parameter space and improve the resolution of the visualised solution landscape.

The resulting convergence plots (Figure 6.8) illustrate which depth regions most strongly influence the RFMR response and help identify parameter degeneracies or poorly constrained variables. The top row shows independent variations in each parameter across the three sublayers. Panel (a) displays the sensitivity of the opening angle ξ, revealing a complex landscape with multiple shallow minima and a wide spread of solutions, indicating strong coupling and degeneracy. This motivates the more systematic sampling approach shown in Figure 6.9.

Panel (b) shows the dependence on azimuthal tilt φ. The top sublayer appears largely degenerate, with a mild preference near 45°, whereas both the bulk and bottom layers exhibit sharp minima at 0° and 90°, indicating strong sensitivity.

Panel (c) shows the precession phase ϕ, where the top layer again appears weakly constrained, the bulk layer strongly favours 0°, and the bottom layer shows a weak but consistent preference for 180°, while these results were quite shallow, the optimiser used the weights from eq. (5.3) and hence these results in particular can be heavily manipulated from increasing penalisation. The motivations that there is no gradual phase lag in this system arises from understanding of the uniform mode in NiFe, and the difficulty in engineering a phase lag in the system in UBERMAG.

Panels (d)–(f) examine intra-sublayer correlations by simultaneously varying all three parameters:ξ, φ, and ϕ, within the top, bulk, and bottom regions, respectively. In all cases, a steep drop-off in signal quality occurs when both ξ and φ are large, consistent with the moment canting out of the scattering plane and suppressing the RFMR signal.

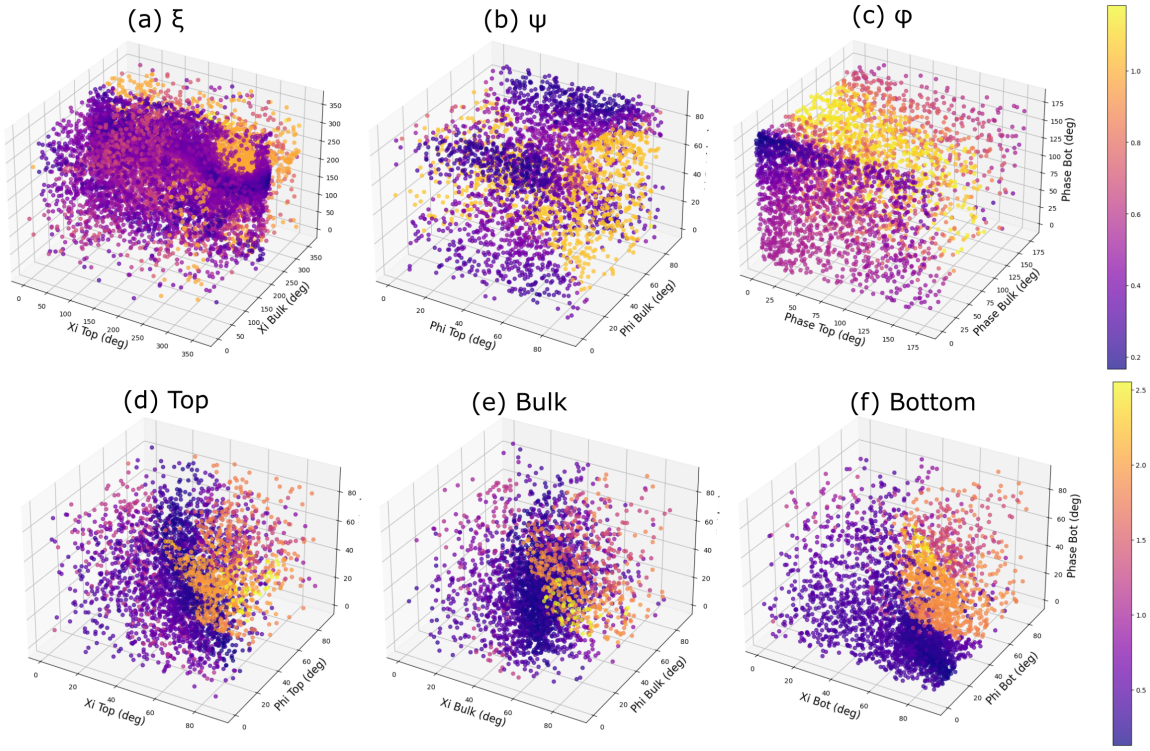


Figure 6.8: 3D sensitivity analysis of the depth-dependent RFMR model for the NiFe layer. Each plot shows the DE trial history coloured by error. (a) Opening angle ξ_i varied across top, bulk, and bottom; (b) azimuthal tilt φ_i across depth; (c) precession phase across depth. (d)–(f) show intra-sublayer correlations for top, bulk, and bottom, respectively, with ξ_i, φ_i, and ϕ_i varied simultaneously.

6.5.2 Model Limitations & Complexity via Sobol Indexing

While the sinusoidal model for the depth-dependent opening angle $\xi(z)$ provides a significantly better fit than the homogeneous precession model, it also imposes a strict periodic constraint on the magnetisation profile. For example, the NiFe layer was sputtered onto a naturally oxidized substrate, with no seed layer, which is known to effect the resulting dynamics [107], and the Pt cap will itself induce SOT [108]. Possibly causing Proximity induced Magnetism (PIM) [109], change to the gyromagnetic ratio [110], and potentially introducing spin pumping [111].

To explore the possibility of more complex or asymmetric precession behaviour, we would like to extend the model by allowing each sublayer's opening angle to vary independently with depth.

However, fitting such a freely-varying $\xi(z)$ profile with data from a single FMR mode leads to strong parameter correlations and degeneracy. To stabilise the fit and enforce physically plausible solutions, we imposed soft pinning conditions by constraining the opening angles at the film interfaces to remain small (typically ~0.05°, based on alignment by eye), while permitting greater variability in the film's interior. Additionally, a smoothness penalty was introduced to discourage nonphysical oscillations in the fitted profile. This was implemented by adding a gradient-based regularization term

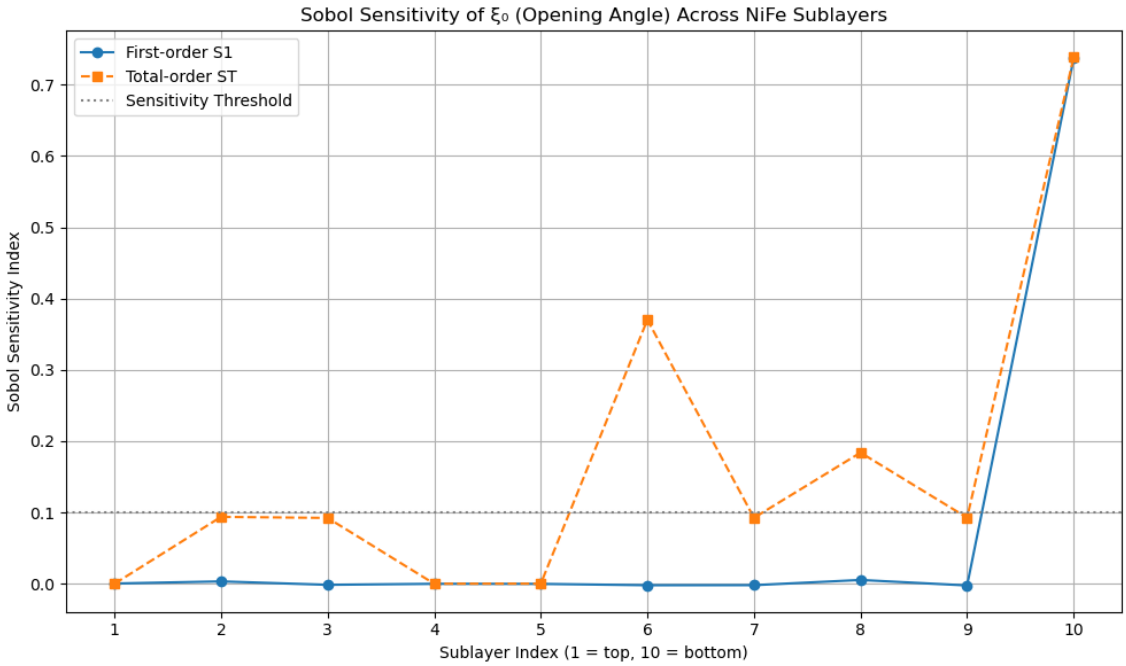


Figure 6.9: Sobol sensitivity indices for the sublayer-resolved opening angle ξ_i in the NiFe film. The first-order indices (S_1) quantify the direct contribution of each sublayer to the variance in RFMR fit quality, while the total-order indices (S_T) capture both direct effects and interactions with other layers. The analysis shows that only a few sublayers, particularly the topmost layer (index 10), contribute significantly, justifying the use of simplified amplitude models such as the sinusoidal profile. A threshold line at 0.1 indicates the cutoff for meaningful sensitivity.

to the objective function:

$$\text{Penalty}_{\text{discontinuity}} = w_1 \left\| \frac{d\xi(z)}{dz} \right\|_2^2 + w_2 \left\| \frac{d\phi(z)}{dz} \right\|_2^2 + w_3 \left\| \frac{d\psi(z)}{dz} \right\|_2^2 \tag{6.5}$$

$$\text{Total Error} = \text{Fit Error} + \text{Penalty}_{\text{discontinuity}} \tag{6.6}$$

where $\xi(z)$, $\phi(z)$, $\psi(z)$ denote the depth-dependent parameters (all in units of degrees), $w_{1,2,3}$ are regularization weights chosen to make the penalty term comparable in scale to the fit error. Through trial and error, we found that $w_1 = 0.01$, $w_2 = w_3 = 0.001$ (approximately 10% of the total error) provided a reasonable balance between fit quality and profile smoothness.

It would be nearly impossible to fit a singular dataset (the RFMR experimental data) of such a complex model, and to compute a Figure of merit that has any physical meaning, instead, to assess whether allowing full freedom in the depth profile of $\xi(z)$ is justified by the data, we performed a global sensitivity analysis using *Sobol indexing*. Sobol sensitivity analysis is a variance-based method that decomposes the total variance of a model's output (in this case, the RFMR fit error) into contributions from each input parameter and their interactions. For a given parameter θ_i, the first-order Sobol index

S_i quantifies the fraction of output variance attributable solely to variations in θ_i, while the total-order index S_{T_i} includes both the direct contribution and all higher-order interactions involving θ_i.

We computed Sobol indices for the 10 independent ξ_i values (one per sublayer), holding all other parameters fixed at their best-fit values. The analysis revealed that only a few sublayers, particularly those near the interfaces, contribute significantly to the fit error variance. This indicates that the RFMR data is primarily sensitive to amplitude variations near the boundaries and largely insensitive to unconstrained variation in the centre of the film.

This finding supports the use of simplified, physically motivated profiles such as the sinusoidal model. While it remains possible that more complex profiles exist, the current data does not contain sufficient information to uniquely reconstruct them. Sobol analysis thus provides a principled justification for reducing the model's degrees of freedom to match the information content of the experiment.

6.6 Waveform Effects

The classification of temporal signals using nonlinear physical systems has gained traction in recent years, particularly in the context of hardware-based neuromorphic computing. Spintronic systems, in particular, exhibit complex magnetisation dynamics that are sensitive to input waveform structure, making them attractive for real-time analogue classification tasks. For example, MTJs have been experimentally shown to process and classify multi-frequency analogue RF signals using the spin-diode effect, with classification accuracies comparable to digital software networks [112]. Similarly, spatially segmented magnetic films with heterogeneous damping constants have been used to realise spintronic reservoir computing (RC), where the nonlinearity and short-term memory of spin dynamics enable transformations of input waveforms into high-dimensional representations for logic tasks such as XOR [113]. More complex,

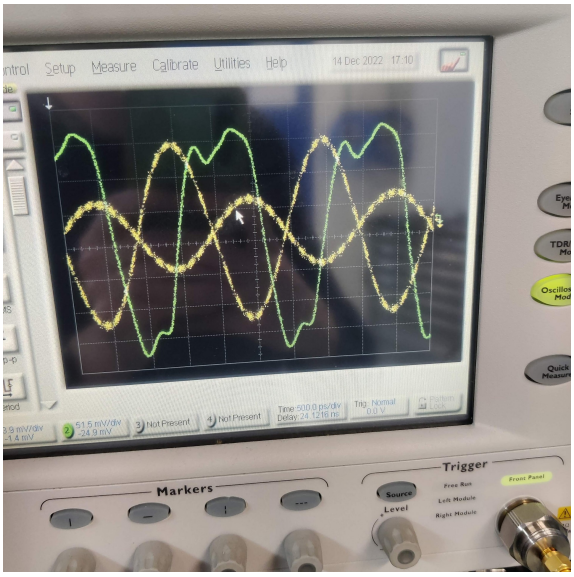


Figure 6.10: Distortions applied to the NiFe driving RF signal via a defective broadband amplifier. The master clock reference signal is shown in yellow (small amplitude), the distorted RF in green, and the corrected signal using a reference amplifier in yellow (large amplitude).

topological systems have been shown to demonstrate this classification too; such as nanomagnet arrays [114], ion migration architecture [115], and skyrmions [116]. This next section pays homage to this work by attempting to demonstrate the same principle of linear classification through analysis of the depth-profile of the out-of-plane FMR mode in NiFe. It should be emphasised that RFMR is not a practical tool for such classification tasks, owing to the highly complex experimental set-up, the significant cost of measurement, the lengthy acquisition times, and the computationally intensive simulations required. Instead, the results presented here are intended as an experimental demonstration, serving as a proof-of-concept to inspire future research using more accessible and efficient methodologies.

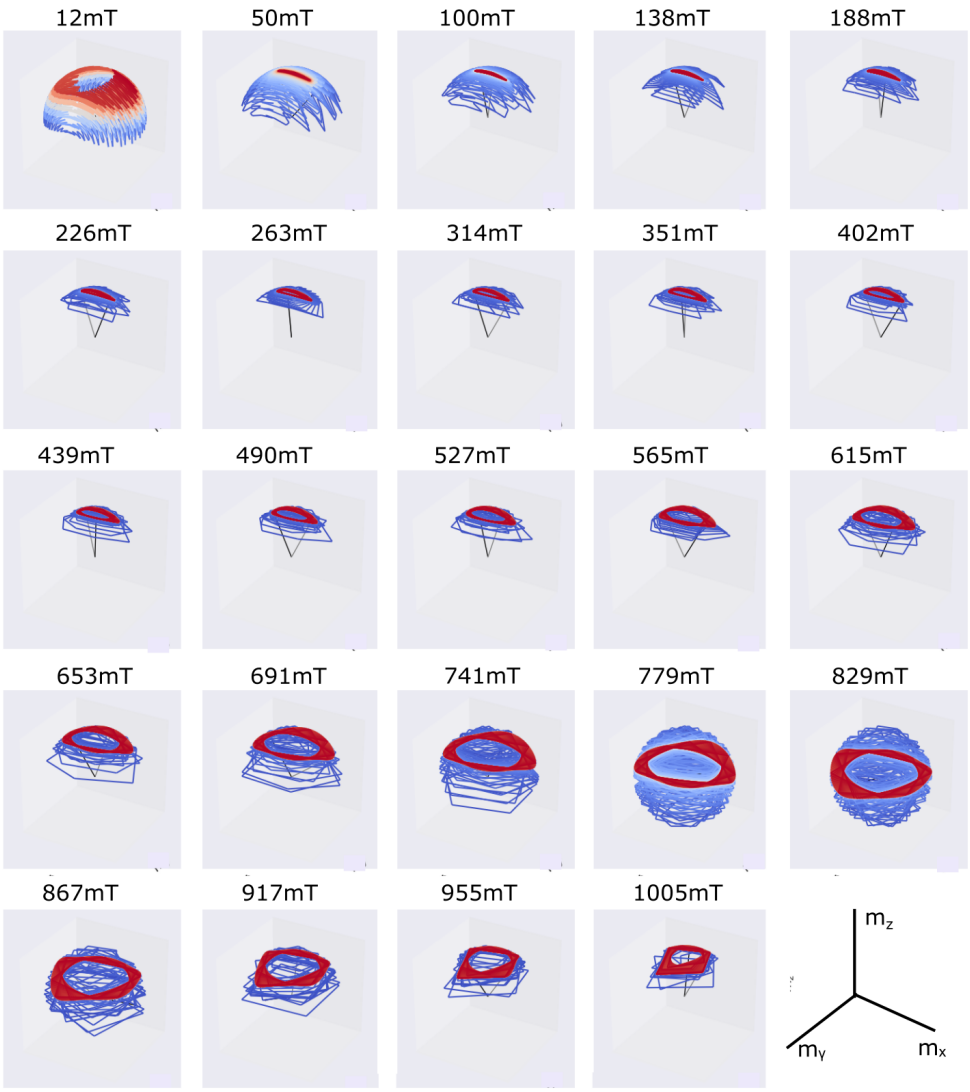


Figure 6.11: Magnetisation precession across a series of increasing static magnetic fields, simulated using a macrospin model driven by a distorted sine RF pulse centred at 2 GHz. Each subplot corresponds to a different applied field, beginning with 12 mT and increasing up to 1 T. The precession trajectories show significant deviation from smooth circular motion, particularly at lower fields, due to the presence of higher harmonics in the distorted drive. coloured paths represent the tip of the magnetisation vector over time, with black and gray arrows marking the initial and final states, respectively.

Our work has up until this point modelled the reflectivity profile assuming a sinusoidal precession within the structure. This is inspired from Figure 6.3 where we see the time-resolved precession of the NiFe macrospin structure under sinusoidal driving force, which while demonstrating complex non-linear behaviour, such as a bimodal structure, there is a distinguishable periodicity to the precession. Whereas in Figure 6.11 we see the same micromagnetic simulation, however now being driven by a distorted RF (defined in Eq. (6.7)). The macrospin structure shows a much more complex behaviour in this state. These micromagnetic results can only be interpreted with Chaos Theory, where they are aptly described by phenomena such as Duffing oscillators [117]. To experimentally probe nonlinear magnetisation dynamics, a deliberately distorted RF waveform was applied to the NiFe layer. This waveform contained harmonic content beyond the fundamental excitation frequency, enabling excitation of higher-order spin wave modes as shown in Figure 6.10. The resulting RFMR response was used as a classification signal, demonstrating that nonlinear distortion of the drive can be exploited to encode information into the spectral and spatial features of the magnetisation dynamics.

While our H_{RF} is far below inducing non-linear dynamics by purely driving the system out of the linear approximation [118, 119], RFMR uniquely provides us with the platform to probe the depth-dependent non-linearity via a deliberately distorted RF waveform.

The nonlinear behaviour observed in Figure 6.11 arises from introducing harmonic content into the driving field of the magnetisation dynamics. This can be formalised by modifying the LLG equation to include a distorted RF excitation, where the effective field $\mathbf{H}_{\text{eff}}$ includes a static bias and a multitone RF drive:

$$\mathbf{H}_{\text{eff}}(t) = H_0\hat{z} + H_1\cos(\omega t)\hat{x} + H_3\cos(3\omega t + \phi)\hat{x} + \cdots \tag{6.7}$$

Here, H_0 is the applied static field, and H_n represent the amplitudes of the nth harmonic components in the distorted RF field. Even if the amplitude H_1 lies within the linear response regime, higher-order terms such as H_3 and H_5 can drive magnetisation into nonlinear trajectories. These effects are visible in both the micromagnetic simulations and in the spectral decomposition of the RFMR signal, as discussed in the following section.

The experimental RFMR plots are shown in Figure 6.12, both RFMR measurements are taken on the OOP Kittel mode of Si/NiFe(25 nm)/Pt(3 nm) at 37 mT, 300 K on Fe L_3 (707 eV) negative circular polarisation, in phase modulation. With the sinusoidal driving shown in (a) and the distorted driving shown in (b). In (c) we show experimental data points corresponding to the fitted amplitude and phase of the fit following eq. (6.2) corresponding to 2 GHz. The blue dots represent sinusoidal driving

RF, and red dots represent distorted RF, error bars are included from the co-variance from the fits. Phase data points are not plotted when the amplitude is below the noise threshold, and both models are fit using the ξ-modulated model. The simulations are run according to the magnetisation profile described in eq. (5.1), hence assuming a sinusoidal precession at the driving frequency. The best-fit is calculated by minimising the following function 5.3 through Differential Evolution.

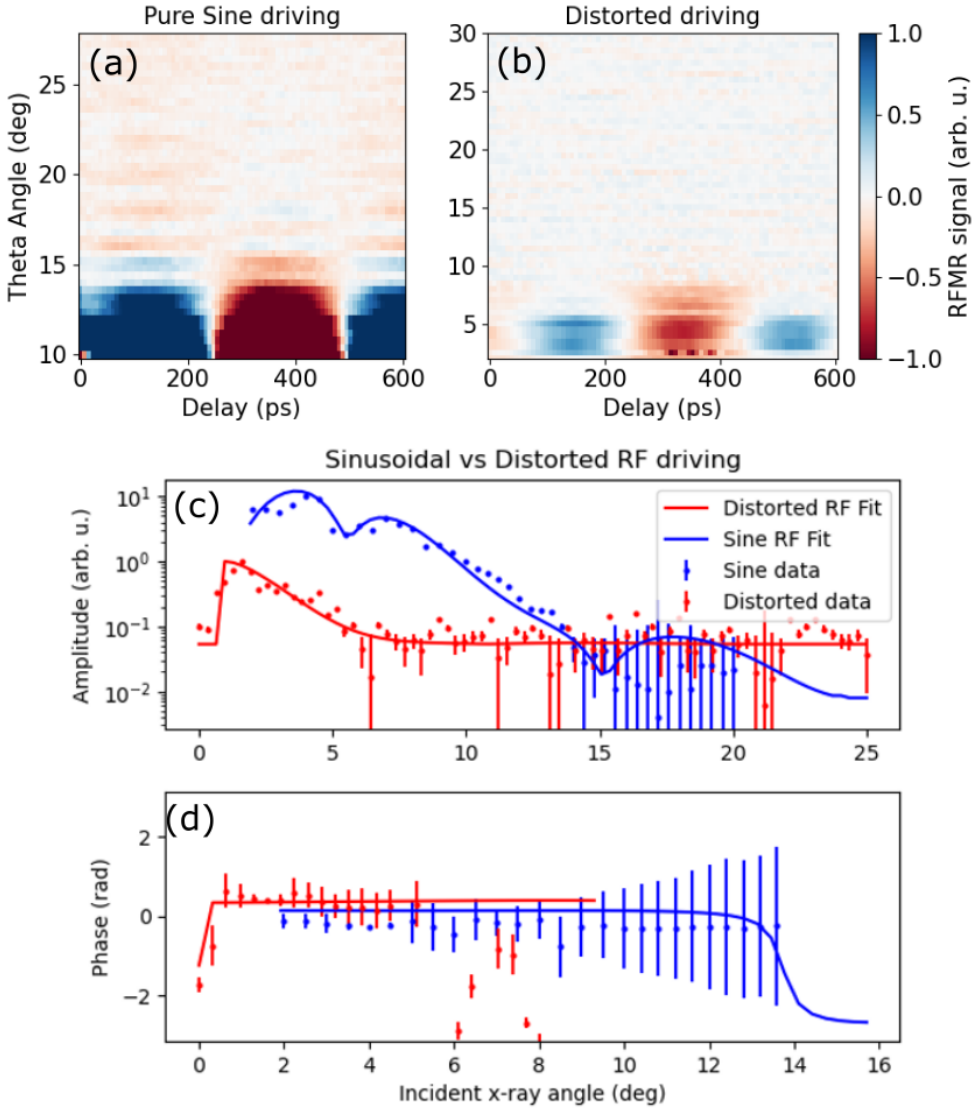


Figure 6.12: (a) RFMR experimental data acquired using a pure sinusoidal RF excitation. (b) RFMR data acquired under a distorted sinusoidal RF excitation. Measurements were performed on the Fe L_3 edge (707 eV) using negative circularly polarised X-rays, with the RF field synchronised to the X-ray probe. Clear differences are observed between the two excitation schemes. (c) Amplitude and (d) phase of the RFMR response, extracted via sinusoidal fits using the depth-dependent amplitude modulation model.

The fitted profiles demonstrates significant differences, firstly the maxima in the sinusoidal precession is an order of magnitude larger, and the distorted RF shows a characteristics of enhanced roughness.

This is not the whole story, as the fits here only computed everything at the 2 GHz signal, the input magnetisation was 2 GHz, and the dynamic signal was assumed to be proportional to a sinusoidal 2 GHz reference. This is addressed in Figure 6.13 by taking the FFT of the experimental data, here significant contributions arising from different frequencies are observed, which are not replicated in it's current best-fit simulation. To address this, an updated model was proposed, which no-longer used eq (5.1) in the reflectivity model, but rather imported the time-series 3D magnetisation profile from micromagnetics, and used that as the fitted magnetisation.

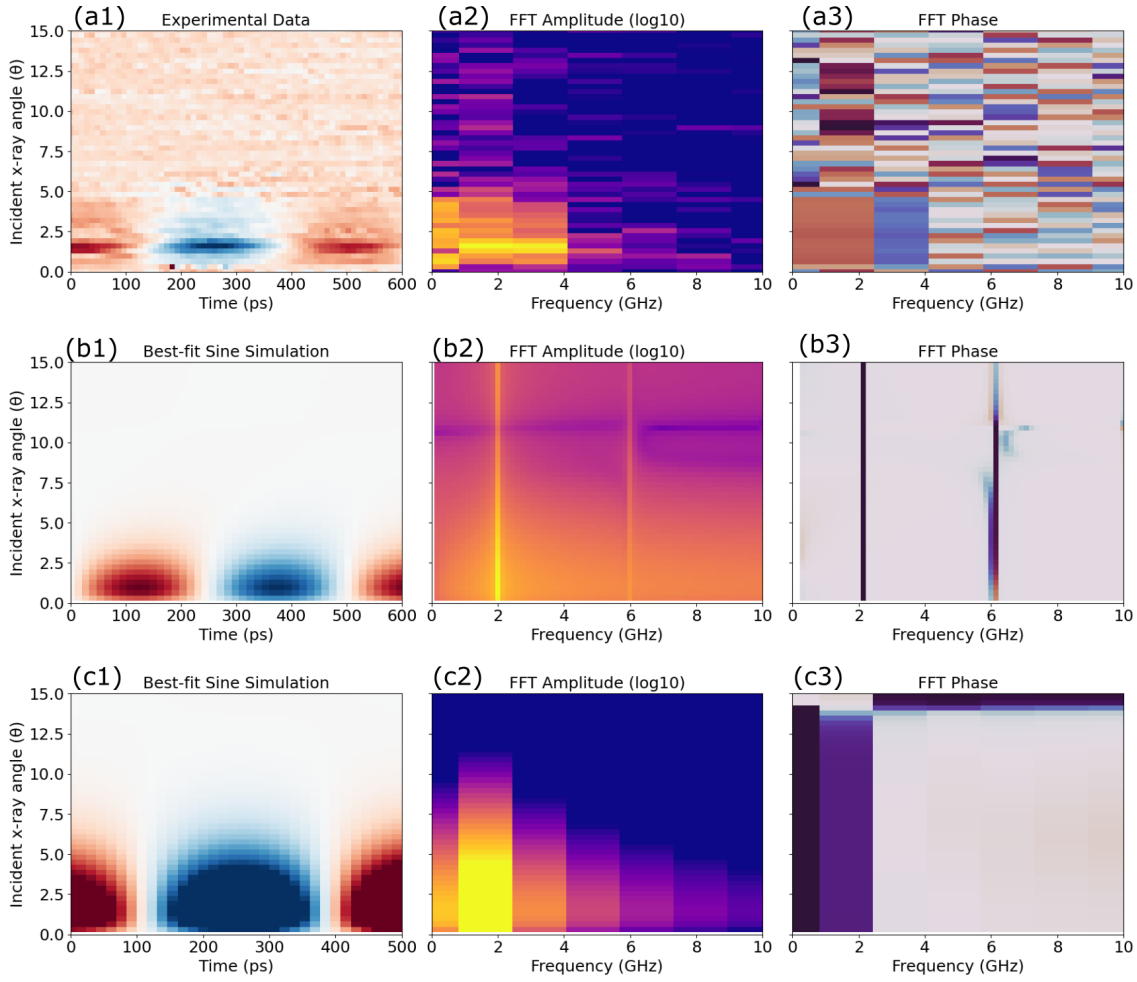


Figure 6.13: (a1–a3) FFT analysis of the experimental RFMR data reveals spectral contributions at multiple excitation frequencies: (a1) raw signal, (a2) extracted amplitude, and (a3) extracted phase. These features are not reproduced in simulations assuming ideal sinusoidal precession: (b1–b3) corresponding simulated signal, amplitude, and phase. However, by importing time-series, 3D depth-resolved magnetisation trajectories from micromagnetic simulations, the model captures the observed spectral structure: (c1–c3) simulated signal, amplitude, and phase. The comparison highlights the necessity of modelling non-driven frequencies to reproduce the full experimental FFT response.

The magnetisation profile shown was created in UBERMAG according to eq. (6.7), by distorting the excitation RF with harmonics at decreasing intensities, in an attempt to match the experimental RF observed in Figure 6.10. From there $\xi(z)$, $\psi(z)$, $\phi(z)$ were no longer applied in a geometric

sense, but as linear transformations at each depth, with each one corresponding to rotating the traced precessional path about a primary axis. This gave us the fitting parameters to return the best-fit.

In Figure 6.13 we show spectral broadening observed in the distorted RFMR response. Further there is a phase offset between the FFT binned contributions at 2 and 4 GHz. This indicates a departure from linear regime dynamics, consistent with non-driven solutions to the LLG under multitone forcing [120], characteristic of Duffing-type anharmonicity in magnetisation oscillators [121, 122]. The sinusoidal model fails to replicate this, with no visible spectral broadening. By importing the micromagnetic results into the reflectivity model, we accurately replicate the spectral broadening, and the phase difference across this. The success of importing full time-domain magnetisation from micromagnetics reinforces the necessity of modelling beyond single-mode harmonic assumptions, as advocated in nonlinear spin-diode and reservoir computing studies [123, 112].

This work demonstrates that the OOP FMR modes in Si/NiFe(25 nm)/Pt(1.5 nm) can itself distinguish unique time-series RF inputs, and can compute at a very basic level, linear classification.

Chapter 7

Depth Profile of Magnetic Trilayers

Building upon the results presented in Chapter 6, we now discuss the depth-dependent magnetisation profile of magnetically coupled trilayer structures. The sample series CoFeB/Cr(t_{Cr})/NiFe was grown comprising 30 distinct samples, systematically varying t_{Cr}, t_{FM}, cap layers, and seed layers. Through comprehensive pre-characterisation utilizing VSM, VNA-FMR, Cu-edge Hard XRR, XMCD, and XRMR, the ferromagnetic layers exhibited an oscillatory, temperature-dependent RKKY interaction, alongside clearly defined optical and acoustic FMR modes observable in both in-plane and out-of-plane applied magnetic fields. Spin-pumping was observed in-plane and complex dynamic coupling was identified under out-of-plane conditions. Analysis of XRMR at 100 mT confirmed that the magnetic profile within each structural layer is non-uniform, necessitating a division into three distinct sublayers for accurate fitting.

UBERMAG simulations revealed the role of IEC on the formation of acoustic and optical modes in CoFeB/Cr/NiFe as a function of t_{Cr}. Layer-specific analysis showed that the CoFeB layer exhibited additional complexity, most notably characterised by a detectable resonance signal across all fields between the acoustic and optical resonance conditions. This suggests a continuous evolution of the mode profile, possibly due to weak dipolar coupling or internal modal structure formation within the CoFeB layer. By emulating XFMR using RFMR measurements taken at the critical angle of the pseudo-spin-valves, we characterised the optical and acoustic modes using measurements taken on Ni, Co, Cr, and Fe L_3 edges. Remarkably, a dynamic signal was recorded for Cr despite the absence of measurable XMCD signal, and its precessional amplitude matched the Ni, while its phase was intermediate between CoFeB and NiFe phases, suggesting of possible coupling with Ni and a mediatory role between the two ferromagnetic layers. The contributions of static and dynamic coupling were explored in the OOP configuration through the analysis of the amplitude and phase relationships across the trilayer and fitting to the linearised solutions of the LLG equation. RFMR

$\theta - 2\theta$ measurements demonstrated unique depth-profiles specific to each resonant mode within the structure. This prompted an explicit calculation of the element-specific mode-dependent scattering factors.

Beyond simple models of acoustic and optical modes, an explicit fitting of experimental data requires subdivision of each FM layer into three sublayers with distinct dynamic properties. Upon reconstruction of the complete depth-profile, the CoFeB layer was found to contain an interfacial sublayer potentially thicker than the structural roughness. Within this interfacial region, CoFeB moments precessed with a 10° offset relative to bulk CoFeB in the acoustic mode, increasing to 30° in the optical mode.

Micromagnetic simulations validated this best-fit model, revealing that introducing dipolar coupling across the Cr spacer effectively decoupled interfacial moments within weakly precessing layers. Sweeping the applied field around the optical mode provided further characterisation of the interfacial CoFeB sublayer, with significant changes to the depth-profile with varying field, possibly attributed to reduced magnetisation at the CoFeB interface altering local resonance conditions.

7.1 Motivations

Magnetic trilayers form the backbone of many technological devices, with applications in data storage media [124, 125] and spintronics [126, 127]. These structures, composed of ferromagnetic (FM) layers separated by non-magnetic insulators or heavy metal spacers, rely on the coupling between FM layers for their functionality. The tunability of key parameters, such as layer thickness, roughness, and interface quality, makes them ideal platforms for engineering advanced spintronic devices.

Magnetic trilayers host a variety of interesting phenomena for RFMR, firstly, the coupling across the FM's is controlled by their separation distance across the spacer. This is understood through the RKKY interaction. Understanding angular momentum transfer across magnetic interfaces is further critical for advancing spintronic devices. The transfer of spin currents between FM layers, mediated by non-FM spacers, is a cornerstone of spintronic functionality. In FM/non-FM/FM trilayers, spin currents generated by precessing magnetisation in one FM layer exert spin-transfer torque (STT) on the adjacent FM layer [128].

Traditional techniques, such as magnetostransport measurements of giant magnetoresistance (GMR) [124, 125] and conventional FMR, infer spin dynamics indirectly through parameters like damping and resonance shifts. Meanwhile, XFMR has enabled element-specific characterisation of spin precession through the XMCD effect [129], providing critical insights into the dynamics of

spin-valves [12, 19, 27, 130, 131, 132, 133]. However, these approaches have limitations in resolving depth-dependent behaviour within individual layers and at interfaces.

RFMR addresses these gaps by providing time-resolved, depth-resolved information on spin dynamics. By employing RFMR, this study investigates the depth-dependent magnetic dynamics in NiFe/Cr/CoFeB pseudo-spin-valves, a system where the Cr spacer layer facilitates complex dynamics and interfacial exchange coupling [28, 78, 79, 130].

7.2 Sample Growth & Characterisation

The magnetic trilayer samples were grown in a DC magnetron sputtering chamber [75] with a base pressure of $\sim 5 \cdot 10^{-10}$ mbar. During thin film growth, a pressure of $\sim 4 \cdot 10^{-3}$ mbar was maintained using Ar as the sputtering gas. The sputtering power was set to 30 W for all ferromagnetic targets and 15 W for the Cr spacer, Si seed layer (3 nm), and cap (1.5 nm). The sample was kept at room temperature and underwent azimuthal rotation during deposition. The samples are referred to as pseudo spin-valves in this text due to the absence of an AFM layer pinning the bottom FM layer. Hence they are not explicitly spin-valves but rather magnetic trilayers, with the goal of emulating the same properties as demonstrated in A.A. Bakers work on the same trilayer grown via MBE [78].

Post-deposition, samples were characterised using VSM-SQUID, XRR, and VNA-FMR [106]. To accommodate RFMR measurements, the substrate thickness was reduced by hand polishing from 500 μm to 100 μm, allowing the sample to face the X-ray beam while being sufficiently close to the RF signal line to experience FMR.

The goal of this study was to investigate IEC, spin-pumping, and interfacial spin-transfer torque as a function of depth in a CoFeB/spacer/NiFe spin-valve structure. Chromium was selected due to its unique electronic properties [134], including a well-defined Fermi surface that supports RKKY-mediated coupling [135], smooth interfaces [136], and its relatively long spin-diffusion length [137], which enables the study of dynamic effects such as spin-pumping across a broad range of thicknesses. Alongside it's own THz resonance [138]. Furthermore, Cr's ability to mediate both static and dynamic coupling mechanisms makes it an ideal candidate for investigating the interplay between these processes [139, 79].

A series of spin-valve samples with Cr spacer layers of varying thicknesses up to 24 nm was prepared for this study, whose Cr/CoFeB interfaces exhibit a low roughness of $\sim$0.3 nm as confirmed by XRR fits, which did not require an additional layer for alloy formation to fit the data.

7.2.1 Interlayer Exchange Coupling

Macrospin Calculations

The interlayer exchange coupling constant between the magnetisations $\mathbf{M_1}$ and $\mathbf{M_2}$ of two ferromagnetic layers separated by a Cr spacer layer [140] will be calculated in the same manner as in Chapter 2, Section 2.2. The equilibrium directions of $\mathbf{M_1}$ and $\mathbf{M_2}$ are determined by the minima of the total free energy per unit area parametrised by the bilinear J_1 and biquadratic J_2 coupling parameters defined via the phenomenological energy density expression [141] :

$$E_{tot} = E_a - J_1(t,T)\frac{\mathbf{M_1}\cdot\mathbf{M_2}}{M_1M_2} - J_2(\frac{\mathbf{M_1}\cdot\mathbf{M_2}}{M_1M_2})^2 \tag{7.1}$$

where a positive J_1 corresponds to ferromagnetic (FM) coupling, with minimal energy when $\mathbf{M_1}$ and $\mathbf{M_2}$ are parallel. Conversely, a negative J_1 indicates AFM coupling, with the lowest energy achieved when $\mathbf{M_1}$ and $\mathbf{M_2}$ are antiparallel. The biquadratic J_2 seeks to align moments at 90° relative orientation, however is often significantly weaker than J_1 [141].

E_a denotes Zeeman Energy and anisotropy for each layer, with $E_a(\psi) = K_\mu \sin^2(\psi) - \mu_0 M_s H \cos(\theta_H - \psi)$ with ψ as the relative moment direction. This however is unvaried in our experiments and not investigated here.

The J_1 exchange coupling in CoFeB/Cr/NiFe spin-valves is primarily governed by both the Ruderman-Kittel-Kasuya-Yosida (RKKY) interaction and a magnetostatic term [142]. At low Cr spacer thicknesses, the RKKY interaction arises from indirect exchange mediated by conduction electrons in the spacer layer. This interaction is highly temperature-dependent, as its attenuation length, $L(T)$, is inversely proportional to temperature [142]. The exchange coupling constant can be expressed as:

$$J_1(t,T) = P(t)\left[\frac{J_0}{t^2}\sin\left(\frac{2\pi t}{\Lambda} + \psi_{\mathrm{RKKY}}\right)\frac{t/L(T)}{\sinh(t/L(T))}\right] + \frac{\mu_0}{4\pi\sqrt{2}}\frac{\pi^2h^2}{\lambda^2}M^2e^{-2\pi\sqrt{2}t/\lambda}. \tag{7.2}$$

where J_0 is the amplitude of the oscillations, Λ is the oscillation period linked to the Fermi surface of Cr, and ψ_{RKKY} is the phase offset. $L(T)$ represents the attenuation length, inversely proportional to temperature, while $P(t)$ accounts for thickness fluctuations derived from XRR fits (approximately 0.3 nm for all samples, as shown in Figure(7.3)). Finally, M is the saturation magnetisation of the ferromagnetic layers.

The total bilinear interlayer coupling, $J_1(t,T)$, is the sum of these contributions. At larger Cr spacer thicknesses, the magnetostatic term becomes more dominant as the RKKY contribution decays exponentially.

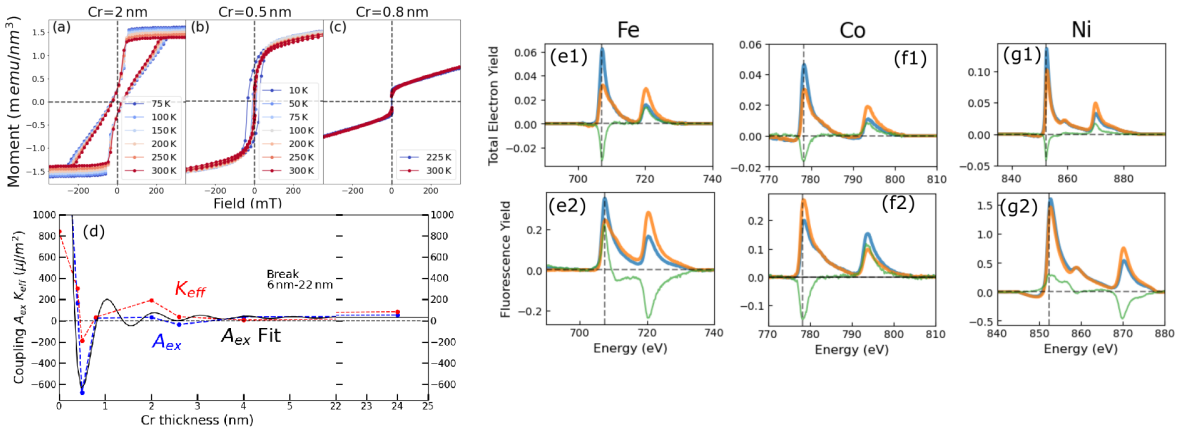


Figure 7.1: Exchange coupling constants A_{ex} and K_{eff} as a function of Cr spacer thickness (in nm). SQUID-VSM measurements showing distinct differences in the exchange coupling with temperature for t_{Cr}=0.5 nm, while t_{Cr}=2 nm and 0.8 nm remain more stable. 300 K VSM calculations for A_{ex} (blue) and K_{eff} (red) through comparison of IP and OOP hysteresis loops. The dashed line represents $A_{ex} = 0$, marking the boundary between FM and AFM coupling regimes for A_{ex}. Fitted to the A_{ex} calculations is the fitted values for Eq.(7.2). For clarity; a vertical break from 6 nm to 22 nm and t_{Cr}=0 nm is cropped but included in Table 7.1 with a value for A_{ex} of 3150 $\frac{\mu J}{m^2}$. (e-g) XMCD measurements on Fe (1), Co (2), Ni (3) in TEY at 1 T, and (a) FY at 100 mT (b), for t_{Cr}=2 nm. FY measurements were taken simultaneously to RFMR measurements. Measurements can be fit with eq: (4.6) to determine $\mathbf{n}''$. Co and Ni moments are anti-aligned at low fields, resulting in XMCD signals with opposite signs in FY. However in TEY measurements at 1 T they align.

Calculations for J_1 and J_2 are inspired from [141], and calculated using the relation:

$$A_{ex} = J_1 \cos\theta - J_2 \cos^2\theta = \frac{H_c(\theta) M_s}{2V} \tag{7.3}$$

Where H_c is the Coercive field (A/m) at varying static field angles θ, M_s is the saturation magnetisation, and V is the volume of the ferromagnetic layer. VSM loops were only done with IP and OOP configurations on all samples, hence the θ behaviour is only estimated, a thorough investigation into J_2 would require a complete angular dependence on the VSM loops.

Calculations and fits for A_{ex} and K_{eff} are inspired from [141], and calculated using the relation:

$$A_{ex} = \frac{1}{t}\int_{H_{OOP}} M(H)\, dH, \quad K_{eff} = \frac{1}{t}\left(\int_{H_{OOP}} M(H)\, dH - \int_{H_{IP}} M(H)\, dH\right) \tag{7.4}$$

Where M(H) is the magnetisation (M) measured at a static field (H), hence the integral describes the area within the hysteresis loop.

The static coupling of NiFe/Cr(t_{Cr})/CoFeB is first studied by VSM loops at 300 K IP and OOP. Variation of A_{ex} and K_{eff} with Cr thickness at 300 K is shown in Figure 7.1. The A_{ex} data are well-fit by Eq. (7.2), requiring both RKKY and magnetostatic contributions. The best-fit model yields an RKKY oscillation period of 10 Å. The coupling is accurately described by just A_{ex} for t_{Cr}<0.5 nm and

t_{Cr}>3 nm, with K_{eff} being non-negligible between. In the case of single layers, only A_{ex} is considered, and the results are shown in Table 7.1, with A_{ex} for NiFe (CoFeB) equal to 2 (5) $\frac{\mu J}{m^2}$. Which is comparable to the A_{ex} value for the completely decoupled spin-valve t_{Cr}=24 nm, where A_{ex}=5 $\frac{\mu J}{m^2}$ for the CoFeB. Deviations of A_{ex} from the fit were attributed to the effects of interfacial roughness and structural inhomogeneities introduced during the sputtering deposition process.

Figure 7.1 illustrates the temperature dependence of the interlayer coupling by SQUID-VSM OOP measurements. For Cr spacer layers with $t = 0.5$ nm, a strong temperature dependence of A_{ex} is observed. In contrast, for $t_{Cr} = 0.8$ nm and $t_{Cr} = 2$ nm, the coupling shows minimal temperature dependence.

In XMCD taken by FY during the RFMR beamtime in Figure 7.1 (e1-g1), and TEY afterwards in Figure 7.1(e2-g2), we explore the magnetic state of the trilayer. We see a non-magnetic peak at 860 eV on the Ni edge although no change in dynamics is measured here in RFMR. Next, we can see in Co measurements that the XMCD is opposite to the measurements of Ni and Fe. Measurements were taken at 100 mT as FMR modes at this field magnitude was in the 2-8 GHz range, as what is accessible in our RFMR set-up. However in TEY measurements taken after the beamtime at 1 T, all moments are aligned. The RASOR diffractometer uses permanent magnets on a motor stage, with a max distance apart of 20 mm and a minimum distance of when the magnets would start to block the X-ray beam physically. This is therefore both a function of X-ray incident angle and applied field angle, but is approximately 2 mm. In the beamtime data shown, the applied field range is ~35 to 170 mT, and hence measuring hysteresis loops in a sample that requires 200 mT to saturate is futile. Next, it can be easily seen that the Co and Ni are aligned antiparallel to each other. Since the Fe is present in both layers, its FY and reflectivity spectra are a convolution of both layers.

7.2.2 Dynamic Coupling

Spin-transfer torque is commonly measured with techniques such as FMR [143] and time-resolved magneto-optical Kerr microscopy [144]. When the applied magnetic field is larger than the saturation field ($H > H_s$), The acoustic and optical modes of coupled FM's can be derived from the Kittel equation, giving [145],

$$\omega_A = \gamma\sqrt{H(H+M_s)} \qquad \omega_O = \gamma\sqrt{(H-H_s)(H-H_s+M_s)} \tag{7.5}$$

Where ω_A is the acoustic mode, ω_O is the optical mode, γ is the gyromagnetic ratio, H is the applied field, M_s is the saturation magnetisation of the structure, and H_s is the saturation field. The

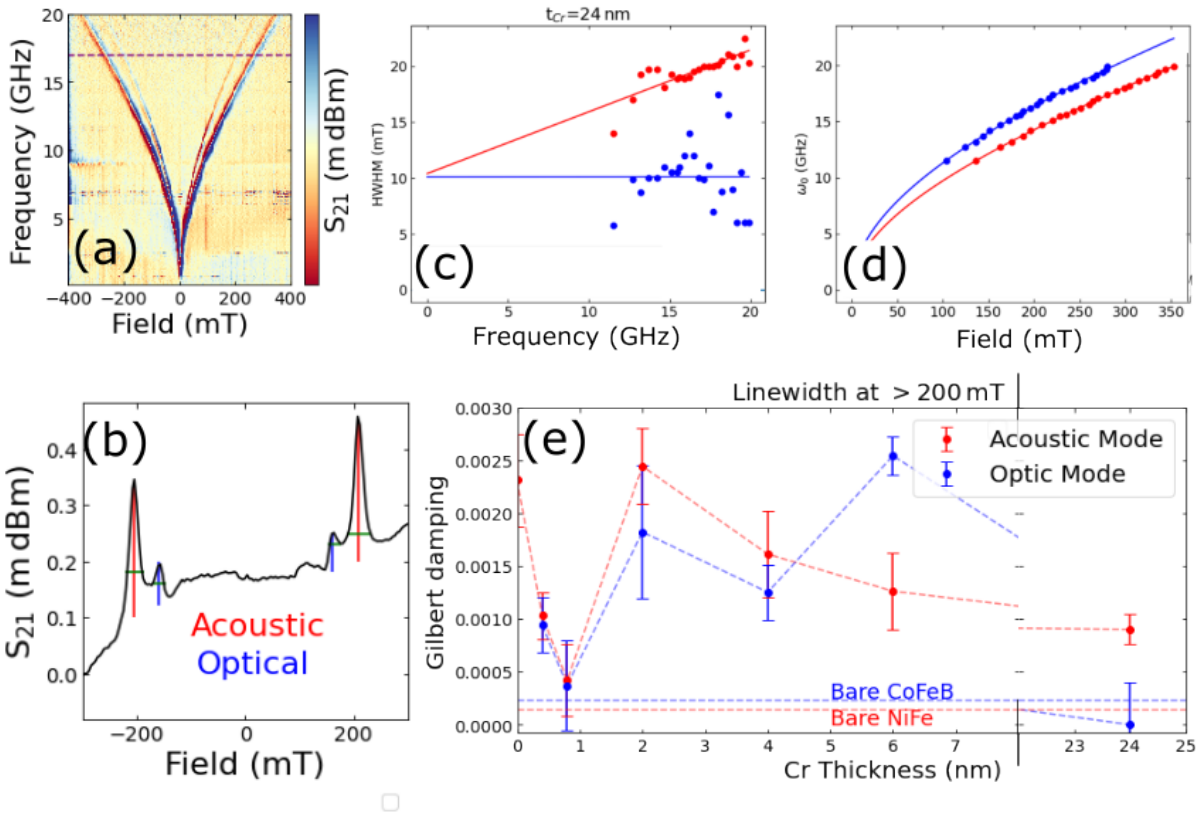


Figure 7.2: Field-dependent ferromagnetic resonance (FMR) measurements for a Cr spacer thickness. (a) VNA-FMR measurements on t_{Cr}=24 nm of S_{21} absorption in an easy-axis geometry, plotted is the derivative of the complex S_{21}, with a dashed purple line at 17.23 GHz. (b) S_{21} as a function of field at 17.23 GHz showing Lorentzian peaks in absorption at the acoustic (red) and optical (blue) modes, with ΔH plotted as green horizontal lines. (c) Linewidth as a function of the resonant frequency, exhibiting a complex behaviour at low fields followed by stabilisation at higher fields. HWHM measurements below $\lesssim$10 GHz displayed significant complexity and were neglected from the linear fit. (d) Corresponding resonant frequency as a function of field, with a Kittel equation fit. (e) Using eq's (7.5) and (7.6), the Gilbert damping can be extracted. Damping is found to have a relationship more complex than an exponential decay, with an oscillatory nature comparable to the A_{ex} values in Figure 7.1. Further distinct damping properties are observed between the optical and acoustic modes in the magnetostatic regime (at t_{Cr}>2 nm). A break in the x-axis is included from 8-22 nm.

FMR linewidth (in mT) as a function of frequency for the Cr spacer thickness of 24 nm is shown in Figure 7.2. The acoustic and optical mode is observed. At low fields ($\lesssim$ 200 mT, or $\lesssim$ 10 GHz), the linewidth exhibits significant complexity, characterised by deviations from the linear fit. This behaviour can be attributed to two key factors: the incomplete saturation of magnetisation and the presence of simultaneous resonances producing anti-damping torques [146, 147].

At low applied fields, the magnetisation in the trilayer structure is not fully saturated, leading to an increased inhomogeneity in the magnetisation dynamics, resulting in a broadened and irregular linewidth [148]. Additionally, due to the overlapping of the optical and acoustic modes, simultaneous resonances of the CoFeB and NiFe can give rise to anti-damping torques, which further modify the linewidth [78]. The limitation here arises due to how the spin current absorption depth can only been

$\mathbf{t}_{\mathrm{Cr}}$ (nm)	$\mathbf{A}_{\mathrm{ex}}$	$\mathbf{K}_{\mathrm{eff}}$	γ	$\mathbf{M_s}$	$\mathbf{H_s}$	$\alpha_{\mathbf{A}}$	$\alpha_{\mathbf{O}}$
0	3150	843	1.0	35.3	–	0.00231	–
0.4	165	307	0.9	33.8	27.4	0.000103	0.00094
0.8	-680	-185	1.4	29.9	9.0	0.000042	0.00037
2	130	33	1.6	18.3	15.2	0.00244	0.00182
4	80	193	1.6	14.1	8.0	0.00161	0.00121
6	10	85	1.3	20.1	4.0	0.00126	0.00254
24	5	–	1.7	10.0	36.0	0.0009	0.00
Bare NiFe	2	–	1.5	12.5	–	0.0001365	–
Bare CoFeB	5	–	1.0	45.1	–	0.000265	–
Si (5 nm)	0.1	0.01	1.5	12.7	2.6	0.00214	0.00099

Table 7.1: Table of Cr thickness (t_{Cr}) and associated parameters: exchange stiffness (A_{ex}) and effective anisotropy (K_{eff}) in μJ/m^2, gyromagnetic ratio (γ) in GHz/mT, saturation magnetisation ($4\pi M_s$) and saturation field (H_s) in mT, of the FM's (calculated by VNA-FMR), α is the Gilbert damping for the acoustic mode (α_A) and optical mode (α_O). Samples with no values for H_s or α_O only showed one Kittel mode.

measured indirectly [149, 150, 151].

To avoid the complexities introduced at low fields, the Gilbert damping is extracted at higher fields (> 200 mT), where the magnetisation is fully saturated, and the linewidth exhibits more linear relationship [152].

$$\Delta H = \Delta H_0 + \frac{2\alpha_{\mathrm{gb}}\omega_0}{\gamma} \tag{7.6}$$

where ΔH is the total linewidth, ΔH_0 is the intrinsic linewidth, α is the Gilbert damping, with spin pumping contribution isolated by $\alpha = \alpha_0 + \alpha_{sp}$. ω_0 is the resonance frequency of precession, and γ is the gyromagnetic ratio.

The linewidth (ΔH) and resonance frequency (ω_0) was extracted as a function of applied field (H) for each Cr spacer thickness (t_{Cr}) in the NiFe/Cr/CoFeB spin-valve system. Fits of these to the eq's (7.5) and (7.6) returned the values for μM_s, H_s, γ, α_{sp}, α_0. The results, presented are in Table 7.1, with α plotted in Figure 7.2, revealing a clear reduction in linewidth beyond the spin diffusion length of Cr. This behaviour is indicative of a suppression of spin pumping due to increased spin diffusion in the Cr spacer [153, 154].

Oscillatory nature is visible in α below the spin diffusion length, this is attributed to several factors, firstly the sample caps vary between samples, next, the oscillatory variations in J_1 have been observed to impact damping [155], while J_1 itself can have a dynamic component that is unique to both the acoustic and optical modes [156]. Next, spin pumping is extremely sensitive to surface roughness [135]. Hence, when the spacer thickness becomes comparable to the interface roughness, a great deal of complexity is introduced into the dynamics.

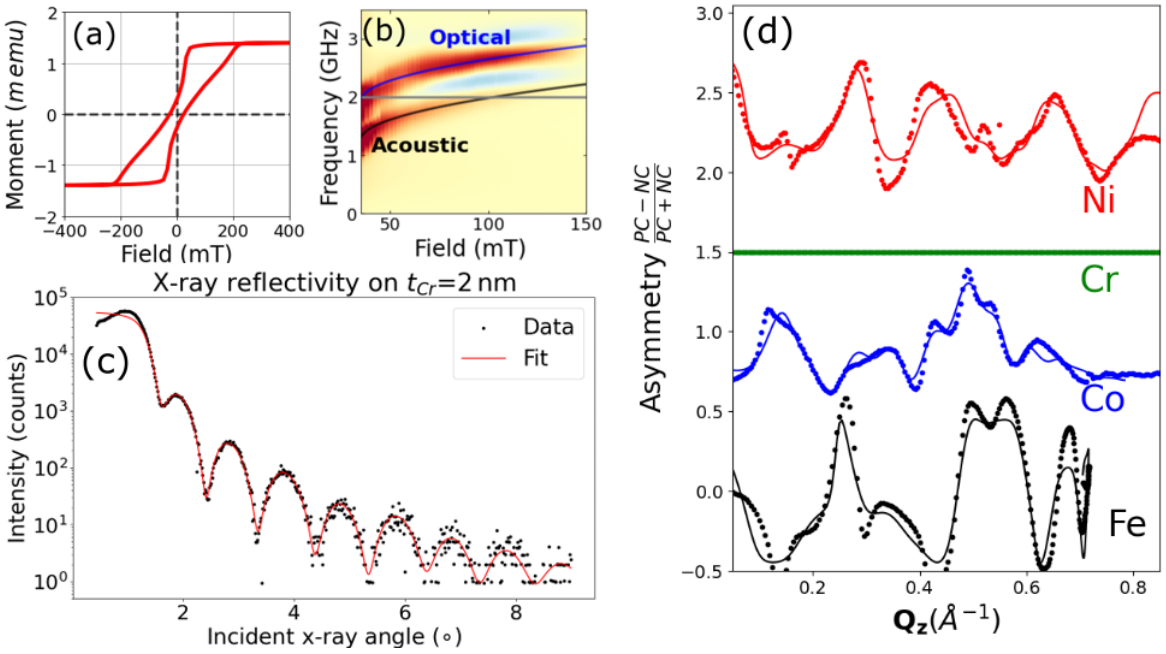


Figure 7.3: Characterisation of the CoFeB(5)/Cr(2)/NiFe(5) pseudo-spin-valve structure. (a) Magnetic hysteresis, showing saturation at ~200 mT. (b) FMR data showing prominent acoustic and optical modes, fitted according to the Kittel equations and the horizontal dashed line corresponds to the driving frequency in the upcoming RFMR experiment. (c) Hard x-ray XRR data and its corresponding GenX fit, which gave a sample of parameters [Si(1.7±0.3)/ CoFeB(4.8±0.3)/ Cr(2.2±0.3)/ NiFe(4.3±0.6)/ Si(0.9± 0.8)] Thickness in nanometres. Asymmetry from XRMR measurements at positive (negative) circular (PC, NC), on the L_3 edges of Ni (853 eV), Cr (573 eV), Co (777 eV) and Fe (707 eV) computed as (PC-NC)/(PC+NC) and plotted against $\mathbf{Q_z}$. XRMR fits were computed using GenX, by considering FM layers to be divided into 6 sub-slices with varying magnetic properties. Measurements were taken at 100 mT, while from (a) saturation was confirmed to be ~200 mT.

Alongside the Cr based trilayers we calculated α for bare NiFe and CoFeB samples, as well as removing the interfacial exchange coupling through Cr [157, 79] by the use of a Si spacer, also shown in the table. Samples with no values for α_O only showed one Kittel mode, hence for bare FM samples, or the thin film with direct exchange coupling (t_{Cr}=0 nm).

7.3 Sample Selection & Characterisation

For the synchrotron-based RFMR study, two samples were selected: a trilayer with a Cr spacer thickness t_{Cr} = 2 nm, for which dynamic coupling was observed to be enhanced in VNA-FMR, and a control sample with a very thick t_{Cr} = 24 nm Cr spacer layer. Samples with ultrathin Cr exhibited significant complexity in their spin-pumping behaviour due to a strong RKKY interaction [134], and extreme sensitivity to sample roughness. When the Cr thickness became comparable to the interfacial roughness, this induced considerable variability [135], which is undesirable for the present study.

Characterisation of the t_{Cr} = 2 nm sample in OOP magnetic fields is shown in Figure 7.3.

Superconducting quantum interference device vibrating sample magnetometry (SQUID-VSM) measurements of the magnetic hysteresis are shown in Figure 7.3(a), suggesting a saturation field of approximately 200 mT. Note that the SQUID-VSM field range was extended to ±5 T (not shown) to confirm full magnetic saturation at ~200 mT. High-field subtracted S_{21} data from in-situ VNA-FMR is shown in Figure 7.3(b), clearly resolving both acoustic and optical FMR modes.

In addition to the magnetic data, hard XRR measurements using Cu K-α radiation (1.54 Å) are shown in Figure 7.3(c). These allow extraction of structural parameters of the heterostructure, including layer thicknesses, densities, and interface roughnesses. The resulting structure was determined to be [Si(1.7±0.3)/CoFeB(4.8±0.3)/Cr(2.2±0.3)/NiFe(4.3±0.6)/Si(0.9±0.8)], with thicknesses in nanometres.

Soft XRR measurements, shown in Figure 7.3(d), were performed at the L_3 edges of the magnetic elements Fe, Ni, Co, and Cr (572, 707, 777, and 852 eV, respectively) in the heterostructure. The Ni signal probes the NiFe layer, Co probes the CoFeB layer, Cr probes the spacer layer, while the Fe signal contains contributions from both ferromagnetic layers. Prior to XRMR measurements, a field of 160 mT was briefly applied using permanent magnets within the diffractometer, and then reduced to 100 mT for the reflectivity scans. While this field was below full saturation, increasing it further would have caused the permanent magnets to block the x-ray beam at high $\mathbf{Q}_z$. Subsequently, RFMR measurements were carried out at 2 GHz under OOP fields of 40 mT and 90 mT. These field values were selected based on VNA-FMR data from Figure 7.3 and correspond to the resonance conditions of the optical and acoustic modes, respectively.

The asymmetry observed at the Ni and Co edges confirms ferromagnetism in the NiFe and CoFeB layers. No circular dichroism asymmetry was observed on Cr, but asymmetry appeared in linear polarisation measurements at high Q_z, this cannot just be attributed to OOP antiferromagnetism in the Cr spacer, due to the unique interactions of the LH and LV polarisation with the crystal structure. The fits to the XRMR Asymmetry gave the ferromagnetic nature of each element with relevant magnetic roughness parameters (interfacial demagnetism, interfacial thickness, roughness). Fits were done by dividing each FM into 2 independent sub-layers, each with their own interfacial magnetism. Results of the fits suggested variations of the static magnetisation direction with depth in both the NiFe and CoFeB at the static fields studied in RFMR [158]. This magnetostatic effect is both caused by RKKY mediated interactions and an anisotropic term seeking to align the moments at 90° [141], as observed in the VSM plots and equation 7.1.

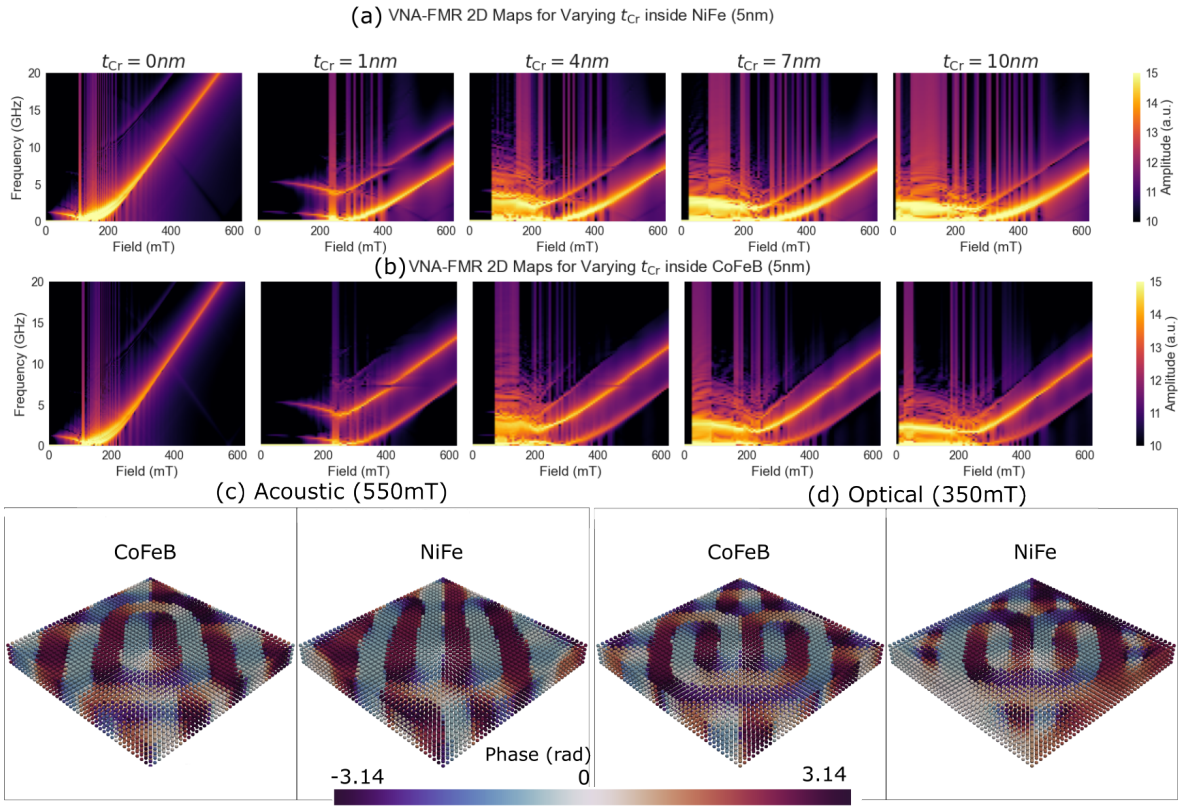


Figure 7.4: UBERMAG simulations revealing the acoustic and optical modes in an OOP configuration show complex modal structures within CoFeB/Cr/NiFe as a function of t_{Cr}. (a) shows the m_y contribution from the NiFe layer; (b) shows the CoFeB layer-specific response. While both layers exhibit signatures of the acoustic and optical modes, their relative intensities depend on which layer predominantly drives the resonance. NiFe primarily contributes to the lower-energy acoustic mode, while CoFeB exhibits stronger response in the higher-energy optical mode. This effect is further strengthened at increasing t_{Cr}. (c,d) For $t_{Cr} = 4$ nm, a 4 GHz frequency slice intersects both modes. Here, we calculate the FFT of each voxel and show the 4 GHz contribution. We display the amplitude and phase of the acoustic mode (left, c) and of the optical mode (right, d).

7.4 Acoustic & Optical Mode Detection Using RFMR

Figure 7.4 presents simulated OOP VNA-FMR spectra for CoFeB/Cr/NiFe as a function of Cr thickness t_{Cr}, using `Ubermag`. These simulations were carried out using the method introduced in Chapter 5, Section 5.7, and previously applied in Chapter 6, Figure 6.2.

When $t_{Cr} = 0$ nm, i.e., in the direct exchange-coupled limit [27], a single dominant mode appears in the spectrum. However, this mode exhibits broadening and temporal splitting at lower fields. A weak higher-order mode is also visible at elevated frequencies, consistent with the additional energy required to drive the NiFe and CoFeB layers out of phase.

Introducing a Cr spacer layer modifies the interlayer coupling from direct exchange to RKKY-mediated interactions, which become particularly significant at ultrathin thicknesses. At $t_{Cr} = 1$ nm, the NiFe layer exhibits a strong response at the lower-energy acoustic mode, while the CoFeB shows a more

intense signal at the higher-energy optical mode. Additionally, CoFeB reveals a third, even higher-frequency mode that is not visible in the NiFe response, indicating layer-specific modal selectivity. Between these modes, a continuous signal is observed in CoFeB, suggestive of potential tunability of the depth profile by varying the applied static field across the optical mode.

As t_{Cr} is further increased to 4 nm, 7 nm, and 10 nm, the modal selectivity between the two layers becomes increasingly pronounced. The NiFe remains strongly coupled to the acoustic mode, while the CoFeB continues to dominate the optical mode. The disparity in modal intensity between layers increases with t_{Cr}, consistent with the suppression of interlayer coupling and the emergence of layer-decoupled dynamics. In panels (c, -f), we present the spatially resolved FFT for $t_{Cr} = 4$ nm, at $\omega = 4$ GHz for the optical (350 mT, panels (c, d)) and acoustic (550 mT, panels (e, f)) modes. The amplitudes of the FFT are shown in panels (c, e), with the corresponding phase values displayed in panels (d, f). Modes were identified by locating the maxima in amplitude within the CoFeB layer for the optical mode and the NiFe layer for the acoustic mode. The FFT was calculated using the method outlined in Chapter 5, Section 5.7.

The plot shows the 3D structure with the caveat that non-oscillating layers, such as the Cr layer, are masked. This results in a visible CoFeB (top) and NiFe (bottom) layer. Amplitude and phase colourbars are included at the bottom, with phase values wrapped from 0 to 2π. It is noteworthy that the optical mode exhibits out-of-phase oscillation, while the acoustic mode is nearly in-phase.

At the Cr/CoFeB interface, IEC from the NiFe layer induces a measurable phase lag due to spin coherence across the Cr spacer [159], which decays beyond the spin current absorption depth. These observations confirm that spin currents are primarily absorbed at the interface, leading to uniform precession in the CoFeB layer, dominated by direct exchange coupling [27]. Our analysis will systematically rule out alternative mechanisms, such as static coupling [27, 31], effective field variations [103], and magnetic proximity effects from Cr [77].

RFMR measurements were conducted on the trilayers, the experimental setup was based on the RFMR methodology described in Chapter 3. The dynamic signal was measured across the Fe, Co, Cr, and Ni L_3 edges. The delay line was swept from 0 to 600 ps, and the resulting amplitude and phase of the sine curves, corresponding to the pumping RF frequency, were recorded.

XFMR can detect STT as the introduction of pure-spin currents emitted from one FM and absorbed by the other, introducing a phase difference between the processing layers [130]. It is worth noting here that spin-pumping measured in the previous section was in-plane, whereas the RFMR is out-of-plane. In Figures (7.5, 7.6) we look at the measured dynamic signal at grazing incidence (θ=5°) for both samples as a function of delay time and applied field. Assuming the output data to be sinusoidal

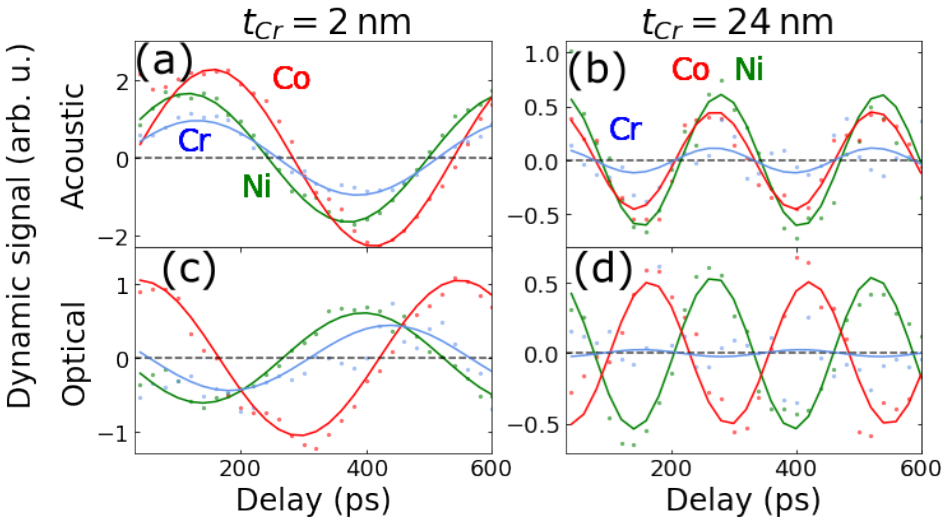


Figure 7.5: RFMR measurements in the acoustic and optical modes. Delay scans illustrating the precession of Co, Ni, and Cr moments in the (a-90 mT, b-165 mT) acoustic and (c-40 mT, d-120 mT) optical modes for (a, c) a trilayer with a Cr spacer thickness (t_{Cr}) of 2 nm at 2 GHz and (b, d) the t_{Cr} = 24 nm control sample at 4 GHz. Solid lines represent sinusoidal fits to the data. The Fe signal is excluded due to its convolution of contributions from both layers.

in nature with only varying phase and amplitude we can fit it with a sine curve of known frequency (pumping RF; 4 GHz in Cr =24 nm, and 2 GHz in Cr=2 nm) and an offset proportional to static signal, we can extract the amplitude and phase of oscillation within the two modes. We define optical mode as the peak in Co Amplitude, and the acoustic mode as the peak in Ni Amplitude. In Cr = 24 nm, we can see a very broad Fe and Co resonance optical mode, corresponding to increased damping due to the misaligned moments across the Cr spacer. The acoustic mode is much weaker in this sample. We can further see the Ni precession presents no phase change between the modes, whereas the Co undergoes a phase inversion. Cr is not found to oscillate in this sample. In the Cr 2 nm sample, we see an optical mode right at the minimum field in the diffractometer, here labelled as 40 mT. At this incident X-ray angle the Ni dynamic signal is too weak to be resolved in the optical mode. However the acoustic mode shows strong resonance in the case of all four elements, with a particular note that all phases are rapidly changing in this resonance. The spin dynamics across our Cr interlayer is governed by a combination of direct exchange coupling across the interfaces, and an AC component of the dynamic coupling through the Cr layer [130, 160, 161].

The behaviour of the pseudo-spin-valve and the control are markedly different as the spacer thickness determines the extent of angular momentum transfer between the ferromagnetic layers. In the case of the control sample with the thick Cr spacer, coupling is completely suppressed and the XFMR signals of Co and Ni are almost completely in-phase (out-of-phase) in the acoustic (optical) mode, shown in Figure 7.5(b) and 7.5(d), respectively.

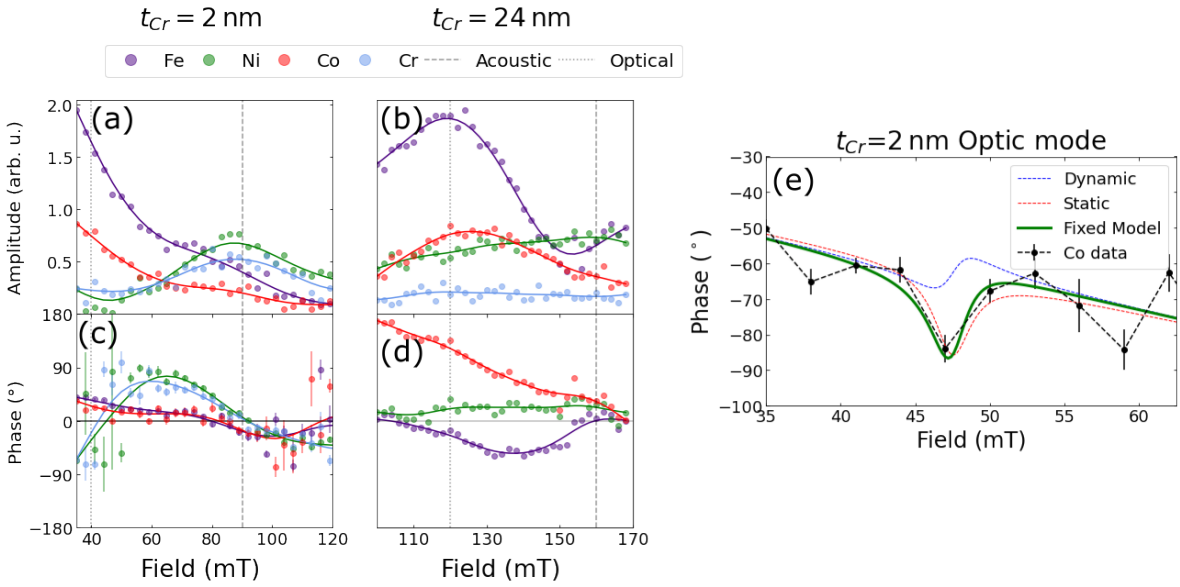


Figure 7.6: Disentangling static and dynamic interlayer coupling in CoFeB/Cr/NiFe using RFMR. (a–d) By fitting each delay scan (shown in Figure 7.5) with a sinusoidal function at the RF excitation frequency, the amplitude and phase of magnetisation precession are extracted as a function of applied field. Field-dependent measurements reveal distinct resonance conditions associated with interlayer-coupled acoustic and optical modes. The extracted amplitudes and phases are plotted with standard uncertainty in phase shown as error bars (smaller than the marker size in the control sample). Solid lines serve as visual guides. Dashed lines indicate the peak amplitude positions of the Co and Ni signals, corresponding to the optical and acoustic modes, respectively. (e) A close-up of the Co precession in the optical mode for the $t_{\mathrm{Cr}} = 2$ nm sample. The field-dependent phase response is compared to macrospin model predictions based on the linearised LLG equation, enabling a decomposition into static and dynamic coupling contributions.

This almost perfect decoupling of the CoFeB and NiFe layers (phase difference of 13° in the acoustic and 215° in the optical mode) confirms that a 24-nm-thick Cr spacer effectively suppresses coupling, resulting in largely independent magnetic layer dynamics [162].

In the case of the pseudo-spin-valve sample with the 2-nm Cr spacer, the two ferromagnetic layers are oscillating in the acoustic mode with a phase-lag of 28.2°, as shown in Figure 7.5(b), while the Cr layer assumes an intermediate phase difference of 17.4°. For the optical mode, shown in Figure 7.5(d), the CoFeB layer undergoes a substantial phase shift of 82.9°, while the NiFe layer experiences a shift of 163°, with the Cr layer again adopting an intermediate phase.

The intermediate phase behaviour of the Cr spacer suggest that it takes the role of a mediator between the ferromagnetic layers. This is expected from VSM measurements, were interfacial exchange coupling across spin-valve was significantly stronger for Cr based spin-valves [79, 157], as opposed to Silicon based spin-valves. As we measured A_{ex}=10 $\frac{\mu J}{m^2}$ for t_{Cr}=5 nm with significant anisotropy, but A_{ex}=0.1 $\frac{\mu J}{m^2}$ for t_{Si}=5 nm with negligible anisotropy.

By repeating these measurements across a sweep of applied static fields, the amplitude and phase

of the Co and Ni can be used to uniquely characterise the resonance conditions. From [27] we take the acoustic mode as the peak amplitude in Ni signal, and the optical mode as the peak in amplitude of the Co. This is done in Figure 7.6 by measuring dynamic signal as a function of applied magnetic field, measured under grazing incidence, which find distinct behaviours for the two Cr spacer thicknesses. Sine curves with the known driving frequencies of 2 and 4 GHz were fitted for the pseudo-spin-valve and control sample, respectively, yielding amplitude and phase as fit parameters, including also a static offset. The static offset was found to be proportional to the amplitude and is not filtered out by the lock-in-amplifier, and hence is related to the precession, but not the specific delay line value, such as potentially the variations with M_Z during dynamics. In Figure 7.6 the trilayer sample t_{Cr}=2 nm, reveals an optical mode at the minimum field of the diffractometer, 40 mT, while the acoustic mode appears at 90 mT. For the t_{Cr}=24 nm the optical mode is observed at 120 mT, and the acoustic at 165 mT. Furthermore, the element specific phase measurements confirm that the optical mode is due to out-of-phase precession, whereas the acoustic mode is due to in-phase precession in both the studied samples.

In the case of the t_{Cr}=2 nm sample, the optical mode demonstrates a 180° inversion in the Ni phase as a signature of resonance, however, the amplitude of Co shows a large increase here, and a broad shift in phase of 30°, denoting strong dynamic coupling between the two [132]. However, in the t_{Cr}=24 nm sample, each mode acts independently, with no strong shift in resonance across any mode.

Computing the spin diffusion length through the method outlined in [161] requires an exponential decay in α against t_{Cr}, hence our oscillations render calculations mute, however literature values suggesting of a spin diffusion length of 2-13 nm [137] are in broad agreement with our measurements. We avoid quantifying this based solely on VNA-FMR results, as other mechanisms may impact gilbert damping, such as in [163], where the induced magnetism in the Pt spacer resulted in a increased damping.

Further significant differences in the damping of the optical and acoustic modes is observed in t_{Cr}>2 nm. This is explained by mutual exchange of non-equilibrium spin currents [164, 165], which should be distinguished from (but coexists with) the oscillating equilibrium exchange coupling mediated by the RKKY interaction [166]. The equilibrium coupling is suppressed when the spacer thickness is thicker than the elastic mean-free path [167] while the dynamic coupling is effective on the scale of the usually much larger spin-flip diffusion length. This results in a coupling-dependent optic mode [168], and a coupling independent acoustic mode above saturation [141].

Finally, In the t_{Cr}=2 nm sample, There is partial overlap between the FMR modes. Simultaneous resonances of the CoFeB and NiFe can give rise to antidamping torques, which further modify the

linewidth [161].

To interpret the depth-dependence in our system we consider how magnetic dynamics can be modelled using the LLG equation, incorporating both static coupling and dynamic exchange. According to this model, static coupling leads to a unipolar (absorptive) feature in the phase, while dynamic coupling leads to a bipolar (dispersive) feature [169]. In a comparison with our RFMR data, we can isolate the response of each layer, and measure its phase variations to determine the coupling mechanism.

In a comparison between the phase plots in Figure 7.6 (e), with the linearised solutions to the macrospin LLG equation also plotted in Figure 7.6 (e), we can see that the optical mode in t_{Cr}=2 nm demonstrates both dynamic and static coupling components. While the Ni moments follow the 180° phase inversion, the Co moments undergo a more complex evolution, requiring both the dynamic and static contributions of the LLG equation.

7.5 Element & Mode-Specific Scattering Factors

Our magnetic trilayer system, with its well-characterised dynamics and structural simplicity, provides an ideal platform for extracting magnetic scattering factors across multiple elements. Using FY-XAS and XMCD as starting points, we obtained both the absorptive ($\Delta\beta$) and dispersive ($\Delta\delta$) components required to model RFMR at the Co, Ni, and Fe L_3 edges.

In a saturated sample, the optical constants are described by [8]

$$\beta = \beta_0 \pm \beta_M \left[\sin\theta\cos\theta_M - \cos\theta\sin\theta_M\sin\phi_M\right] \tag{7.7}$$

$$\delta = \delta_0 \pm \delta_M \left[\sin\theta\cos\theta_M - \cos\theta\sin\theta_M\sin\phi_M\right], \tag{7.8}$$

Where ϕ_M and θ_M describe the spherical coordinates of magnetisation direction. However complexity is introduced for us as RFMR was conducted in phase-modulation, meaning that the RFMR signal was the change in photodiode current associated with inverting the precessional cone. We only probe the oscillating component of θ_M, rendering direct comparisons to μ_B mute. In the following Figure 7.7 we demonstrate the stark incident x-ray angle dependence on our experimentally measured $\Delta\delta$. The intuition here is that we are below saturation in our experiment, hence our θ_M is itself a variable with respect to θ. For these reasons we simplified our model and used Eq. (4.12), and restricted our discussion to phase of moment oscillation, despite the model limitations (Section 4.3).

Optical constants δ and β were calculated according to [8]. β is directly measured absorption using

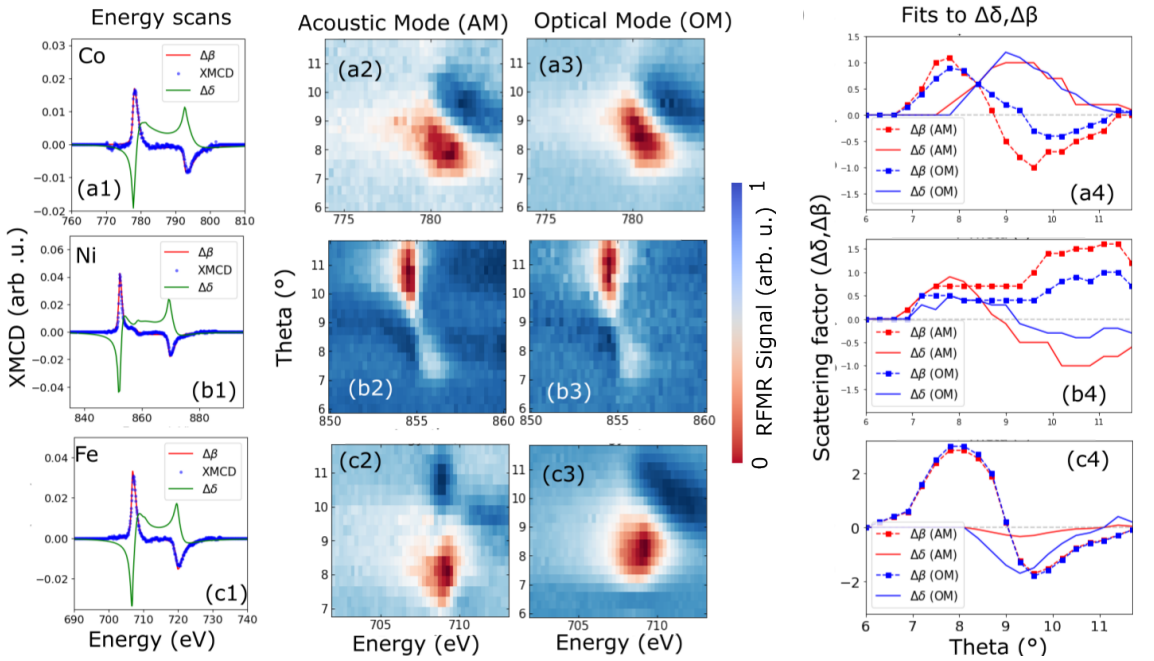


Figure 7.7: *Determining the optical constants.* Each row corresponds to a different element (Co (a), Ni (b), Fe (c)), with four columns per row. Left (1): TEY XMCD used to extract $\Delta\beta(\omega)$; the dispersive component $\Delta\delta(\omega)$ is derived via Kramers–Kronig. Center-left (2): RFMR spectra in the acoustic mode (AM). Center-right (3): RFMR spectra in the optical mode (OM). Right (4): fitted values of $\Delta\beta(\theta)$ and $\Delta\delta(\theta)$ using Eq. (4.1).

a Fluorescence Yield detector placed 70° from the specular direction, then taking the Kramers-Kronig transformation to obtain δ. Both α and β were uniquely calculated for each element and FMR mode. Details on the scattering factor considerations in RFMR can be found in the Chapter 5. Form Factors are taken from the Henke tables [81].

In Figure 7.7, we present data from the Cr = 2 nm trilayer. Here, we fit the calculated scattering factors $\mathbf{f'_m} \propto \Delta\delta$ and $\mathbf{f''_m} \propto \Delta\beta$ to dynamic RFMR measurements across a range of momentum transfer $\mathbf{Q_z}$, focused on the L_3 absorption edges.

Across all elements, we observe smooth variations in the optical constants as a function of incident angle θ. Since the total reflectivity is governed by Eq. (4.1), the measured RFMR signal includes contributions from both $\Delta\delta$ and $\Delta\beta$.

Figure 7.7 is arranged with one row per element (Co=(a), Ni=(b), Fe=(c)), and four columns representing distinct aspects of the analysis: (left=(1)) static XMCD fits obtained from background-subtracted FY-XAS spectra; (centre-left=(2)) RFMR acoustic mode (AM); (center-right=(3)) RFMR optical mode (OM) colormaps showing the dynamic signal as a function of X-ray energy and incident angle; and (right=(4)) extracted fits of $\Delta\beta$ and $\Delta\delta$ versus angle for both AM and OM.

Co (top row, (a)): Co is only present in the CoFeB layer and its magnetic response is primarily associated with the optical mode. The XMCD spectrum (a1) shows sharp asymmetry around the L_3

and L_2 edges (778.2 eV and 793.25 eV). Fitting reveals a FWHM of 0.25 eV below and 2.5 eV above the L_3 edge, and 0.5 eV / 3.5 eV for the L_2 edge. XMCD gives a strong magnetic contrast used to extract $\Delta\beta$, with Kramers–Kronig transformation yielding $\Delta\delta$. In the AM RFMR map (a2), magnetic fringes are observed at $\theta = 8.0°$ and $\theta = 10.6°$. At the lower-angle fringe, the signal closely replicates the XMCD shape, suggesting a dominant absorptive contribution ($\Delta\beta$) with minimal reflection. At 10.6°, a sign inversion in $\Delta\delta$ appears. Between these fringes, the signal strongly resembles the dispersive component predicted by the Kramers–Kronig transform. The OM response (a3) shows a similar structure, but with significantly enhanced $\Delta\beta$ in the higher-angle fringe. This behaviour indicates increasing depth sensitivity and dynamic phase variation in the optical mode. The fitted curves (a4) show consistent $\Delta\delta$ between modes but a doubling of $\Delta\beta$ in OM, suggesting reflection from a dynamic interface within the CoFeB. While not universally true, but confirmed from simulations on this sample, the lower angle fringe in Co is more dominant in a homogeneously precessing layer, whereas the second arises from depth-dependence variations of the dynamics.

Ni (middle row, (b)): Ni is only present in the top layer of the trilayer, its dynamics are depth-uniform, and its magnetic response is primarily associated with the acoustic mode. In the XMCD spectrum (b1), we observe asymmetric Lorentzian peaks at 852 eV (L_3), 870 eV (L_2), and a third peak at 860 eV. These fits provide the imaginary part of the charge scattering factor. Subtracting PC and NC polarised spectra yields the XMCD signal, from which we extract the imaginary component of the magnetic scattering $\Delta\beta$, and subsequently obtain $\Delta\delta$ via K-K transformation. The RFMR colormaps for AM and OM (b2, b3) display similar behaviour: consistent amplitude profiles across angle, with no inversion or significant contrast between modes. This uniformity is reflected in the fitted $\Delta\beta$ and $\Delta\delta$ profiles (middle right), which show negligible difference between AM and OM, consistent with the expected in-phase precession of Ni moments in both modes.

Fe (bottom row, (c)): In the Fe XAS spectrum (c1), we observe asymmetric peaks at 707.1 eV (L_3) and 720.0 eV (L_2), with FWHMs of 0.5 eV below and 1.5–2.5 eV above the L_3 edge, depending on polarisation (PC vs NC). The AM RFMR map (c2) shows two peaks at $\theta \approx 8.0°$ and $\theta \approx 10.6°$, dominated by $\Delta\beta$. In contrast, the OM (c3) exhibits a similarly strong $\Delta\beta$ response, but a markedly enhanced $\Delta\delta$, consistent with reflection at a dynamical interface deeper in the stack. The fitted profiles (c4) reveal that the AM is almost purely absorptive, with minimal dispersive contribution. This supports a model where $\mathbf{R}_{\text{imag}} \propto \vec{k} \cdot \vec{M}$ dominates in AM, whereas OM gains a phase-sensitive contribution due to spatial variation in the precessing magnetisation. Notably, the extracted $\Delta\beta$ and $\Delta\delta$ are consistent with a Kramers–Kronig relationship despite being independently fitted.

A final observation concerns a subtle feature near 709 eV in Fe, visible only in RFMR reflectivity

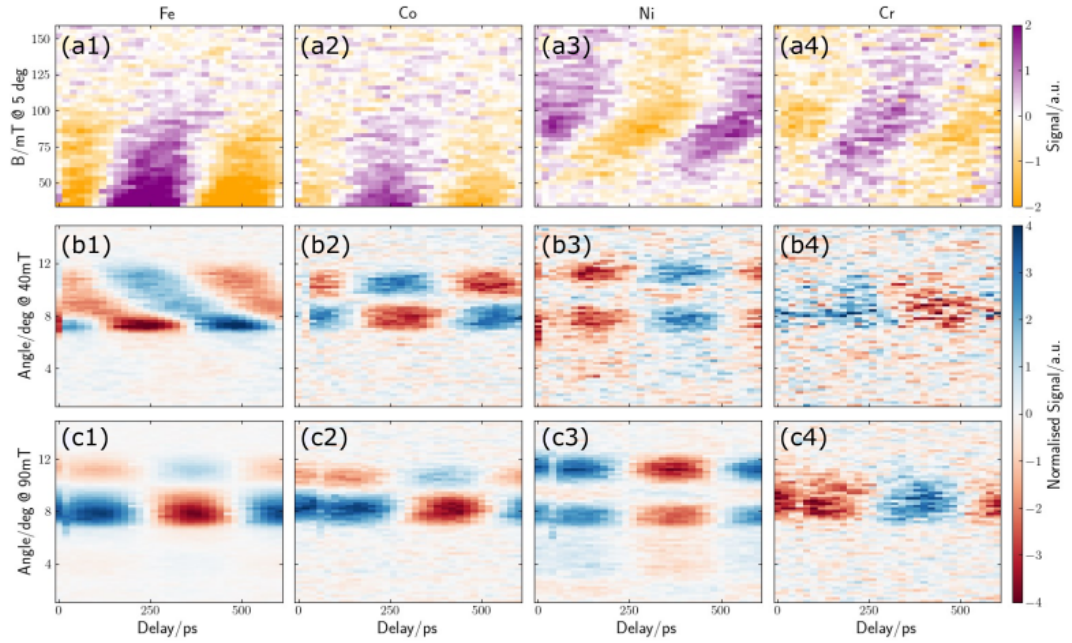


Figure 7.8: *RFMR measurements on CoFeB(5 nm)/Cr(2 nm)/NiFe(5 nm):* A 4×3 grid of experimental colormaps, each with the x-axis corresponding to a delay line sweep from 0 to 600 ps. Each column represents a different photon energy, corresponding to the L_3 absorption edges of Fe (707 eV), Co (777 eV), Ni (853 eV), and Cr (573 eV). The top row shows magnetic field scans at a fixed incidence angle of $\theta = 5°$, with the applied field swept from 40 to 170 mT. From the amplitude and phase profiles, we identify the optical mode at 40 mT and the acoustic mode at 90 mT. The middle row shows incident angle sweeps ($\theta = 2° \rightarrow 15°$) at the optical mode field (40 mT), while the bottom row shows equivalent angular scans at the acoustic mode field (90 mT).

at high incident angle where penetration depth is maximised, and only when the moments are anti-aligned with $\vec{k}_i$. This feature is not observable in TEY or FY spectra but emerges in fixed-Q_z energy scans (see Figure 4.1(c)). In NC polarisation, it manifests as a dip in intensity at 707 eV and an enhancement at 709 eV. While too subtle for XRR fitting, it may indicate an additional spin-split state induced along the seed layer of Si, potentially forming FeSi, and only via visible grazing-incidence magnetic reflectivity.

7.6 Mapping Depth-dependent Dynamical Structure in RFMR

The depth-dependent dynamical structure within the magnetic trilayer can be examined by varying $\mathbf{Q_z}$, with a focus on the interfacial offset observed in CoFeB. In Figure 7.8 we show the experimental data for the L_3 edges of Fe (1), Co (2), Ni (3), Cr (4). In (a) we show the field scan results, and in (b) we show the optical mode (40 mT) and in (c) we show the acoustic mode (90 mT). In Figure 7.9 the RFMR modelling framework is employed to interpret RFMR results, providing qualitative insights. In a coupled bilayer with identical layers precessing at a relative phase ϕ, three unique symmetry points ($\phi = 0°, 90°, 180°$) emerge for reflectivity. Using the structural parameters for the

t_{Cr}=2 nm sample and Fe L_3 scattering conditions, the simulated amplitude [Figure 7.9(b)] and phase [Figure 7.9(c)] profiles reveal two distinct peaks. Peak 'P1' arises from constructive interference between the surface and substrate layers in the absence of phase differences, while peak 'P2' requires a phase difference, indicating scattering from a dynamical interface. Furthermore, a non-collinear phase difference ($\phi \neq 0°, \pm 180°$) is necessary to change the dynamic phase.

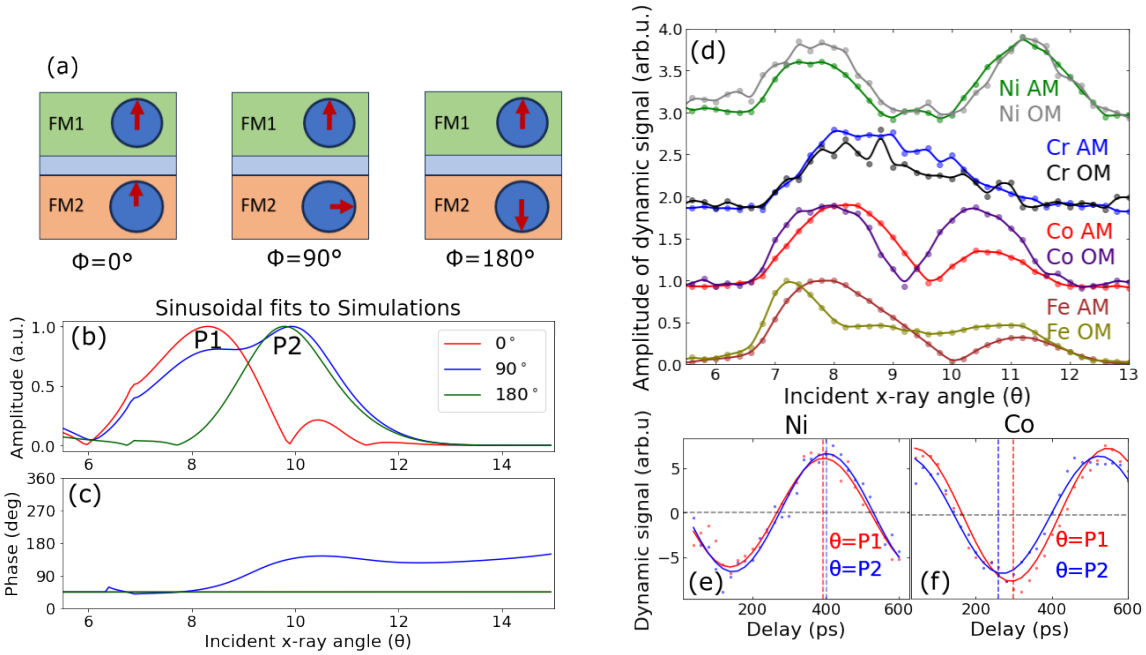
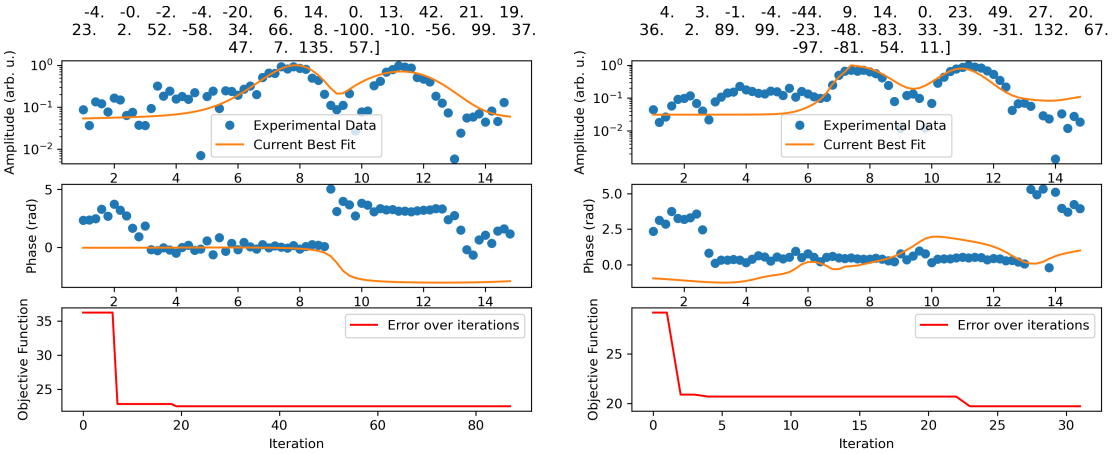


Figure 7.9: Interpreting RFMR measurements with reflectivity models to determine depth-dependent dynamics in NiFe(5)/Cr(2)/CoFeB(5). (a) In a spin-valve structure precessing with a relative phase ϕ, three unique symmetry points in reflectivity occur at ϕ = 0°, 90°, and 180°. In (b, c) we show simulated RFMR measurements from these points, with the fitted amplitude and phase to sinusoidal fits shown in (b) and (c), respectively, with amplitude peaks labelled as 'P1' and 'P2'. Calculations were done using the structural parameters for our spin-valve and the scattering factors for Fe per layer. (d) Experimental RFMR data across all elements in the spin-valve. With the fitted amplitude to the sinusoidal data plotted, showing the acoustic (AM) and optical (OM) modes. normalised and offset for clarity, highlighting distinct amplitude profiles across the Co and Fe measurements. (e, f) The individual delay scans at P1 and P2 for Ni OM (e) and Co OM (f) showing coherence in the Ni measurements and a phase difference in Co.

Moving to experimental results previously shown in Figure 7.8, the extracted amplitude from delay scans as a function of $\mathbf{Q_Z}$ is shown in Figure 7.9(d) for all elements in the spin-valve, with normalisation and offsets for clarity. By comparing these experimental profiles with the simulations [Figure 7.9(a, b, c)], intuition is gained without the need of an explicit model. The Ni measurements exhibit two amplitude peaks with no difference between acoustic and optical modes and no phase variation, suggesting uniform precession throughout the structure. Hence, these peaks must arise from the same scattering condition, likely due to amplitude modulation within the film [143]. This behaviour and its relation to interfacial offsets require further exploration.

Cr measurements display a single smooth peak with no mode-dependent variation.

Contrasting with the Co results, which show distinct amplitudes for each mode, which should not exist in a homogeneously precessing layer. The second peak in Co measurements is significantly stronger in the optical mode, as supported by the simulations [Figure 7.9(b)]. This is suggestive of enhanced contrast across an interface within the layer. A similar pattern is observed in Fe, with notable similarities between 'Fe AM' ($\phi = 0°$) and 'Fe OM' ($\phi = 90°$). However to determine whether these mode changes in Fe can be described accurately with a bilayer or trilayer model, a detailed XRMR analysis must take place.



(a) Optical mode (OM) best-fit parameters.

(b) Acoustic mode (AM) best-fit parameters.

Figure 7.10: Examples of the DE algorithm fitting the Ni L_3 AM and OM measurements.

Once we have identified our resonant modes, we can garner the information on the depth-dependent structure from recording delay scans (0-600 ps) across a sweep of $\mathbf{Q_z}$. This data will be fitted with our reflectivity model to extract best-fit parameters for the amplitude and phase of precession of each layer throughout the depth. In a complex system RFMR models naturally take in up to hundreds of free parameters, and due to the relatively weak signal probed in reflectivity, extreme caution must be taken to systematically remove any variables from the model that can be determined through pre-characterisation. Firstly, structural characteristics can be understood from XRR, in-particular by fitting XRR data across a whole sample series, including single thin film slabs for each layer, strict boundaries can be placed on the thickness, roughness, density, and alloy formation of each layer. This was done in this trilayer, with the XRR fit for the t_{Cr}=2 nm sample shown in Figure 7.3. From there, by conducting XRMR measurements on each edge, the ferromagnetic nature of each element can be understood, alongside the relevant magnetic roughness parameters (interfacial demagnetism, interfacial thickness, roughness), as shown in Figure 7.3. Next XMCD can be used to calculate absorption, with the KK transformation giving the dispersive component of the structure factor, here

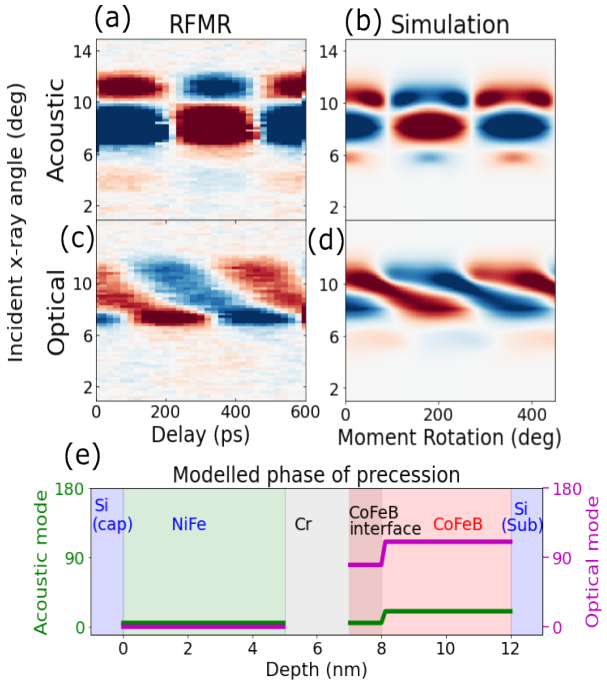


Figure 7.11: Depth-dependence of the Fe dynamics. (a, c) RFMR measurements on the Fe L_3 edge performed with a 2 GHz RF pump and phase modulation at ~3 kHz, showing data for (a) the acoustic mode at 90 mT and (c) the optical mode at 40 mT. (b, d) Simulations using the RFMR model, incorporating structural parameters from hard XRR fits and magnetic parameters derived from XMCD and XRMR measurements. These simulations provide depth-dependent profiles for the entire heterostructure as Fe is contained in both ferromagnetic layers. (e) Depth-dependent phase variations extracted from the simulations, illustrating the dynamic behaviour within the multilayer

shown in Figure 7.7.

With the structural parameters fit from hard XRR, the magnetic parameters fit from asymmetry, and the structure factors understood from XAS/XMCD, we can now generate reflectivity profiles that exclusively take in ψ, ϕ, ξ , f_{layer}, F_{10}, F_{11}, F_{1-1}, to fit the experimental data. For this we used the DE algorithm defined in Chapter 5.

In Figure 7.10 we show the results from the Ni AM and OM fits. However alongside this we show the objective function versus iteration. The particular set-up here resulted in approximately 30 iterations computed each day, so these algorithms were each left to fit for three days. You can see that the objective function does quickly begin to converge within a few hours, but the true result is not achieved before a few days of iterating.

The RFMR spectra for the acoustic and optical modes at the Fe L_3 edge, along with their corresponding fitted profiles, are presented in Figure 7.11. For the both modes, a bilayer model is insufficient to explain the results, the best model fit incorporates a CoFeB interfacial layer with a thickness of 0.8 nm.

This interfacial layer exhibits a phase offset intermediate between the NiFe and the bulk CoFeB,

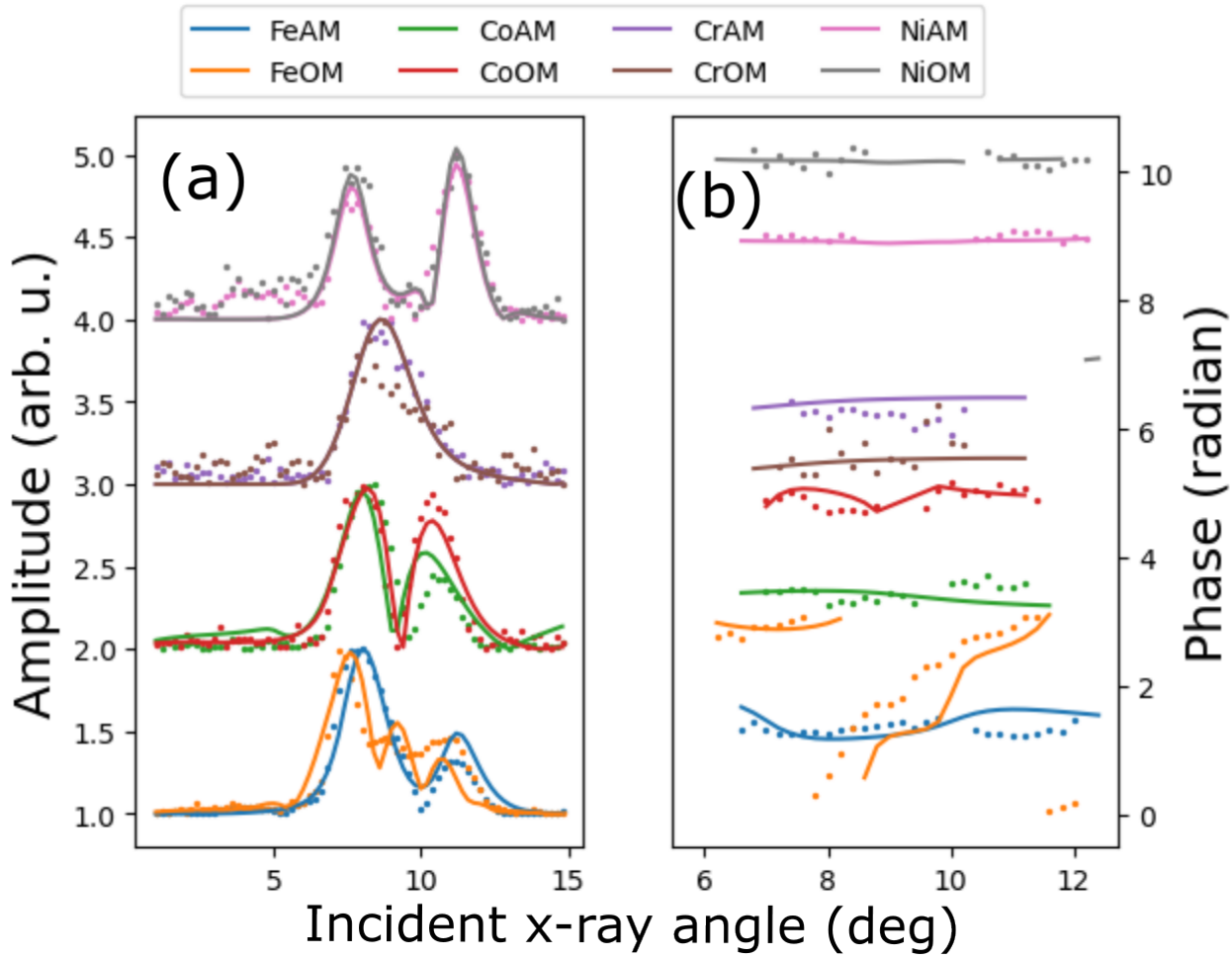


Figure 7.12: The amplitude and phase from the RFMR data presented in Figure 7.8 using equation (5.1), with the best-fits alongside, the depth-varying parameters are plotted in Figure 7.13.

in the acoustic mode measured at $-10°$ and $-20°$, respectively. In the optical mode, the interfacial and bulk CoFeB layers oscillate with phase offsets of $80°$ and $110°$ relative to the NiFe layer. The 2-nm Cr spacer in the spin-valve sample facilitates enhanced coupling, enabling strong dynamic interactions between the NiFe layer and the CoFeB/Cr interface.

7.7 Increasing Cr Thickness

The coupling between the NiFe and the CoFeB can be reduced by increasing the Cr thickness, this will however, leave the effective magnetic parameters of interfacial demagnetism, interfacial anisotropy, and magnetic proximity induced at the Cr interfaces. By conducting RFMR measurements on CoFeB(20 nm)/Cr(24 nm)/NiFe(20 nm)/Pt(3 nm), the role of indirect coupling between the NiFe and CoFeB has on the dynamics at the CoFeB/Cr and Cr/NiFe can be studied. Increasing the Cr spacer thickness beyond the diffusion length of Cr eliminates phase variations in the dynamic signal, resulting in uniform precession, as shown in Figure 7.14. Here we see the fitted amplitude and phase of the

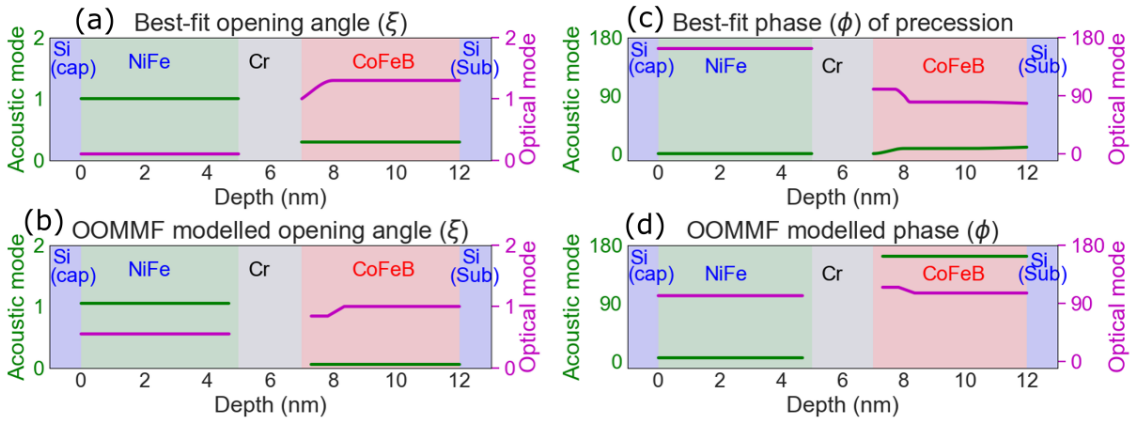


Figure 7.13: Comparison of dynamic magnetisation profiles across depth between best-fit RFMR models and OOMMF micromagnetic simulations. (a) and (b) show the depth-resolved opening angle (ξ) and precession phase (ϕ) obtained from fitting the RFMR experimental data. (c) and (d) show the corresponding profiles simulated using OOMMF for the acoustic and optical modes. All plots are aligned to a schematic cross-section of the NiFe/Cr/CoFeB stack, highlighting material boundaries. The agreement in trends validates the use of depth-dependent fitting to extract precessional dynamics, with deviations at the interface attributed to interlayer coupling and damping effects.

dynamic signal against $\mathbf{Q_z}$ for the t_{Cr}=2 nm and t_{Cr}=24 nm in the acoustic mode. Notably in t_{Cr}=2 nm, significant fringes exist in the amplitude signal, while in t_{Cr}=24 nm there is no observable variations in phase of the signal at any $\mathbf{Q_z}$.

This behaviour excludes magnetic proximity effects from the antiferromagnetic Cr as a significant contributor to the observed dynamics as they are, to first order, independent of the Cr thickness [140]. At Fe L_3 , the penetration depth of the X-ray is about 40 nm in our trilayers. As our control sample was CoFeB(20)/Cr(24)/NiFe(20) we further investigated by changing photon energy and hence increasing penetration depth, while intriguing and complex changes to the scattering factors were observed, we can confirm there was still no depth-dependence on the phase of magnetic precession.

7.8 Depth-Profile Induced by Dynamic Coupling

The ability to engineer depth-dependent dynamics is examined by analysing RFMR measurements near the optical mode at 40 mT, as shown in Figure 7.15. Repeated measurements were conducted at static fields ranging from 34 to 44 mT, allowing for the experimental extraction of the amplitude and phase of the Q_z-dependent dynamic signal.

In Figure 7.15(a) we plot the raw data for 6 static field values. In Figure 7.15(b) we show the fitted amplitude and phase vs $\mathbf{Q_z}$. At 40 mT, two distinct amplitude fringes are observed, one at $\theta = 8.0°$, As supported by [Figure 7.9(b)] this corresponds to constructive interference arising from the magnetic contrast between NiFe and CoFeB, and another at 10.6°, associated with magnetic contrast within

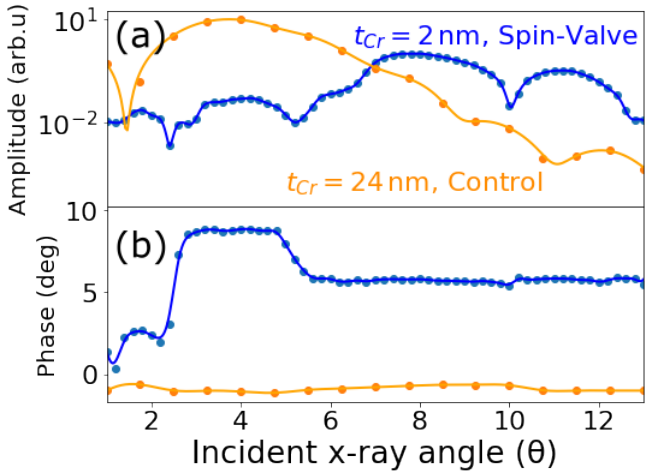


Figure 7.14: Amplitude and Phase of RFMR measurements taken on Cr=2 nm (blue) and Cr=24 nm (orange) in Fe acoustic. In a comparison with the schematics in Figure 7.9, we conclude the lack of phase variation in Cr=24 nm is due to the absence of depth-dependent variations.

the CoFeB layer. Deviations from resonance lead to changes in these features. Below 40 mT, the intensity of the 8.0° fringe diminishes, while above 40 mT, the 10.6° fringe decreases in intensity. Near resonance, a linear relationship emerges between phase and incident x-ray angle, highlighting coherent magnetic dynamics. However, further from resonance, as seen in the 34 mT data, a 180° phase inversion is observed between the maxima, indicating a shift in the interference conditions. These results underscore the nuanced interplay of magnetic contrast and dynamic coupling driven by spin-pumping near and far from resonance conditions.

To interpret the experimental results, depth-dependent dynamics were simulated using the RFMR model, with tightly restrained magnetic bounds. This model integrated structural parameters derived from hard XRR (Figure 7.3), magnetic profiles from XRMR (Figure 7.3), scattering factors from XMCD (Figure 7.7) initial dynamic estimates based on element-specific measurements (Figure 7.12), and the expected qualitative behaviour observed in Figure 7.6(a). Specifically, the NiFe layer was expected to undergo a 180° phase shift, while the CoFeB layer exhibited more subtle phase variations. The simulated amplitude and phase profiles of the dynamic signal, presented in Figure 7.15(c), qualitatively reproduced the experimental trends, including a smooth amplitude transition between peaks and a near-linear phase response close to resonance. The RFMR model employed a trilayer structure consisting of magnetically active layers: NiFe, interfacial CoFeB, and bulk CoFeB. Fe scattering parameters were used to simulate the dynamic reflectivity, and the results underscored the need for a separate fit of the interfacial CoFeB layer. This separate treatment was necessary to accurately capture the relative peak amplitudes and ensure consistency with the phase relationships of the bulk layers. Additional phenomena such as amplitude modulation, higher-order harmonics,

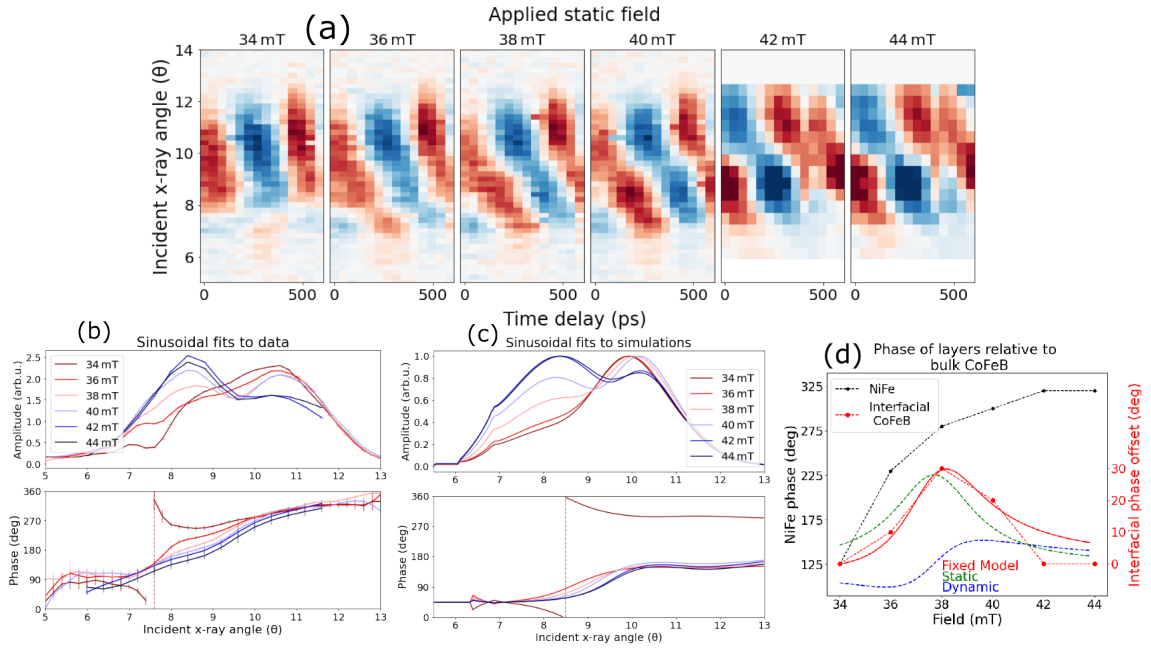


Figure 7.15: *Field dependence on the depth-profiling in the optical mode:* (a) By sweeping the applied field across the optical mode, RFMR measurements on the Fe L_3 edge can be used to track the phase variation of each layer within the thin film during resonance. (b) Fitted amplitude and phase of the sinusoidal data taken during the measurement. (c) Using the RFMR model from Figure 7.11, we simulate the trilayer to co-fit phase and amplitude, and determine the depth-dependent profile, with the amplitude and phase of the simulated dynamic signal shown. (d) For each static field, the best-fit values for the relative phase of the NiFe (blue) and interfacial CoFeB (red) to the bulk CoFeB, taken from the simulations are shown as data-points. Overlaid are the solutions to the linearised macrospin LLG, with the dynamic (blue) and static (red) contributions separately solved.

precessional cone canting, and elliptical precession were also considered. However, these contributions were found to have negligible influence on the fit quality, emphasizing the robustness and simplicity of the model.

To simplify the analysis, the simulation was reduced to two free parameters: the relative phase between NiFe and bulk CoFeB, and the relative phase between interfacial CoFeB and bulk CoFeB. The fitted parameters and their evolution during FMR are presented in Figure 7.15(d). As expected, NiFe exhibited a 200° phase shift, whereas interfacial CoFeB displayed a complex phase profile. These observations align with the solutions to the linearised macrospin LLG equation, as shown in Figure 7.15(d), which illustrate the hypothesised roles of static exchange (red) and dynamic exchange (blue) interactions.

The best-fit parameters from the trilayer model [Figs. 7.11(e) and 7.15(c)] allowed for an estimation of the interfacial CoFeB length, in the CoFeB sink. The resulting value, ~0.8 nm, is significantly larger than the structural roughness in the sample (≈0.3 nm) and is interestingly consistent with theoretical predictions for coherence length in 3D transition metals such as Fe, Co, and Ni [128, 161, 170]. Simulations with continuous $1/e$ decay forms [150] were tested but did not improve the fit

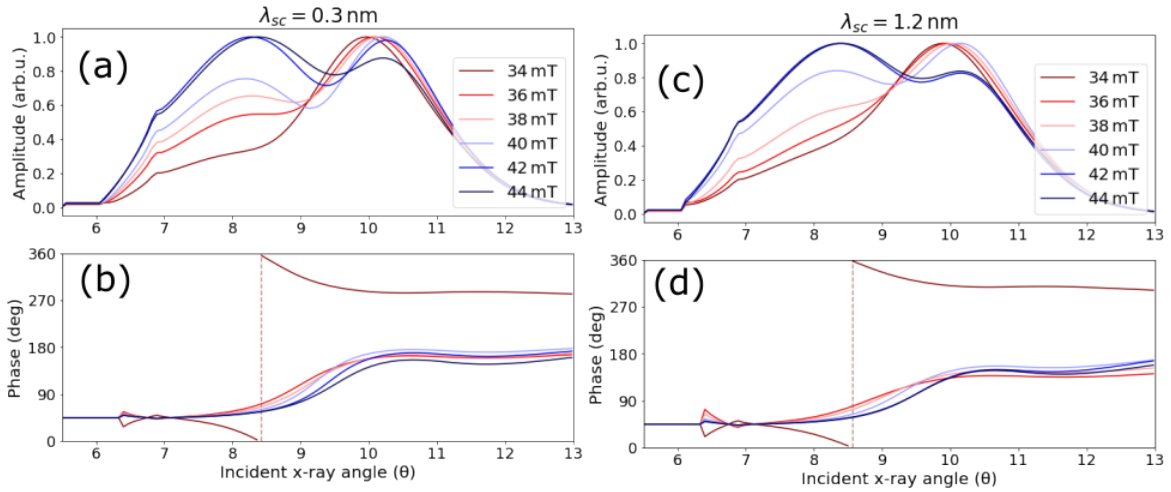


Figure 7.16: A visualisation of the sensitivity analysis into the thickness of the interfacial CoFeB layer. This parameter was found to govern the fringe periodicity in our model, and when reduced to the structural roughness, the simulated fringes disagreed with experimental observations. Sensitivity analysis estimates that the interfacial CoFeB thickness, is approximately 0.8 ± 0.3 nm.

quality and were excluded for simplicity. The interfacial CoFeB phase lag can likely be attributed to dynamic coupling rather than alternative mechanisms, based on several key observations. Firstly, XRR analysis confirmed smooth interfaces with no evidence of alloying, ruling out structural artifacts [103]. Secondly, the phase lag was confined to the CoFeB layer; more precisely, to the Cr/CoFeB interfacial region. The absence of the effect in the Ni data ruled out static coupling between the ferromagnetic layers [27, 31]. Further, increasing the Cr spacer thickness to 24 nm in the control sample eliminated the depth-dependent phase lag, ruling out magnetic proximity effects from the antiferromagnetic Cr spacer [77].

7.9 Sensitivity Analysis

Our RFMR results allowed for estimations into the CoFeB interfacial layers thickness. Figure 7.16 illustrates the simulated effects of varying interfacial region, in the manner of an exponential decay. For $t_{interfacial}$ = 0.3 nm, amplitude fringes are sharp and distinct, while for $t_{interfacial}$ = 1.2 nm, fringes broaden and smear. However it was observed that $t_{interfacial}$ had negligible impact on the phase behaviour. The best fit value for our data was 0.8 nm in the optical mode. The variations in this value from sweeping fields across an FMR mode were too subtle too be resolved, reinforcing that observed variations in the dynamic signal arise primarily from relative phase changes at the interface rather than intrinsic modifications to $t_{interfacial}$.

Chapter 8

Depth Profile of Complex Heterostructures

The Landau–Lifshitz–Gilbert equation governs magnetisation dynamics in all magnetic media, and its macrospin solution yields tractable analytical results, such as the Kittel equation. However, this approach fails to capture the full richness of behaviour in systems where the magnetic environment varies significantly with position, such as in complex heterostructures. This Chapter addresses this challenge by combining the results from all previous Chapters and applying them to such a system. In such cases, the LLG equation admits a broader family of solutions (depth-localized or hybridized modes) in which certain layers exhibit unique dynamic response, or where a depth-dependent variation in phase, cone angle, or precession axis causes mutual cancellation of opposing contributions. These effects can render a mode invisible to inductive techniques such as VNA-FMR, which are sensitive only to the net dynamic susceptibility integrated over the film volume [171].

The environment for this type of depth-dependent modal structure requires complex heterostructures. In this work, we apply RFMR to investigate the depth-profile of distinct FMR modes in a chiral heterostructure, $[\mathrm{Ta/CoFeB/MgO}]_4$. While each FM layer in this heterostructure is chemically identical, the unique magnetic environment arising from the interactions with adjacent FM layers, alongside the complex interplay of interfacial effects [47] and spin-orbit interactions arising from the Ta and MgO interfaces [172] provides ample opportunities for complex dynamic behaviour [173, 150].

The samples were fabricated by collaborators at Beijing University with a controlled wedge profile, enabling systematic thickness-dependent studies. Preliminary characterisation was performed using SQUID-VSM (OOP), angle-resolved VSM, angle-resolved VNA-FMR, MFM at remanence, XMCD, and XRMR. These revealed a spin-reorientation transition from out-of-plane to in-plane magnetisation at $t_{CoFeB} \gtrsim 1.45\,\mathrm{nm}$ [174, 41], as the effective PMA is overcome by shape demagnetisation at this thickness [175], above which a strong in-plane FMR mode dominates. A weak Dzyaloshin-

skii–Moriya interaction was inferred from the presence of chiral domain walls at remanence [46], although attempts to resolve these via REXS were inconclusive. UBERMAG simulations, based on experimentally extracted parameters, accurately reproduced the SRT at ≈ 1.5 nm and were consistent with the MFM, VNA-FMR, and VSM results. Subsequent simulations focused on the depth profiles of the resonant modes and revealed the existence of complex precessional behaviour that is not captured by the Kittel formalism and is largely invisible to VNA-FMR. The resulting depth-profiles were found to be highly sensitive to dipolar fields and demagnetism when t_{FM}=1.5 nm, hence a novel implementation of structural roughness was incorporated into UBERMAG to better interpret that spatial variations in depth-profiles around the SRT.

We evaluated the analytical expression for the dynamic longitudinal susceptibility χ_{xx}, and found that certain eigenmodes exhibit minimal χ_{xx} despite coherent precession across the structure. This accounts for the absence of observable signal in VNA-FMR measurements. Moreover, we observed that even small depth-dependent variations in the magnetisation direction ($\theta(z)$) significantly shift the local resonance condition when the static field is along the magnetisation direction ($\theta_H - \theta(z)) \approx 0^\circ$. However, by introducing a finite tilt θ_H away from any easy-axis direction, a degeneracy emerges in the resonance conditions across the structure, restoring coherence and enhancing the collective response.

While invisible in our VNA-FMR set-up, we report the experimental observation of two unique FMR modes within this system via RFMR, characterised by distinct differences in their resonant condition and effective magnetic anisotropy [176]. Our results show that the lower-energy mode exhibits its strongest precession with a directly out-of-plane static field (θ_H=0°), whereas the higher-energy mode reveals a canted easy axis, with the maxima in dynamic signal occurring when the static field deviates 22° from the surface normal. By leveraging RFMR's depth-resolved capabilities, we further attribute this canting to a reduction in the precessional opening angle at the MgO/CoFeB interface, varying cone direction with depth, and a phase lag throughout the depth, suggesting that interfacial effects play a significant role in shaping the dynamic response of the system. We further attribute this complex modal structure to the SRT by conducting a thickness-dependence analysis across multiple samples of varying t_{CoFeB}. Here we observe that the adequate models to describe the XRMR and RFMR profiles go from homogeneous→ linear $\theta(z)$ and $\phi(z)$ with depth → complexity beyond our experimental confidence with decreasing thickness. Here we explore if we can exploit this depth-dependence via tuning the temperature. Micromagnetic simulations confirm the existence of complex, non-elliptical precession trajectories in ultra-thin film modes arising from the confinement of the macrospin to a reduced volume. These ultra-dense trajectories correspond to stable periodic

orbits, time-periodic solutions of the LLG equation under periodic driving. Since RFMR measures only the component of the oscillation along the beam propagation direction, different orbits can appear degenerate. To resolve this, we performed RFMR using all three principal polarisation channels (PC, LH, LV). By co-fitting the resulting spectra, and investigating their non-driven frequency response, we reconstructed the full three-dimensional precessional vector as a function of depth.

8.1 Motivations

While $[\text{Ta/CoFeB/MgO}]_N$ heterostructures are of interest for magnetic tunnel junctions [177], and when repeated multiple times can host a diverse range of topological phases [178], they possess significant complexity to analyse, hence standard VNA-FMR analysis is ill suited to characterise these depth-dependent resonant modes when N>2. The process outlined in the following sections attempts to go beyond the simple analytical solution for Kittel modes to prepare the reader for the complex VNA-FMR and RFMR experimental results for our $N = 4$ films. We begin by motivating with UBERMAG-based simulations of the multilayer stack. Experimental measurements (discussed further in Section 8.4) were used to estimate the structural and magnetic parameters, with depth-dependent refinements guided by literature.

Table 8.1: Magnetic and structural parameters used for each material layer in the N=4 heterostructure.

Layer	t (nm)	M_s (A/m)	A (J/m)	α	K_u (J/m^3) [0, 0, 1]	D (J/m^2)
Ta	3.0	0	1.0×10^{-18}	1.0×10^{-4}	0	0
CoFeB (/Ta)	0.5	1.2×10^{6}	1.0×10^{-11}	0.04	6.0×10^{5}	1.2×10^{-3}
CoFeB (bulk)	t_{Bulk}	1.1×10^{6}	1.3×10^{-11}	0.02	2.0×10^{5}	1.2×10^{-3}
CoFeB (/MgO)	0.5	1.2×10^{6}	1.0×10^{-11}	0.04	6.0×10^{5}	1.2×10^{-3}
MgO	2.0	0	1.0×10^{-18}	1.0×10^{-4}	0	0

The simulated structure consists of four repeats of [Ta(3 nm)/CoFeB/MgO(2 nm)], where each CoFeB layer is subdivided into three regions: 0.5 nm interfacial layers and a t_{Bulk} central region. The full stack is discretised into a $20\times20\times52$ mesh with a cell size of $3\times3\times0.5$ nm^3. Material parameters are assigned layer-wise to capture depth-dependent magnetic properties, including variations in M_s, A, α, K_u, and interfacial DMI. Figure 8.1 shows the simulated ground state of the system. By reducing t_{FM} below 1.50 nm (corresponding here to $t_{\text{Bulk}} < 0.50$ nm), we observe a transition in the easy axis of magnetisation from in-plane to out-of-plane. This spin reorientation transition arises from the competition between exchange, anisotropy, demagnetisation, and DMI within the model. In real systems, this effect is further enhanced by structural roughness, which is not included in this idealised model.

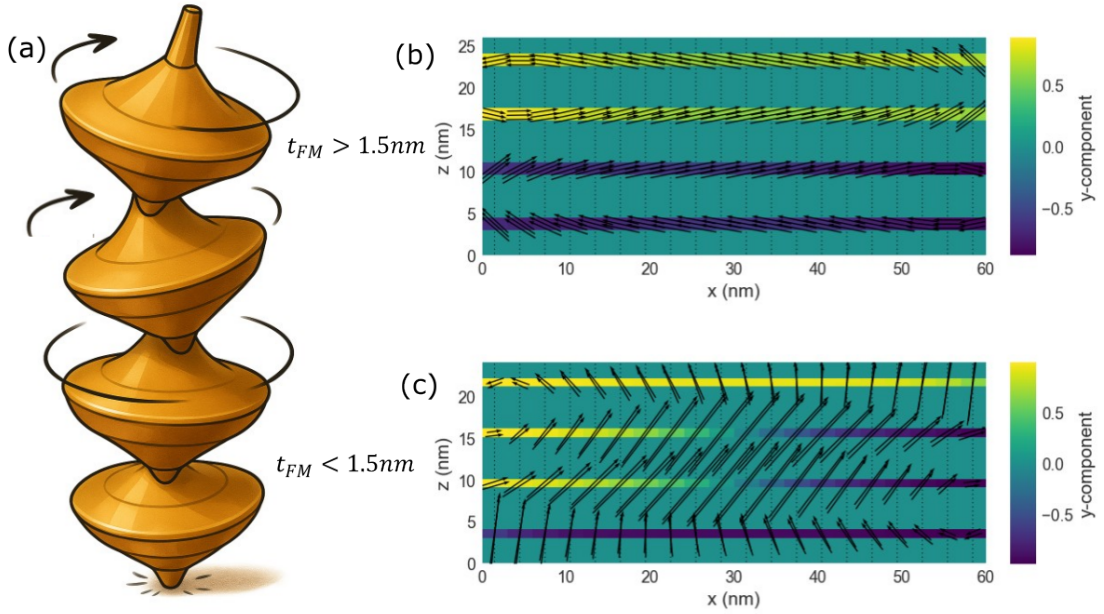


Figure 8.1: (a) Cartoon illustrating potential non-linear dynamics in N=4. (b, c) Simulated spin structures in the N=4 heterostructure. Increasing t_{bulk} above 0.5 nm ($t_{\text{CoFeB}} > 1.5$ nm) with H_0=8 mT induces a transition from OOP to IP ground state even under weak OOP field.

8.2 Susceptibility in Complex Heterostructures

In magnetic multilayers, such as the [Ta/CoFeB/MgO]$_4$ stack studied here, weakened interlayer coupling and spatially varying anisotropy lead to depth-dependent magnetisation dynamics [179, 180]. These are not captured by a single macrospin model but require a depth-resolved treatment of the magnetic response. The LLG can be extended to include N coupled equations. Here we build upon the results from FMR on tetra layer Cr Cl_3 vdW magnets to include how spatial variations in M_s, K_u can produce unique depth-dependent modes with differing susceptibility [181], and hence signatures in VNA-FMR. Beginning from considering the LLG for 4 coupled oscillators

$$\frac{d\hat{\boldsymbol{m}}_A}{dt} = -\mu_0\gamma\,\hat{\boldsymbol{m}}_A \times [H_0\hat{\boldsymbol{z}} - J\hat{\boldsymbol{m}}_B - M_s(\hat{\boldsymbol{m}}_A \cdot \hat{\boldsymbol{x}})\hat{\boldsymbol{x}}]\,, \tag{8.1}$$

$$\frac{d\hat{\boldsymbol{m}}_B}{dt} = -\mu_0\gamma\,\hat{\boldsymbol{m}}_B \times [H_0\hat{\boldsymbol{z}} - J\hat{\boldsymbol{m}}_A - J\hat{\boldsymbol{m}}_C - M_s(\hat{\boldsymbol{m}}_B \cdot \hat{\boldsymbol{x}})\hat{\boldsymbol{x}}]\,, \tag{8.2}$$

$$\frac{d\hat{\boldsymbol{m}}_C}{dt} = -\mu_0\gamma\,\hat{\boldsymbol{m}}_C \times [H_0\hat{\boldsymbol{z}} - J\hat{\boldsymbol{m}}_B - J\hat{\boldsymbol{m}}_D - M_s(\hat{\boldsymbol{m}}_C \cdot \hat{\boldsymbol{x}})\hat{\boldsymbol{x}}]\,, \tag{8.3}$$

$$\frac{d\hat{\boldsymbol{m}}_D}{dt} = -\mu_0\gamma\,\hat{\boldsymbol{m}}_D \times [H_0\hat{\boldsymbol{z}} - J\hat{\boldsymbol{m}}_C - M_s(\hat{\boldsymbol{m}}_D \cdot \hat{\boldsymbol{x}})\hat{\boldsymbol{x}}]\,. \tag{8.4}$$

In the above equations, the unit vectors (e.g., $\hat{\boldsymbol{m}}_A$) refer to the direction that a given macrospin is pointing, and the subscript references the individual layer. Here H_0 is the externally applied magnetic

field. The interlayer exchange field strength is denoted by J. The saturation magnetisation is denoted by M_s. The last term in each equation of motion is the demagnetisation field from thin-film shape anisotropy. It should be noted that, for the tetralayer, layers B and C experience two separate exchange fields owing to the fact that the interior layers are coupled to two layers each, while the surface layers are only coupled to one layer.

The transverse dynamic susceptibility can be generalised to include spatial variation across the film thickness z as:

$$\chi_{xx}(\omega, z) = \left| \frac{M_S(z)\left[H_0\cos(\theta(z)-\theta_H) + M_{\text{eff}}(z)\cos(2\theta(z))\right]}{\left[H_0\cos(\theta(z)-\theta_H) + M_{\text{eff}}(z)\cos^2\theta(z)\right]\left[H_0\cos(\theta(z)-\theta_H) + M_{\text{eff}}(z)\cos(2\theta(z))\right] - \dfrac{\omega^2}{\gamma^2}} \right|, \tag{8.5}$$

which extends the macrospin result of Lindner [176] to systems with spatially inhomogeneous $M_S(z)$, $M_{\text{eff}}(z)$, $\theta(z)$.

In the macrospin model, $\theta(z)$ can be calculated by setting the net torque on each layer to zero. Layer B and C should have very similar θ, however due to the asymmetric interfaces as the MgO/CoFeB and CoFeB/Ta, the same generalization can not be applied to layers A and D, as seen in the micromagnetic results in Figure 8.1. However for the simplicity of this derivation, $\theta(z)$ is approximated to be linear with z, as illustrated in Figure 8.3.

To interpret the complex VNA-FMR spectra observed in micromagnetic simulations (see Sec. 8.3) and the further experimental results (see Sec. 8.4.2), we analytically model the spin dynamics of a four-layer system, each layer treated as a macrospin coupled to its nearest neighbours via a weak interlayer exchange or dipolar coupling J [182, 183]. This yields a 4×4 linear eigenvalue problem describing the collective dynamics of the system under periodic RF driving.

Assuming identical magnetic parameters for all layers, the coupled-mode equation in the small-angle limit becomes:

$$\mathbf{M} = \omega_0^2\mathbb{I} + J\gamma^2 \begin{pmatrix} 0 & 1 & 0 & 0 \\ 1 & 0 & 1 & 0 \\ 0 & 1 & 0 & 1 \\ 0 & 0 & 1 & 0 \end{pmatrix}, \tag{8.6}$$

where $\omega_0 = \gamma(H_0 + M_{\text{eff}})$ is the uncoupled resonance frequency, and γ is the gyromagnetic ratio. Solving this yields four eigenfrequencies ω_n and associated eigenvectors $\vec{v}_n$, each describing the depth profile of a resonant mode.

This is a well-known problem in solid-state physics and can be solved analytically for tridiagonal Toeplitz matrices [184]. In an N-layer chain with uniform interlayer coupling J, the linearised system forms a tridiagonal matrix whose eigenfrequencies follow the general expression:

$$\omega_n^2 = \omega_0^2 + 2J\gamma^2 \cos\left(\frac{n\pi}{N+1}\right), \quad n = 1, \ldots, N, \tag{8.7}$$

where $\omega_0^2 = \gamma^2 (H_{\text{eff}})^2$ is the uncoupled layer resonance frequency. The corresponding eigenvectors $\vec{v}_n$ define the spatial mode profiles across the stack.

For $N = 4$, the four normalised eigenmodes can be identified as:

- **Uniform mode** ($n = 1$) : all layers precess in phase: $\vec{v}_1 \propto [1, 1, 1, 1]$.
- **Twisted mode** ($n = 2$) : smooth phase winding: $\vec{v}_2 \propto [1, a, -a, -1]$, with $a > 0$.
- **Antisymmetric mode** ($n = 3$) : antisymmetric about the center: $\vec{v}_3 \propto [1, 0, 0, -1]$.
- **Folded mode** ($n = 4$) : higher-order standing wave: $\vec{v}_4 \propto [1, -1, -1, 1]$.

Each eigenvector $\vec{v}_n$ is complex, encoding both amplitude and phase with depth. These modes are shown in Figure 8.2 (a), where their field-dependent resonance frequencies are shown as lines and extracted from the mode-resolved susceptibility spectra ($\log_{10}(\text{Im}[\chi_{total}])$).

These interlayer modes arise from weak coupling $J \ll A_{\text{ex}}/d^2$, distinct from perpendicular standing spin waves (PSSWs) which require strong intralayer exchange and appear at much higher frequencies [185]. This allows the N=4 system to be treated as a macrospin chain.

These eigenmodes span the complete solution space of the linearised Landau-Lifshitz equation, and any linear non-eigenmode, such as a precession with a depth-dependent phase lag [16], can be expressed as a linear combination of them. The FMR intensity is considered following Ref. [186], and is defined as

$$I = \frac{\left[\int_0^d m_x(z)\, dz\right]^2}{\int_0^d \left(\frac{m_x^2(z)+m_z^2(z)}{2M}\right) dz}, \tag{8.8}$$

where m denotes the time-dependent magnetisation component in each layer, z is the depth coordinate, and d is the total thickness of the sample. At fixed excitation field amplitude, the FMR intensity is expected to scale with the magnetisation volume. However, the contribution of each mode to the longitudinal susceptibility χ_{xx} is determined by its projection onto the uniform driving field $\vec{h}_{\text{RF}} \propto [1, 1, 1, 1]$ [187, 188, 189].

The results of the calculations in Figure 8.2 (a) provide theoretical support for the complex spectral features observed in the simulated VNA-FMR maps shown in Figs. 8.4(a) and 8.5(a), particularly

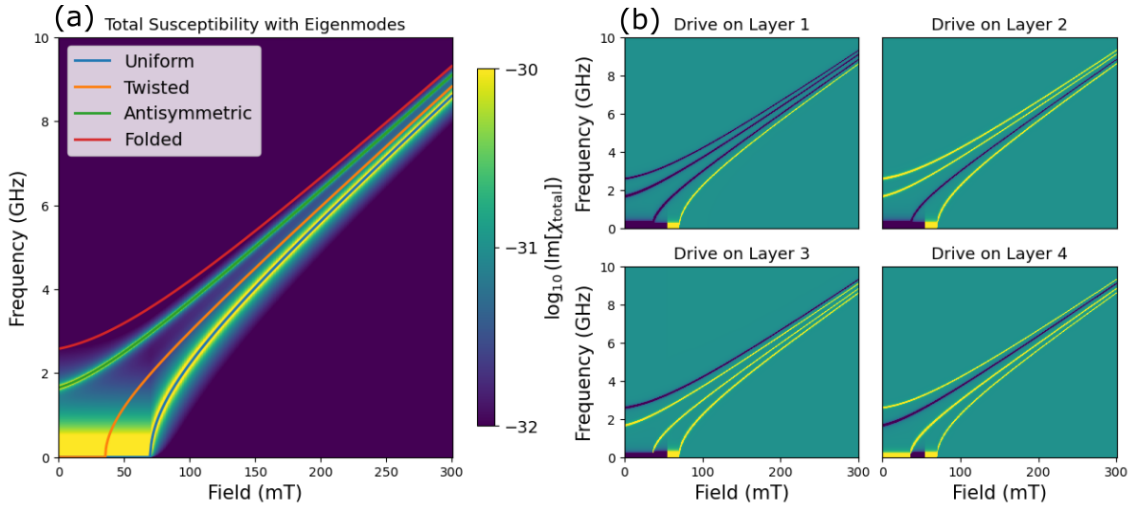


Figure 8.2: (a) Analytical solution of the field–frequency dependence of the total transverse susceptibility $\log_{10}(\mathrm{Im}[\chi_{xx}^{\mathrm{total}}])$ from eq. (8.5) in a four-layer coupled system. Overlaid curves show the peak frequencies of the uniform, twisted, antisymmetric, and folded eigenmodes. However by resolving the layer-specific eigenmodes (b), individual contributions become visible. Plotted is the layer-specific values for the eigenmodes projected onto H_{RF} that allows for negative values, as opposed to normally the measured χ_{xx} is $\langle \nu_n | H_{RF} \rangle$).

within the low-field regime where multiple modes coexist. The values in the simulation are $\gamma = 2\pi \cdot 28 \times 10^9 \frac{rad}{s \cdot T}$, $M_{eff} = 0.2\,T$, $J_1 = 0.005\,T$, $J_2 = 0$, $\theta_H = 0°$ (OOP), $\theta = 90°$ (IP, orthogonal to H_{RF}), $\alpha = 0.01$. Although four eigenmodes are present, only two exhibit significant absorption due to their overlap with the spatially uniform drive field: (i) the fully in-phase uniform mode, and (ii) a twisted mode exhibiting partial cancellation. The remaining two modes, while formally present, contribute negligibly, these are up to 30 orders of magnitude weaker in this theoretical model, due to destructive interference in their net RF response.

By decomposing the susceptibility into layer-resolved components, all four eigenmodes become fully discernible, highlighting the potential of RFMR to isolate otherwise obscured resonances. These eigenmode calculations thus provide an essential baseline for interpreting the experimental VNA-FMR spectra presented in Figure 8.9, where visibility is constrained by weak mode amplitudes and measurement noise [190].

It should be emphasized that only OOP eigenmodes were computed. In realistic experimental conditions, where magnetic anisotropy, structural roughness around a thickness-driven SRT, spatially non-uniform RF driving fields, and slight misalignments in applied field direction (which are unavoidable), the emergence of depth-dependent magnetisation orientations becomes highly relevant [191]. This scenario is further illustrated in Figure 8.3, which plots the total susceptibility $\chi_{xx}(\omega)$ for a system with a depth-graded equilibrium magnetisation angle ($\frac{d(\theta(z))}{dz} \neq 0$). The gradual angular offset mimics the onset of perpendicular anisotropy characteristic of systems near the spin-reorientation

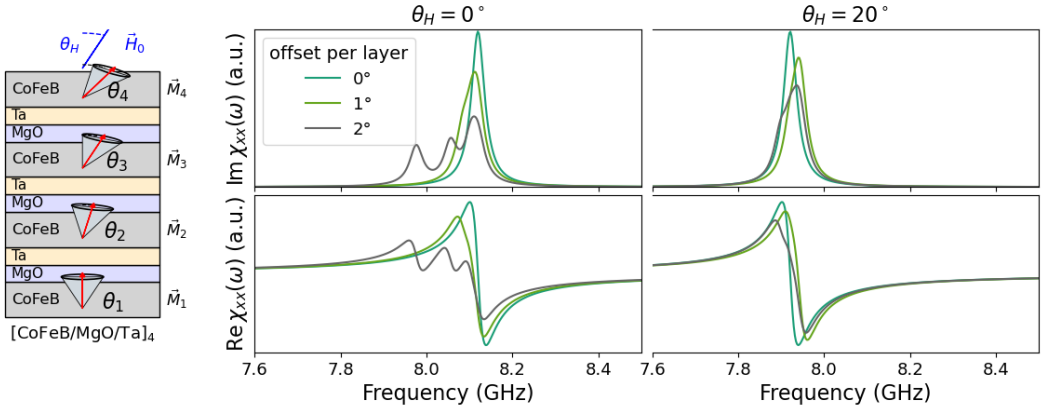


Figure 8.3: Analytical transverse susceptibility $\chi_{xx}(\omega)$ for a four-layer system with increasing depth-dependent magnetisation tilt, shown for two applied field angles. Here we have isolated the uniform mode's contribution to $\chi_{xx}(\omega)$ and set J=0. Layer-to-layer orientation offsets mimic variations near the spin reorientation transition in N=4, even with 1° per layer, there is suppression of net response due to destructive interference between non-collinear precessions. When the field is applied along the easy-axis, small changes in the magnetisation orientation result in significant changes to the resonance peak, however by tilting the field off the preferential axis, a degeneracy is formed, simplifying the structure, as what is seen in the results section Figure 8.14.

transition (SRT) and is illustrated in the left of the Figure. This depth-dependent variation introduces mode splitting and reduces spectral intensity by dephasing interlayer precession. In particular, if the magnetisation offset per layer is 0°, a coherent strong resonance condition is observed in the susceptibility at ≈8.1 GHz. However, the application of even 2° reduces the intensity at this condition to less than a third of the aligned case. Further, unique features emerge at other frequencies, each corresponding to a layer's individual resonance condition. The application of a static field tilted at $\theta_H = 20^\circ$ restores coherence across the stack, recovering the suppressed spectral weight as all layers are driven out of their easy axes. This effect is quantitatively captured by the depth-dependent form of Eq. (8.5).

8.3 Modal Structure in Complex Heterostructures

Moving from the analytical macrospin model of the susceptibility of $[Ta/CoFeB/MgO]_4$. We now turn our focus onto the micromagnetic results. VNA-FMR was simulated on this structure in the same manner as described in section 5.7

Here, the relaxation process was not performed under a static OOP configuration, but rather initiated at time $t = t_0$ with a time-dependent applied field characterised by $H(t) = (0, H_{\mathrm{RF}} \sin(\omega t + \phi), H_{\mathrm{DC}})$, effectively freezing the precessional phase during initialization. This approach prevents large-angle motion during the onset of RF excitation. The system was then driven by an IP RF field of frequency ω and amplitude $H_{\mathrm{RF}} = 80\,\mu\mathrm{T}$, applied concurrently with a static OOP bias field. The field

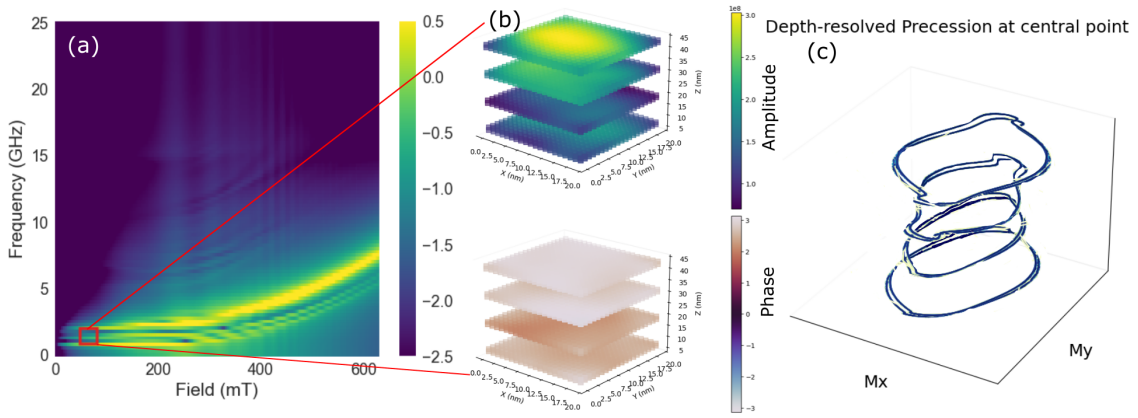


Figure 8.4: Demagnetism driven localised susceptibility and precessional dynamics in $N = 4$ (a) Simulated VNA-FMR spectral map for a N=4 with a 1.5 nm CoFeB layer, driven under an OOP static field. Multiple resonant modes are observed as sharp peaks in the power spectral density. (b) Spatially-resolved magnetisation response at the selected off-resonance pixel (highlighted in the red box in (a)), showing the spatial distribution of FFT amplitude (top) and phase (bottom) at $\omega = 1$ GHz and $H_0 = 60$ mT. (c) A tornado plot showing the time-domain trajectory of the magnetisation vector (m_x, m_y, m_z) across depth, evaluated at the central (x, y) location. Each trace corresponds to a single depth sub-layer, illustrating the complex precessional motion throughout the multilayer stack.

was applied exactly OOP to simplify the effect of demagnetism on creating degenerate eigenmodes. The magnetisation dynamics were simulated over a total time of 9 ns with a temporal resolution of 50 ps. Spectral features were extracted via FFT at each spatial point for the components m_x, m_y, and m_z.

VNA-FMR in Figure 8.4(a) was calculated using the parameters from the table 8.1 and by setting H_{RF} to 0 mT and recording the relaxation process, and converting the time-domain data to frequency-domain via an FFT.

Once the resonance modes were characterised, a three-dimensional reconstruction of the magnetisation was performed by fixing the external field and excitation frequency to a chosen on- or off-resonance condition. The system was driven at this frequency, and the time-domain magnetisation data were recorded for each simulation cell. A spatially resolved FFT was then applied to extract the frequency-domain response. The middle panel of Figure 8.4(b) displays the resulting FFT amplitude at 1 GHz (the driving frequency) but this technique can equally be used to analyse non-driven spectral contributions. Notably, the results reveal a rich dynamic response even at frequencies not aligned with VNA-FMR resonance peaks, demonstrating that complex, non-Kittel-type modes can be sustained in complex heterostructures.

In the right panel of Figure 8.4(c), we present the time-domain magnetisation trajectories for the central x-y cells, sliced along the z-axis (i.e., the 10×10 cell at the centre of the 20×20 in-plane grid). Importantly, the precession profiles differ between layers and are not uniformly elliptical.

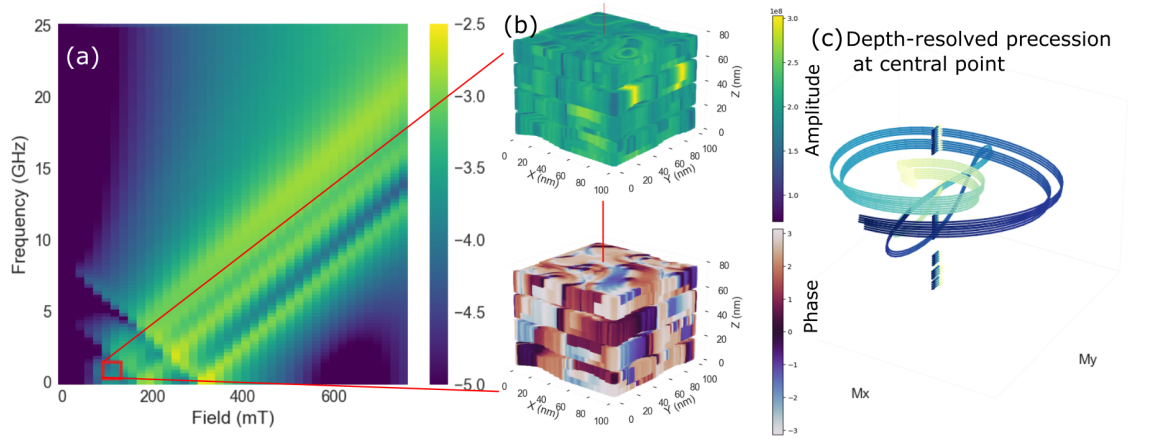


Figure 8.5: Structural roughness driven localised susceptibility and precessional dynamics in $N = 4$ A novel implementation of Perlin Noise into interfaces in N=4 can allow for localised susceptibility, in particular near an SRT, where thicknesses and distances between adjacent FM layers becomes exceedingly important in determining their magnetisation direction. (a) Simulated VNA-FMR spectral map for a N=4 with a 0.5 nm CoFeB bulk layer, driven under an OOP static field. (b) Depth-resolved magnetisation response at the selected off-resonance pixel (highlighted in red), showing the spatial distribution of FFT amplitude (top) and phase (bottom) at $\omega = 1$ GHz and $H_0 = 60$ mT. (c) A tornado plot showing the time-domain trajectory of the magnetisation vector (m_x, m_y, m_z) across depth, evaluated at the central (x, y) location.

Instead, each trajectory corresponds to a stable periodic orbit, described by Flouquets Theorem as a class of solutions to the LLG equation under periodic driving [192], highlighting the diversity of depth-dependent dynamic modes in these systems.

The depth-dependent magnetisation dynamics observed in this system are strongly influenced by dipolar fields and demagnetisation effects. However, the central aim here is to identify sources of depth dependence that may be experimentally confirmed via RFMR, where the signal lies along the scattering plane reducing the effect of non-uniform excitation, and the sample is centred to reduce demagnetism effects. In particular, near the SRT, the thickness of each ferromagnetic layer (t_{FM}) and the interlayer spacing become critical, such that even modest structural roughness can significantly affect the local magnetic environment.

While Ubermag does not natively support structural roughness, its Python-based architecture allows for extensive customisation. In this PhD, a novel implementation was developed to introduce interfacial roughness using *Perlin noise*, a procedural algorithm commonly used in terrain generation due to its ability to produce smooth, correlated variations. Each interface in the heterostructure was assigned a unique Perlin noise map with tunable amplitude and grain size, mimicking realistic morphological features observed in sputtered multilayers. The grain size was held constant across the structure, while the roughness amplitude could vary with layer index.

To fully utilize this implementation, the mesh resolution was increased from a $20 \times 20 \times 52$ grid

with cell sizes of $3 \times 3 \times 0.5\,\mathrm{nm}^3$ to a $100 \times 100 \times 260$ grid with cell sizes of $3 \times 3 \times 0.1\,\mathrm{nm}^3$, and demagnetisation effects were disabled and periodic boundary conditions were applied to x and y. Incorporating vertical imprinting of roughness from one layer into the next was deemed intractable within the current framework, as it would require a non-trivial recursive construction process to avoid the artificial accumulation of topographical features across the stack. Aside from disabling demagnetism (due to the periodic boundary conditions), all other magnetic parameters in the system were also chosen according to Table 8.1.

The results in Figure 8.5 demonstrate that, even in the absence of demagnetisation (such as at the central spot of the sample probed by the beam in RFMR), the variations in dipolar fields due to structural roughness alone are sufficient to generate pronounced depth-dependent variation in the dynamic susceptibility. The VNA-FMR spectrum (a) exhibits complex low-field modes. By isolating an off-resonance pixel, the central panel (b) reveals that amplitude and phase of the magnetisation response exhibit strong spatial modulation, with clear domain-like phase boundaries coinciding with contours of the Perlin roughness map. The use of a cyclic colormap highlights phase wrapping across $[-\pi, \pi]$. The right panel (c), showing time-domain precession vectors at a fixed in-plane coordinate ($x = 0, y = 22\,\mathrm{nm}$), reveals qualitatively distinct trajectories across depth: one region exhibits stable elliptical motion, while another supports a distorted, figure-of-eight orbit. The intervening layers remain effectively quiescent.

The simulations confirm that certain modes, such as stable periodic orbits, are invisible to VNA-FMR. This finding necessitates using depth-sensitive RFMR to experimentally resolve these hidden dynamics, which is the focus of the subsequent sections.

8.4 Preliminary Characterisation

Building from the micromagnetics, and susceptibility analysis, this subsection presents preliminary characterisation of the $[\mathrm{Ta/CoFeB/MgO}]_4$ heterostructure series to establish a foundational understanding of its static and dynamic magnetic properties. A $\mathrm{Ta}(5\,\mathrm{nm})/[\mathrm{Ta}(3\,\mathrm{nm})/\mathrm{CoFeB}(t_{\mathrm{CoFeB}})/\mathrm{MgO}(2\,\mathrm{nm})]_4$ series was grown on a semi-insulating Si substrate with 100 nm thick thermally formed SiO_2 layer by magnetron sputtering. The thickness of the CoFeB layer was continuously varied by growing a wedge shape to tune the PMA [193]. Following growth, The thickness range of the CoFeB was confirmed to be 0.55-1.70 nm across the sample. A series was creating by cleaving the sample into 23 sub-samples across the CoFeB gradient, hence each having a negligible CoFeB gradient ($\lesssim$0.05 nm across a $\sim$3 mm sample width). The sample series was studied via SQUID-VSM and VNA-FMR,

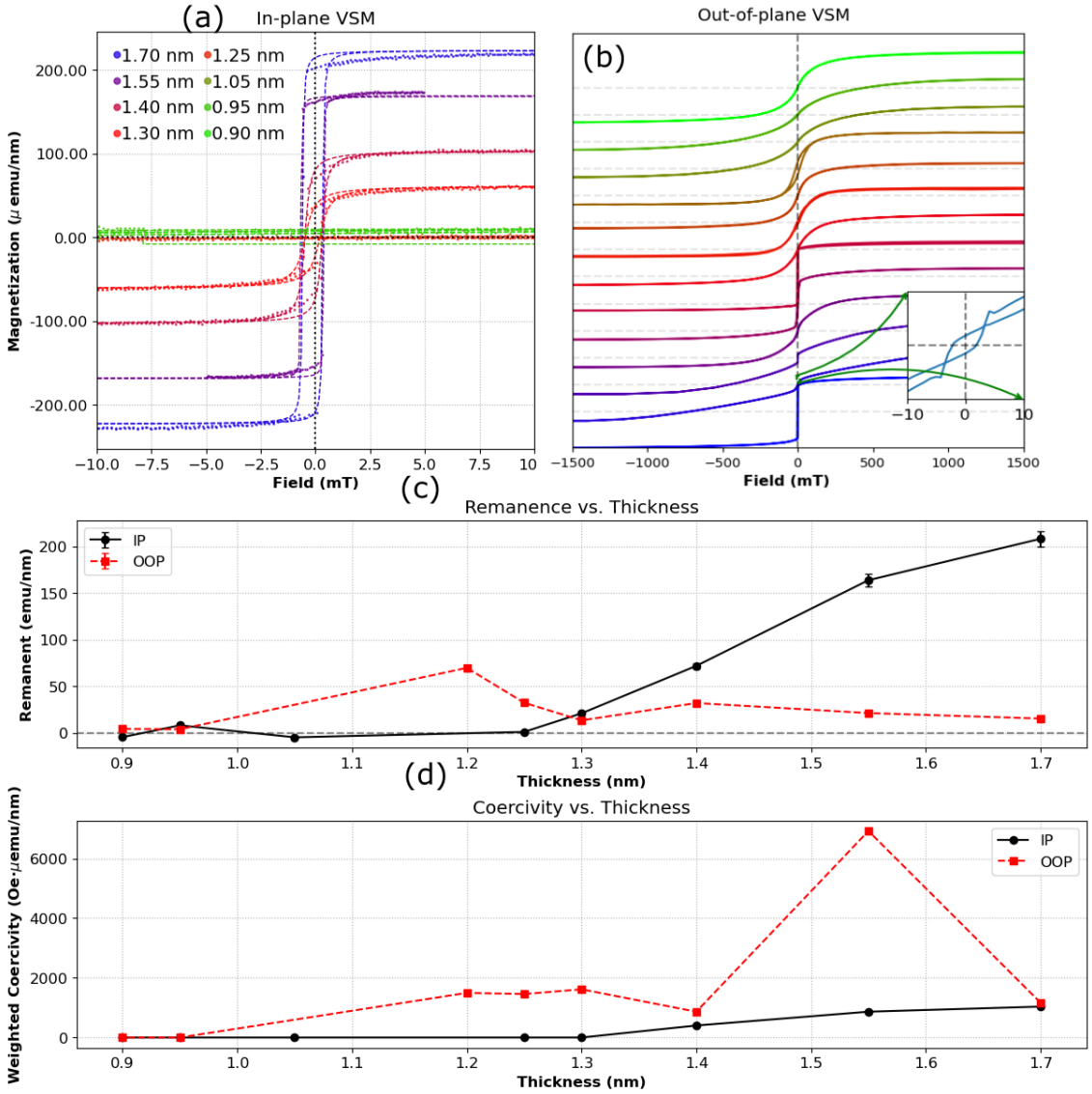


Figure 8.6: VSM analysis of [Ta/CoFeB/MgO]$_4$ multilayers showing a thickness-driven spin reorientation transition (SRT). (a) IP and (b) OOP hysteresis loops are fitted with arctangent functions. The evolution of (c) remanence and (d) coercivity with thickness confirms a spin reorientation transition near 1.3 nm, demarcating a crossover from PMA to IP anisotropy.

they confirm key features, such as the presence of a spin reorientation transition and the evolution of resonance modes with thickness, that are essential for interpreting the depth-resolved RFMR results that follow. Together, they demonstrate that the system exhibits the magnetic complexity required to justify a more detailed, layer-sensitive analysis.

8.4.1 Vibrating Sample Magnetometry

Figure 8.6 presents VSM measurements of the sample series [Ta(3)/CoFeB(x)/MgO(2)]$_4$, with x varying from 0.90 to 1.70 nm. Magnetic fields were applied up to 1 kOe IP (a) and 2 kOe OOP (b), though the plots are cropped to emphasize the hysteresis behaviour. Samples with $x < 0.90$ nm

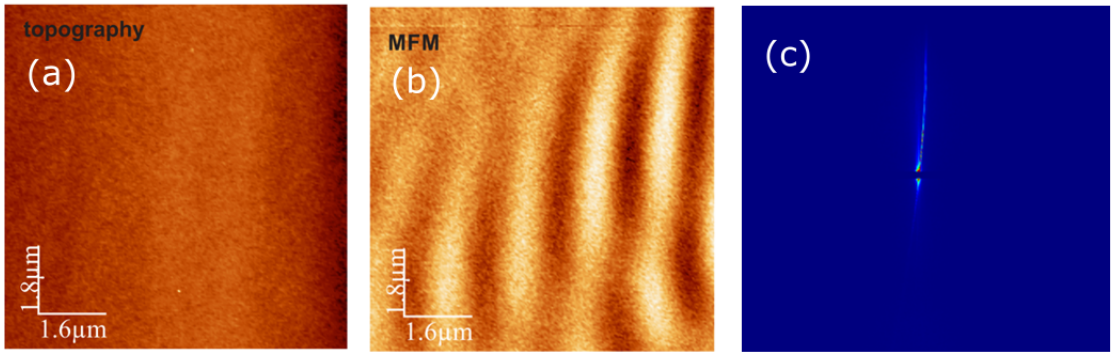


Figure 8.7: (a) AFM and (b) MFM measurements taken on [Ta/CoFeB(1.5 nm)/MgO]$_4$ at remanence in room temperature showing a striped magnetic domain. However these magnetic satellites could not be identified in (c) REXS, figure shows the straight through beam partially blocked by the beam stop.

exhibited negligible saturation and are omitted. All magnetisation data were corrected for linear time drift and underwent a diamagnetic background subtraction based on the linear fit to high-field regions. Hysteresis loops were fitted with arctangent functions to extract remanence and coercivity values. The remanence plot reveals a clear crossover near 1.3 nm, marking a SRT from perpendicular to in-plane anisotropy. To mitigate non-magnetic background contributions, coercivity is reported as a weighted quantity ($H_c \times M_{\text{sat}}$). The sharp suppression of OOP remanence, alongside the rise in IP coercivity with increasing thickness, confirms the transition in magnetic anisotropy.

AFM and MFM measurements on the multilayer stack shown in Figure 8.7 confirm the presence of a stripe-domain magnetic configuration at remanence. Stripe domains arise in thin films that possess a uniaxial magnetocrystalline anisotropy with an easy axis perpendicular to the film plane [194, 195, 196]. Such textures are commonly observed in ferromagnet/heavy-metal multilayers [197] and their dynamical response is now well understood [198].

Because the MFM signal is sensitive only to the stray field emerging from surface and volume magnetic charges, it provides no direct information on the spin configuration across the film thickness or within the domain-wall width. This internal magnetisation profile is nevertheless crucial for analysing dynamic behaviour, since complex heterostructures can deviate significantly from the ideal Bloch-wall structure [199]. To access this information, REXS was attempted in order to locate the magnetic satellite peaks and enable subsequent RFMR measurements. However, no satellites were detected across the sample series, precluding this approach in the present study.

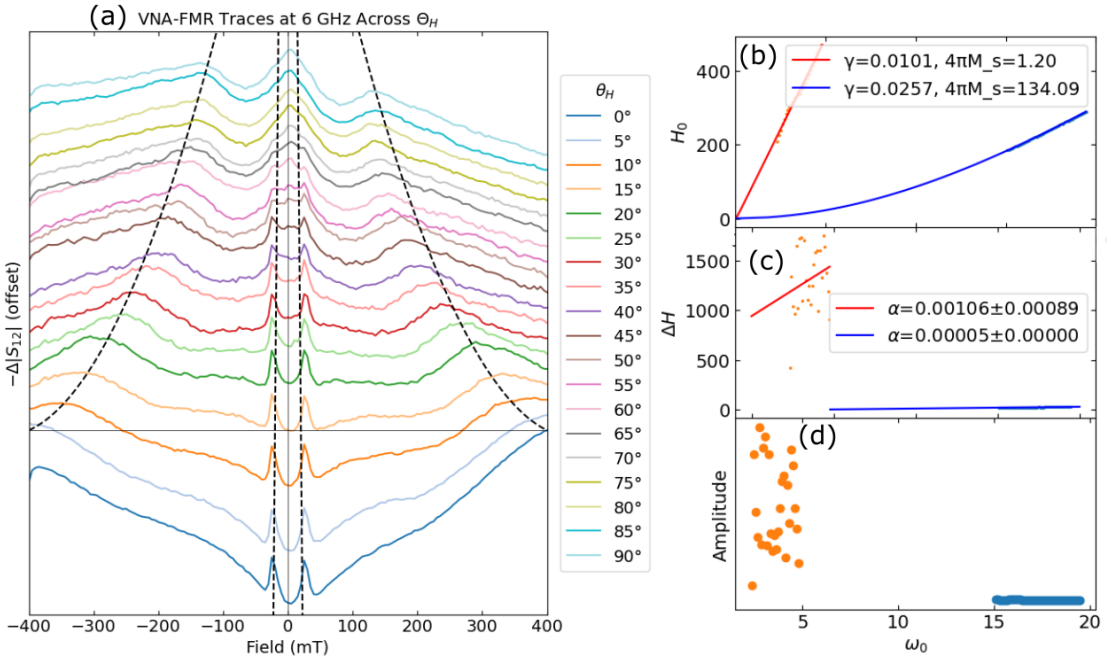


Figure 8.8: (a) VNA-FMR S_{21} traces at 6 GHz from -400 mT to +400 mT. Data was high-field subtracted then offset for clarity. Two modes are visible, a low-field mode, which shows little change in H_0 with changing θ_H, but diminishes in intensity at OOP fields, and a broader higher field mode which shows significant change in H_0 with changing θ_H. (b-d) Both low- and high-frequency modes (blue and orange respectively) are fit at $\theta_H = 0°$ with 2.11. (b) shows the resonance field H_0 versus frequency ω_0, fitted with the Kittel equation. (c) displays the linewidth ΔH versus frequency, with linear fits used to extract α. (d) shows the amplitude of each mode.

8.4.2 Ferromagnetic Resonance

To grasp the complex modes in the [Ta(3)/CoFeB(1.50 nm)/MgO(2)]$_4$ heterostructure, we performed vector network analyzer ferromagnetic resonance (VNA-FMR) measurements as a function of applied field angle θ_H, ranging from IP (0°) to OOP (90°). The resulting angular-resolved spectra are shown in Figure 8.8(a). At low angles (0°–50°), a sharp and well-defined resonance branch consistent with an IP Kittel mode is observed. As the field angle increases, this resonance loses intensity, and by 60°–90°, an OOP mode becomes dominant.

To extract quantitative magnetic parameters, VNA-FMR spectra were analysed by fitting both the low- and high-frequency resonant modes, as shown in Figure 8.8(b, c, d). Fitting the resonance fields $H_0(\omega)$ with the Kittel relation (eq. 2.11) enables extraction of the gyromagnetic ratio γ and effective saturation magnetisation $4\pi M_s$ for each mode. Concurrently, linewidth analysis yields estimates of the Gilbert damping parameter α from the linear slope of $\Delta H(\omega)$ (eq. 2.12).

Finally, Figure 8.9 presents a broader view of the thickness dependence using both OOP and IP VNA-FMR measurements. In OOP we do not observe any Kittel-like modes, but by comparing the relative intensity between the isotropic low-field mode and the anisotropic high-field mode, we extract

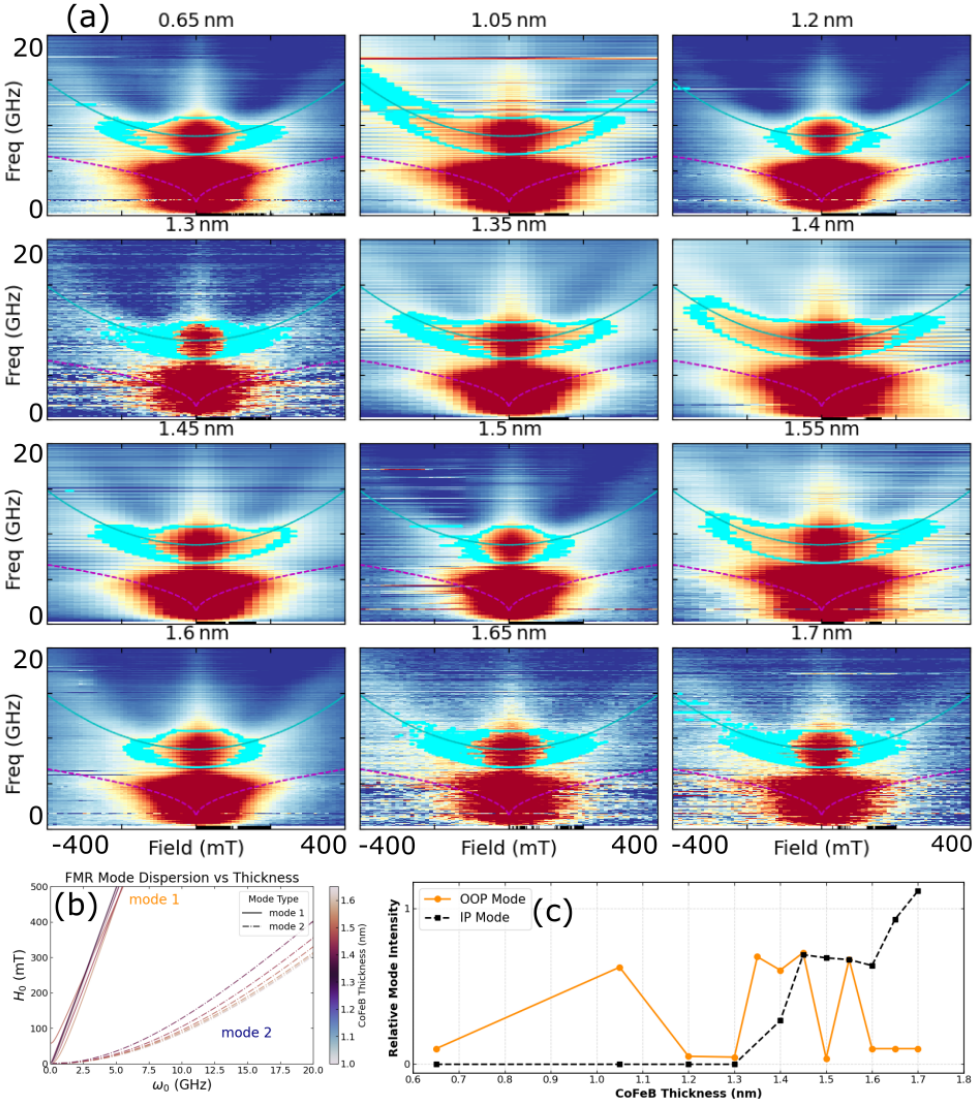


Figure 8.9: (a) OOP VNA-FMR on [Ta(3)/CoFeB(t_{CoFeB})/MgO(2)]$_4$ reveals clustered resonant intensities near the analytically predicted eigenmode positions from Figure 8.2.(b) IP VNA-FMR spectra showing extracted mode positions across samples. (c) A comparative analysis of the relative intensity between the second IP mode and the clustered OOP mode yields a thickness-dependent modal intensity trend, serving as an alternative metric for modal strength vs. t_{FM}.

a secondary metric for modal strength. This is achieved by applying a clustering algorithm to the 2D field vs frequency maps in the OOP geometry, targeting each of the expected modes (cyan and purple dashed lines). Regions of enhanced absorption are identified as resonance conditions, with their boundaries highlighted by the blue contours. The integrated intensity of each mode is then calculated and plotted in Figure 8.9(c). The resulting modal intensity ratio shows a pronounced dependence on t_{FM}, reflecting the evolving mode character and hybridization effects with thickness.

In Figure 8.9(b) we show the same experimental proceedure, now in the IP geometry, and exclusively show the fitted modes as a function of t_{CoFeB} for simplicity. Above the SRT, a high-frequency mode (mode 2 IP) is observed, which follows the Kittel formalism; fits versus t_{CoFeB} reveal an upward

shift to higher fields with decreasing thickness. Around the SRT, two distinct modes appear in the data (as previously shown in Figure 8.8(b–d)), whereas well below the SRT only the lower-frequency mode (mode 1 IP) remains visible. In (c) we plot the intensity of mode 2 as the 'IP' mode, and compare it to the OOP mode, the figure shows the relative intensity of each mode, where the IP mode has a higher intensity at thicker t_{CoFeB}, whereas the OOP intensity has a complicated behaviour, but increases around the SRT, and mimics the remanence and coercivity measurements from the VSM in Figure 8.6.

8.5 XMCD & XRMR

To extract the energy-dependent complex scattering factors necessary for XRMR modelling, we fitted the FY spectra from Figure 8.10 using a sum of three asymmetric Lorentzians. The fitting procedure was applied separately to the PC and NC spectra, with constraints informed by the expected multiplet structure of the Fe and Co $L_{3,2}$ absorption edges. Prior to fitting, all spectra were dark-current subtracted, interpolated onto a uniform energy grid, and background-corrected using a linear pre- and post-edge model with step-like edge jumps to approximate the tabulated Henke absorption profile. The

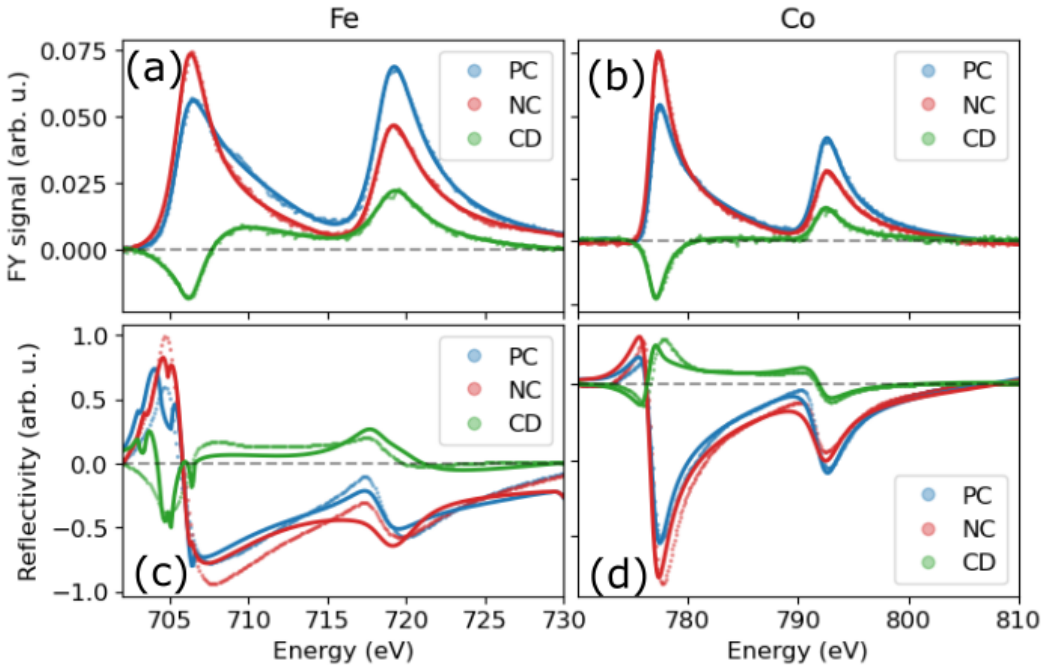


Figure 8.10: XMCD measured in both FY (a, b) and reflectivity (c, d) at the Fe (a, c) and Co (b, d) $L_{3,2}$ edges in [Ta/CoFeB(1.50 nm)/MgO]$_4$. FY was collected at 70° from specular with incident X-rays at 9°. A magnetic field of 40 mT was applied 22° from the surface normal. Positive circular, negative circular, and their difference (CD) are shown alongside fits used to extract complex scattering factors. A third peak slightly above the L_3 edge for both ferromagnets was required to achieve good agreement, suggestive of partial oxidation.

imaginary part of the scattering factor, $\mathrm{Im}[f]$, was taken from the fitted spectra. The real part, $\mathrm{Re}[f]$, was then reconstructed using a Kramers–Kronig transform implemented via the Hilbert transform. Charge and magnetic contributions were isolated as done in Chapter 4. The final XRMR reflectivity was computed using all four contributions (f_c', f_c'', f_m', f_m''), weighted by four fitting parameters a, b, c, and d that scale each component in the model.

For Fe, the FY fitting produced three peaks at $(705.72, 708.26, 718.71)$ eV with respective amplitudes $(0.038, 0.029, 0.062)$ in the PC spectrum. The NC fit showed slight variation with amplitudes $(0.068, 0.011, 0.041)$ at similar energies. The broad width of the second peak in both PC and NC ($\gamma \sim 8.8$–10.2 eV) likely captures overlapping transitions at the L_3 edge. For Co, the PC peaks were located at $(776.91, 775.42, 792.11)$ eV, while the NC values were closely matched.

To illustrate the outcome of the reflectivity-weighted optical constants, we report the fitted scattering factor $f(E)$ at representative energies:

Fe		**Co**	
$E = 706.40$ eV:	$f = -0.0442 - 0.6961i$	$E = 777.40$ eV:	$f = 0.0469 - 0.6795i$
$E = 715.00$ eV:	$f = -0.1499 - 0.0539i$	$E = 790.00$ eV:	$f = -0.0034 - 0.0522i$
$E = 719.30$ eV:	$f = 0.0313 - 0.4455i$	$E = 792.50$ eV:	$f = 0.0005 - 0.3832i$

Notably, the Fe fit quality is lower, which we attribute to limitations of the model in treating a single-interface system, as discussed in Chapter 4, an attempt was made to move beyond the analytical calculation using the single interface mode, by incorporating the exact recursive matrices used in our RFMR model, however this proved too complicated to interpret. Hence the solution was to smooth the data using a Savitzky–Golay filter to suppress high-frequency numerical artifacts, and explicitly fit the scattering factors as open bounds in the upcoming modelling.

8.5.1 Depth Profile via XRMR

Following XMCD measurements, the energy was fixed at the Fe L_3 absorption edge (704.5 eV), an OOP magnetic field of 60 mT was applied, and specular θ–2θ XRMR scans were conducted using both PC and NC polarisations. Figure 8.11 shows the resulting $[\mathrm{Ta/CoFeB/MgO}]_4$ total intensity ($I_{\mathrm{tot}} = \mathrm{PC} + \mathrm{NC}$) and asymmetry ($A = (\mathrm{PC} - \mathrm{NC})/(\mathrm{PC} + \mathrm{NC})$), alongside the corresponding fits.

Although initial fits to I_{tot} were performed using GenX, the long-term objective of fitting RFMR data necessitated the development of a Python-based pipeline capable of co-fitting both I_{tot} and asymmetry. This XRMR pipeline was built in the same manner as the RFMR model in Chapter 5, and hence agrees with the GenX results. It relies primarily on convergence via a DE optimiser (see Sec. 5.4), with additional features for by-eye alignment, least-squares optimisation, and sensitivity

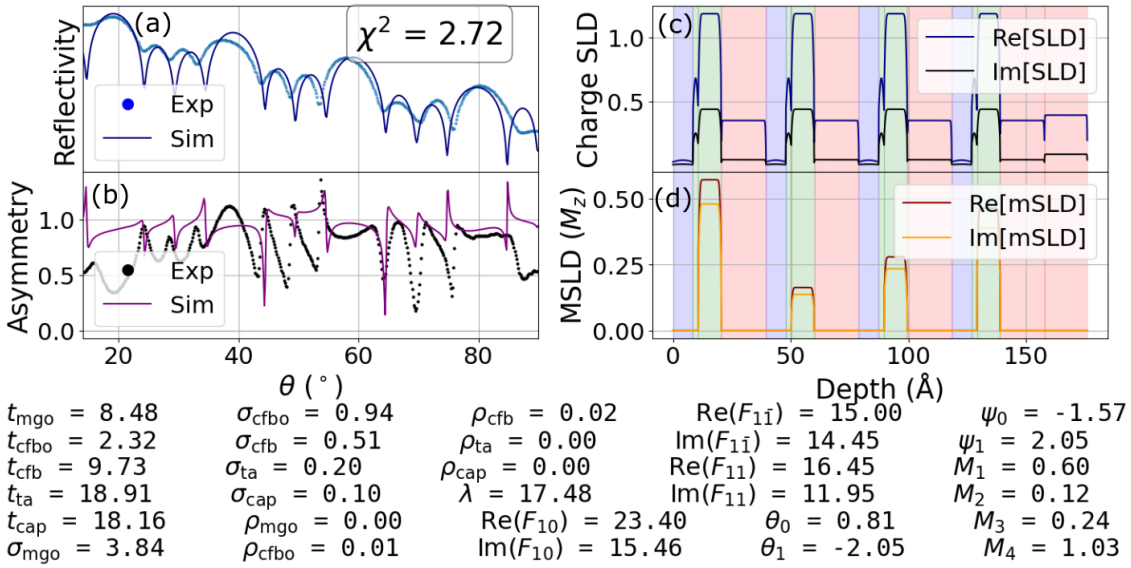


Figure 8.11: XRMR specular reflectivity scans of the multilayer [Ta/CoFeB(1.2 nm)/MgO]$_4$ measured at the Fe L_3 edge (704.5 eV) using positive (PC) and negative (NC) circular polarisation with $\theta_H = 0°$ (OOP) and $H = 60$ mT, corresponding to a closed hysteresis but unsaturated state. (a) Total reflectivity $I_{tot} = (PC + NC)/2$. (b) Asymmetry ratio $A = (PC - NC)/(PC + NC)$. The fitting routine was weighted to prioritize the asymmetry signal, with an average error weighting ratio of $I_{tot} : A = 1 : 2$, and the reduced figure of merit (FOM) is shown. Small deviations in periodicity are attributed to limitations in the N=4 stack model. (c) Fitted charge scattering length density (SLD) profile. (d) Fitted magnetic SLD profile. Structural parameters were initially aligned by eye and refined using DE (see Sec. 5.4), followed by co-fitting of both I_{tot} and asymmetry using variable scattering factors and magnetisation parameters across the sample series. A final L-BFGS minimisation was used for convergence. Accurate fits required the inclusion of a thin oxidized CoFeB interlayer at each MgO/CoFeB interface.

analysis.

Magnetism was defined as a macrospin in spherical coordinates for each CoFeB layer with θ, ψ and M_0, each uniquely assigned. The model assumes an explicit $N = 4$ repetition of the [Ta/CoFeB/MgO] unit cell, with identical structural parameters in each repeat. Some agreement with experimental I_{tot} data was achieved when allowing for thin oxidation layers at each MgO/CoFeB interface. However, the periodicity of experimental XRMR fringes was found to vary non-uniformly across $\mathbf{Q}_z$, as though the axis were nonlinearly compressed or stretched. This irregularity is tentatively attributed to small deviations in the layer thicknesses and roughnesses across the stack, arising from the recursive nature of sputtering on top of previously deposited layers.

An attempt was made to account for these deviations by fitting each of the 18 individual layers independently, but this overwhelmed the DE optimiser and rendered the resulting model uninterpretable. Thus, we retained the simpler $N = 4$ repetition model for clarity and tractability.

Further complexity emerged when examining the series of XRMR datasets shown in Figure 8.13. While the samples are nominally cleaved from a single wedge, and thus expected to share all structural

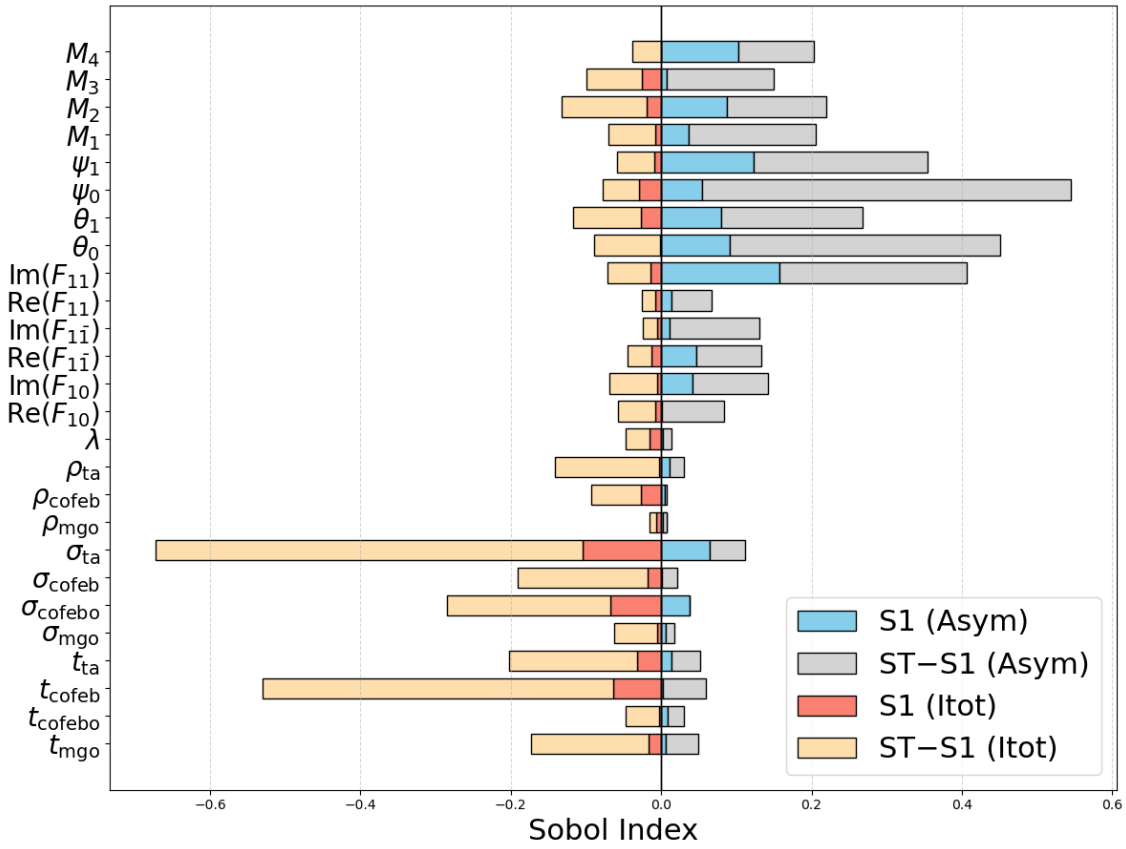


Figure 8.12: Sobol sensitivity analysis of XRMR fitting parameters. shown in Figure 8.11, The left panel shows the structural contributions, where the asymmetry terms were excluded from the objective function (Asymmetry weight = 0). The right panel shows the magnetic asymmetry contributions, where I_{tot} contributions were excluded from the objective. For each parameter, the main effect (S_1) indicates its individual influence, while the total effect (S_T) includes all correlations and interactions with other parameters.

properties aside from a linearly increasing t_{CFB}, this assumption did not yield viable fits. Instead, each sample required its own unique structural fit, most likely to accommodate spatial variations in deposition rate and roughness across the wedge. Notably, It was found that incorporating the magnetic profile was significantly easier: each sample exhibited a similar underlying magnetic asymmetry pattern, which was only stretched or compressed to account for the imprinted structural parameters, and scaled. This observation led to the conclusion that a more effective and interpretable strategy was to explicitly fit the full model for one representative sample, and then vary only a single scalar parameter (here, M_z) across the remaining samples to reproduce the asymmetry. Further from there, the simplification that θ(z) and ψ(z) both only varied linearly with depth provided a model that could be interpretable, and avoided over-fitting.

Several fitting strategies were trialed, including global fits of both I_{tot} and asymmetry, and alternating fits where only magnetic parameters were adjusted against asymmetry until convergence. Ultimately, an iterative refinement strategy proved most effective: beginning with a full fit for one

sample and propagating minimal parameter changes to neighbouring samples in the series.

The resulting model shown in Figure 8.11 reveals enhanced magnetisation at the outer CoFeB layers in the [Ta/CoFeB(1.20 nm)/MgO]$_4$ heterostructure. A Sobol sensitivity index analysis is shown in Figure 8.12, revealing that the choice of free parameters is justified, with each parameter showing significant influence on the model. The importance of this iterative process is illustrated in Figure 8.12, where it can be seen that most parameters influence both the Itot and Asymmetry profiles, meaning that you cannot 'freeze-out' or fit part of the data with prior constraints. The full series of fits is presented in Figure 8.13. While each sample required an entirely new structural fit, the only free magnetic parameter varied across the series was the scalar M_z, with its thickness dependence plotted alongside. The error bars on $M_z(t_{\mathrm{CFB}})$ were determined via a 3D sensitivity analysis over the average θ, ψ, and M_0, and represent the 90% confidence threshold of the global optimum.

8.6 Characterising Unique FMR Modes

8.6.1 Field Scan Results

RFMR measurements were conducted at two fixed frequencies; 2 GHz and 6 GHz at 300 K, at Fe L_3 (here 704.5 eV) in positive circular polarisation, while phase-modulating the RF pump. The dynamic signal was obtained by sweeping the delay line over a range of 0-600 ps, and fitting the resulting responses with sine curves at the pumping RF frequency to extract both the amplitude and phase. By recording the dynamic signal against the static field's magnitude and angle, the resonant FMR modes could be located.

Figure 8.14(a, b) overlays the field–dependent amplitude RFMR measurements at $\omega = 2$ and 6 GHz. Both quantities were obtained by fitting the time–domain delay scans (0–600 ps) with sine functions at the pump frequency.

A single, well–defined resonance is observed at $H_0 = 138 \pm 2$ mT with a half–width at half–maximum $\Delta H = 40 \pm 3$ mT. The complex susceptibility is satisfactorily captured with

$$A(H) = A_0 \frac{(1-a)\frac{\Delta H}{2} + a(H - H_0)}{(H - H_0)^2 + \left(\frac{\Delta H}{2}\right)^2} + C, \tag{8.9}$$

$$\varphi(H) = \varphi_0 + B \arctan\left[\frac{2(H - H_0)}{\Delta H}\right], \tag{8.10}$$

where a quantifies the skewness introduced by inhomogeneous broadening, *e.g.* Equation (8.10) yields the canonical π-phase inversion across resonance, whose damping is set by ΔH.

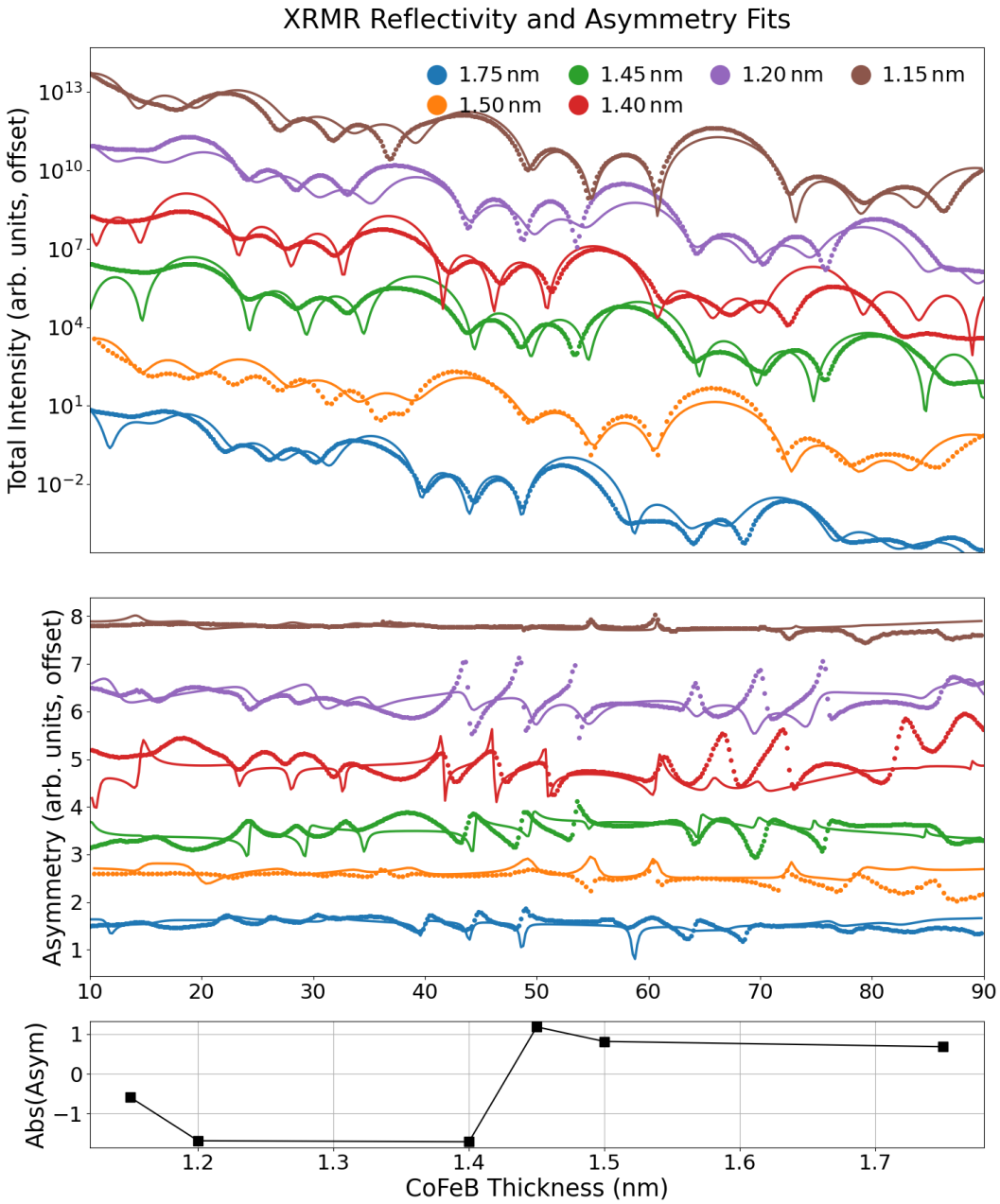


Figure 8.13: XRMR specular scans for [Ta/CoFeB(t_{CoFeB})/MgO]$_4$ taken at Fe L_3 edge (704.5 eV) for PC and NC polarisation, with θ_H=0° (OOP) in a saturating field of 100 mT across the ranges 1.15 nm<t_{CoFeB}<1.70 NM. Data shows surprisingly large differences between PC+NC (Total Intensity) for each sample, but common features across all Asymmetry profiles. optimiser was weighted to preferentially fit the Asymmetry. Model was fit by iteratively reducing bounds throughout series of DE, LFBGS, and manual alignment. Finally each sample was fit via DE to determine unique structural profile, and tightly bound magnetic profile based on Figure 8.11. (Bottom) By noticing that Asymmetry was so similar across each sample, we show here the scaling factor required to reproduce each one (max/min* sign).

In contrast, the low–frequency spectrum is dominated by a very broad feature centred at $H_0 = 168 \pm 5\,\mathrm{mT}$ with an anomalously large $\Delta H \approx 155\,\mathrm{mT}$. The amplitude must be modelled as a sum of two asymmetric Lorentzians, $A(H) = \sum_{i=1}^{2} A_i(H) + C$, to reproduce the high–field peak and a shallow shoulder at $H \simeq 50$–$60\,\mathrm{mT}$. Due to the overlapping resonances, the shoulder's sign (positive ≈40 mT mode *vs.* negative ≈58 mT mode) does not allow an unambiguous assignment. The same extreme broadening stretches the arctangent in Eq. (8.10) so far that the phase appears to vary almost linearly with field, masking the π jump that would otherwise mark each individual resonance. It is likely the resonant condition for this mode is below the minimum field of the diffractometer, explaining why there is no rapid change in phase found here.

VNA-FMR traces (gray lines in Figure 8.14) corroborate the main high-field resonances at both frequencies. Interestingly, VNA–FMR resolves the low-field branch at 6 GHz but not at 2 GHz, in stark disagreement with RFMR. This disparity is readily explained by the different depth sensitivities: RFMR integrates the complex standing-wave pattern of the heterostructure along the X-ray penetration depth, whereas VNA–FMR weights each layer uniformly.

The multimode behaviour is consistent with the analytical susceptibility map in Figure 8.3. For a field applied exactly along a principle axis ($\theta_H = 0°$), even minute tilts of the equilibrium magnetisation cause large shifts of H_0, leading to apparent mode broadening. Canting the field ($\theta_H \neq 0$) lifts this degeneracy and recovers sharp resonances, as observed for the 6 GHz branch. Hence perhaps the 2 GHz spectrum reflects a collective, depth-dephased excitation with strong layer-dependent damping, while the 6 GHz mode remains predominantly macrospin-like.

From there the static field was fixed at each resonant condition, and delay scans were further repeated, however now varying $\mathbf{Q_z}$ to construct the reflectivity profile of the FMR mode. By aligning the $\mathbf{Q_z}$ data with the XRMR model, detailed depth profiles of the magnetic dynamics were constructed, allowing for a clear distinction between the depth profile of each FMR mode. The Fe results will be discussed, while measurements were repeated on the Co L_3 edge, and at negative circular polarisation, which broadly agreed with the results presented.

8.6.2 Reflectivity Results

Before discussing the RFMR θ–2θ measurements, we first summarize the sample's magnetic characterisation. In Figure 8.6(b), we show OOP SQUID-VSM measurements. While the hysteresis loop closes around 10 mT, full saturation is only reached above 1 T. Consequently, RFMR measurements are conducted in the unsaturated state [158].

In Figure 8.8(b), we present VNA-FMR spectra acquired in the OOP geometry. Although mea-

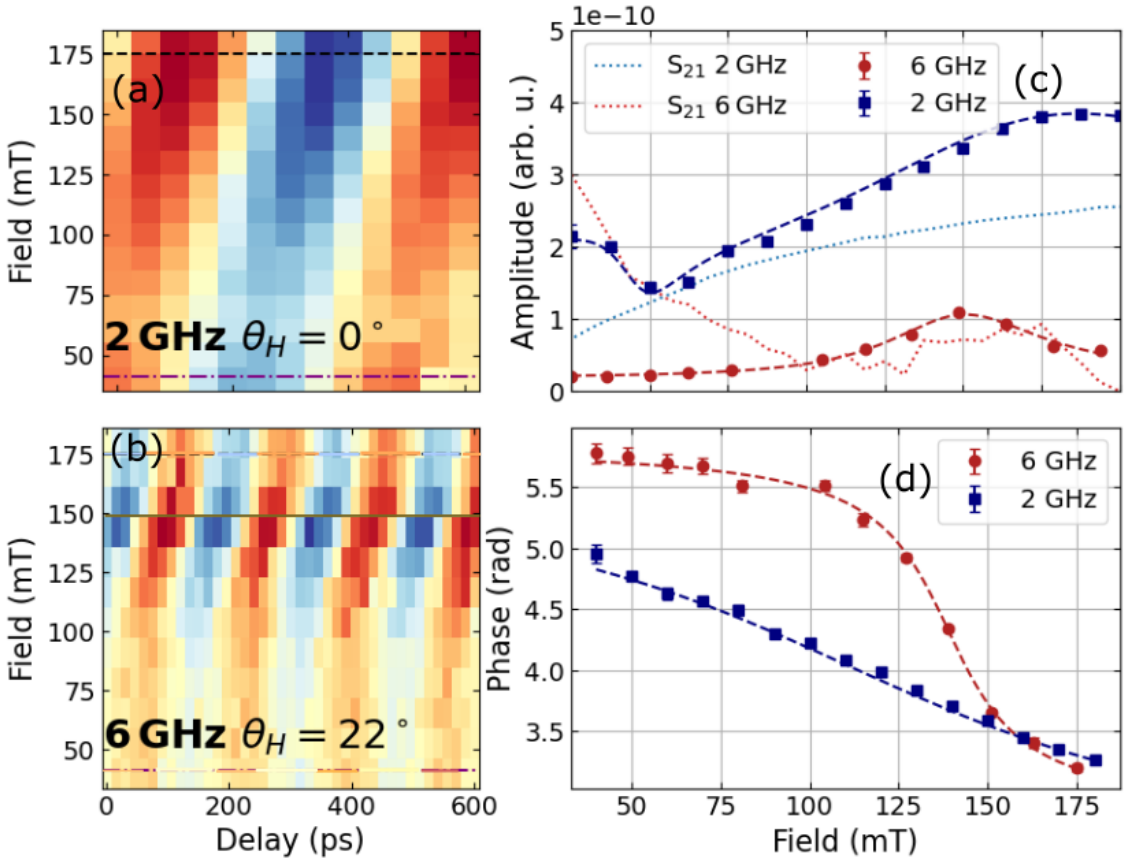


Figure 8.14: FMR mode characterisation. (a, b) RFMR field scans taken at $\theta = 5°$, $2\theta = 10°$, 300 K, 704.5 eV, PC polarisation, with ~3 kHz phase modulation, for the 2 GHz mode at $\theta_H = 0°$ (a) and the 6 GHz mode at $\theta_H = 22°$ (b). Horizontal dashed lines indicate field positions corresponding to peaks in the dynamic signal amplitude. (a) Demonstrates a broad FMR mode (black dashed line) at 179 mT and a sharper FMR mode (purple, dash-dot line) visible at 41 mT. (b) shows a distinct resonance mode at 150 mT (purple, dash-dot line). (c) Amplitude vs field for each mode, fitted with asymmetric Lorentzian functions, two peaks identified at 2 GHz and one at 6 GHz. VNA-FMR traces are overlaid for comparison. (d) Phase vs field, fitted with arctangent functions.

surements were performed from −400 to +400 mT and up to 20 GHz, they are however cropped on the range relevant to RFMR. A weak isotropic mode is visible at low fields and is notably stronger under in-plane bias. However, due to the overlap of multiple modes at low fields [146], this mode was excluded from RFMR analysis. Two broad high-field modes are observed, but their linewidth and weak signal render precise parameter extraction (e.g., Gilbert damping) unreliable [161].

Figure 8.15 (a) show $\mathbf{Q_z}$-dependent RFMR scans taken at the dashed lines in Figure 8.14(a) and (b), i.e., 179 mT at $\theta_H = 0°$ and 150 mT at $\theta_H = 22°$, respectively.

The model chosen for fitting the RFMR data was inspired by the XRMR fitting pipeline. The $N = 4$ approximation was considered inadequate, likely due to cumulative variations in thickness, density, and roughness across repeats, introduced by the recursive nature of sputtering. Furthermore, significant intra-layer dynamic variation was inferred, as models assuming a single macrospin per

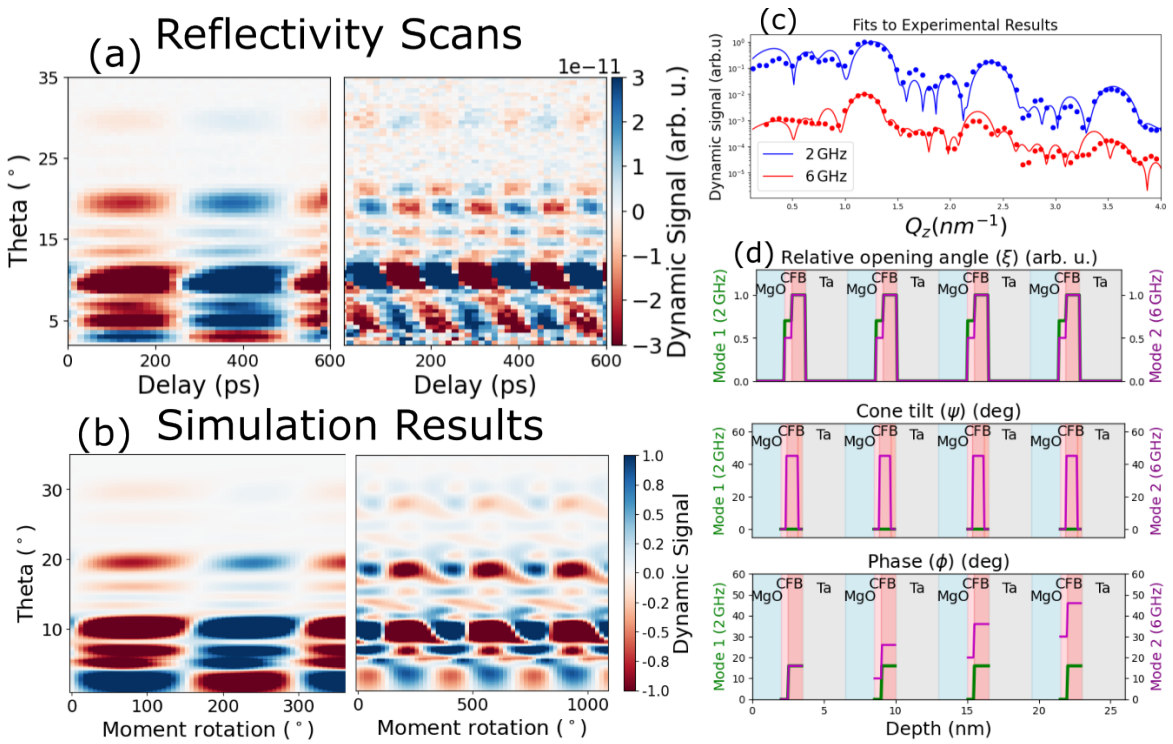


Figure 8.15: In (a) we show $\mathbf{Q_z}$ scans taken at 179 mT 2 GHz, and 150 mT 6 GHz. The sharper Kittel mode showed anisotropy, hence 6 GHz measurements were taken at $\theta_H = 22°$ where the signal was maximised. Underneath in (b) we show comparative simulation results compared. (c) By fitting sine curves to the data and simulations, the amplitude of the dynamic signal can be extracted to allow for a fitting procedure. Shown in blue (red) dots is the fitted amplitude to 2 GHz (6 GHz) data, and the blue (red) line is 2 GHz (6 GHz) simulation. (d) The best-fit parameters for (ξ, ψ, and ϕ) are shown below. With the results highlighted in green for Mode 1 (2 GHz) and purple for mode 2 (6 GHz).

repeat could not reproduce the experimental periodicity. To capture these effects, each CoFeB layer was divided into three magnetic sublayers with independently fitted demagnetism (demag_L, demag_U), magnetic roughness ($d_{\sigma L}$, $d_{\sigma U}$), and interfacial thicknesses (d_{rL}, d_{rU}). This led to a high-dimensional parameter space, which overwhelmed the DE optimiser.

We therefore pursued a hybrid fitting strategy: DE-based global optimisation was followed by rigorous manual alignment ("by eye") and local refinement via gradient-based minimisation. This approach, detailed in Chapter 5, Section 5.6, yielded convergence. However, due to the strong manual tuning, parameters were not exhaustively explored but remained physically reasonable, and the model cannot be claimed as minimal.

The simulation results are plotted in Figure 8.15(b), With amplitude of the sine curves for the experimental and simulation results shown in (c), with the depth profile of ($\xi(z)$, $\psi(z)$, $\phi(z)$) for each mode shown in (d). The RFMR data can be interpreted through these RFMR simulations: each mode exhibits a unique precession opening angle at the MgO/CoFeB interface. This may result from FeO formation or localized demagnetisation effects [172, 200]. In mode 1, precession is entirely out-of-

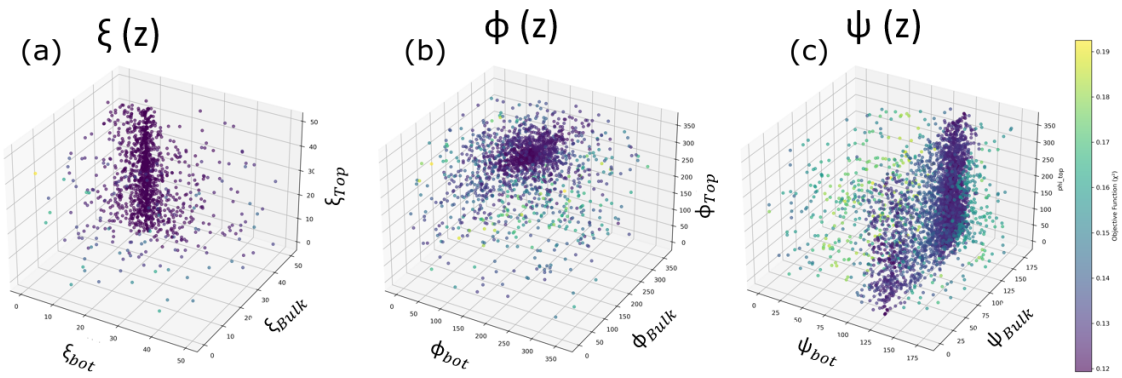


Figure 8.16: 3D sensitivity analysis of the depth-dependent RFMR model for the N=4 structure. Each plot shows the result of Differential Evolution optimisation over three grouped sublayers (top, bulk, bottom) for a different dynamic parameter type. (a) Opening angle ξ_0 (b) Phase ϕ_0 (c) Azimuthal tilt φ_0.

plane ($\psi = 0°$ by definition, see Eq. (5.1)), whereas in mode 2, a depth-dependent tilt angle emerges. This complexity could reflect interfacial DMI at the Ta/CoFeB interface [201, 202] and is illustrated in Figure 8.3. Additionally, the phase profile in mode 2 displays significant depth inhomogeneity, suggesting weakened exchange coupling, consistent with prior results [16], and the intermixing of eigenmodes from Figure 8.2.

It would be a far more fruitful discussion to discuss the absolute value of opening angle in each of these modes. Computing the opening angle in transmission-based XFMR involves calculating the static XMCD ($\mathbf{M_z}$) by taking measurements in normal incidence, then measuring the dynamic XMCD ($\mathbf{M_y}$) in grazing incidence, and solving $\xi = \arctan(\frac{M_y}{M_z})$ [12]. In RFMR this is not as trivial. Normal incidence cannot be done in reflectivity, and due to multiple reflections within the film, the measurement of M_y also cannot be certain without matching the RFMR data to XRMR models, which beyond the scope of this work. However the relative opening angle between the Fe moments in each layer can be modelled from RFMR alone. Further, due to differences in responses of the RFMR circuitry to the different RF frequencies, a different excitation power was delivered to the sample for each harmonic, hence drawing conclusions on the relative opening between modes would be disingenuous.

This model focused on parameters strongly influencing the RFMR signal. Further sections in this thesis aim to implement stricter priors and explore subtle depth-dependent effects, including the influence of SOT, DMI, and interfacial quality on the RFMR signal.

8.6.3 Sensitivity Analysis

Despite the attempts to simplify the model, a significant number of parameters in our model remain under-constrained, with best-fit values arising largely from numerical optimisation. Additionally, many parameters exhibit strong correlations, either having similar effects on the RFMR response, or being modulated by other variables.

One clear example is the depth-dependent precessional phase. While the model can reproduce experimental spectra well using smooth depth-dependent phase profiles, multiple parameter combinations yield similar results. This degeneracy is further complicated by coupling to the local opening angle, which modulates each layer's signal contribution.

To address parameter degeneracy and isolate physically meaningful trends, we conducted a sensitivity analysis, based on previous Bayesian analysis [203], and using the strict $N = 4$ model, in which each CoFeB layer was subdivided into three sub-layers, designated as MgO/CoFeB (bottom), CoFeB (middle), and CoFeB/Ta (top). All structural and scattering parameters were fixed at their best-fit values (from Figure 8.15), and only one dynamic magnetisation variable was varied at a time: ξ (opening angle, left), ϕ (phase, center), or ψ (tilt, right). For each parameter sweep, a new DE fit was run, and every individual trial was plotted against its tested parameter values, coloured by its resulting FOM. Global minima manifest as dense clusters of dark-blue points, with confidence intervals inferred from the extent of this cluster before the FOM increases by ~10%.

Several conclusions emerge. First beginning from the opening angle results, the model is effectively degenerate with respect to the CoFeB/Ta interfacial sub-layer (top of each repeat unit), this may be attributed to how our model recursively propagates the waveform through the depth of the structure, resulting in the top layer effectively serving as a reference layer. Sensitivity is instead driven by relative changes in ξ across depth. The optimal fit suggests a significantly reduced opening angle at the MgO/CoFeB interface compared to the bulk, with fitted values of $\xi_{\text{bot}} = 1 \pm 0.3^\circ$ and $\xi_{\text{bulk}} = 4.5 \pm 0.5^\circ$. Next, each ϕ value was found to play a significant role, with consistent results indicating that ϕ_{bot} lags behind the other two sub-layers by approximately 30–50°, while ϕ_{bulk} and ϕ_{top} remain largely in-phase. Surprisingly, the model showed minimal sensitivity to ψ_{bulk} and ψ_{top}, with convergence in this parameter space driven almost entirely by the weak magnetic contribution at the MgO/CoFeB interface. This yielded a sharply converged value of $\psi_{\text{bot}} = 110 \pm 3^\circ$, relative to the surface normal. The discrepancy between these sensitivity results and the overall best fit shown in Figure 8.15 arises from the stricter $N = 4$ constraint here, which limits the variation to intra-layer depth only. Relaxing this constraint would lead to a 12-dimensional parameter space for each plot, rendering visualisation

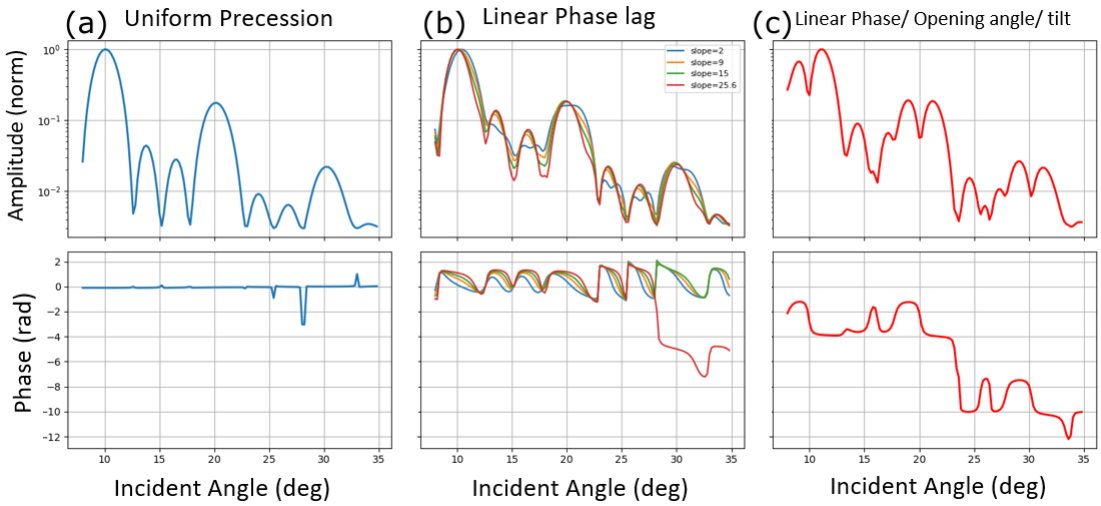


Figure 8.17: Simulated RFMR amplitude and phase profiles with increasing depth-dependence in dynamic parameters: homogeneous precession (a), linear phase lag only (b), and full depth-varying model (c). Model was built from modifications to the best-fit model in Figure 8.15.

impossible.

8.7 Exploiting Spin-Reorientation to Generate Depth-Dependent Dynamics

Based on the preliminary characterisation and micromagnetic simulations, the CoFeB thickness t_{CoFeB} is systematically varied to induce SRT at 1.50 nm. We show this transition can be a controlled tuning parameter to probe the emergence of depth-dependent dynamics using RFMR. Our approach builds upon best-fit structural and scattering parameters extracted from XRMR measurements. We build from the RFMR modelling process in the previous section, but return to a more qualitative standpoint here by comparing distinct models under the N=4 macrospin approximation (i.e. each CoFeB layers moment is treated as one macrospin, and structural parameters are assumed constant across repeats). Based on previous results, one can argue this is an oversimplification of the system, however reintroducing the full complexity of even the structural parameters renders systematic analysis impossible.

To explore the role of depth-dependent dynamics, we simulate RFMR responses while systematically modifying the depth profile of dynamic magnetisation parameters, namely the precession opening angle $\xi(z)$, in-plane tilt $\phi(z)$, and phase delay $\psi(z)$. Figure 8.17 demonstrates this progression: starting from (a) a homogeneous model in which all dynamic parameters are constant with depth, we sequentially introduce a linear phase lag ($d\psi/dz \neq 0$) in (b), and then allow all dynamic variables to vary linearly across the CoFeB stack in (c). These simulations show that even a modest

phase lag can significantly distort the reflectivity fringes and introduce nontrivial structure into the Q_z-dependent phase profile.

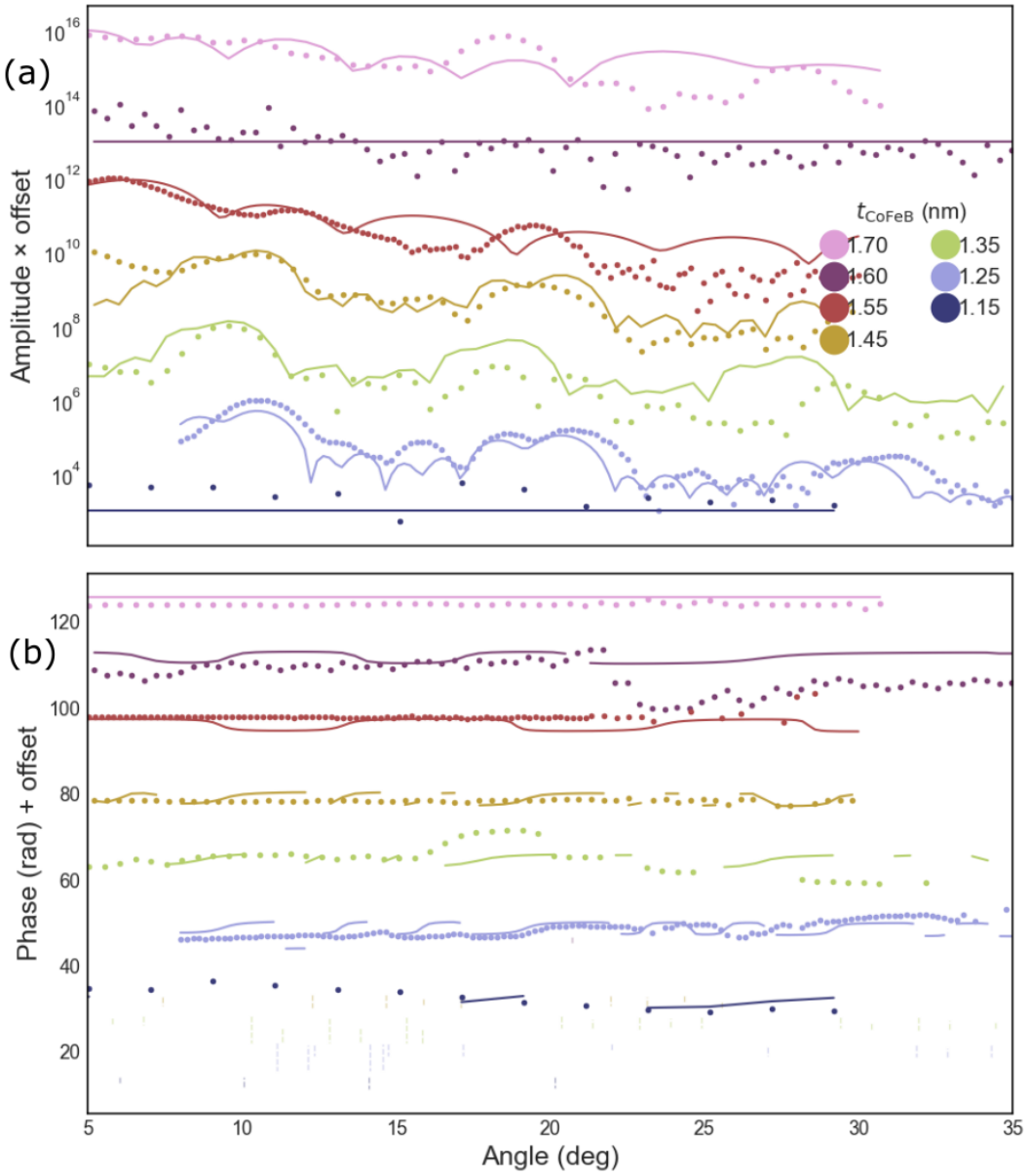


Figure 8.18: Experimental RFMR results for a series of [Ta/CoFeB(t_{CoFeB})/MgO]$_4$ multilayers across the spin reorientation transition (SRT). The extracted precession phase remains flat for thicker films but begins to vary below $t_{CoFeB} = 1.45$ nm, and shows no coherent signal below 1.25 nm. Fits were constructed using a DE optimiser based on the $N = 4$ macrospin model, beginning with a detailed fit to the $t_{CoFeB} = 1.25$ nm sample and iteratively adjusting model bounds for neighbouring thicknesses to capture observed changes in the signal. No detectable RFMR signal was observed at 1.60 nm or 1.15 nm, consistent with weak magnetisation measured via XRMR. The reduced amplitude agreement at 1.55 nm and 1.70 nm is likely due to manual polishing and alignment on a roughened surface. Nevertheless, as the phase remains flat and is well reproduced by the model, the data for these samples are included for completeness.

Figure 8.18 compares these qualitative models to experimental RFMR amplitude and phase data across a series of CoFeB thicknesses from 1.15 nm to 1.70 nm. At the thick end ($t_{CFB} > 1.45$ nm),

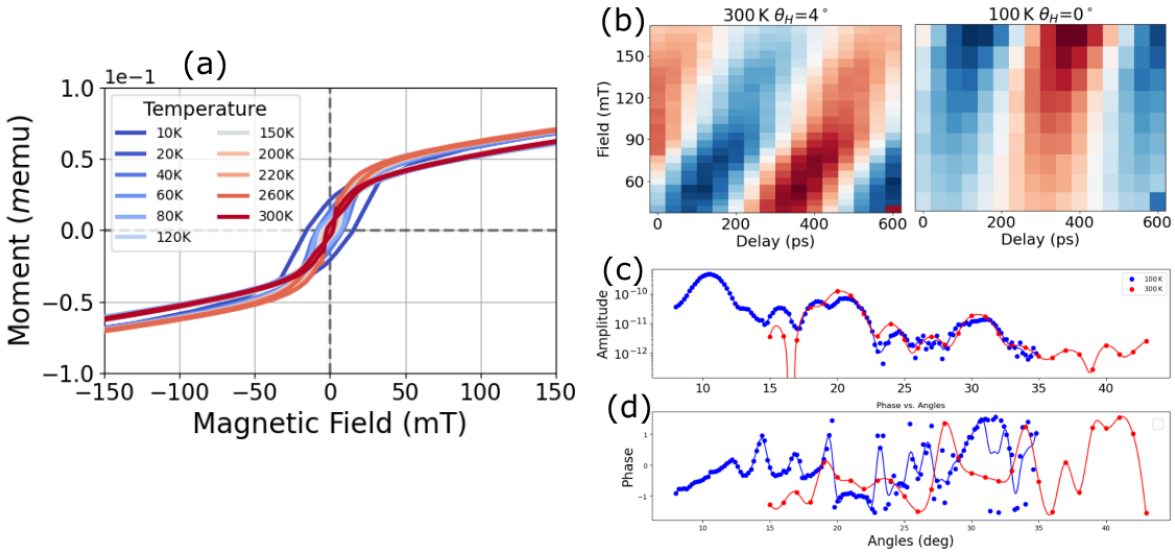


Figure 8.19: (a) SQUID-VSM measurements at various temperatures for a single multilayer sample of composition [Ta(3)/CoFeB(1.50)/MgO(2)]$_4$. Hysteresis loops were recorded between 10 K and 300 K, showing gradual changes in saturation and coercivity. (b, c) In corresponding RFMR measurements, some shifts in the resonance condition were observed at lower temperatures; however, the available data do not allow firm conclusions regarding changes in the underlying modal structure. Data points are connected with guide-to-the-eye lines.

the phase remains approximately flat with Q_z, consistent with a uniform precession model. Between 1.25–1.45 nm, the phase shows systematic evolution with angle, while the amplitude remains relatively unchanged, indicative of a depth-varying phase lag as captured by the linear $\psi(z)$ model. Below 1.25 nm, no coherent RFMR signal is detected despite strong VSM magnetisation, suggesting a loss of coherent macrospin dynamics, potentially due to stochastic or chaotic motion in the ultra-thin limit. These observations support a scenario in which proximity to the spin reorientation transition enables depth-resolved tailoring of dynamic modes in thin magnetic films.

8.7.1 Temperature Dependence

In Figure 8.19 we show SQUID-VSM measurements on [Ta/CoFeB/MgO]$_4$ t_{CoFeB}=1.50 nm with significant variations in coercivity with temperature, with a crossover into a double-hysteresis at 300 K. Moving to RFMR in (b) we show a qualitative comparisons between 100 K (θ_H=4°) and 300 K (θ_H=0°). Significant differences are observed in H_0 and 2 GHz, however the resulting RFMR profiles were too similar to warrant a modelling reconstruction. This was most likely due to the temperature range being too small for the chosen sample, whereas a more thorough investigation into more extreme temperatures across more samples would likely find a stronger case for temperature dependence.

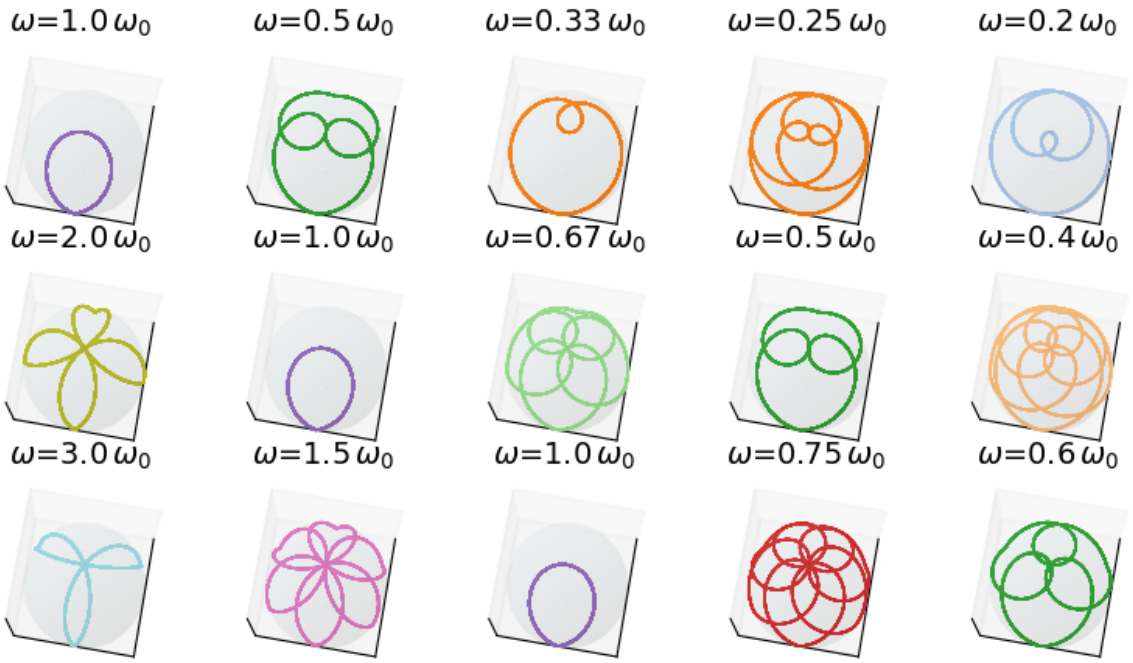


Figure 8.20: Periodic stable orbits of a 2D oscillator under continuous RF driving at frequency ω, analogous to steady-state solutions of the LLG equation, projected onto a 3D sphere. Each orbit ($r(\theta) = \cos\left(\frac{n}{d}\theta\right)$) yields a sinusoidal component in RFMR delay scans at $\omega = \omega_0$, but can be uniquely identified through polarisation-resolved measurements (PC, LH, LV).

8.8 Beyond the Macrospin Model: Ultra-Dense Non-Linear Magnetisation Dynamics

The macrospin approximation, while successful in describing uniform precession in many FMR-based devices, is ultimately governed by the fascinating Landau-Lifshitz-Gilbert equation [204]. From a chaos theory perspective, even simple dynamical systems can exhibit rich, nonlinear behaviour under the right conditions [205]. As shown in the RFMR fits Figure 8.18, and their complimentary dynamic range (Signal to Noise ratio) Figure 8.21(a), the RFMR signal in our $[\mathrm{Ta/CoFeB}(t_{\mathrm{CFB}})/\mathrm{MgO}]_4$ multilayer series exhibits an abrupt suppression below a critical thickness of 1.25 nm. Crucially, this loss of signal does not follow a simple reduction in magnetic volume: SQUID-VSM data (Figure 8.6(c)) confirm that finite out-of-plane remanence persists well below this threshold. This discrepancy indicates a transition in the underlying magnetisation dynamics at the ultrathin limit.

This can potentially be explained by Figure 8.20, which shows the family of stable periodic orbits arising from continuous RF driving at frequency ω. These are described by the functional form $r(\theta) = \cos\left(\frac{n}{d}\theta\right)$ and mapped onto the surface of a unit sphere to represent constrained magnetisation trajectories. The resulting curves span a discrete set of closed orbits, each defined by a rational

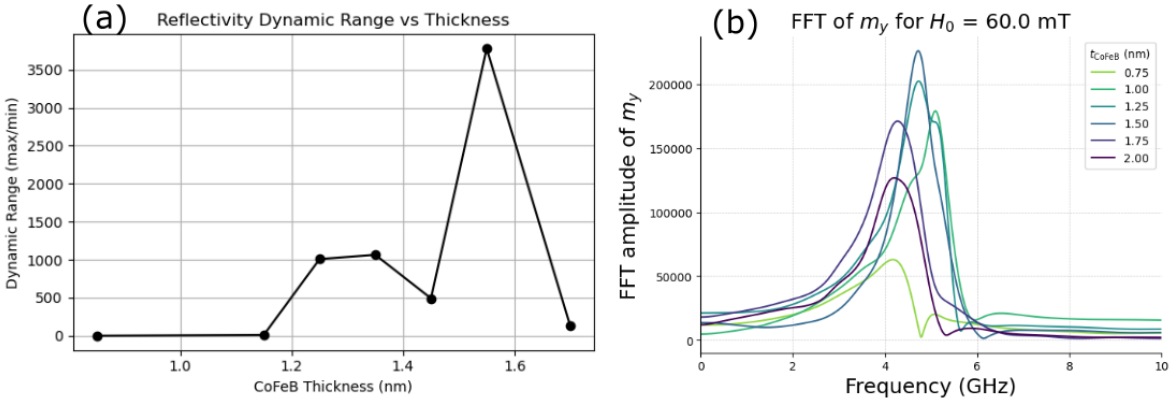


Figure 8.21: Evolution of magnetisation dynamics across the spin reorientation transition (SRT) in [Ta/CoFeB(t_{CoFeB})/MgO]$_4$ multilayers. (a) Experimental RFMR dynamic range (defined as the max/min of the signal amplitude) as a function of CoFeB thickness, showing an abrupt collapse below $t_{\mathrm{CoFeB}} \approx 1.25$ nm. This sharp drop is inconsistent with a gradual loss of magnetic volume and suggests a transition in the nature of the magnetisation dynamics. (b) Micromagnetic simulations of the average m_y FFT amplitude across the stack under a static field of 60 mT and central excitation frequency $\omega_0 \approx 5$ GHz reveal distinct resonance profiles above and below the SRT. At $t_{\mathrm{CoFeB}} = 1.50$ nm, a coherent precession mode is observed, while below 1.00 nm, the response becomes spatially fragmented and incoherent, indicative of strongly anharmonic and potentially non-linear dynamics at ultrathin thicknesses.

winding ratio $\omega/\omega_0 = n/d$, analogous to steady-state solutions of the LLG equation under periodic forcing. Plotted are examples with n=1→3 and d=1→5. Each orbit yields a sinusoidal component in RFMR delay scans at $\omega = \omega_0$.

To investigate the origin of this signal suppression, we performed micromagnetic simulations using the UBERMAG framework, modelling the FMR modals structure in $N = 4$. In Figure 8.21(b) we show varying t_{CoFeB} 0.75→2.0 nm at 60 mT. Above the SRT, the FFT amplitude of M_y peaks at 5.0 GHz, confirming coherent precession due to FMR. At thicknesses approaching the SRT, simulations reveal significant spectral broadening and mode hybridization. Across the SRT the resonance condition has shifted to 5.5 GHz. suggesting competition between interfacial anisotropies, exchange confinement, and dipolar fields. Finally below the SRT there is a complete annihilation of the coherent precession in this system. These results are consistent with a breakdown of the coherent macrospin mode into a spatially fragmented, non-linear regime.

To experimentally observe this, we performed polarisation-resolved RFMR measurements on the thinnest sample with a measurable signal. Using the unique sensitivity of circular (PC) and linear (LH, LV) polarisations, we isolate all three vectorial components of the dynamic magnetisation vector. This enables full vector reconstruction of the precession trajectory as a function of depth and pump–probe delay.

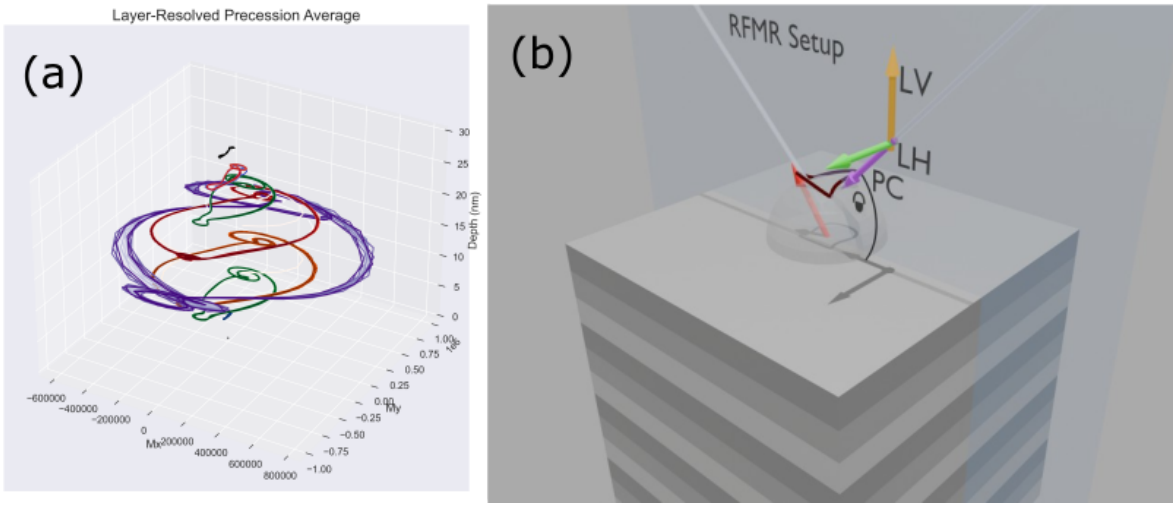


Figure 8.22: Complex FMR dynamics in complex heterostructures and their detection via RFMR. (a) Micromagnetic simulation of FMR in a $[Ta/CoFeB/MgO]_4$ multilayer shows that engineered depth-dependent magnetic properties, such as reduced saturation magnetisation at interfaces and suppressed exchange across MgO/Ta barriers, lead to intricate, non-uniform mode structures exhibiting spatially varying tilt and ellipticity. (b) Schematic of the RFMR experimental setup, illustrating polarisation-resolved detection using positive circular (PC), linear horizontal (LH), and linear vertical (LV) modes. This polarisation-resolved approach enables the decomposition of the full three-dimensional dynamic magnetisation vector, allowing depth-varying and non-sinusoidal precession profiles to be uniquely identified.

8.8.1 Experimental Measurement of Complex Dynamics

The complex orbitals shown in Figure 8.20 can appear degenerate if probed only along one direction. Furthermore, in RFMR, the temporal resolution is limited by the 35 ps X-ray pulse width and a maximum pump-probe delay of 600 ps, restricting a 2 GHz measurement to just over one period. Harmonics at lower frequencies cannot complete a full cycle within this window. Experimentally, it is more effective to increase count-time per point rather than sampling density, due to settling time constraints in the delay line and LIA. Thus, delay scans are typically acquired at or above the Nyquist rate (e.g., 25 ps spacing for a 4 GHz signal), sufficient for fitting the fundamental frequency but inherently suppressing higher-order effects.

These limitations mean that even subtle nonlinearities, such as those illustrated in Figure 8.20, are effectively buried. A practical workaround is to exploit the asymmetry between polarisation channels (PC, LH, LV). Even though M is constant, the PC channel captures contributions along the beam propagation, while LH probes the orthogonal in-plane direction. LV, orthogonal to both, is sensitive to out-of-plane dynamics. Co-fitting these channels enables full 3D vector reconstruction, beyonf the macrospin model, allowing unique identification of periodic stable orbits that are otherwise indistinguishable in single-polarisation delay scans.

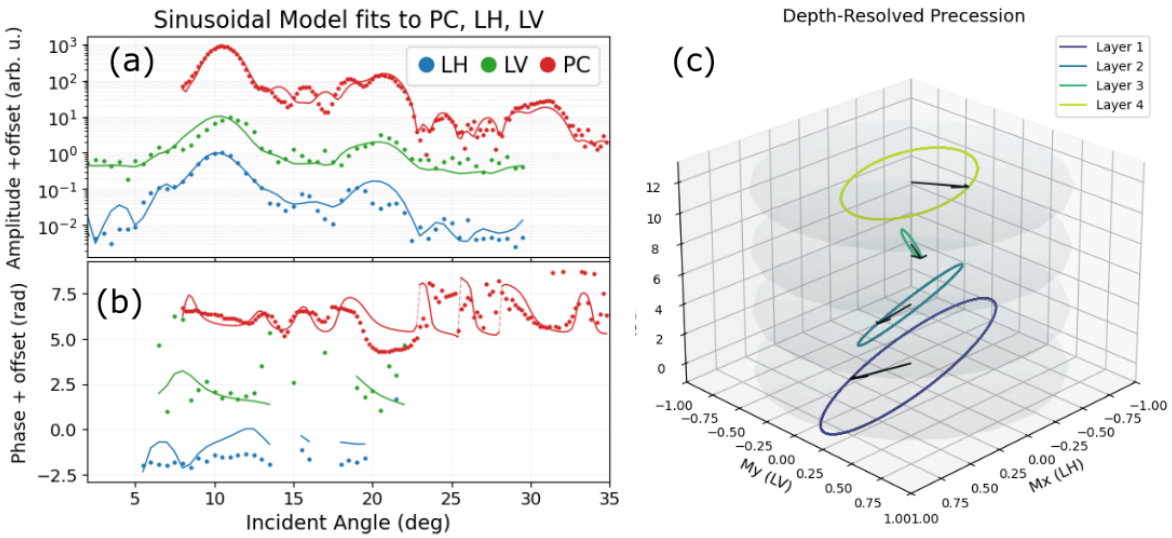


Figure 8.23: (a) RFMR spectra measured using three incident X-ray polarisations: circular (PC, red), linear horizontal (LH, blue), and linear vertical (LV, green). Each curve shows the fitted dynamic reflectivity signal amplitude as a function of incidence angle, revealing polarisation-dependent sensitivity to distinct magnetisation components. (c) Best-fit parameters (ξ and ψ trace the ellipse, and then ϕ denoted as the arrow) show each layer's trajectory as a 3D precessional path traced on a unit sphere, with asymmetry between LH, LV, and PC components. These highlight differences in opening angle and phase across the CoFeB stack, revealing non-uniform magnetisation dynamics across depth.

8.8.2 Three-Dimensional Vectorial Precession of Complex Dynamics in Heterostructures

In Figure 8.23 we show experimental measurements on [Ta/CoFeB/MgO]$_4$ with $t_{\mathrm{cfb}} = 1.25\,\mathrm{nm}$ (the thinnest sample with measurable RFMR signal) under PC (red, 4 GHz), LV (green, 6 GHz), and LH (blue, 6 GHz) polarisations. To interpret these data, we generalize Fig. (5.1) to a vectorial form of precession:

$$\begin{aligned}\mathbf{M}(t) = [M_x(t), M_y(t), M_z(t)] = \\ [M_0 \sin(\xi_{\mathrm{PC}}) \cos(\omega t + \phi_{\mathrm{PC}} + n\pi), \\ M_0 \sin(\xi_{\mathrm{LH}}) \left(\sin(\omega t + \phi_{\mathrm{LH}} + n\pi) \cos(\psi_{\mathrm{LH}}) - \sin(\psi_{\mathrm{LH}})\right), \\ M_0 \cos(\xi_{\mathrm{LV}}) \left(\cos(\omega t + \phi_{\mathrm{LV}} + n\pi) \sin(\psi_{\mathrm{LV}}) + \cos(\psi_{\mathrm{LV}})\right)]\end{aligned} \tag{8.11}$$

We include best-fit models using a macrospin approximation (each CoFeB layer oscillates as a single entity) and assume an $N = 4$ model where each structural repeat is identical. We further impose linear depth dependence for $M_0(z)$, $\xi(z)$, and $\phi(z)$, while allowing $\mathrm{d}\phi/\mathrm{d}z \in [-180°, +180°]$, thus enabling both acoustic and optical mode structures. It was determined that $\psi(z)$ is degenerate within this model since cone tilts are already captured by directional variations in the opening angle. This reduces the model to 6 free variables: ξ_0, $\mathrm{d}\xi/\mathrm{d}z$, $M_{0,0}$, $\mathrm{d}M_0/\mathrm{d}z$, ϕ_0, $\mathrm{d}\phi/\mathrm{d}z$, with an additional six parameters from the scattering factors determined via sensitivity analysis. Best fits were obtained by

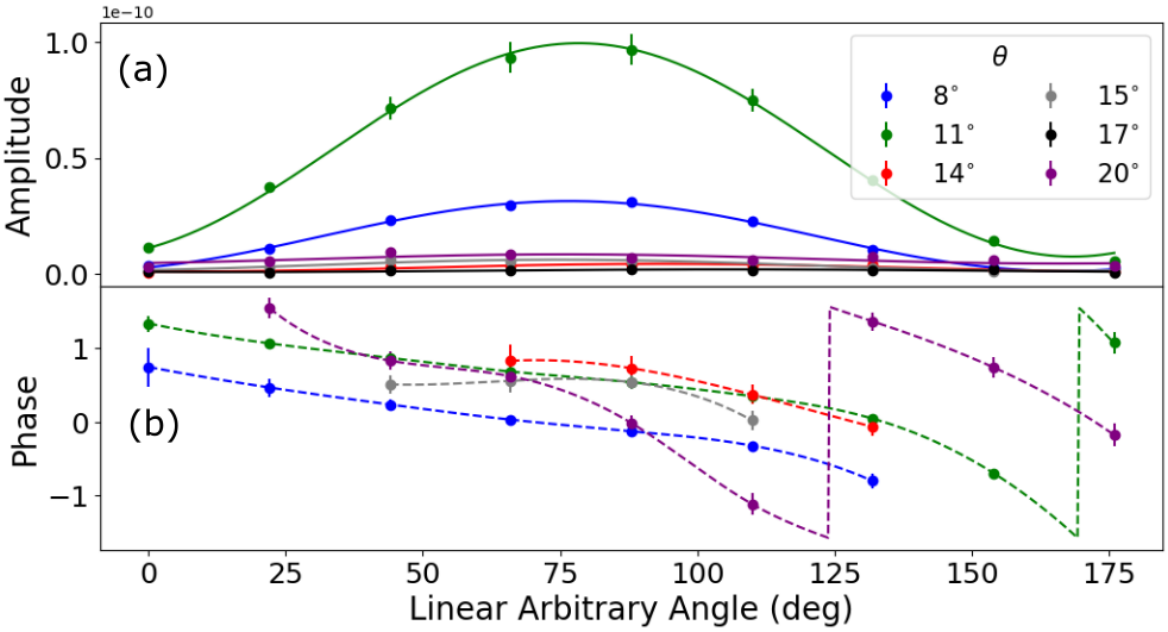


Figure 8.24: RFMR response as a function of linear arbitrary polarisation angle (LAA) for a range of fixed incident X-ray angles θ. (a) Extracted precession amplitude as a function of LAA. A sinusoidal dependence is expected and fit to the data, showing good agreement across all incident angles. (b) Corresponding precession phase extracted from the same fits. Phase values are only plotted when the amplitude exceeds a reliability threshold. Dashed lines represent interpolated and low-pass filtered phase traces, included as a guide to the eye.

minimising the custom cost function (Fig. 5.3). optimisation combined gradient descent with DE, but all datasets were ultimately refined using DE within physically motivated and mathematically guided bounds and shown in Figure 8.23. Experimental and simulated data were initially fitted with $A(\mathbf{Q}_z)$ and $P(\mathbf{Q}_z)$ assumed continuous; only for visualisation was $P(\mathbf{Q}_z)$ wrapped to $[0, 2\pi]$ (jumps shown shown as vertical dashed lines). Amplitude and phase curves are vertically offset for clarity, and phase values are not shown when amplitude falls below the noise threshold. Inconsistencies in the fit are attributed to simplifications in the model, specifically the $N = 4$ structural repetition and macrospin approximation. While this result emerges purely from a mathematical optimisation, a sensitivity analysis confirmed that it corresponds to a true local (or global) minimum within the defined parameter space. It is particularly satisfying that the resulting depth-dependent magnetisation profile is consistent with both the independent XRMR measurements from Figure 8.11, which indicate enhanced magnetism near the outer CoFeB layers, and the UBERMAG simulations, which reveal distinct variations in ellipticity as a function of depth. This interpretation is further supported by Figure 8.24, where we demonstrate the changing polarisation dependence of the magnetisation dynamics. While the amplitude of the dynamic signal follows a sinusoidal dependence on linear arbitrary angle (LAA) polarisation, as expected from previous results [18, 19], the phase exhibits a steeper variation with LAA at higher $\mathbf{Q_z}$. This behaviour is indicative of increasing phase offsets between precessing layers

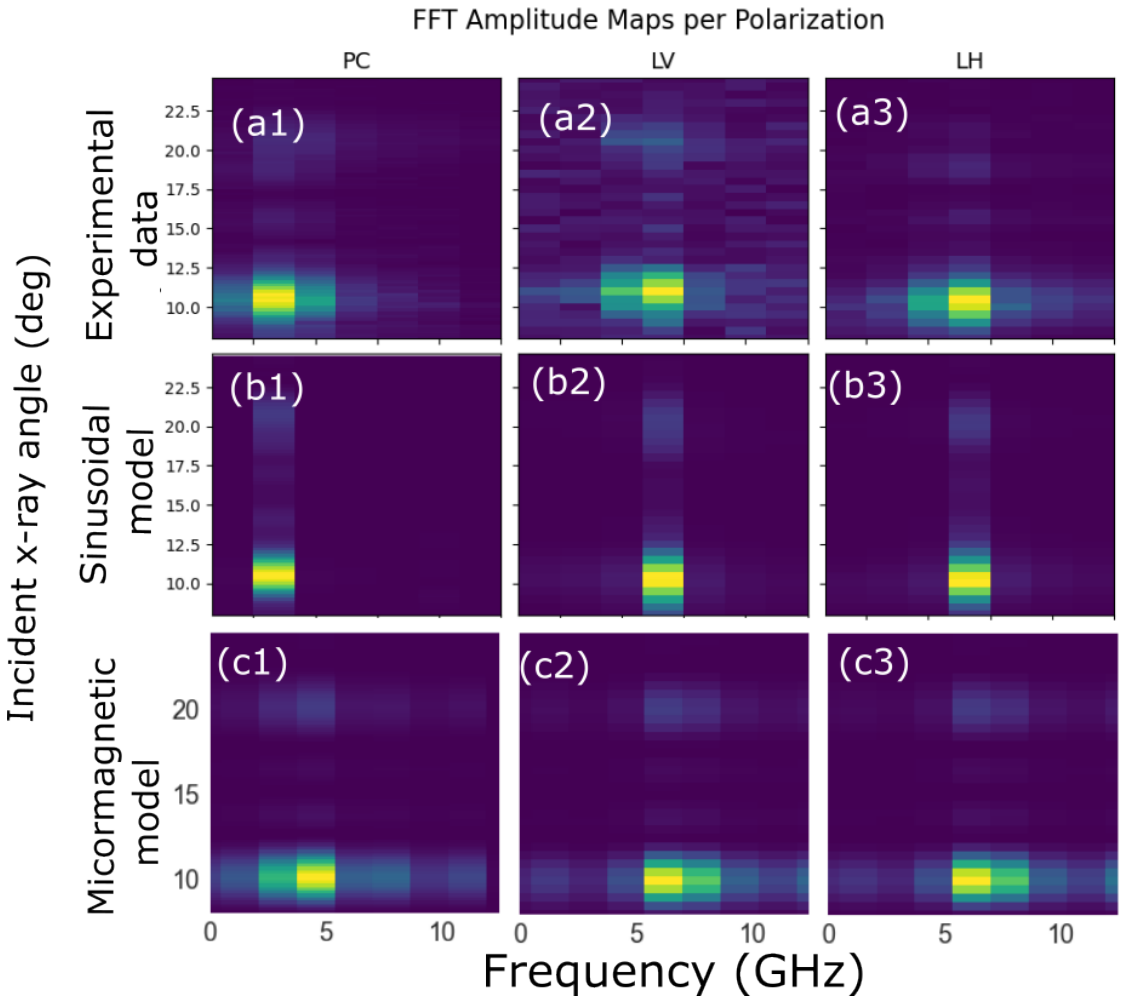


Figure 8.25: Comparison of experimental (a), sinusoidal simulated reflectivity (b), and micromagnetic reflectivity model (c) FFT spectra of the RFMR signal. With each polarisation channel (PC=(1)), (LV=(2)), (LH=(3)). The experiment shows spectral leakage and harmonic content, not reproduced by the sinusoidal precession model.

with depth, consistent with a model of out-of-phase, depth-dependent precession [16].

In Figure 8.25, we compare the FFT spectra of experimental and simulated signals. The experimental data exhibit clear spectral leakage and contributions from non-driven frequencies, which are absent in the simulation assuming purely sinusoidal precession. Since non-periodic components are suppressed by the phase-modulated lock-in detection, we attribute this leakage to stable periodic orbits and their modal hybridization with the Kittel mode. To capture this, we replace the analytic sinusoidal precession in our model with time-series magnetisation data extracted from a micromagnetic simulation of $[Ta/CoFeB/MgO]_4$ under continuous excitation from Figure 8.21(b). This method, described in Chapter 6, Sec. 6.6, allows non-driven frequencies to propagate through the reflectivity calculation, accurately reproducing the experimental FFT features and lending support to our interpretation of stable periodic orbits emerging in this ultra-dense, non-linear system.

By including the micromagnetic results into the reflectivity model, we can accurately capture the

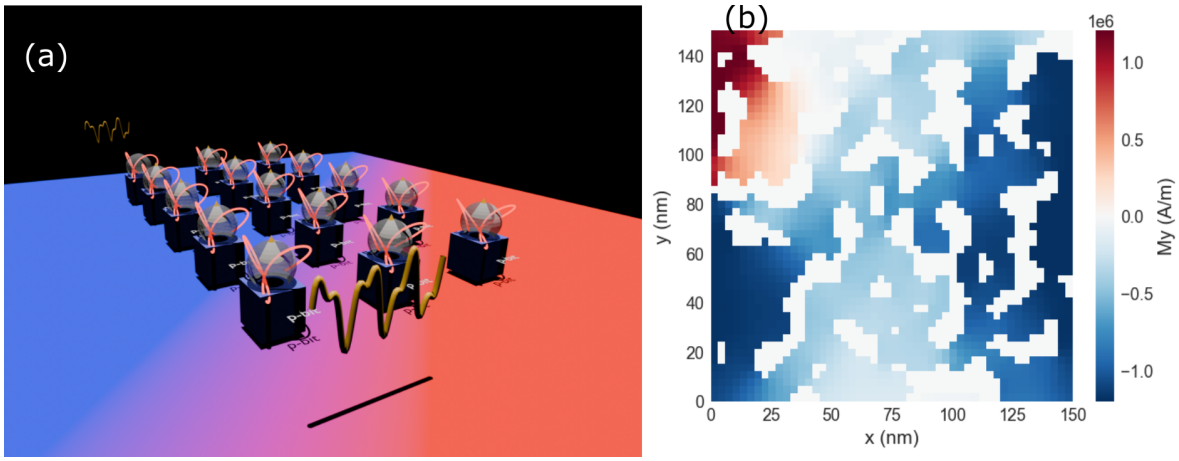


Figure 8.26: Concept and simulation of a neuromorphic computing device based on dipolar-coupled $[Ta/CoFeB/MgO]_4$ nanopillar arrays. (a) Schematic of the proposed architecture, in which input excitation is delivered via a coplanar waveguide (CPW) to a structured array of $[Ta/CoFeB/MgO]_4$ nanopillars. (b) UBERMAG simulations of the activation dynamics show spatially varying resonance patterns, driven by dipolar coupling across the array. The propagation pathways evolve non-linearly as a function of local magnetic conditions, which are tuned through thickness-dependent SRT, enabling dynamic reconfigurability essential for neuromorphic information processing.

experimental data spectral broadening. Simulations were tested to attempt to reconstruct the specific amplitudes and phases of the non-driven frequencies, however introducing these as open variables into the DE completely overwhelmed the optimiser and rendered results uninterpretable.

8.8.3 Device Implications

The future of computation lies in embracing complexity [206, 207]. Traditional von Neumann architectures are inherently deterministic and thus ill-suited for the complex, reasoning-based tasks increasingly required by next-generation intelligent systems. In response, significant research has explored alternative paradigms inspired by the architecture of the human brain [208]. Among these, wave-based and physically governed computing has long been a core goal in emerging computational paradigms [209, 210]. Prominent examples include device proposals based on spin-wave interference and non-linear dynamics [211, 212, 213], typically implemented on YIG substrates incorporating PMA scatterers to induce non-linearity at high excitation amplitudes.

Our concluding remarks are directly inspired by this concept, but we postulate that similar non-linear behaviour can be achieved in a denser system, operating at lower amplitudes, by replacing the YIG-based architecture with arrays of $[Ta/CoFeB/MgO]_4$ nanopillars. Through tuning the FMR depth-profile of individual pillars (such as through temperature (see Section 8.7.1), strain, or optical switching) one can construct a trainable array for non-linear computation, such as Boolean logic gates [214] or signal processing [215].

This concept is qualitatively illustrated in Figure 8.26(a), which shows a schematic rendered in *Blender*. A central input signal is launched via a coplanar waveguide (CPW) and excites the first row of nanopillars. Dipolar interactions between nearest neighbours enable signal propagation across the array, with readout occurring at the far end, mimicking the mechanism proposed in prior neuromorphic models [216].

To further explore this architecture, Figure 8.26(b) shows a simulated example of such an array using `Ubermag` to model magnetisation dynamics. In this model, the substrate (here $N = 4$) was modified via altering the structural roughness using the *Perlin Noise* implementation detailed early. The roughness factor and thickness were designed to locally vary the magnetisation thickness across the SRT. As the system relaxes there is spontaneous emergence of non-linear propagation pathways across the matrix, suggesting a potential basis for future ultra-dense computing paradigms.

Chapter 9

Conclusions & Outlook

This thesis has developed and applied *Reflectivity Ferromagnetic Resonance* as a method for probing depth-resolved magnetisation dynamics in magnetic thin films and multilayers. By integrating the nanometre-scale depth sensitivity of X-ray Resonant Magnetic Reflectivity with the picosecond-scale temporal resolution of X-ray detected Ferromagnetic Resonance, this work has sought to reconstruct layer-specific, three-dimensional precessional motion. A cornerstone of this research was the recognition of the need for, and hence the development of, an advanced modelling framework capable of simulating and fitting RFMR data.

The capabilities of RFMR were demonstrated through a series of three progressive case studies. First, the analysis of a single magnetic NiFe film revealed that a macrospin model is likely insufficient, with the uniform mode with damped precession at the interfaces providing an enhanced fit. This study also highlighted the technique's sensitivity to the RF waveform, where the depth-profile was constructed via co-fitting RFMR measurements taken with distinct RF waveform excitations (sinusoidal and distorted).

The investigation was then extended to magnetic trilayers. A detailed study of the NiFe/Cr/CoFeB trilayer system was conducted. SQUID-VSM and VNA-FMR revealed an RKKY interaction, in-plane spin-pumping, and acoustic and optical modes when the field was applied out-of-plane. The depth-profile of the static magnetisation was mapped using element-specific XRMR. Using RFMR, the phase and amplitude of precessional magnetisation were resolved within the individual layers, revealing distinct depth-dependent behaviours for each FMR mode. Both the optical and acoustic modes could be identified, and mapped in RFMR. Within the CoFeB layer, a phase lag was potentially observed within an interfacial region of thickness ~0.8 nm, which was absent in both the Cr and NiFe layers. Finally, the FMR mode depth profile was shown to be tunable via the applied static field. This

was corroborated by micromagnetic simulations suggesting that dipolar coupling between weakly precessing layers can induce phase lags.

Finally, the full power of RFMR was deployed to study a complex [Ta/CoFeB/MgO]$_4$ heterostructure. The project was initially simplified to a four-oscillator model, reducible to a Toeplitz matrix, yielding four eigenmodes, each with a unique depth dependence. Micromagnetic simulations (using experimentally extracted parameters) visualised a spin reorientation transition (SRT) at approximately 1.50 nm. To better model this, an implementation of Perlin noise was incorporated into `Ubermag` to emulate structural roughness. This roughness imprinted onto the magnetic state, particularly near the SRT, and produced stark changes in the local susceptibility. VSM, VNA-FMR, MFM, XMCD, and XRMR were conducted on the sample series [Ta/CoFeB/MgO]$_4$ with $t_{\mathrm{CoFeB}} = 1.70\,\mathrm{nm} \rightarrow 0.85\,\mathrm{nm}$. RFMR was used to identify two unique FMR modes, which were invisible to conventional, volume-integrating techniques such as VNA-FMR. Models suggested the lower energy mode demonstrated more homogeneous precession across the film, with an easy-axis parallel to the surface normal and a reduction in the opening angle at the MgO/CoFeB interfaces of 30%, however the higher energy mode shows an easy axis 22° off the surface normal, with an increased reduction of the opening angle to 50% at these interfaces. A thickness-dependent study across the SRT revealed significant complexity in [Ta/CoFeB/MgO]$_4$ with $t_{\mathrm{CoFeB}} < 1.2\,\mathrm{nm}$. Micromagnetic simulations were conducted at and below this threshold, suggesting that the macrospin model begins to break down in these ultrathin layers, with non-linear dynamics emerging. By leveraging RFMR measurements at multiple polarisations, the full three-dimensional vectorial precession was reconstructed as a function of depth at $t_{\mathrm{CoFeB}} < 1.25\,\mathrm{nm}$. This analysis uncovered complex, non-elliptical precession trajectories, interpreted as stable periodic orbits of the LLG equation, and underscored the importance of interfacial effects and the spin reorientation transition in generating these non-linear dynamics. Based on these findings, a hypothetical device architecture was proposed, incorporating ultra-dense non-linear magnetisation dynamics to enable complex signal processing.

Looking forward, this work lays the foundation for future investigations into a wide array of magnetic phenomena. Immediate applications of RFMR include detailed studies of spin-current absorption and the emergence of chirality in non-collinear magnetic systems. With the advent of upcoming beamlines such as Diamond Light Source's flagship beamline, I17, the enhanced coherence will enable the extension of synchrotrons to probe the FMR depth profiles of more exotic quantum materials, including those with topological spin textures such as skyrmions. However, the true future of this time- and depth-resolved technique lies with potential incorporation into XFELs, where the femtosecond time resolution will open up new possibilities for scientific research.

9.1 List of Contributions

- **Talk:** Testing the Ferromagnetic Resonance Macrospin Model in Magnetic Trilayers – IOP Magnetism, Sheffield (2025)
- **Talk:** Stacking Spinning Tops: How to Distinguish Magnetic Dynamics Between Chemically Identical Layers – IOP Magnetism, Loughborough (2024)
- **Talks:** Reflectivity Ferromagnetic Resonance: A Novel Technique for Depth-Resolved Magnetisation Dynamics – IOP Magnetism, Manchester (2023) & Oxford Symposium for Quantum Materials (2022)
- **Talks:** Analysis and Detection of Liquid Skyrmion State Using REXS – IOP CMQM, Bath (2022) & Cambridge Internal Skyrmion Project Meeting (2022)
- **Poster & Talk:** Measurement of the Pseudo-Liquid Skyrmion State Using REXS – IOP Magnetism, York (Poster, 2022) & Warwick Internal Skyrmion Project Meeting (Talk, 2021)
- **Software Contribution:** A Python implementation to model depth-dependent magnetisation dynamics, available on GitHub:JackBollard.

Bibliography

[1] J. Pendry. “Tripping the light fantastic.” In: *Nature* 294, (1981), 109–110.

[2] G. Greaves et al. “Near-edge X-ray absorption spectra for metallic Cu and Mn”. In: *Nature* 294 (1981), pp. 139–142.

[3] G. Greaves et al. “Two million hours of science”. In: *Nat. Mater.* 7 (2008), pp. 827–830.

[4] G. van der Laan and A. I. Figueroa. “X-ray magnetic circular dichroism—A versatile tool to study magnetism”. In: *Coord. Chem. Rev.* 277-278 (2014), pp. 95–129.

[5] B. Thole, G. Van Der Laan, and G. Sawatzky. “Strong Magnetic Dichroism Predicted in the $M_{4,5}$ X-Ray Absorption Spectra of Magnetic Rare-Earth Materials”. In: *Phys. Rev. Lett.* 55.19 (1985), 2086 – 2088.

[6] G. Van Der Laan et al. “Experimental proof of magnetic x-ray dichroism”. In: *Phys. Rev. B* 34.9 (1986), 6529 – 6531.

[7] G. van der Laan. “Soft x-ray resonant magnetic scattering of magnetic nanostructures”. In: *C. R. Phys.* 9.5 (2008), p. 570.

[8] S. Macke and E. Goering. “Magnetic reflectometry of heterostructures”. In: *J. Phys.: Condens. Matter* 26.36 (2014), p. 363201.

[9] J. Daillant and A. Gibaud, eds. *X-ray and Neutron Reflectivity: Principles and Applications*. Vol. 770. Lecture Notes in Physics. Springer Berlin Heidelberg, 2009, pp. XIV + 350.

[10] S. Brück. “Magnetic Resonant Reflectometry on Exchange Bias Systems”. Ph.D. thesis. University of Stuttgart, 2009.

[11] D. M. Burn et al. “Spin orbit torque driven magnetization reversal in CoFeTaB/Pt probed by resonant x-ray reflectivity”. In: *Phys. Rev. B* 106 (9 2022), p. 094429.

[12] G. van der Laan. “Time-resolved x-ray detected ferromagnetic resonance of spin currents”. In: *J. Electron Spectrosc. Relat. Phenom.* 220 (2017), pp. 137–146.

[13] E. Arenholz and S. O. Prestemon. “Design and performance of an eight-pole resistive magnet for soft x-ray magnetic dichroism measurements”. In: *Rev. Sci. Instrum.* 76.8 (2005), p. 083908.

[14] G. van der Laan and T. Hesjedal. “X-ray detected ferromagnetic resonance techniques for the study of magnetization dynamics”. In: *Nucl. Instrum. Methods Phys. Res., Sect. B* 540 (2023), pp. 85–93.

[15] T. Beale et al. “RASOR: An advanced instrument for soft x-ray reflectivity and diffraction”. In: *Rev. Sci. Instrum.* 81 (2010), p. 073904.

[16] D. M. Burn et al. “Depth-resolved magnetization dynamics revealed by x-ray reflectometry ferromagnetic resonance”. In: *Phys. Rev. Lett.* 125 (2020), p. 137201.

[17] D. A. Arena. “Shining a Light on Hidden Spin Dynamics”. In: *Physics* 13 (2020), p. 83.

[18] D. M. Burn et al. “Mode-resolved detection of magnetization dynamics using diffractive ferromagnetic resonance”. In: *Nano Lett.* 20 (2020), pp. 345–352.

[19] D. M. Burn et al. “Magnetization dynamics in ordered spin structures revealed by diffractive and reflectometry ferromagnetic resonance”. In: *AIP Adv.* 11 (2021), p. 015327.

[20] V. Chardonnet et al. “Toward ultrafast magnetic depth profiling using time-resolved x-ray resonant magnetic reflectivity”. In: *Struct. Dyn.* 8.3 (2021), p. 034305.

[21] “The circles of light”. In: *Nat. Rev. Mater.* 3.9 (2018), pp. 281–282.

[22] O. Yalcin. *Ferromagnetic Resonance*. Rijeka: IntechOpen, 2013.

[23] J. F. Cochran, B. Heinrich, and A. S. Arrott. “Ferromagnetic-resonance in a system composed of a ferromagnetic substrate and an exchange-coupled thin ferromagnetic overlayer”. In: *Phys. Rev. B* 34 (1986), pp. 7788–7801.

[24] P. J. Metaxas et al. “Dynamic binding of driven interfaces in coupled ultrathin ferromagnetic layers”. In: *Phys. Rev. Lett.* 104 (2010), p. 237206.

[25] W. E. Bailey et al. “Precessional dynamics of elemental moments in a ferromagnetic alloy”. In: *Phys. Rev. B* 70 (2004), p. 172403.

[26] M. K. Marcham et al. “Phase-resolved x-ray ferromagnetic resonance measurements of spin pumping in spin valve structures”. In: *Phys. Rev. B* 87 (2013), 180403(R).

[27] G. B. G. Stenning et al. “Magnetization dynamics in an exchange-coupled NiFe/CoFe bilayer studied by x-ray detected ferromagnetic resonance”. In: *New J. Phys.* 17 (2015), p. 013019.

[28] M. Dabrowski et al. “Coherent transfer of spin angular momentum by evanescent spin waves within antiferromagnetic NiO”. In: *Phys. Rev. Lett.* 124 (2020), p. 217201.

[29] M. Dabrowski et al. “Optically and microwave induced magnetization precession in [Co/Pt]/NiFe exchange springs”. In: *ACS Appl. Mater. Interfaces* 12 (2020), pp. 52116–52124.

[30] D. M. Burn et al. “Spin pumping through nanocrystalline topological insulators”. In: *Proc. SPIE.* 34.27 (2023), p. 275001.

[31] A. A. Baker et al. “Spin pumping in Ferromagnet-Topological Insulator-Ferromagnet Heterostructures”. In: *Sci. Rep.* 5 (2015), p. 7907.

[32] J. Wieczorek et al. “Separation of ultrafast spin currents and spin-flip scattering in Co/Cu(001) driven by femtosecond laser excitation employing the complex magneto-optical Kerr effect”. In: *Phys. Rev. B* 92 (17 2015), p. 174410.

[33] I. Kumberg et al. “Ultrafast laser-induced magneto-optical changes in resonant magnetic x-ray reflectivity”. In: *Phys. Rev. B* 108 (5 2023), p. 054439.

[34] H. Zabel and S. D. Bader. *Magnetic Heterostructures: Advances and Perspectives in Spinstructures and Spintransport*. Vol. 227. Springer Tracts in Modern Physics. Berlin, Heidelberg: Springer, 2007.

[35] W. Li et al. “Anatomy of Skyrmionic Textures in Magnetic Multilayers”. In: *Adv. Mater.* 31 (2019), p. 1807683.

[36] A. Hirohata et al. “Review on spintronics: Principles and device applications”. In: *J. Magn. Magn. Mater.* 509 (2020), p. 166711.

[37] J. M. D. Coey. *Magnetism and Magnetic Materials*. Cambridge: Cambridge University Press, 2010.

[38] B. Heinrich et al. “Magnetic anisotropies and exchange coupling in ultrathin fcc Co(001) structures”. In: *Phys. Rev. B* 44 (17 1991), pp. 9348–9361.

[39] J. F. Cochran et al. “Magnetic anisotropies in ultrathin fcc Fe(001) films grown on Cu(001) substrates”. In: *Phys. Rev. B* 45 (1992), pp. 4676–4685.

[40] G. Kirichuk et al. *Origin of perpendicular magnetic anisotropy in ultra-thin metal films studied by in-situ neutron reflectometry*. Preprint. 2025.

[41] J. Yu et al. “Thermal annealing effect on FeCoB soft underlayer for perpendicular magnetic recording”. In: *J. Appl. Phys.* 91.10 (2002), pp. 8357–8359.

[42] W. X. Wang et al. “The perpendicular anisotropy of Co40Fe40B20 sandwiched between Ta and MgO layers and its application in CoFeB/MgO/CoFeB tunnel junction”. In: *Appl. Phys. Lett.* 99.1 (2011), p. 012502.

[43] C.-W. Cheng et al. “Effect of cap layer thickness on the perpendicular magnetic anisotropy in top MgO/CoFeB/Ta structures”. In: *J. Appl. Phys.* 110.3 (2011), p. 033916.

[44] I. Dzyaloshinskii. “A thermodynamic theory of “weak” ferromagnetism of antiferromagnetics”. In: *J. Phys. Chem. Solids* 4.4 (1958), pp. 241–255.

[45] T. Moriya. “Anisotropic superexchange interaction and weak ferromagnetism”. In: *Physical Review* 120.1 (1960), pp. 91–98.

[46] J. Torrejon et al. “Interface control of the magnetic chirality in CoFeB/MgO heterostructures with heavy-metal underlayers”. In: *Nat. Commun.* 5 (2014), p. 4655.

[47] X. Ma et al. “Interfacial control of Dzyaloshinskii-Moriya interaction in heavy metal/ferromagnetic metal thin film heterostructures”. In: *Phys. Rev. B* 94 (18 2016), p. 180408.

[48] P. Grünberg et al. “Layered Magnetic Structures: Evidence for Antiferromagnetic Coupling of Fe Layers across Cr Interlayers”. In: *Phys. Rev. Lett.* 57.19 (1986), pp. 2442–2445.

[49] C. F. Majkrzak et al. “Observation of a Magnetic Antiphase Domain Structure with Long-Range Order in a Synthetic Gd–Y Superlattice”. In: *Phys. Rev. Lett.* 56.25 (1986), pp. 2700–2703.

[50] A. Fert et al. “Layered magnetic structures: interlayer exchange coupling and giant magnetoresistance”. In: *J. Magn. Magn. Mater.* 140-144 (1995), pp. 1–8.

[51] B. Heinrich and J. A. C. Bland. *Ultrathin Magnetic Structures II: Measurement Techniques and Novel Magnetic Properties*. Springer, 1994.

[52] U. Kobler et al. “Higher order interaction terms in coupled Fe/Cr/Fe sandwich structures”. In: *J. Magn. Magn. Mater.* 103.1–3 (1992), pp. 236–244.

[53] A. Azevedo et al. “Biquadratic exchange coupling in sputtered (100) Fe/Cr/Fe”. In: *Phys. Rev. Lett.* 76.25 (1996), pp. 4837–4840.

[54] C. Chesman et al. “Magnetic trilayers with bilinear and biquadratic exchange couplings: Criteria for the measurement of J_1 and J_2”. In: *Phys. Rev. B* 58.1 (1998), pp. 101–104.

[55] S. S. P. Parkin, N. More, and K. P. Roche. “Oscillations in exchange coupling and magnetoresistance in metallic superlattice structures: Co/Ru, Co/Cr, and Fe/Cr”. In: *Phys. Rev. Lett.* 64 (19 1990), pp. 2304–2307.

[56] P. Bruno and C. Chappert. “Oscillatory coupling between ferromagnetic layers separated by a nonmagnetic metal spacer”. In: *Phys. Rev. Lett.* 67 (12 1991), pp. 1602–1605.

[57] M. Stiles. “Interlayer exchange coupling”. In: *J. Magn. Magn. Mater.* 200.1 (1999), pp. 322–337.

[58] P. W. T. Pong et al. “Detection of pinholes in magnetic tunnel junctions by magnetic coupling”. In: *J. Appl. Phys.* 103 (2008), 07A902.

[59] R. Damon and J. Eshbach. “Magnetostatic modes of a ferromagnet slab”. In: *J. Phys. Chem. Solids* 19.3 (1961), pp. 308–320.

[60] P. Grünberg. “Magnetostatic spinwave modes of a ferromagnetic double layer”. In: *J. Appl. Phys.* 51.8 (1980), pp. 4338–4341.

[61] S. Li et al. “Tunable Optical Mode Ferromagnetic Resonance in FeCoB/Ru/FeCoB Synthetic Antiferromagnetic Trilayers under Uniaxial Magnetic Anisotropy”. In: *Adv. Funct. Mater.* 26.21 (2016), pp. 3738–3744.

[62] Y. Chen et al. “Designing and Tuning Magnetic Resonance with Exchange Interaction”. In: *Adv. Mater.* 27.8 (2015), pp. 1351–1355.

[63] C. Kittel. “On the theory of ferromagnetic resonance absorption”. In: *Phys. Rev.* 73 (1948), pp. 155–161.

[64] L. D. Landau, E. M. Lifshitz, and L. P. Pitaevskii. *Statistical Physics, Part 2*. Vol. 9. Course of Theoretical Physics. Oxford: Pergamon Press, 1980.

[65] T. Gilbert. “Classics in Magnetics A Phenomenological Theory of Damping in Ferromagnetic Materials”. In: *IEEE Trans. Magn.* 40 (2004), pp. 3443 –3449.

[66] A. A. Baker et al. “Modelling ferromagnetic resonance in magnetic multilayers: Exchange coupling and demagnetisation-driven effects”. In: *J. Appl. Phys.* 115.17 (2014), p. 17D140.

[67] M. Blume. “Magnetic scattering of x rays (invited)”. In: *J. Appl. Phys.* 57.8 (1985), pp. 3615–3618.

[68] J. Stöhr and H. C. Siegmann. *Magnetism: From Fundamentals to Nanoscale Dynamics*. 1st ed. Springer, 2006.

[69] J. Hill and D. McMorrow. “X-ray resonant exchange scattering: Polarization dependence and correlation functions”. English. In: *Acta Crystallogr. A* 52 (1996), pp. 236–244.

[70] J. P. Hannon et al. “X-Ray Resonance Exchange Scattering”. In: *Phys. Rev. Lett.* 61 (10 1988), pp. 1245–1248.

[71] L. Nevot and P. Croce. “Caractérisation des surfaces par réflexion rasante de rayons X. Application à l’étude du polissage de quelques verres silicates”. In: *Rev. Phys. Appl. (Paris)* 15.3 (1980), pp. 761–779.

[72] S. A. Stepanov and S. K. Sinha. “X-ray resonant reflection from magnetic multilayers: Recursion matrix algorithm”. In: *Phys. Rev. B* 61 (22 2000), pp. 15302–15311.

[73] J. Zak et al. “Magneto-optics of multilayers with arbitrary magnetization directions”. In: *Phys. Rev. B* 43 (8 1991), pp. 6423–6429.

[74] A. Frisk et al. “Glancing-angle deposition of magnetic in-plane exchange springs”. In: *Phys. Rev. Appl.* 20 (4 2023), p. 044027.

[75] A. Frisk et al. “Controlling In-Plane Magnetic Anisotropy of Co Films on MgO Substrates using Glancing Angle Deposition”. In: *Phys. Status Solidi A* 220.11 (2023), p. 2300010.

[76] S. K. Sinha et al. “X-ray and neutron scattering from rough surfaces”. In: *Phys. Rev. B* 38 (1988), p. 2297.

[77] Y. Chang et al. “Charge transfer and hybridization effects in Ni_3Al and Ni_3Ga studies by x-ray-absorption spectroscopy and theoretical calculations”. In: *J. Appl. Phys.* 87 (2000), pp. 1312–1317.

[78] A. A. Baker et al. “Anisotropic absorption of pure spin currents”. In: *Phys. Rev. Lett.* 116 (2016), p. 047201.

[79] A. M. Kaiser et al. “Nano and picosecond magnetization dynamics of weakly coupled CoFe/Cr/NiFe trilayers studied by a multitechnique approach”. In: *Phys. Rev. B* (13 2011), p. 134406.

[80] G. van der Laan. “Study of antiferromagnetic NiO using grazing incidence reflectivity and soft X-ray absorption”. In: *J. Magn. Magn. Mater.* 192.2 (1999), pp. 297–304.

[81] B. L. Henke, E. M. Gullikson, and J. C. Davis. “X-Ray Interactions: Photoabsorption, Scattering, Transmission, and Reflection at $E = 50$–$30{,}000$ eV, $Z = 1$–92”. In: *At. Data Nucl. Data Tables* 54.2 (1993), pp. 181–342. `https://henke.lbl.gov/optical_constants/` (Optical Constants Database).

[82] C. T. Chantler et al. *Chantler Atomic Scattering Factors*. 2005.

[83] C. T. Chantler. “Journal of Physical and Chemical Reference Data”. In: *J. Phys. Chem. Ref. Data* 24.1 (1995), pp. 71–643.

[84] C. T. Chantler. “Journal of Physical and Chemical Reference Data”. In: *J. Phys. Chem. Ref. Data* 29 (2000), pp. 597–1056.

[85] J. Stöhr and H. König. “Determination of spin- and orbital-moment anisotropies in transition metals by angle-dependent X-ray magnetic circular dichroism”. In: *Phys. Rev. Lett.* 75.20 (1995), 3748 – 3751.

[86] R. Nakajima, J. Stöhr, and Y. Idzerda. “Electron-yield saturation effects in l-edge x-ray magnetic circular dichroism spectra of Fe, Co, and Ni”. In: *Phys. Rev. B* 59.9 (1999), 6421 – 6429.

[87] J. M. Tonnerre et al. “Soft X-Ray Resonant Magnetic Scattering from a Magnetically Coupled Ag /Ni Multilayer”. In: *Phys. Rev. Lett.* 75 (4 1995), pp. 740–743.

[88] N. Telling et al. “Fe $M_{2,3}$ X-ray resonant magnetic reflectivity on epitaxial Fe3 – δO_4 thin films”. In: *Physica B* 345.1 (2004), p. 157.

[89] D. R. Lee et al. “X-ray resonant magnetic scattering from structurally and magnetically rough interfaces in multilayered systems. I. Specular reflectivity”. In: *Physical Review B* 68.22 (2003).

[90] J. Zak et al. “Theory of magneto-optical effects in films with arbitrary magnetization directions”. In: *Physical Review B* 46.9 (1992), pp. 5883–5893.

[91] M. Björck and G. Andersson. “GenX: An extensible X-ray reflectivity refinement program utilizing differential evolution”. In: *J. Appl. Crystallogr.* 40 (2007), pp. 1174–1178.

[92] J. Krieft et al. “Advanced data analysis procedure for hard x-ray resonant magnetic reflectivity discussed for Pt thin film samples of various complexity”. In: *J. Phys. D: Appl. Phys.* 53.37 (2020), p. 375004.

[93] R. Storn and K. Price. “Differential Evolution: A Simple and Efficient Adaptive Scheme for Global Optimization Over Continuous Spaces”. In: *J. Glob. Optim.* 23 (1995).

[94] J. Qiang, C. Mitchell, and A. Qiang. “Tuning of an Adaptive Unified Differential Evolution Algorithm for Global Optimization”. In: *IEEE Congr. Evol. Comput. (CEC)*. 2016, pp. 4061–4068.

[95] J. Lampinen. “A Constraint Handling Approach for the Differential Evolution Algorithm”. In: *Proc. 2002 Congress Evol. Comput. (CEC’02)*. Vol. 2. 2002, pp. 1468–1473.

[96] L. Yang and A. Shami. “On hyperparameter optimization of machine learning algorithms: Theory and practice”. In: *Neurocomputing* 415 (2020), pp. 295–316.

[97] A. Tyagi. *Visualization and Optimization Techniques for High Dimensional Parameter Spaces*. Preprint. 2022.

[98] Z. Yang, K. Tang, and X. Yao. “Differential Evolution for High-Dimensional Function Optimization”. In: *IEEE Congr. Evol. Comput.* 2007, pp. 3523–3530.

[99] R. Kleinberg, Y. Li, and Y. Yuan. “An alternative view: When does SGD escape local minima?” In: *arXiv preprint arXiv:1802.06175* (2018).

[100] Y. N. Dauphin et al. “Identifying and attacking the saddle point problem in high-dimensional non-convex optimization”. In: *Adv. Neural Inf. Process. Syst.* 2014, pp. 2933–2941.

[101] F. Romor, M. Tezzele, and G. Rozza. “ATHENA: Advanced Techniques for High dimensional parameter spaces to Enhance Numerical Analysis”. In: *Software Impacts* 10 (2021), p. 100133.

[102] A. M. Gianni et al. “Enhancing Differential Evolution: A Dual Mutation Strategy with Majority Dimension Voting and New Stopping Criteria”. In: *Symmetry* 17.6 (2025).

[103] A. A. Baker et al. “Proposal of a micromagnetic standard problem for ferromagnetic resonance simulations”. In: *J. Magn. Magn. Mater.* 421 (2017), pp. 428–439.

[104] E. Lu, K. S. Buchanan, and K. L. Livesey. “Perpendicular standing spin waves in films with interfacial Dzyaloshinskii-Moriya interaction”. In: *Phys. Rev. B* 111 (6 2025), p. 064432.

[105] S. Zhang et al. *Spin Dynamics Mode Locking between Helimagnetism and Ferromagnetism*. Preprint. 2024.

[106] E. Arenholz and S. O. Prestemon. “Design and performance of an eight-pole resistive magnet for soft x-ray magnetic dichroism measurements”. In: *Rev. Sci. Instrum.* 76 (2005), p. 083908.

[107] H. Yan et al. “High-Quality NiFe Thin Films on Oxide/Non-Oxide Platforms via Pulsed Laser Deposition at Room Temperature”. In: *Adv. Mater. Interfaces* 11.9 (2024), p. 2300265.

[108] S Mizukami, Y Ando, and T Miyazaki. “Ferromagnetic resonance linewidth for NM/$Ni_{80}Fe_{20}$/NM films (NM=Cu, Ta, Pd and Pt)”. In: *J. Magn. Magn. Mater.* 226-230 (2001), pp. 1640–1642.

[109] C. Swindells et al. “Proximity-induced magnetism and the enhancement of damping in ferromagnetic/heavy metal systems”. In: *Appl. Phys. Lett.* 119.15 (2021), p. 152401.

[110] K. Sasage et al. “Modulation of gyromagnetic ratio in $Ni_{81}Fe_{19}$ thin film due to spin pumping”. In: *J. Magn. Magn. Mater.* 322.9 (2010), pp. 1425–1427.

[111] S.-I. Kim et al. “Abnormal spin-pumping effect at Pt/NiFe interface by an oxidation of ferromagnet”. In: *Curr. Appl. Phys.* 14.12 (2014), pp. 1743–1747.

[112] N. Leroux et al. “Classification of multi-frequency RF signals by extreme learning, using magnetic tunnel junctions as neurons and synapses”. In: *APL Mach. Learn.* 1.3 (2023), p. 036109.

[113] J. Chen, Y. Song, and A. Hirose. “Spintronic reservoir computing with interpretable nonlinearity”. In: *Phys. Rev. Res.* 7.1 (2025), p. 013310.

[114] A. J. Edwards, D. Bhattacharya, P. Zhou, et al. “Passive frustrated nanomagnet reservoir computing”. In: *Commun. Phys.* 6 (2023), p. 215.

[115] S. Das et al. “Magneto-ionic synapse for reservoir computing”. In: *Phys. Rev. Appl.* 23 (5 2025), p. 054043.

[116] T. Yokouchi et al. “Pattern recognition with neuromorphic computing using magnetic field–induced dynamics of skyrmions”. In: *Sci. Adv.* 8.39 (2022), eabq5652.

[117] “The Duffing Oscillator”. In: *Chaos: A Program Collection for the PC*. Berlin, Heidelberg: Springer Berlin Heidelberg, 2008, pp. 157–184.

[118] H. G. Bauer et al. “Nonlinear spin-wave excitations at low magnetic bias fields”. In: *Nat. Commun.* 6.1 (2015).

[119] M. P. Wismayer et al. “Nonlinear behavior for the uniform mode and horizontal standing spin-wave modes in metallic ferromagnetic microstrips: Experiment and theory”. In: *Phys. Rev. B* 85 (6 2012), p. 064411.

[120] G. Bertotti, I. D. Mayergoyz, and C. Serpico. “Chapter 7 - Magnetization Dynamics under Time-Harmonic Excitation”. In: *Nonlinear Magnetization Dynamics in Nanosystems*. Ed. by G. Bertotti, I. D. Mayergoyz, and C. Serpico. Elsevier Series in Electromagnetism. Oxford: Elsevier, 2009, pp. 153–192.

[121] W. Wawrzynski. “Duffing-type oscillator under harmonic excitation with a variable value of excitation amplitude and time-dependent external disturbances”. In: *Sci. Rep* 11.1 (2021), p. 2889.

[122] M. Maihöfer et al. “Transition state theory characterizes thin film macrospin dynamics driven by an oscillatory magnetic field: Inertial effects”. In: *Commun. Nonlinear Sci. Numer. Simul.* 115 (2022), p. 106764.

[123] G. Tanaka et al. “Recent advances in physical reservoir computing: A review”. In: *Neural Netw.* 115 (2019), pp. 100–123.

[124] D. Suess et al. “Exchange spring recording media for areal densities up to 10Tbit/in^2”. In: *J. Magn. Magn. Mater.* 290-291 (2005), pp. 551–554.

[125] R. Victora and X. Shen. “Composite media for perpendicular magnetic recording”. In: *IEEE Trans. Magn.* 41.2 (2005), pp. 537–542.

[126] S. Parkin and S.-H. Yang. “Study of spin pumping through alpha-Sn thin films”. In: *Phys. Status Solidi RRL* 15 (2021), p. 2100137.

[127] S. L. Zhang et al. “Topological computation based on direct magnetic logic communication”. In: *Sci. Rep.* 5 (2015), p. 15773.

[128] Y. Tserkovnyak et al. “Nonlocal magnetization dynamics in ferromagnetic heterostructures”. In: *Rev. Mod. Phys.* 77 (2005), p. 1375.

[129] G van der Laan. “Applications of soft x-ray magnetic dichroism”. In: *J. Phys.: Conf. Ser.* 430.1 (2013), p. 012127.

[130] J. Li et al. “Direct detection of pure AC spin-current by x-ray pump-probe measurements”. In: *Phys. Rev. Lett.* 117 (2016), p. 076602.

[131] L. Gladczuk et al. “Spin-current mediated exchange coupling in MgO-based magnetic tunnel junctions”. In: *Phys. Rev. B* 103 (2021), p. 064416.

[132] A. A. Baker et al. “Spin pumping in magnetic trilayer structures with an MgO barrier”. In: *Sci. Rep.* 6 (2016), p. 35582.

[133] A. I. Figueroa et al. “Spin pumping through a topological insulator probed by x-ray detected ferromagnetic resonance”. In: *J. Magn. Magn. Mater.* 400 (2016), p. 178.

[134] P. Grünberg et al. “Layered Magnetic Structures: Evidence for Antiferromagnetic Coupling of Fe Layers across Cr Interlayers”. In: *Phys. Rev. Lett.* 57 (19 1986), pp. 2442–2445.

[135] C. Peng, C. Dai, and D. Dai. “Oscillatory interlayer magnetic exchange coupling in $Ni_{80}Fe_{20}$/Cr multilayer structures”. In: *J. Appl. Phys.* 72.9 (1992), pp. 4250–4253.

[136] N. Salashchenko and E. Shamov. “Short-period X-ray multilayers based on CrSc”. In: *Opt. Commun.* 134.1 (1997), pp. 7–10.

[137] C. Du et al. “Systematic variation of spin-orbit coupling with d-orbital filling: Large inverse spin Hall effect in 3d transition metals”. In: *Phys. Rev. B* 90 (14 2014), p. 140407.

[138] Q. Zhang et al. “Terahertz emission from CoFeB/Cr/Pt trilayers: The role of Cr as both a spin current transporter and generator”. In: *Appl. Phys. Lett.* 118 (2021), p. 232401.

[139] R. Topkaya et al. “Ferromagnetic resonance studies of exchange coupled ultrathin Py/Cr/Py trilayers”. In: *J. Appl. Phys.* 108.2 (2010), p. 023910.

[140] P. Grünberg et al. “Layered Magnetic Structures: Evidence for Antiferromagnetic Coupling of Fe Layers across Cr Interlayers”. In: *Phys. Rev. Lett.* 57 (19 1986), pp. 2442–2445.

[141] M. Belmeguenai et al. “Frequency- and time-domain investigation of the dynamic properties of interlayer-exchange-coupled $Ni_{81}Fe_{19}/Ru/Ni_{81}Fe_{19}$ thin films”. In: *Phys. Rev. B* 76 (10 2007), p. 104414.

[142] J. Leal and M. Kryder. “Interlayer coupling in spin valve structures”. In: *IIEEE Trans. Magn.* 32.5 (1996), pp. 4642–4644.

[143] M. Dabrowski et al. “Canted standing spin-wave modes of permalloy thin films observed by ferromagnetic resonance”. In: *New J. Phys.* 23 (2021), p. 023017.

[144] C. Safeer et al. “Magnetization dynamics driven by displacement currents across a magnetic tunnel junction”. In: *Phys. Rev. Appl.* 22 (2 2024), p. 024019.

[145] A. A. Timopheev et al. “Dynamic exchange via spin currents in acoustic and optical modes of ferromagnetic resonance in spin-valve structures”. In: *Phys. Rev. B* 89 (14 2014), p. 144410.

[146] A. A. Baker et al. “Antidamping torques from simultaneous resonances in ferromagnet-topological insulator-ferromagnet heterostructures”. In: *J. Magn. Magn. Mater.* 473 (2019), pp. 470–476.

[147] J.-V. Kim and C. Chappert. “Magnetization dynamics in spin-valve structures with spin pumping”. In: *J. Magn. Magn. Mater* 286 (2005), p. 56.

[148] T. Taniguchi and H. Imamura. “Enhancement of the Gilbert damping constant due to spin pumping in noncollinear ferromagnet/nonmagnet/ferromagnet trilayer systems”. In: *Phys. Rev. B* 76.9 (2007), p. 092402.

[149] A. Ghosh et al. “Penetration Depth of Transverse Spin Current in Ultrathin Ferromagnets”. In: *Phys. Rev. Lett.* 109 (12 2012), p. 127202.

[150] A. Brataas, Y. Nazarov, and G. Bauer. “Spin-transport in multi-terminal normal metal-ferromagnet systems with non-collinear magnetizations”. In: *Eur. Phys. J. B* 22.1 (2001), 99–110.

[151] C. J. Durrant et al. “Dependence of spin pumping and spin transfer torque upon $Ni_{81}Fe_{19}$ thickness in $Ta/Ag/Ni_{81}Fe_{19}/Ag/Co_2MnGe/Ag/Ta$ spin-valve structures”. In: *Phys. Rev. B* 96 (14 2017), p. 144421.

[152] S. S. Kalarickal et al. “Ferromagnetic resonance linewidth in metallic thin films: Comparison of measurement methods.” In: *J. Appl. Phys.* 99.9 (2006), p. 093909.

[153] M. D. Stiles and A. Zangwill. “Anatomy of spin-transfer torque”. In: *Phys. Rev. B* 66.1 (2002), p. 014407.

[154] A. Brataas et al. “Spin battery operated by ferromagnetic resonance”. In: *Phys. Rev. B* 66 (6 2002), p. 060404.

[155] A. A. Timopheev et al. “Dynamic exchange via spin currents in acoustic and optical modes of ferromagnetic resonance in spin-valve structures”. In: *Phys. Rev. B* 89 (14 2014), p. 144410.

[156] K. Lenz et al. “Evidence of spin-pumping effect in the ferromagnetic resonance of coupled trilayers”. In: *Phys. Rev. B* 69 (2004), pp. 144422–.

[157] A. Ruiz-Calaforra et al. “The role of the non-magnetic material in spin pumping and magnetization dynamics in NiFe and CoFeB multilayer systems”. In: *J. Appl. Phys.* 117 (2015), p. 163901.

[158] V. Bansal et al. “Depth-resolved magnetization profile of MgO/CoFeB/W perpendicular half magnetic tunnel junctions”. In: *AIP Adv.* 12 (2022), p. 035129.

[159] W. E. Bailey et al. “Detection of microwave phase variation in nanometre-scale magnetic heterostructures”. In: *Nat. Commun.* 4 (2013).

[160] B. Heinrich et al. “Spin Pumping at the Magnetic Insulator (YIG)/Normal Metal (Au) Interfaces”. In: *Phys. Rev. Lett.* 107 (6 2011), p. 066604.

[161] B. Heinrich et al. “Dynamic exchange coupling in magnetic bilayers”. In: *Phys. Rev. Lett.* 90.18 (2003), p. 187601.

[162] P Klaer et al. “Element-specific ferromagnetic resonance in epitaxial Heusler spin valve systems”. In: *Journal of Physics D: Applied Physics* 44.42 (2011), p. 425004.

[163] P. Omelchenko, B. Heinrich, and E. Girt. “Measurements of interlayer exchange coupling of Pt in Py|Pt|Py system”. In: *Appl. Phys. Lett.* 113.14 (2018), p. 142401.

[164] Y. Tserkovnyak, A. Brataas, and G. E. W. Bauer. “Spin pumping and magnetization dynamics in metallic multilayers”. In: *Phys. Rev. B* 66 (22 2002), p. 224403.

[165] S. Takahashi. “Giant enhancement of spin pumping in the out-of-phase precession mode”. In: *Appl. Phys. Lett.* 104.5 (2014), p. 052407.

[166] T. Chiba, G. E. W. Bauer, and S. Takahashi. “Magnetization damping in noncollinear spin valves with antiferromagnetic interlayer couplings”. In: *Phys. Rev. B* 92 (5 2015), p. 054407.

[167] Z. Zhang et al. “Using Ferromagnetic Resonance as a Sensitive Method to Study Temperature Dependence of Interlayer Exchange Coupling”. In: *Phys. Rev. Lett.* 73 (2 1994), pp. 336–339.

[168] K. Tanaka et al. “Linewidth broadening of optical precession mode in synthetic antiferromagnet”. In: *Appl. Phys. Express* 7.6 (2014), p. 063010.

[169] L. Gladczuk et al. “Study of spin pumping through alpha-Sn thin films”. In: *Phys. Status Solidi RRL* 15 (2021), p. 2100137.

[170] J. C. Slonczewski. “Current-driven excitation of magnetic multilayers”. In: *J. Magn. Magn. Mater* 159 (1996), pp. L1–L7.

[171] E. Saavedra, A. Riveros Rodriguez, and J. Palma. “Effect of nonuniform perpendicular anisotropy in ferromagnetic resonance spectra in magnetic nanorings”. In: *Sci. Rep* 11 (2021), p. 14230.

[172] M. Montazeri et al. “Magneto-optical investigation of spin–orbit torques in metallic and insulating magnetic heterostructures”. In: *Nat. Commun.* 6 (2015), p. 8958.

[173] A. Jenkins et al. “Single-spin sensing of domain-wall structure and dynamics in a thin-film skyrmion host”. In: *Phys. Rev. Mater.* 3 (8 2019), p. 083801.

[174] B. Miao et al. “Thickness-driven spin reorientation transition in ultrathin films”. In: *Sci. China Phys. Mech. Astron.* 56.1 (2013), pp. 70–84.

[175] J. Okabayashi et al. “Origin of perpendicular magnetic anisotropy in $Co_xFe_{3-x}O_{4+\delta}$ thin films studied by x-ray magnetic circular and linear dichroisms”. In: *Phys. Rev. B* 105 (13 2022), p. 134416.

[176] J Lindner and K Baberschke. “In situ ferromagnetic resonance: an ultimate tool to investigate the coupling in ultrathin magnetic films”. In: *J. Phys.: Condens. Matter* 15.4 (2003), R193.

[177] X. Li et al. “Predictive Materials Design of Magnetic Random-Access Memory Based on Nanoscale Atomic Structure and Element Distribution”. In: *Nano Lett.* 19.12 (2019), pp. 8621–8629.

[178] W. Li et al. “Anatomy of Skyrmionic Textures in Magnetic Multilayers”. In: *Adv. Mater.* 31 (2019), p. 1807683.

[179] J. Lindner et al. “Non-Gilbert-type damping of the magnetic relaxation in ultrathin ferromagnets: Importance of magnon-magnon scattering”. In: *Phys. Rev. B* 68.6 (2003), p. 060102.

[180] A. F. Franco and P. Landeros. “Ferromagnetic resonance of an heterogeneous multilayer system with interlayer exchange coupling: An accessible model”. In: *J. Phys. D: Appl. Phys.* 49 (2016), p. 385003.

[181] J. Sklenar and W. Zhang. “Self-Hybridization and Tunable Magnon-Magnon Coupling in van der Waals Synthetic Magnets”. In: *Phys. Rev. Appl.* 15 (4 2021), p. 044008.

[182] A. Layadi and J. Artman. “Study of antiferromagnetic coupling by ferromagnetic resonance (FMR)”. In: *J. Magn. Magn. Mater.* 176.2 (1997), pp. 175–182.

[183] A. Layadi. “Effect of biquadratic coupling and in-plane anisotropy on the resonance modes of a trilayer system”. In: *Phys. Rev. B* 65 (10 2002), p. 104422.

[184] R. Álvarez Nodarse, J. Petronilho, and N. Quintero. “Spectral properties of certain tridiagonal matrices”. In: *Linear Algebra Appl.* 436.3 (2012), pp. 682–698.

[185] M. Jalali et al. “Interlayer coupling of the Kittel mode and the perpendicular standing spin wave in magnetic multilayers”. In: *J. Magn. Magn. Mater.* 591 (2024), p. 171621.

[186] Z. Zhang et al. “Angular dependence of ferromagnetic resonance in exchange-coupled Co/Ru/Co trilayer structures”. In: *Phys. Rev. B* 50 (9 1994), pp. 6094–6112.

[187] Z. Celinski, K. B. Urquhart, and B. Heinrich. “Using ferromagnetic resonance to measure the magnetic moments of ultrathin films”. In: *J. Magn. Magn. Mater.* 166 (1997), pp. 6–16.

[188] S. Zhang et al. “Angular dependence of ferromagnetic resonance in exchange coupled Co/Ru/Co trilayer structures”. In: *Phys. Rev. B* 50 (1994), pp. 6094–6099.

[189] A. Layadi and J. O. Artman. “Ferromagnetic resonance in a coupled two-layer system”. In: *J. Magn. Magn. Mater.* 92 (1990), pp. 143–150.

[190] M Belmeguenai et al. “Microwave spectroscopy with vector network analyzer for interlayer exchange-coupled symmetrical and asymmetrical NiFe/Ru/NiFe”. In: *J. Phys.: Condens. Matter* 20.34 (2008), p. 345206.

[191] T. Martin et al. “Pulsed inductive measurement of ultrafast magnetization dynamics in interlayer exchange coupled NiFe/Ru/NiFe films”. In: *J. Appl. Phys.* 101.9 (2007), p. 09C101.

[192] C. A. Klausmeier. “Floquet theory: a useful tool for understanding nonequilibrium dynamics”. English. In: *Theor. Ecol.* 1.3 (2008), pp. 153–161.

[193] G. Yu et al. "Strain-induced modulation of perpendicular magnetic anisotropy in Ta/CoFeB/MgO structures investigated by ferromagnetic resonance". In: *Appl. Phys. Lett.* 106.7 (2015), p. 072402.

[194] A. Hubert and R. Schäfer. *Magnetic Domains: The Analysis of Magnetic Microstructures*. Berlin, Heidelberg: Springer, 1998, pp. 297–329.

[195] C. Kooy and U. Enz. "Experimental and theoretical study of the domain configuration in thin layers of $BaFe_{12}O_{19}$". In: *Philips Res. Rep.* 15 (1960), pp. 7–29.

[196] Z. Malek and V. Kambersky. "On the theory of the domain structure of thin films of magnetically uniaxial materials". In: *Czechoslov. J. Phys.* 8 (1958), pp. 416–423.

[197] L. Belliard et al. "Stripe domain morphology versus layer thickness in CoPt multilayers". In: *J. Appl. Phys.* 81 (1997), pp. 5315–5317.

[198] O. Acher et al. "Microwave permeability of ferromagnetic thin films with stripe domain structure". In: *J. Appl. Phys.* 81 (1997), pp. 4057–4063.

[199] A. Hubert and W. Rave. "How well defined are flux closure domains?" In: *J. Magn. Magn. Mater.* 196-197 (1999), pp. 325–328.

[200] S. Woo et al. "Observation of room-temperature magnetic skyrmions and their current-driven dynamics in ultrathin metallic ferromagnets." In: *Nat. Mater.* 15 5 (2015), pp. 501–6.

[201] W. Jiang et al. "Blowing magnetic skyrmion bubbles". In: *Science* 349.6245 (2015), pp. 283–286.

[202] G. Yu et al. "Room-Temperature Skyrmion Shift Device for Memory Application". In: *Nano Lett.* 17.1 (2017), pp. 261–268.

[203] A. R. McCluskey et al. "Advice on describing Bayesian analysis of neutron and X-ray reflectometry". In: *J. Appl. Crystallogr* 56.1 (2023), pp. 12–17.

[204] M. Lakshmanan. "The fascinating world of the Landau–Lifshitz–Gilbert equation: an overview". In: *Philos. Trans. R. Soc. A Math. Phys. Eng. Sci.* 369.1939 (2011), 1280–1300.

[205] G. Bertotti et al. "Nonlinear aspects of Landau–Lifshitz–Gilbert dynamics under circularly polarized field". In: *J. Magn. Magn. Mater.* 226-230 (2001), pp. 495–497.

[206] A. V. Chumak et al. "Magnon spintronics". In: *Nat. Rev. Mater.* 3.7 (2018), pp. 57–64.

[207] A. V. Chumak. “Magnonics: From fundamentals to applications”. In: *Spintronics Handbook: Spin Transport and Magnetism*. Ed. by I. Zutic, J. Fabian, and S. Das Sarma. 2nd. Boca Raton, FL: CRC Press, 2019, pp. 247–302.

[208] B. Flebus et al. “The 2024 magnonics roadmap”. In: *J. Phys.: Condens. Matter* 36.36 (2024), p. 363501.

[209] W. Porod. *Let Physics Do the Computing: Analog Computation Revisited*. Keynote, Int. Symp. Circuits Syst. Des. (ISCASD). 2020.

[210] G. Csaba et al. “Non-Boolean Computing Based on Linear Waves and Oscillators”. In: *2015 45th Eur. Solid-State Device Res. Conf. (ESSDERC)*. IEEE, 2015, pp. 212–215.

[211] A. Papp, W. Porod, and G. Csaba. “Nanoscale neural network using non-linear spin-wave interference”. In: *Nat. Commun.* 12 (2021), p. 6422.

[212] N. Zenbaa et al. “A universal inverse-design magnonic device”. In: *Nat. Electron.* 8 (2025), pp. 106–115.

[213] G. Csaba, A. Papp, and W. Porod. “Perspectives of using spin waves for computing and signal processing”. In: *Phys. Lett. A* 381.17 (2017), pp. 1471–1476.

[214] A. Papp et al. “Nanoscale spectrum analyzer based on spin-wave interference”. In: *Sci. Rep.* 7 (2017), p. 9245.

[215] Q. Wang et al. “A magnonic directional coupler for integrated magnonic half-adder”. In: *Nat. Electron.* 6 (2023), pp. 112–119.

[216] S. Stepney. “The neglected pillar of material computation”. In: *Physica D* 237.9 (2008), pp. 1157–1164.